

An Investigation into the Drug Release Mechanisms of Polymeric Solid Dispersions



University of East Anglia

Salman Mohammad Abdur Rahman
School of Pharmacy
June 2020

Thesis submitted for the fulfilment of degree of Doctor of Philosophy at the
University of East Anglia

© This copy of the thesis has been supplied on the condition that anyone who consults it is understood to recognise that its copyright rests with the author and that use of any information derived therefrom must be in accordance with current UK Copyright Law. In addition, any quotation or extract must include full attribution

Acknowledgement

First and foremost, I would like to thank **Allah** for giving me the perseverance and ability to help me through a challenging time of my life and enabling the completion of the PhD.

I would like to graciously thank my primary supervisor **Dr Sheng Qi** and my secondary supervisor **Professor Peter Belton** for having given me their utmost supervision, encouragement, patience, and support throughout my PhD in the best and worst of times. I would also like to extend my gratitude to the numerous faculty members in the school of pharmacy, namely to **Dr Laszlo Fabian** for enriching my knowledge and capabilities in the field of computational pharmaceutics, to **Dr Chris Morris** for helping me have fun learning much of biochemistry, and to **Professor Yaroslav Khimyak** for keeping my sense of humour alive and challenging me to think more critically. I would also like to thank **Dr Robert Whittaker** from the school of mathematics, with whom I had many long and interesting discussions about the mathematical aspects of my project. I would also like to thank the school of computer sciences for giving me access to their high performance computing and graphics laboratory for performing simulations.

I would like graciously thank my fellow PhD students in the drug delivery group: **Jehad Nasereddin, Zuzana Hlaskova, Fahad Alqahtani**, who helped me in the lab and the office in all capabilities, and especially to **Sherif Hamdallah, Randa Zoqlam, and Chak Tam** for taking the time to read my thesis out of their busy schedule. I would like to extend my gratitude to the postdoctoral staffs: **Dr Muqdad Alhijaj** and **Dr Janine Wilkinson** who have provided additional mentoring and guidance in the lab. I would also like to thank the numerous visiting and project students who helped me throughout my PhD collecting and analysing parts of my data as part of their project.

Lastly, I would like to thank my family, especially my **mother**, for keeping me motivated and supported me through the good and bad times of my PhD.

ABSTRACT

Personalised polypills, which includes multiple drugs in a single pill tailored for individual patients, has gained a lot of research interests with the emergence of pharmaceutical 3D printing. A distinct feature of polypill is to be able to release each drug in a controlled manner. However, currently, there are limited tools to aid the design of such solid dosage forms with desired drug release kinetics. In this work, the drug release mechanisms of a wide range of solid dispersions formed using polymers and model drugs covering a wide range of physicochemical properties were investigated to generate a large dataset with an attempt to develop a simulation strategy for achieving a desired drug release profile.

Building a dataset and using the dataset toward simulation building the data to be reproducible and reliable. The sources of errors throughout the manufacturing and the performance measurements of 3D printed example solid dosage forms were first investigated to assess the reproducibility and reliability of the experimental data generated to build the dataset. This was the focus of chapter 3. Thereafter, chapter 4 systematically investigated the behaviour of a wide range of pure polymers to enable the prediction of the behaviour of polymer blends. The polymer behaviour studied include hydration, swelling, and erosion. Addition of the drug and investigating the effect on formulation behaviour was the focus of chapter 5. Chapter 6 used statistical approaches such as principal component analysis as a factor reduction technique and *K*-means clustering to classify the behaviour of the polymer-drug dispersions. These statistical approaches successfully demonstrated that correlating polymer behaviours and drug release profiles can be used to predict the selection of polymer(s) for a given drug to achieve a desired drug release profile. Further upscaling of the dataset is crucial to enhance analysis.

Access Condition and Agreement

Each deposit in UEA Digital Repository is protected by copyright and other intellectual property rights, and duplication or sale of all or part of any of the Data Collections is not permitted, except that material may be duplicated by you for your research use or for educational purposes in electronic or print form. You must obtain permission from the copyright holder, usually the author, for any other use. Exceptions only apply where a deposit may be explicitly provided under a stated licence, such as a Creative Commons licence or Open Government licence.

Electronic or print copies may not be offered, whether for sale or otherwise to anyone, unless explicitly stated under a Creative Commons or Open Government license. Unauthorised reproduction, editing or reformatting for resale purposes is explicitly prohibited (except where approved by the copyright holder themselves) and UEA reserves the right to take immediate 'take down' action on behalf of the copyright and/or rights holder if this Access condition of the UEA Digital Repository is breached. Any material in this database has been supplied on the understanding that it is copyright material and that no quotation from the material may be published without proper acknowledgement.

Table of Contents

Chapter 1: Introduction	1
1.1 Background.....	2
1.1.1 Hot Melt Extrusion (HME)	2
1.1.1.1 Types of extruders & Extrusion process.....	2
1.1.1.2 Materials for HME	4
1.1.2 Fused Deposition Modeling 3D printing (FDM 3DP)	6
1.1.2.1 Pharmaceutical applications of HME coupled with 3D printing	7
1.1.2.2 Commercialization Limitations.....	8
1.1.3 Solid dispersions.....	10
1.1.3.1 Eutectic Type	12
1.1.3.2 Amorphous precipitation	14
1.1.3.3 Solid solutions	14
1.1.3.4 Glass suspension and Glass solutions	16
1.1.3.5 Complex formation	16
1.1.3.6 Phase behaviour of solid dispersions	17
1.2 Main scope of this project.....	21
1.2.1 Polymer behaviour in aqueous media	21
1.2.1.1 Hydration.....	23
1.2.1.2 Swelling	24
1.2.1.3 Erosion.....	26
1.2.2 Drug release behaviour of solid dispersions	29
1.2.3 Predicting drug release profiles	33
1.2.4 Objectives of the research	34
Chapter 2: Materials and Methods	36
2.1 Introduction.....	36
2.2 Materials	36
2.2.1 Paracetamol (PCM)	36
2.2.2 Lidocaine (LID)	37
2.2.3 Ibuprofen (IBU).....	37
2.2.4 Hypromellose acetate succinate (HPMCAS)	38
2.2.5 Zein.....	39
2.2.6 Poly (Ethylene Oxide) (PEO)	40
2.2.7 Poly-(Vinyl Alcohol) (PVA)	41
2.2.8 Poly (ϵ -caprolactone) (PCL)	42
2.2.9 Poly (vinylpyrrolidone-co-Vinyl Acetate) (PVPVA)	42

2.2.10 Eudragit® RS 100	43
2.2.11 Soluplus®	44
2.2.12 Xanthan Gum (XG).....	44
2.2.13 Acrylonitrile butadiene styrene (ABS)	45
2.3 Processing methods	46
2.3.1 Hot Melt Extrusion (HME)	46
2.3.2 FDM 3D Printing (FDM 3DP).....	46
2.4 Material characterisation methods.....	47
2.4.1 Differential scanning calorimetry (DSC)	47
2.4.2 Thermogravimetric Analysis (TGA).....	49
2.4.3 Fourier transform infrared (FTIR).....	50
2.4.4 Ultraviolet Spectrophotometry (UV-vis)	52
2.4.5 Drug Loading Efficiency	53
2.4.6 In vitro dissolution studies	54
2.5 Advanced Statistical Methods.....	55
2.5.1 K-means Clustering.....	56
2.5.2 Principal Component Analysis (PCA)	56
2.5.3 Artificial Neural Network (ANN).....	58
Chapter 3: Investigation into the origins of errors in drug release measurements of polymeric solid dispersions prepared by FDM 3D printing.....	60
3.1 Introduction.....	60
3.1.1 Accuracy vs Precision	61
3.1.2 Types of errors	61
3.2 Materials	62
3.3 Methods	63
3.3.1 Hot melt extrusion (HME)	63
3.3.1.1 Drug content uniformity of the HME extrudates	63
3.3.2 FDM 3D Printing	64
3.3.2.1 Reproducibility of 3DP torus	65
3.3.2.2 Weight uniformity	66
3.3.2.3 In vitro drug release studies	66
3.3.2.4 Calculation of cumulative error in drug release data.....	66
3.4 Results and discussion.....	69
3.4.1 Characterization of samples.....	69
3.4.2 In vitro drug release studies.....	69
3.4.3 HME Studies	73
3.4.3.1 Measuring drug content uniformity of HME.....	73
3.4.4 FDM 3DP studies	75

3.4.4.1	Reproducibility of FDM 3DP object dimension	75
3.4.4.2	Weight uniformity	79
3.4.5	Cumulative error in drug release	81
3.4.5.1	Case I: δM_0 from 3DP tori volume measurements	81
3.4.5.2	Case II: δM_0 from 3DP tori mass measurements	82
3.4.6	Process Optimization	83
3.5	Limitations	84
3.6	Conclusion	85
	Chapter 4: Characterisation of the polymers and polymer blends behaviour in aqueous media	86
4.1	Introduction.....	86
4.2	Materials and Methods	87
4.2.1	Preparation of Filaments.....	87
4.2.2	Measurement of Polymer behaviour	88
4.2.3	Characterization of polymer blends.....	89
4.3	Results and Discussion	90
4.3.1	Overview of polymer behaviour in aqueous media	90
4.3.2	Hydration behaviour	93
4.3.3	Swelling behaviour	97
4.3.4	Erosion behaviour	100
4.3.5	Characterization of blends	102
4.3.6	Miscible and semi-miscible blend behaviour	103
4.3.7	Towards predicting polymer blend behaviour in aqueous media	108
4.3.8	Categorization summary	113
4.4	Limitations of the study	116
4.5	Conclusion	116
	Chapter 5: Categorizing the effect of drug types on polymer behaviour	118
5.1	Introduction.....	118
5.2	Materials and methods	118
5.2.1	Preparation of filaments	119
5.2.2	Measurement of factors	119
5.2.3	Choice of polymers and drugs.....	119
5.3	Results and Discussion	120
5.3.1	Effect of Ionisation state of the model drug on drug release of solid dispersions	130
5.3.1.1	Case I	130
5.3.1.2	Case II	131
5.3.1.3	Case III	132
5.3.2	Effect of ionisation state of the model drug on polymer hydration (positive weight change).....	133
5.3.3	Effect of drug loading on polymer hydration	138

5.3.4 Effect of ionisation on polymer swelling.....	140
5.3.5 Effect of drug loading on polymer swelling	143
5.3.6 Effect of ionisation state of the model drug on polymer erosion.....	144
5.3.7 Effect of ionisation on overall polymer behaviour.....	146
5.4 Conclusion	147
Chapter 6: Classification of drug release profiles.....	149
6.1 Introduction.....	149
6.2 Methods	150
6.2.1 Clustering	150
6.2.2 Principal component analysis (PCA).....	150
6.2.3 Artificial neural network (ANN).....	151
6.3 Result and discussion	151
6.3.1 Polymers classification	151
6.3.2 Drug release curves classification	153
6.3.3 Relating polymer behaviour clusters to drug release clusters.....	159
6.3.4 Scenario I.....	160
6.3.5 Scenario II.....	161
6.3.6 ANN as a predictor refinement technique	163
6.4 Limitations	165
6.5 Conclusion	165
Chapter 7: Conclusion remarks and future outlook	167
7.1 Reproducibility	167
7.2 Predictability	170
7.3 Future works	172
7.3.1 Scaling	172
7.3.2 Simulation	173
7.3.3 Personalization.....	174
Reference	176
Appendix	193
DSC thermograms	193
FTIR spectra	200

List of Figures

Figure 1-1: (a) SSE with one screw and one shaft and TSE two screws on two shafts. (b) the two types of twin screws for TSE. (c) top: intermeshing screws, middle: intermeshing counter-rotating, and bottom: non-intermeshing counter-rotating screws. Adapted from reference (6, 8).	3
Figure 1-2: HME schematic (6).	4
Figure 1-3: Schematic illustration of the FDM 3D printing technology. Adapted from reference (28).	6
Figure 1-4: Schematic of HME followed by 3DP as a single continuous process. The output can be FDM 3D printed tablets (right) or polypill (left). Adapted from reference (38).	8
Figure 1-5: Natural fiber filament problems that may be encountered in FDM 3DP and the possible solutions (56).	10
Figure 1-6: The different states of drug molecule in the polymer (61).	11
Figure 1-7: Solid dispersion classification based on properties and number of categories in each in brackets (67).	12
Figure 1-8: Phase diagram of Eutectic mixtures of substance A and B. Adapted from reference (60).	13
Figure 1-9: (Left) Continuous solid solution. (Right) Discontinuous solid solution (84).	15
Figure 1-10: (Left) Substitutional solid solution crystal lattice and (right) interstitial solid solution. Black circles=Solute molecule and white circle=solvent molecules (60).	15
Figure 1-11: Volume of various states of materials as affected by temperature (117).	19
Figure 1-12: Schematic plots of shifts expected in Tg for the three blend scenarios (123).	21
Figure 1-13: Schematic of the surface layer of a polymer during dissolution. The chain disentanglement is in opposite direction to solvent diffusion. Adapted from reference (126).	22
Figure 1-14: Illustrations of swelling cases. The top is Case I transport, the middle is anomalous transport, and the bottom is Case II transport (143).	26
Figure 1-15: The combination of processes leading to erosion (153).	27
Figure 1-16: A) Surface erosion and (B) Bulk erosion. The strength, mass, and MW due to erosion in both cases are shown (156, 164).	29
Figure 1-17: Diffusion controlled monolithic geometries. C_{ini} is the initial concentration and C_s is the saturation concentration (184).	32
Figure 2-1: The classification of cellulose based polymers. HPMCAS is categorized as cellulose succinate encircled in red (224).	38
Figure 2-2: HPMCAS structure	39
Figure 2-3: PEO structure	40
Figure 2-4: PVA structure	41
Figure 2-5: PCL structure	42
Figure 2-6: PVPVA structure	43
Figure 2-7: Eudragit RS structure. The R groups are from reference (277).	44
Figure 2-8: Soluplus structure.	44
Figure 2-9: XG structure. From reference (291).	45
Figure 2-10: Chemical structures of ABS raw materials.	46
Figure 2-11: Schematic of the furnace interior of a heat flux DSC (298).	48
Figure 2-12: Schematics of power compensated DSC (298).	48
Figure 2-13: DSC thermogram showing thermal kinetic events. The area under the curve can be calculated to give the enthalpy of the event (298).	49
Figure 2-14: Schematic of a Michelson interferometer (306).	51
Figure 2-15: a) ATR crystal schematic. b) DRIFTS measurement schematic. Adapted from (306, 310)	52
Figure 2-16: UV data capture process (313).	53
Figure 2-17: USP Apparatus II as described by USP standards (318).	55
Figure 2-18: Standard K-means algorithm (319).	56

Figure 2-19: Original data in cartesian coordinates on the left and the output on the right after PCA is performed. The transformed coordinates are in term of PC1 and PC2, which are the two axes (322).	57
Figure 2-20: Scree plot of 12 components. The red dashed line indicates the threshold for retention. Three of the components have eigenvalues greater than 1 and are therefore retained for analysis. This means the creation of loading plots, in this case, will be with three axes, PC1, PC2, and PC3.	58
Figure 2-21: a) A mammalian neuron. The black rectangle signifies the input layer while the blue signifies the output. The nodes and sheath are the hidden layer. (b) ANN computational structure Z_m is the input, W_{lm} is the weighting of features, and $f_n(z)$ is the output. Adapted from reference (327)	59
Figure 3-1: Mapping the error process pathway of drug release and optimization	60
Figure 3-2: The four outcomes of varying accuracy and precision	61
Figure 3-3: Measurement concept of errors from probability curves. Adapted from reference (343).....	62
Figure 3-4: Schematic of filament sampling. Red dots indicate 1cm (not shown in triplicates) samples taken at 5cm interval indicated by the red rectangle across the filaments.	64
Figure 3-5: Elliptical cylinder where a is the semi-major axis; b is the semi-minor axis, and L is the length ...	64
Figure 3-6: a) In polar coordinates, the diffusion occurs in one dimension in the radial direction (r) indicated by the blue arrows while is θ the angle at which the radial diffusion takes place. b) The starting cylinder if curved and joined end to end forms a torus which is effectively an infinite cylinder.	65
Figure 3-7: Inner radius (r) and outer radius (R) for torus V and SA calculation. A is the annulus (the diameter of the ring) and is equal to the height (h). D is the diameter of the torus.....	66
Figure 3-8: UV absorbance distribution for 15 μ g/ml sample over ten repeated measurements. The dotted line is the measured mean.	70
Figure 3-9: UV absorbance distribution of ten samples. The dotted line is the measured mean.	71
Figure 3-10: A percentwise in terms of the that affects the UV spectrometer.	72
Figure 3-11: Convergence of δA_s . The solid curve represents the maximum and minimum absorbance ($A \pm \delta A$) at various sample sizes. The dotted-dashed line represents the mean absorbance that is reached at large sample sizes. The double line is the UV absorbance limit at 1AU. The scope of the graph has been cut to 1000 samples. Beyond this, the graph is asymptotic and the change is gradual.	72
Figure 3-12: Measurement concept for HME weight uniformity at 170°C. Blue dashed line marks the true (target) value that is theoretically expected. The red dashed line is the EXP mean. The black dashed curve is the probability distribution curve.	74
Figure 3-13: Error subtypes for HME processing temperature. The 5 or 10 in brackets beside temperature indicate the residence time. The trendline fitted to 5 minutes is shown on the bottom left while the trendline for 10 minutes is on the bottom right.	75
Figure 3-14: Cooling gradient from the object (black torus shape) while successive layers are being deposited. The arrows represent outgoing convection. A greater thickness of the arrow represents higher heat flux. The lateral side will always shrink the fastest and prone to have the highest deviation. Red region shows the most heated area while the yellow region shows the cooler moderate region and the green region shows the lowest heated area.	76
Figure 3-15: a) Ten ABS tori. b) A closeup of torus # 10 showing the double printing effect upon solidification.	77
Figure 3-16: Measurement concept for the diameter of PVA. The blue dashed line marks the true value expected from THRY specification. The red dashed line is the EXP mean. The black dashed curve is the probability distribution curve.....	78
Figure 3-17: Error types categorized for 3DP resolution in x , y , and z directions.....	79
Figure 3-18: Weight vs volume distribution of the printed tori from the two polymers.....	80
Figure 3-19: The absolute error in drug release attainable at each sample time point. The red solid curve represents absolute error from the volume calculations of 3DP oral dosage while the red dashed line represents absolute error from the mass calculations from 3DP oral dosage.	82
Figure 3-20: drug release of PCM under optimized manufacture process condition. The red curve is the possible error bound for this drug release profile.	83

Figure 4-1: The filament cross-section in 3D perspective. Length is denoted by (l) while the diameter is denoted by (d).....	89
Figure 4-2: Mass and volume changes with the time of polymers in pH 1.2. The polymers that do not show any changes are omitted (PCL, Eudragit, and HPMCAS). The axis for all graphs has been replaced with a generic $(X-X_0)/X_0$. For hydration, the generic $(X-X_0)/X_0$ is $(M_t-M_0)/M_0$ where the M has been stated in equation 4-1. For volume, the generic $(X-X_0)/X_0$ is $(V_t-V_0)/V_0$ where the V parameters have been stated equation 4-3. For erosion, the generic $(X-X_0)/X_0$ is $(M_t-M_0)/M_0$ where the M has been stated in equation 4-4. Erosion is plotted in reverse from a ratio of 1 eroding to a final ratio of 0. The solid lines/dashed line presented here are only connecting data points.....	91
Figure 4-3: Mass and volume with time of polymers in pH 6.8. The polymers that do not show any changes are omitted (PCL and Eudragit). The axis for all graphs have been replaced with a generic $(X-X_0)/X_0$. For hydration, the generic $(X-X_0)/X_0$ is $(M_t-M_0)/M_0$ where the M have been stated in equation 4-1. For volume, the generic $(X-X_0)/X_0$ is $(V_t-V_0)/V_0$ where the V parameters have been stated equation 4-3. For erosion, the generic $(X-X_0)/X_0$ is $(M_t-M_0)/M_0$ where the M have been stated in equation 4-4. The solid lines/dashed line presented here are only connecting data points.	92
Figure 4-4: Top) The hydration ratio all the nine polymers in pH 1.2. Bottom) The hydration ratio all the nine polymers in pH 6.8. The timescale for non-hydratable polymers have been shortened.	95
Figure 4-5: a) Schematic representation of diffusion, erosion and swelling fronts and different layers of swelling dosage (179). (b) PEO exhibiting swelling front and erosion front. (c) Xanthan gum without a clear swelling front.....	97
Figure 4-6: The swelling ratios of swellable polymers in pH 1.2 on top and pH 6.8 at the bottom.	99
Figure 4-7: Top) The erosion ratio of eroding polymers in pH 1.2. Bottom) the erosion ratio of erodible polymers in pH 6.8	101
Figure 4-8: DSC thermogram of the HPMCAS (red), Soluplus (black), and HPMCAS-Soluplus 50/50 blend (blue). The T_g is shown on the thermogram, and with the corresponding polymer colours.	102
Figure 4-9: DSC of HPMCAS (green dash), PEO (red line), and HPMCAS-PEO 50/50 blend (black line). The melting and recrystallization temperatures and the corresponding enthalpies are given (J/g) while the T_g for HPMCAS is given.....	103
Figure 4-10: Top left) Hydration ratios of HPMCAS/Soluplus compared to pure polymers in pH 1.2. Top right) Hydration ratios of HPMCAS/PEO and pure polymer in pH 1.2. Bottom left) Swelling ratios of HPMCAS/Soluplus and pure polymer in pH 1.2. Bottom right) Swelling ratios of HPMCAS/PEO and pure polymer in pH 1.2. pH 6.8 exhibits negative hydration (erosion) for the blends and have been omitted here. The grey last data point for some polymers indicates the beginning of erosion. HPMCAS, being insoluble has data over longer duration but this has been omitted as it is constant at a ratio of zero.	105
Figure 4-11: The erosion ratios for miscible HPMCAS/soluplus 50/50 in pH 1.2 (red) and pH 6.8 (blue) and the polymers individually.	107
Figure 4-12: HPMCAS/Soluplus experimental vs calculated hydration and swelling ratios in pH 1.2 and 6.8	109
Figure 4-13: HPMCAS/PEO experimental vs calculated hydration and swelling ratios in pH 1.2 and 6.8	110
Figure 4-14: Experimental and calculated erosion ratios of HPMCAS/Soluplus and HPMCAS/PEO in pH 1.2 and pH 6.8	112
Figure 5-1: Drug release and HPMCAS behaviour for lidocaine formulations. The generic ratio $((X-X_0)/X_0)$ has been presented, which can be substituted by wet mass in the case of hydration, volume in the case of swelling, and dry mass in the case of erosion. the drug release is plotted on the secondary y-axis. Erosion is always plotted in inverse increasing from an initial ratio of 1.....	121
Figure 5-2: Drug release and HPMCAS behaviour for ibuprofen formulations. The generic ratio $((X-X_0)/X_0)$ has been presented, which can be substituted by wet mass in the case of hydration, volume in the case of swelling, and dry mass in the case of erosion. the drug release is plotted on the secondary y-axis. Erosion is always plotted in inverse increasing from an initial ratio of 1.....	122

Figure 5-3: Drug release and HPMCAS behaviour for paracetamol formulations. The generic ratio $((X-X_0)/X_0)$ has been presented, which can be substituted by wet mass in the case of hydration, volume in the case of swelling, and dry mass in the case of erosion. the drug release is plotted on the secondary y-axis. Erosion is always plotted in inverse increasing from an initial ratio of 1.....	123
Figure 5-4: Drug release and zein behaviour for lidocaine formulations. The generic ratio $((X-X_0)/X_0)$ has been presented, which can be substituted by wet mass in the case of hydration, volume in the case of swelling, and dry mass in the case of erosion. the drug release is plotted on the secondary y-axis. Erosion is always plotted in inverse increasing from an initial ratio of 1.....	124
Figure 5-5: Drug release and zein behaviour for ibuprofen formulations. The generic ratio $((X-X_0)/X_0)$ has been presented, which can be substituted by wet mass in the case of hydration, volume in the case of swelling, and dry mass in the case of erosion. the drug release is plotted on the secondary y-axis. Erosion is always plotted in inverse increasing from an initial ratio of 1.....	125
Figure 5-6: Drug release and zein behaviour for paracetamol formulations. The generic ratio $((X-X_0)/X_0)$ has been presented, which can be substituted by wet mass in the case of hydration, volume in the case of swelling, and dry mass in the case of erosion. the drug release is plotted on the secondary y-axis. Erosion is always plotted in inverse increasing from an initial ratio of 1.....	126
Figure 5-7: Drug release and PEO behaviour for lidocaine formulations. The generic ratio $((X-X_0)/X_0)$ has been presented, which can be substituted by wet mass in the case of hydration, volume in the case of swelling, and dry mass in the case of erosion. the drug release is plotted on the secondary y-axis. Erosion is always plotted in inverse increasing from an initial ratio of 1.....	127
Figure 5-8: Drug release and PEO behaviour for ibuprofen formulations. The generic ratio $((X-X_0)/X_0)$ has been presented, which can be substituted by wet mass in the case of hydration, volume in the case of swelling, and dry mass in the case of erosion. the drug release is plotted on the secondary y-axis. Erosion is always plotted in inverse increasing from an initial ratio of 1.....	128
Figure 5-9: Drug release and PEO behaviour for paracetamol formulations. The generic ratio $((X-X_0)/X_0)$ has been presented, which can be substituted by wet mass in the case of hydration, volume in the case of swelling, and dry mass in the case of erosion. the drug release is plotted on the secondary y-axis. Erosion is always plotted in inverse increasing from an initial ratio of 1.....	129
Figure 5-10: Schematic overview of the charge of zein, lidocaine, and ibuprofen. The pH scale has only been shown until pH 8. Beyond this, any charge attained was not part of the experimental pH. Paracetamol was omitted as it is neutral in all pH. The dashed line shows the two pH at which studies were performed.	132
Figure 5-11: HPMCAS hydration ratio and HPMCAS formulation hydration ratios in pH 1.2.....	134
Figure 5-12: Top) PEO hydration ratio and PEO formulation ratios in pH 1.2. Bottom) PEO hydration ratio and PEO formulation hydration ratio in pH 6.8.	136
Figure 5-13: Top) zein hydration ratio and zein formulation ratios in pH 1.2. Bottom) Zein hydration ratio and zein formulation hydration ratios in pH 6.8.....	137
Figure 5-14: HPMCAS formulation hydration ratio in pH 1.2. Hydration ratios are not shown for pH 6.8 as no hydration but erosion takes place of the formulation.....	138
Figure 5-15: Formulation hydration ratio and time to reach hydration ratio comparison. A weight ratio above 1 indicates faster hydration while between 0 and 1 indicates slower hydration. Negative ratio is indicating erosion. The time ratio (secondary axis) indicates how fast the higher drug loading caused the formulation to reach the maximum hydrated ratio. The time ratio (H30%/H10%) is the time of maximum hydration ratio at 30% drug loading divided over maximum hydration ratio at 10% drug loading. A value of less than 1 indicates faster swelling for the 30% formulation.....	140
Figure 5-16: Top) Zein and zein formulation swelling ratios in pH 1.2. Bottom) Zein and zein formulation swelling ratios in pH 6.8.....	141
Figure 5-17: Top) PEO and PEO formulation swelling ratios in pH 1.2. Bottom) PEO and PEO formulation swelling ratios in pH 6.8.....	142
Figure 5-18: Swelling ratio comparison for swellable formulations. The time ratio (secondary axis) indicates how fast the higher drug loading caused the formulation to reach the maximum swelling ratio. A volume ratio above 1 indicates faster swelling while between 0 and 1 indicates slower swelling.....	143

Figure 6-1: Top) The integration of chapter 4 and chapter 5 data to classify the data. The dashed line indicates separation. Bottom) The logical pathway of investigation when the drug and drug release duration is provided for achieving a desired drug release profile.	149
Figure 6-2: Top left) Formulation curves in pH 1.2. Top right) Formulation curves in pH 6.8. Bottom left) PCA performed curve in pH 1.2. Bottom right) PCA performed curve in pH 6.8	155
Figure 6-3: PCA rotated loading plot of formulations in pH 1.2. Greater values of PC 1 possibly represent longer release times of formulations and greater PC 2 values possibly represent higher amounts of drug released of the formulations. The rotation method chosen was Varimax rotation. K-means Clustering was done on the points. Clusters numbers are labelled below the cluster.	156
Figure 6-4: PCA rotated loading plot of formulations in pH 6.8. Greater values of PC 1 possibly represent higher amounts of drug released of the formulations and greater PC 2 values possibly represent longer release times of formulations. The rotation method chosen was Varimax rotation. K-means Clustering was done on the points. Clusters numbers are labelled below the cluster.	158
Figure 6-5: Concept of associating polymer behaviour with drug release	159
Figure 6-6: PEO-lidocaine experimental and predictor curve compared in pH 1.2	161
Figure 6-7: Some drugs in the BCS system	162
Figure 6-8: Paracetamol loaded zein formulation and predictor curve compared in pH 1.2	163
Figure 6-9: ANN performed for the output of drug release time in pH 1.2 with four inputs. The bias is automatically added by ANN.	164
Figure 6-10: Normalized ranking of input factors from ANN	164
Figure 7-1: HME-3DP as a continuous process. The die through which filament exits the HME is also the beginning of the 3D printing process. Adapted from reference (457).	168
Figure 7-2: The individual sample in different positions during the dissolution after the sample was introduced. The individual drug release profile is shown before the mean is calculated.	169
Figure 7-3: Problems encountered with small datasets for analysis. Type I error is the rejection of a true null hypothesis while a type II error is the acceptance of a false null hypothesis, which occurs in statistical hypothetical testing.	173
Figure 7-4: Possible milestones to achieving a personalised drug release profile	173
Figure 7-5: Top) Animation of drug particle releasing from a torus using blender software. Three snapshots of the torus are shown at different times. The arrow shows the progression of time for the snapshots. Bottom) The accompanying generated drug release profile.	174
Figure 7-6: Concept of a torus polypill designed to have different release profiles. The drug release profile for drug 1 is an example of a periodic drug release profile. The dashed line indicates the continuation of the formulation not visible on the diagram plane.	175

List of tables

Table 1-1: Common plasticizers used in oral dosage (10).....	5
Table 1-2: Classification of the six solid dispersion types. For the states, C=crystalline, A=amorphous, and M=molecularly dispersed. Adapted from reference (57).	12
Table 1-3: Tg theory with advantages and disadvantages (97).....	17
Table 1-4: Summary of free volume numbers from four models (97).....	18
Table 2-1: Physical properties of the three model drugs.....	37
Table 2-2: The succinate and acetyl group ratios in different HPMCAS grades and their soluble pH (225, 228).	38
Table 3-1: Materials used as per error study aspects summarized.	63
Table 3-2: The variations of calibration and the goodness of fit (R^2) measuring the three curves in deionized water. y is the absorbance and x is the corresponding concentration obtained from best fits.	70
Table 3-3: Drug w/w of filament cut samples at the two residence times and various temperatures.	73
Table 3-4: Tori dimension comparison. THRY denotes design specification while EXP denotes experimental measurement.	75
Table 3-5: Curve fitted parameters using Peppas model for drug release profile.....	84
Table 4-1: Polymer extrudates at their temperatures with behaviors observed	87
Table 4-2: Vangernaud model fitted to hydratable polymers.	97
Table 4-3: The swollen polymers fitted to the generalized model and their goodness of fit (R^2). K_s is the swelling constant and n is the swelling index.	100
Table 4-4: The erosion rates of erodible polymers in both pH fitted to exponential decay.....	100
Table 4-5: Hydration parameters fitted to the Vangernaud model in pH 1.2. (*) indicates the error here is omitted as it is too small.	106
Table 4-6: swelling constant (S_k) and swelling mechanism for the blends in both pH. Cases of no swelling are denoted by -	106
Table 4-7: The erosion constant of the polymers and blends in both pH and the goodness of fit	106
Table 4-8: Blend and polymer kinetics. The (*) indicates no while the (✓) indicates yes for the category of the row.	111
Table 4-9: Polymer swelling and solubility in pH 1.2 and pH 6.8 given by yes (Y) or no (N).....	114
Table 4-10: The peak hydration and swelling times of the polymer and blend in pH 1.2 and pH 6.8.....	114
Table 4-11: Polymer kinetics dataset of hydration, swelling, and erosion in pH 1.2 and pH 6.8	115
Table 5-1: The % of charged species of the drugs in the buffers. The charged form of the drug in the buffer is given by column 3.	120
Table 5-2: Drug release constant (K_D) \pm SD and the mechanism of release of the formulations in pH 1.2 and pH 6.8. t_{50} is the half release time that allows for comparison.	133
Table 5-3: The swelling constant (K_s), the swell index(n), and their goodness of fit (R^2) for polymers and drug loadings in pH 1.2 and pH 6.8.	144
Table 5-4: Erosion rates ($E_k \pm SD$) of polymers and formulations in pH 1.2 and pH 6.8.	146
Table 5-5: Polymer behaviour compared for ionised drug loadings. The arrows indicate if the factor is increasing or decreasing as a result. The = sign denotes change of the same magnitude. N/A is noted when the specific factor does not apply to the polymer.	148
Table 6-1: Hydration t_{50} of polymers.....	152
Table 6-2: Swelling t_{50} of polymers	152
Table 6-3: Erosion t_{50} of polymers.....	152

Table 6-4: Clusters of all factors for pH 1.2. Polymers of the factors clustered are displayed in the cell unit. The cluster category row indicates the interpretation of each cluster for the preceding factor in the row..	152
Table 6-5: Clusters of all factors for pH 6.8. Polymers of the factors clustered are displayed in the cell unit. The cluster category row indicates the interpretation of each cluster for the preceding factor.	153
Table 6-6: Component matrix in pH 1.2	154
Table 6-7: Component matrix in pH 6.8	154
Table 6-8: Polymer categorization from PCA components for drug release	157
Table 6-9: K-means cluster centres for factors from K-means clustering in pH 1.2 and pH 6.8.	159
Table 6-10: Clusters relating polymer behaviour and drug release summarized. The basis of effect interpretation (low, high, etc.) is based on the cluster distinction as noted in Table 6-4 and Table 6-5. The effect interpretation of release time and amount from the clustering of the loading plot is introduced here.	160
Table 7-1: Summary of the types of irreproducibility and the proposed solution in each case.	170

Chapter 1: Introduction

Since the 1950s, there has been accumulative evidence indicating a substantial account of variability for drug response is genetically determined with age, nutrition, health status, environmental exposure, epigenetic factors, and concurrent therapy was proposed and formed the foundation of the modern practice of personalised therapy (1). Therefore, a new discipline arose from genetics, biochemistry, and pharmacology known as pharmacogenetics. The continuous development of this new field led to and guides the modern practice of personalized medicine. The aim of personalized medicine is simply to tailor drug therapy with the best response and safety margin to ensure the most effective clinical outcome for each patient (2). While much of the vision of personalized medicine can be attributed to advancement in genetics, the implementation of personalized medicine requires the advancements in the pharmaceutical materials science and processing to enable viable methods to cost-effectively produce small batch personalised medicine to meet each patient's needs. Additive manufacturing methods such as fused deposition modelling 3D printing has demonstrated the potential as a manufacturing tool to enable such small batch production. The process is operated by using a 3D digital design to guide the layer-by-layer production of each single dosage form (3). However, for the pharmaceutical field, currently, there is no systematic formulation approach that can rapidly provide the design that can tailor the drug and the drug release pattern to the needs of each patient.

This project initiated by examining the accuracy of the FDM 3D printing process. The research then moved the focus on to developing a prediction approach which allows the formulation scientists to rapidly develop suitable solid dispersion based formulation tailored for each patient's clinical needs (i.e. a particular drug with a particular type of controlled release pattern).

The Introduction chapter is divided into two main sections, Background and Main Scope of this project. The **Background** section provides relevant information on the scientific concepts related to the type of formulations (solid dispersions) and the processing methods (FDM 3D printing and hot melt extrusion) used

in this project. This information is used as a knowledge foundation of experimental Chapter 3. The **Main scope of this project** section reviewed and discussed the fundamental knowledge on the behaviour of polymer behaviour and drug release kinetics from polymer-based solid dispersions. This information forms the foundation for the research development of Chapter 4, 5 and 6.

1.1 Background

1.1.1 Hot Melt Extrusion (HME)

HME is the process wherein raw materials are heated and mixed by applying shear stress and forced to exit through a die under controlled conditions (4). Originally and still widely used by the plastic industry, HME was introduced to and has been rapidly adopted by pharmaceutical manufacturing. The most frequent application of HME in the pharmaceutical industry is as a manufacturing process to produce solid dispersion based products.

1.1.1.1 Types of extruders & Extrusion process

Screw extruders are one of the three types of extrusion machines. The other two types are ram and radial screen extruders (5). Screw extruders are the most importantly used in the pharmaceutical industry (6). Within the screw types, there are three classifications: Single-screw extruders (SSE) with a smooth barrel, twin-screw extruders (TSE) with corotating or counter-rotating with intermeshing screws, and multi-screw extruders (MSE) with a rotating or static shaft. SSE is the most widely used due to its mechanical simplicity. SSE consists of one rotating screw in a smooth barrel that yields in a good melt, stable pressure, and temperature in the barrel. It is also characterized by a long residence time which provides good mixing but is itself a disadvantage (7). Excessively long residence time can lead to degradation of the material due to the prolonged exposure to heat. TSE was introduced with having two agitator assemblies on two parallel shafts. The use of two screws allows different conditions along the zones of the extruder. The screws can be either co-rotating or counter-rotating and can be intermeshing or non-intermeshing (8). Intermeshing TSE is the most used as the design allows for self-cleaning which prevents raw materials from being in the barrel and overheating (6). Non-intermeshing is less used due to their design but capable of producing high torque which is used for processing of highly viscous material (9, 10). TSE has two advantages over SSE; the first

being reduced residence time typically between 5-10 mins and second being enhanced mixing due to the design of screws which employ a disruptive mixing and dispersive mixing (11). In disruptive mixing, the materials are blended evenly while, in dispersive mixing, the material is broken down into finer morphologies (6). Hence, the enhanced mixing. TSE is preferred over SSE especially for thermolabile drugs (9). In this work, TSE was used. Figure 1-1 shows SSE, TSE, and the different screw types.

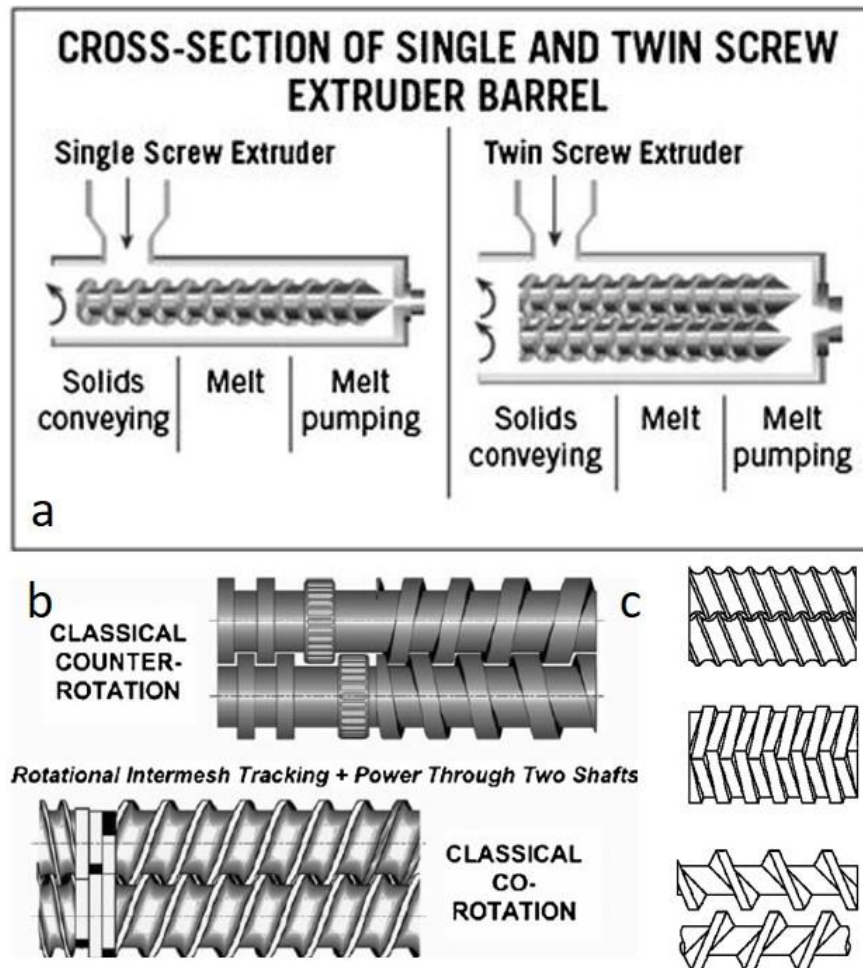


Figure 1-1: (a) SSE with one screw and one shaft and TSE two screws on two shafts. (b) the two types of twin screws for TSE. (c) top: intermeshing screws, middle: intermeshing counter-rotating, and bottom: non-intermeshing counter-rotating screws. Adapted from reference (6, 8).

The various types of extruders have three common distinct zones of operation. The first is the feeding, the second is the transition, and the third is the metering zone (6, 10-12). The material is fed through the hopper which is the feeding section. The material is then transported to the transition zone where it is melted, compressed, and mixed. As the compression takes effect, the pressure is increased, and the material moves along the barrel until it reaches the metering zone in the form of homogeneous plastic melt

ready for extrusion. The metering zone reduces the non-uniformity by minimizing the thickness variation, ensuring laminar flow, and smooth exit through the die cavity (11). The typical HME is shown in Figure 1-2.

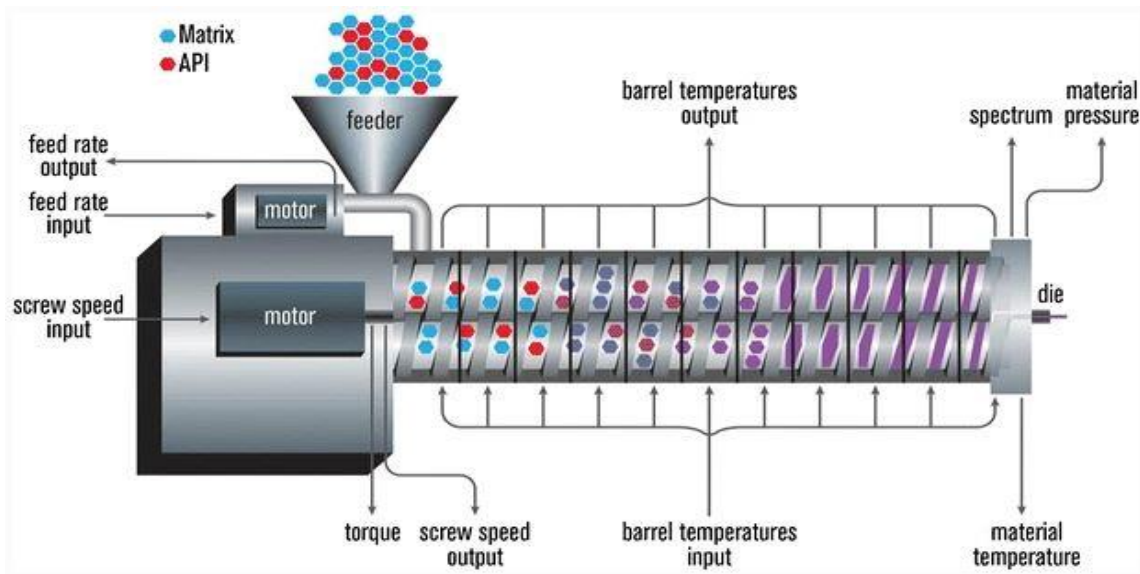


Figure 1-2: HME schematic (6).

1.1.1.2 Materials for HME

The materials used for HME should possess the following characteristics. They must meet the same levels of purity and safety as materials used in traditional oral dosage, must be able to deform easily inside the extruder and solidify on exiting it, must be thermostable and maintain an acceptable physical and chemical stability during the HME process and afterwards during long-term storage, and lastly, the desired *in vitro* release and *in vivo* performance should be achieved by the product. The pharmaceutical materials used for HME are a combination of drug and functional excipients. The functional excipients are classified as matrix carriers, release modifying agents, plasticizers, antioxidants, and thermal lubricants (6, 10).

- Active Pharmaceutical Ingredients (APIs)

Some of the advantages are that HME is an anhydrous process which avoids degradation due to hydrolysis by aqueous media often added in the granulating media. The drug has to be thermally stable during the HME process and as such, pre-characterization of the drug chemical and physical properties is crucial. Crystalline drugs, characterized by their lattice structure, are thermodynamically more stable compared to their counterpart amorphous forms (6). However, poorly-soluble crystalline drugs have a much slower dissolution rate than the amorphous form of the drug. HME is often used with an attempt to form a molecular dispersion of the drug in the polymer matrices to improve the dissolution rate of the drug. The

state of the drug in HME such as fully dissolved (molecular dispersion), or fully undissolved (phase separated solid dispersion with crystalline drug), or a combination of both, can impact the performance (i.e. drug release rate) and the stability of the oral dosage form (13).

- **Carriers**

Carriers are used during HME as embedding component for the drug. These carriers are melt-capable and are classified into polymeric carriers containing polymers and non-polymeric carriers containing low melting point wax. The polymeric carriers can be hydrophilic polymers such as polyethylene oxide or hydrophobic carriers such as zein and ethyl cellulose (14, 15). Reports of non-polymeric carrier have included the use of sugars and acids (12, 16). The choice of carriers depends on drug-polymer miscibility, polymer stability, the desired release mechanism, and function of the final dosage form (6).

- **Plasticizers**

Plasticizers are low molecular weight compounds that can affect in one or more of the three ways. They can cause the carrier to be less rigid, lower the processing temperature which can avoid the degradation of thermolabile drug, and reduce the shear forces needed for extrusion (6, 10, 17). The plasticization phenomenon occurs because plasticizers increase the free volume between polymer chains which lead to lower melt viscosity so that less heat (lower HME operational temperature) and shear forces are required to make the polymer chains move in the direction of the flow (18). Additionally, plasticizers ease the fusion process (melting) of semi-crystalline polymers (19). Common plasticizers, approved by the FDA, in pharmaceutical dosages are enlisted in Table 1-1. The materials used in HME is discussed next.

Table 1-1: Common plasticizers used in oral dosage (10).

Type	Examples
Citrate esters	triethyl citrate, tributyl citrate, acetyl, triethyl citrate, acetyl tributyl citrate
Fatty acid esters	butyl stearate, glycerol monostearate, stearyl alcohol
Sebacate esters	dibutyl sebacate
Phthalate esters	diethyl phthalate, dibutyl phthalate, dioctyl phosphate
Glycol derivatives	Polyethylene glycol, propylene glycol
Vitamin E TPGS	D- α -tocopheryl polyethylene glycol 1000 succinate
Others	triacetin, mineral oil, castor oil

1.1.2 Fused Deposition Modeling 3D printing (FDM 3DP)

According to statistics, FDM has been the most common 3D technology used for prototyping accounting for 36% in 2017, 46% in 2018 (20), 57% in 2019 (3), and most commonly used for pharmaceutical applications until 2018 (21). FDM 3DP is a type of the material extrusion 3DP process (22, 23) wherein, a heated nozzle is used (24). The feeding material, in the form of filaments, is fed via rollers into the nozzle. Filaments are then heated by heating elements into a molten state to allow for extrusion through the nozzle tip (25). The nozzle can move in the x, y-direction while the platform is movable in the z-directions to produce the final desired geometry layer by layer, which fuses as the printed filament cools (26, 27). Upon deposition, the material cools and solidifies onto a platform. The schematic illustration of FDM is shown in Figure 1-3.

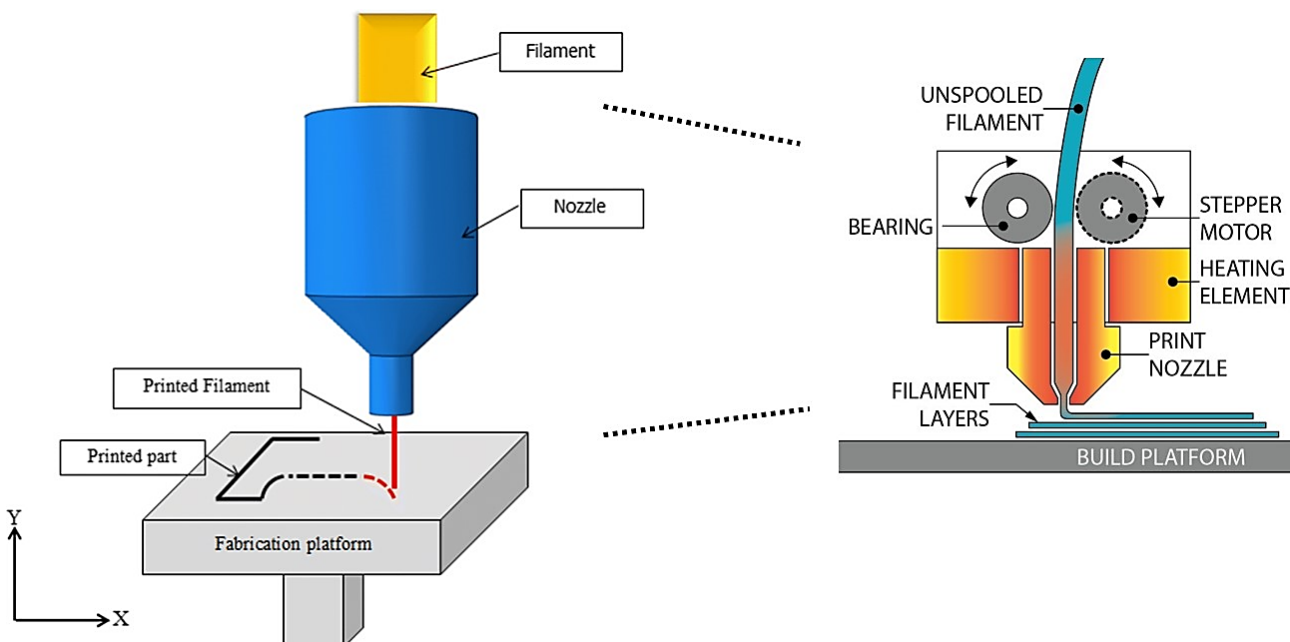


Figure 1-3: Schematic illustration of the FDM 3D printing technology. Adapted from reference (28).

In terms of loading drug into the FDM filaments, currently in use, are two common methods of preparation: impregnation and hot melt extrusion (29, 30). For impregnation, the filament is immersed (soaked) in a solution of the drug for an extended duration, usually a minimum of 24 hours. This method was used by Goyanes et al (31) but the drug loading achieved in such cases is quite low, approximately 15% at most (32). The alternate method is by preparing the custom made drug loaded filament using hot melt extrusion which has better drug loading capacity than the impregnation and is discussed next (33).

1.1.2.1 Pharmaceutical applications of HME coupled with 3D printing

A major advantage of HME is to form solid dispersions with suitable polymeric excipients that provide the solubility enhancement for poorly soluble drugs (34). The different mechanisms proposed in the literature on how solid dispersions can improve drug solubility are improving wettability, preventing recrystallization, and stabilizing amorphous formulations (35). The melt and mixing process during HME converts crystalline drugs to the amorphous form by dispersing it in a carrier and prevents drug recrystallization through the formation of non-covalent bonds between the drug and the carrier chain or through the steric hindrance phenomenon (10). Due to the drug dissolved in the hydrophilic carrier, dissolution in gastrointestinal fluids is enhanced compared to that of the native crystalline form of drugs. Review of HME made oral solid dosage form from 1990 to 2015 has been given by Major et al (36).

As discussed previously, for FDM 3DP, the filaments can be created using HME (37, 38). All pharmaceutical filaments have to be custom made using HME as all of the commercially available filaments are not made of pharmaceutical grade materials (39). The use of HME is to create a filament that incorporates the drug in a polymer and extruded via the use of a modified die to match the circumferential dimensions of the FDM 3DP nozzle. HME is capable of producing thermoplastic filaments that can withstand tensile and compression forces of the printing process (40, 41). Coupling HME with 3D printing has shown the advantage of producing tablets with high drug loading capacities as high as 40% of the oral dosage (6, 38). For research, higher drug loading has received attention due to the potential of increasing patient compliance (42). Increased patient compliance is one of the benefits, which has been demonstrated in clinical trials of polypills for cardiovascular disease with 81% adherence vs 46% adherence when taking the medications separately (43). A Polypill is the combination of two or more drugs in one pill designed to increase patient compliance. Figure 1-4 illustrates the overview of HME coupled with 3DP printing process.

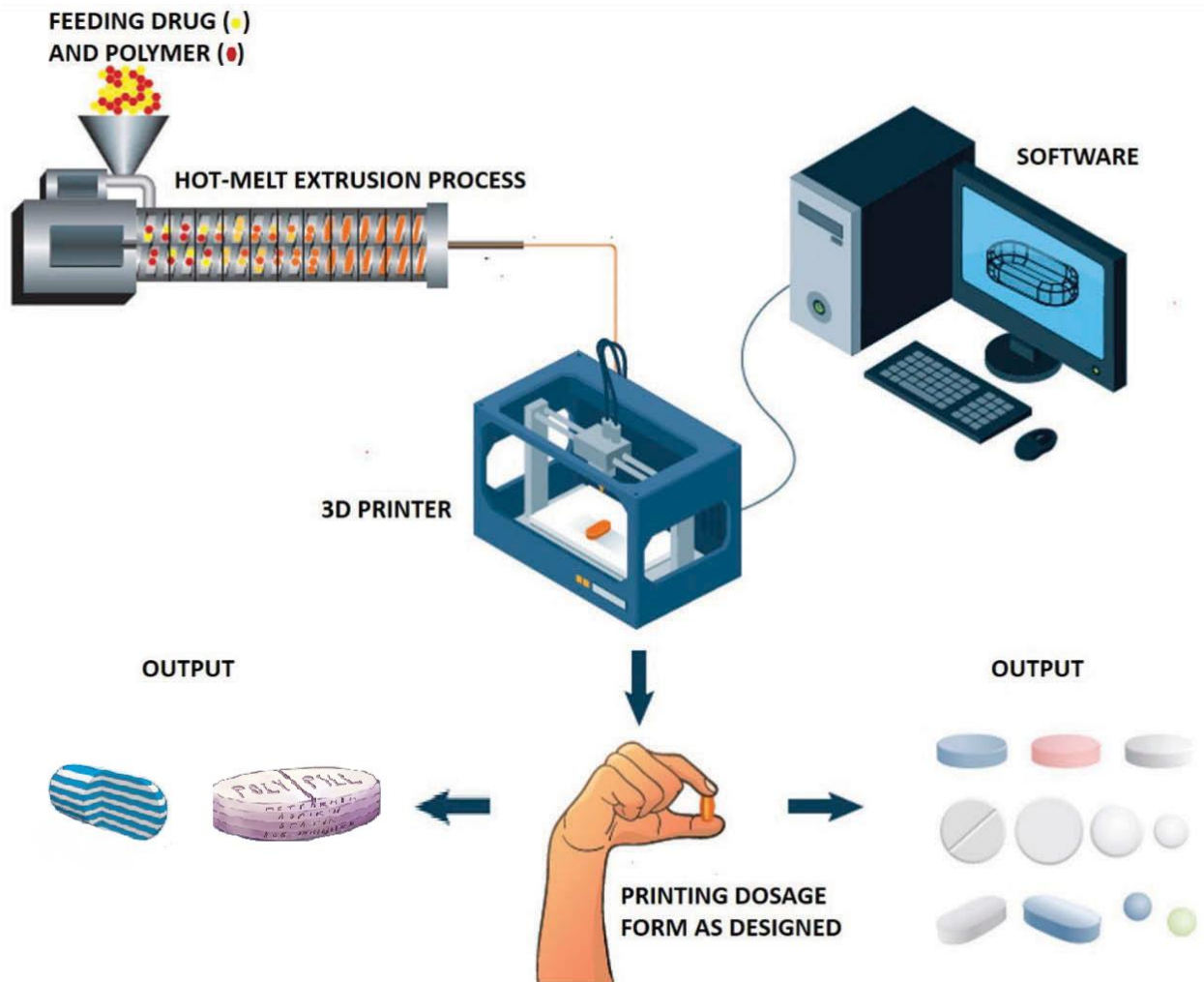


Figure 1-4: Schematic of HME followed by 3DP as a single continuous process. The output can be FDM 3D printed tablets (right) or polypill (left). Adapted from reference (38).

The oral solid dosage forms that have been printed using this approach reported in the literature are of four types. They are controlled release dosage forms (CRDFs), sustained release dosage forms (SRDFs), immediate release dosage forms (IRDFs), and polypills (37). CRDFs aim to control the plasma concentration of the drug after administration (44). SRDFs aim to maintain the rate of drug release over a sustained period (44). IRDFs aim to release the drug as fast as possible, generally with first order kinetics so that a fast therapeutics onset can be achieved (44).

1.1.2.2 Commercialization Limitations

FDM 3D printing is still a prototype machine and in its infancy stages in pharmaceuticals. As such, it is expected that limitations and issues may exist. Such limitations and issues have been mentioned in literature (24, 25, 45-48). Alhijaj et al reported the impacts of processing parameters on the 3D printed dosages by looking at the physical variations such as weight, dimensions, and individual stand width and

deduced correlations of one or more parameters to the physical variations using principal component analysis (48). In the case of oral solid dosage forms, the microstructure is an important key feature if polypills are to be made in the standard size of traditional tablets (24). This was shown by works of Goyanes et al wherein a polypill was printed. Since the polypill had two formulation filaments to be printed, it required precision of printer resolution at microscale to match the theoretical dimensions, which was not best achieved. This was evident by observing the high variations in the drug release profiles of approximately $\pm 40\%$ among some formulation replicates (49) but $\pm 5\%$ in others. This indicates the inconsistency in FDM 3DP currently in use. Weeren et al focused on quality of parts printed by FDM exported computationally as STL files by investigating deformities between designed specification and printed object, and categorized as surface and internal defects (50). Increasing print speed is challenging, as there is generally a trade off between feature resolution and print speed (51). The high temperatures required for printing has been recognized as a barrier limiting the materials available for FDM printing, as many materials degrade at higher temperatures (52). Okwuosa et al focused on 3DP at lower temperatures and using thermofillers to avoid degradation (53).

There are also works citing economical issues that suggest 3D printing is still not feasible for mass production. Injection molding (another manufacturing method) is more cost effective per parts as production rates rise but 3D printing cost per part remains the constant (54). However, printing reduces time of production significantly but increases the number of steps to the final OSDF (21). There are great benefits to 3DP and additive manufacturing in general, which have already been discussed. Another casing point of a benefit possibly, is the manufacturing of orphan drugs which are very cost ineffective on mass production scale (55). Mazzanti et al has reviewed the challenges of using filaments and outlined specifically the problems of using natural polymers for FDM printers by diving them into two categories of processing and appearance problems while simultaneously providing possible solutions for each case, shown in Figure 1-5 (56).

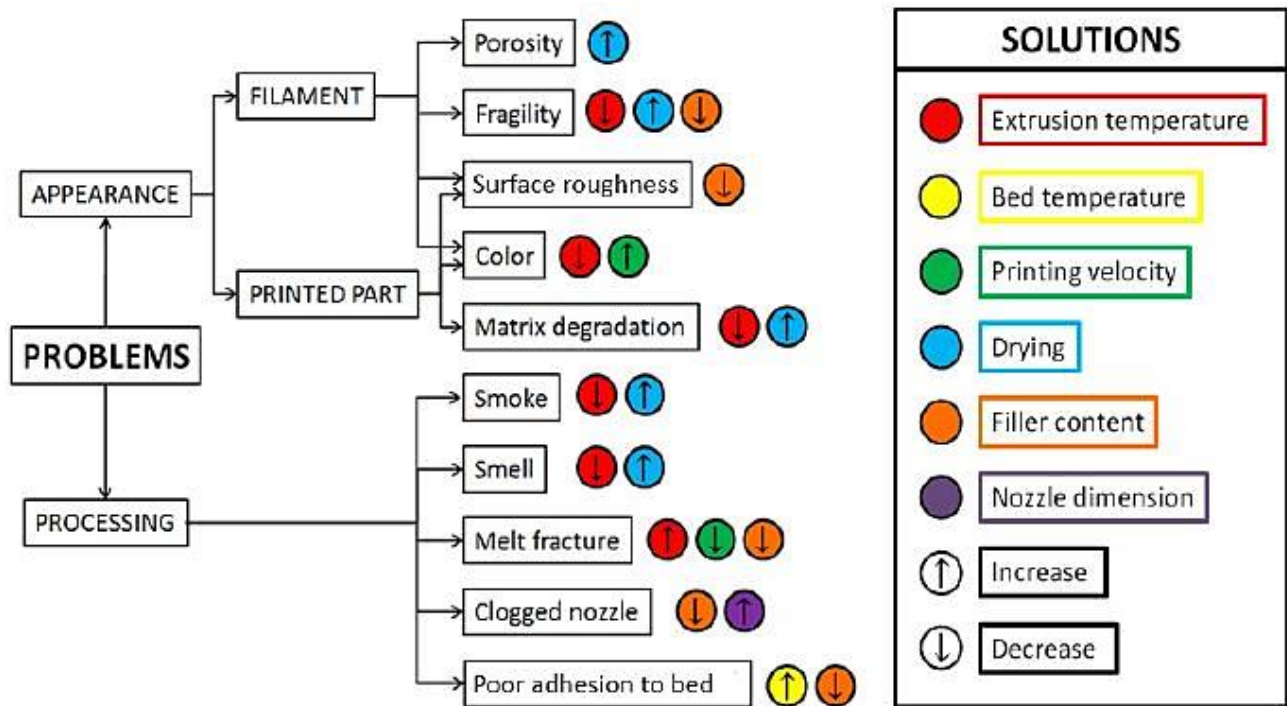


Figure 1-5: Natural fiber filament problems that may be encountered in FDM 3DP and the possible solutions (56).

The melting through HME results in obtaining a solid molecular dispersion. The types and controlling factors of solid dispersions are an important factor, which is discussed next.

1.1.3 Solid dispersions

The term solid dispersion refers to the distribution of one or more drug in a carrier at solid state by melting (fusion), solvent, or melting solvent method to improve the solubility of poorly soluble drug (57). Sekiguchi et al were the first to report the melting (fusion) method in the early 1960s (58). Sekiguchi et al initially proposed that solid dispersion can only exist as a eutectic mixture in a microcrystalline state but Goldberg et al subsequently reported this to not necessarily exist in microcrystalline state but also in other molecular arrangements (58, 59). Based on the molecular arrangement, Chiou and Riegelman classified six different types of solid dispersion (60), shown in Table 1-2. The state of matrix or the drug is one of the three: crystalline, amorphous, or molecularly dispersed, shown in Figure 1-6. In this project, the main kind of solid dispersion is amorphous solid dispersions often referred to as glass solution in the original six classifications. In such systems, the drug and excipients are molecularly dispersed in one single phase.

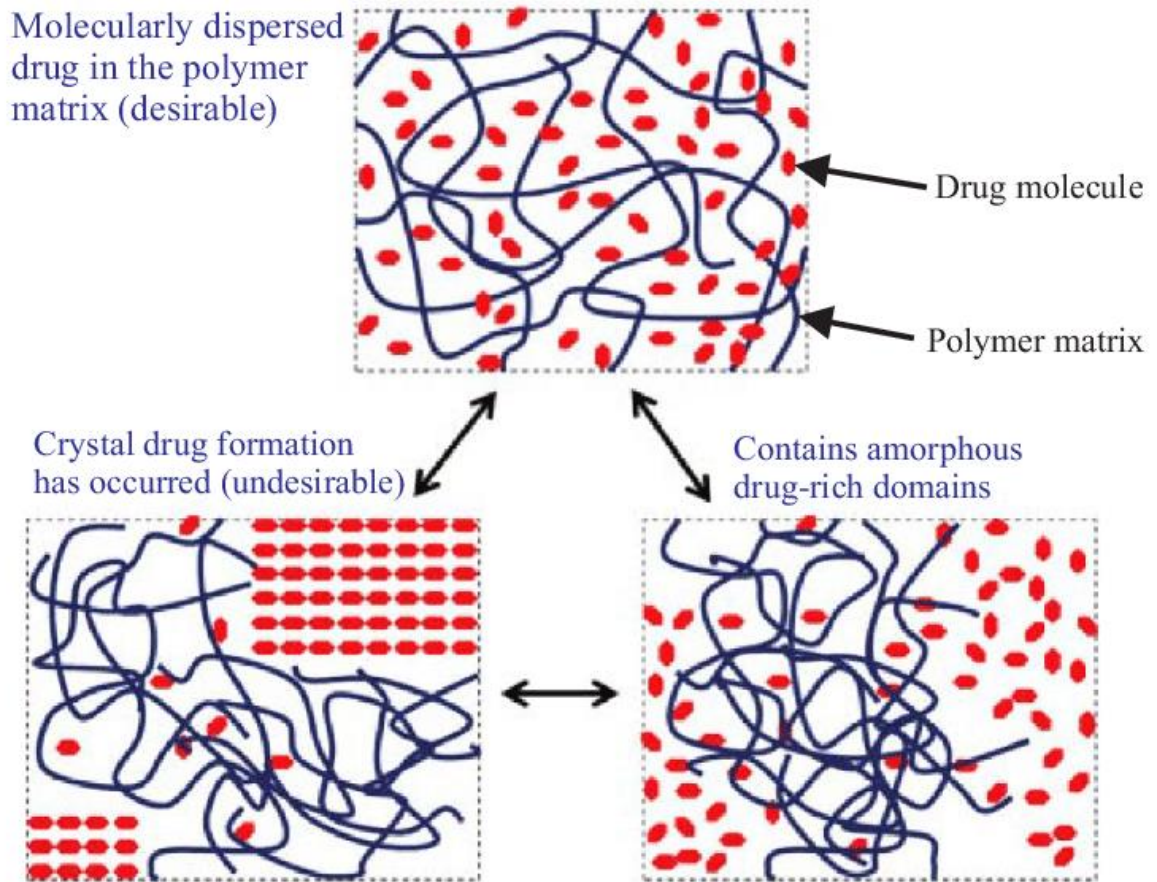


Figure 1-6: The different states of drug molecule in the polymer (61).

Due to observations of monotectic, peritectic structures, Vasconcelos et al proposed a different classification system based on carrier properties: the first generation consisting of crystalline polymer, second generation consisting of amorphous carriers, and third generation consisting of surfactant carriers (62). Vo et al modified this by adding a fourth generation of insoluble and swellable polymers (63). Furthermore, Meng et al classified binary solid dispersion into six categories based on the state of the API which is similar to the classification proposed by Chiou and Riegelman (64). All classification schemes are equally valid, and here the first of them, proposed by Chiou and Riegelman, will be discussed. Figure 1-7 illustrates the different classification categories. Recently, multicomponent solid dispersion systems have been cited as an efficient drug delivery system to improve bioavailability and drug solubility (65, 66). In such systems, as the name suggests, different compartments contain different solid dispersion systems with the API and polymer being molecularly dispersed.

Table 1-2: Classification of the six solid dispersion types. For the states, C=crystalline, A=amorphous, and M=molecularly dispersed. Adapted from reference (57).

Solid dispersion type		Matrix state	Drug state	Number of phases
I	Eutectics	C	C	2
II	Amorphous precipitation	C	A	2
III	Solid solutions			
	Continuous solid solution	C	M	1
	Discontinuous solid solution	C	M	2
	Substitutional Solid Solution	C	M	1 or 2
	Interstitial Solid Solution	C	M	2
IV	Glass suspension	A	C	2
V	Complex formation	A	A	2
VI	Glass solution	A	M	1

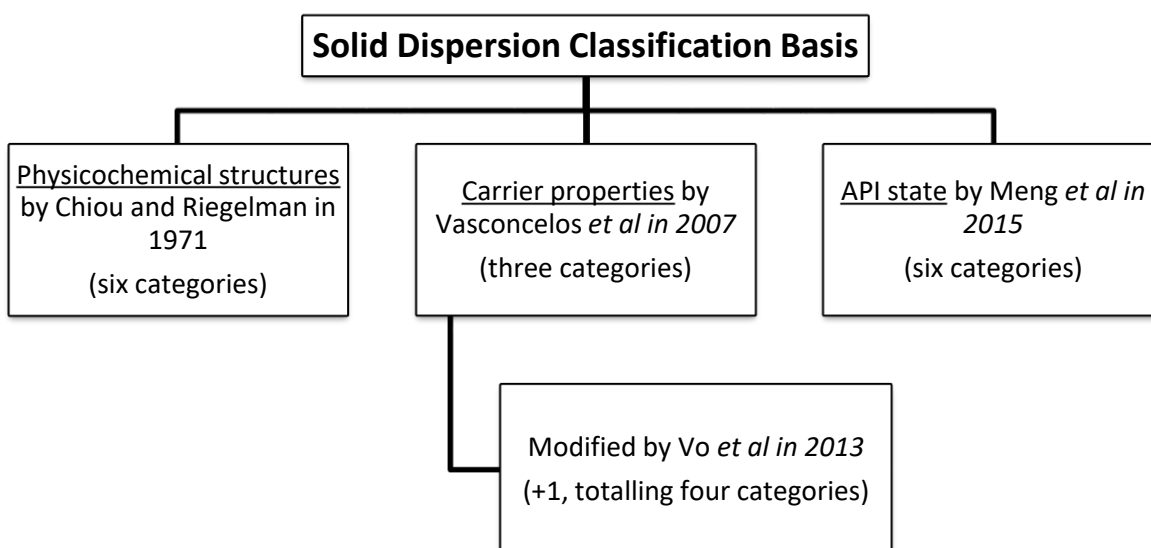


Figure 1-7: Solid dispersion classification based on properties and number of categories in each in brackets (67).

1.1.3.1 Eutectic Type

Eutectic mixtures are made from rapid solidification of fused liquid of two components which show complete liquid miscibility and almost no solid-solid solubility (68). The phase diagram for the eutectic mixture is shown in Figure 1-8. Such systems are regarded as an intimately blended physical mixture of the two crystalline components (69, 70).

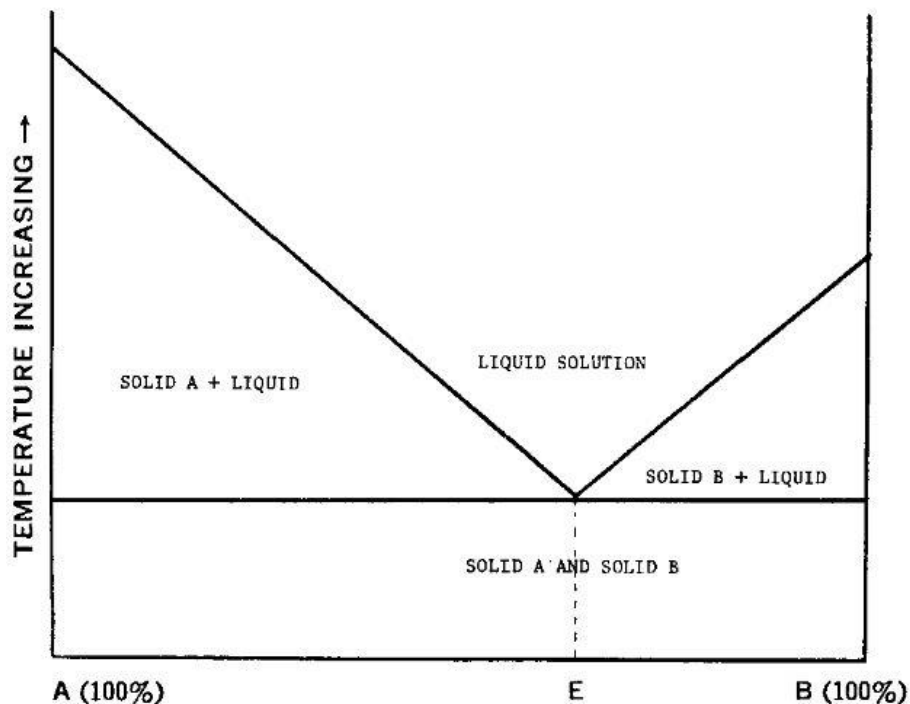


Figure 1-8: Phase diagram of Eutectic mixtures of substance A and B. Adapted from reference (60).

The liquid miscibility is attained in the liquid solution phase of both A and B. In the adjacent phase, either A or B exist as a solid while the other is liquid. Point E is known as the eutectic temperature where the mixture freezes or melts and lower than either of the constituents (71). As the temperature is decreased, both A and B become solid and crystallized particles. The crystals, with their increased surface area and reduced particle size increase the dissolution rates along with other factors. This increase drug solubility with very small crystallite sizes, solubilization effect of the carrier in a microenvironment surrounding the drug particle in initial stages of dissolution, absence of agglomeration between fine crystallites of API that hinder dissolution, excellent wettability and dispersibility of API in a water-soluble matrix, and crystallization in the metastable form which has higher solubility leading to faster dissolution (60). Use of eutectic mixture is to form solid dispersion of a crystalline API in a crystalline polymer to enhance the dissolution of the drug. Carrier may be either hydrophilic or hydrophobic. Law et al demonstrated increased dissolution of insoluble fenofibrate in a eutectic mixture of PEG 8000 (hydrophilic polymer) of ratio 25:75 (API:polymer), while Figueirêdo et al demonstrated increased dissolution for both insoluble benznidazole (an antichagasic API) in eutectic mixture with insoluble posaconazole (an antifungal hydrophobic API) or ratio 80:20 (API BNZ:API PCZ) (72, 73).

1.1.3.2 Amorphous precipitation

In this state, the API precipitate out in amorphous form within the crystalline carrier. This is the main difference between the eutectic mixture and amorphous precipitation. The amorphous form has the highest energy of the pure form of API and produces faster dissolution compared to the crystalline form (60). Mullins et al showed that amorphous novobiocin has a tenfold higher solubility than its crystalline form (74). The principle of crystalline carrier is the same as a eutectic mixture. The crystalline carrier, being water-soluble, exhibit forming small particles, reducing aggregation, increased wettability, decreasing crystallinity, and transforming metastable polymorph (75). Crystalline carriers such as urea (76), organic acids (77), and sugars have been used (78).

1.1.3.3 Solid solutions

A solid solution is made of solid solute dissolved in a solid solvent and often called mixed crystal due to the crystals of two component being homogenously distributed as a one phase system (79). It was suggested that due to solid in a solid medium, the molecular size of the solid solute is at a minimum, and can have faster dissolution than eutectic mixtures (80). Solid solutions can be classified into two categories either based on the level of miscibility or the crystalline structure of the solid solution (81, 82). Based on miscibility, the categorization is either continuous or discontinuous and based on the crystal structure, the categorization is either substitutional or interstitial solid solutions. In continuous solid solution, the components are miscible across all proportions. It has been theorized that total lattice energy of the continuous solid solution at various compositions should be greater than that of either pure components because the strength of the bond between the two different components at the solid state should be greater than that between the same species of molecules (79). Such solid solution has not been reported in pharmaceuticals but has been reported to be made in engineering for lithium batteries by Noh et al (83). In contrast, discontinuous solid solutions, there is limited solubility of the two components above the eutectic temperature. This is more possible in reality a one component is capable of dissolving the other component to a certain degree. As the temperature is lowered, the solubility decreases, and the solid solution exists in a narrower region. The phase diagrams for continuous and discontinuous solid solution shown in Figure 1- 9.

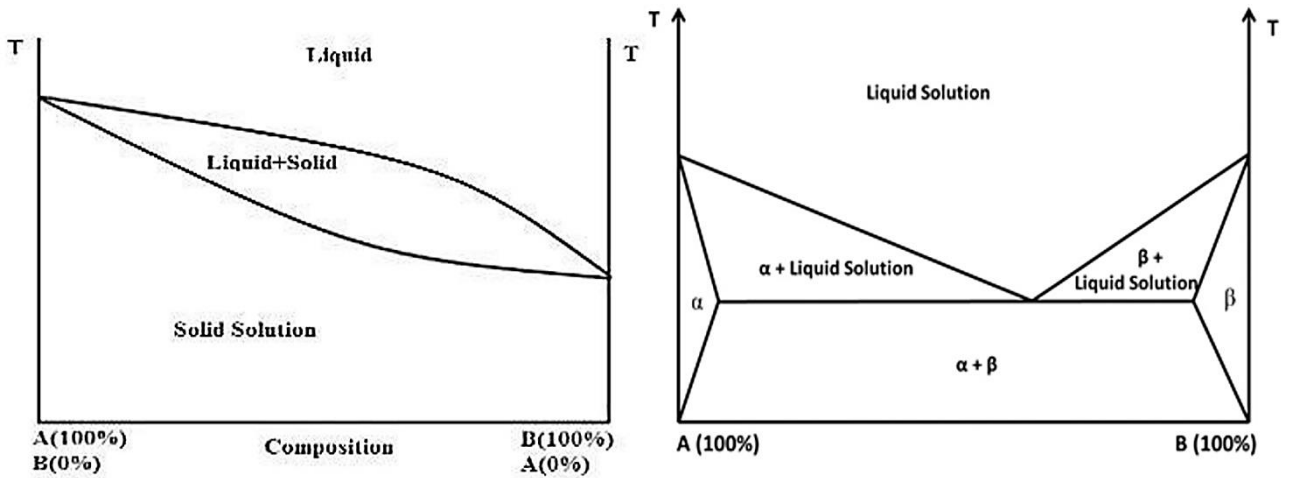


Figure 1- 9: (Left) Continuous solid solution. (Right) Discontinuous solid solution (84).

In terms of crystalline structure, one group is substitutional solid solutions. In substitutional solid solutions, the solvent molecule is substituted by solute molecules in the crystal lattice structure. The resultant can be a continuous or discontinuous solid solution. Such substitution is possible if the molecular sizes of the two components do not differ more than 15% according to Hume-Ruthery rule (82, 85). In contrast, in interstitial solid solutions, the solute molecule occupies the interstitial space between the solvent molecules in the crystal lattice. For interstitial solid solutions to form, three factors must be present. The first is the diameter of the solute molecule should be less than 59% of the solvent molecule diameter. The second is the volume of the solute molecule should be less than 20% of the solvent molecule. The third is the pattern in which the solute and solvent molecule is arranged should favour the formation of an interstitial solid solution (60). Figure 1-10 shows the difference in the lattice structure of the substitutional and interstitial solid solution.

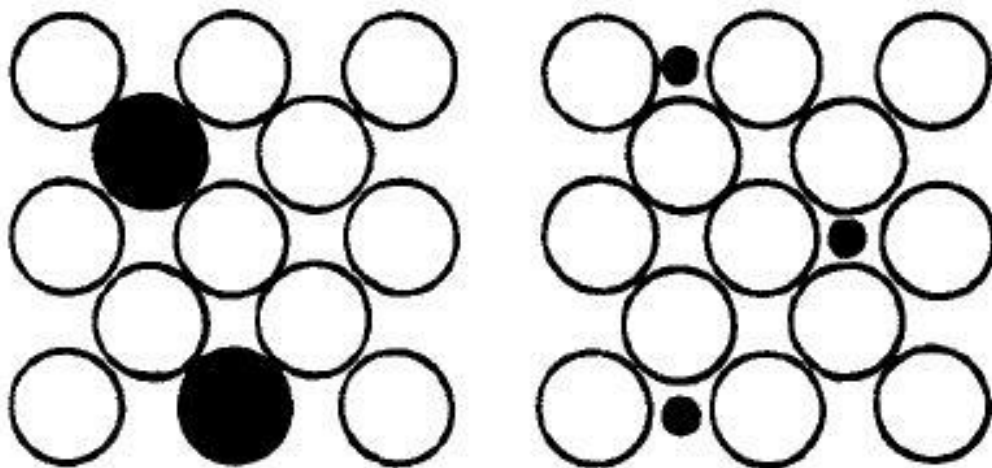


Figure 1-10: (Left) Substitutional solid solution crystal lattice and (right) interstitial solid solution. Black circles=Solute molecule and white circle=solvent molecules (60).

1.1.3.4 Glass suspension and Glass solutions

The concept of the formation of a glass solution as another potential modification of a dosage form which can increase drug dissolution by Chiou and Riegelman (60). The term 'glass' is used to describe a pure chemical or a mixture of chemicals in a glassy state. A glass solution is a homogenous system in which the glassy or vitreous form of the carrier solubilizes the drug molecule in its matrix (86). Glass suspension is a mixture wherein the precipitate is suspended in glass solvent. The glassy state is achieved by rapid quenching of the melt (87). This glassy state is characterized by transparency and brittleness below the T_g . It continuously softens upon heating and gives a broad melting point. Heating the glassy state of pure compounds can transform it into a crystalline state. Various physicochemical properties such as viscosity, refractive index, thermal conductivity, compressibility, etc. change within the glass transition region when a substance is heated or cooled (60). Simonelli et al were the first to demonstrate high dissolution rates for glass suspensions using PVP with saphathiazole (88).

1.1.3.5 Complex formation

Complex formations are modified particles that are a conjugate of the drug and carrier molecules forming a binary system. The complex formation is common. Sekiguchi et al found eleven cases of compound formations out of twelve-phase diagrams while Guillory et al found four compound formations out of nine phase diagrams investigated (89, 90). Furthermore, If the complex forms during the preparation method, it does not indicate they will re-form in the liquid phase and vice versa. The formation of the drug from the complex formed depends on stability, dissociation constant, solubility and intrinsic absorption rate of the complex (60). In one study by Benet et al, the dissolution rates increased by onefold for a complex of griseofulvin and polyethylene glycol 6000 (91).

The physical state of the drug and the excipients are vitally important for impacting on the stability and drug release behaviour of the solid dispersions. Therefore, the phase behaviour of solid dispersions is discussed in the following section.

1.1.3.6 Phase behaviour of solid dispersions

Despite the potentials of solid dispersions for improving the dissolution of the poorly soluble drug, the number of research articles for solid dispersion outweighs the number of commercial products of solid dispersion (92). The low number is due to physicochemical instability in the manufacturing process or during storage with the eventual effect of the solid dispersion exhibiting phase separation or recrystallization (93, 94). Understanding the phase behaviour of a solid dispersion is critical for predicting the stability of the solid dispersion. The phase behaviour of a solid dispersion can be probed by a range of thermodynamic parameters such as glass transition temperature and molecular mobility. These all can be used to predict the storage stability of solid dispersions. Here the glass transition temperature is discussed in detail as it was used directly in this project to identify the physical state and the phase behaviour of the solid dispersions studied. It is also one of the most widely used parameters to predict stability and to help identify the appropriate storage conditions of amorphous dispersions (95, 96).

- Theories of Glass transition

Previously, it was stated that T_g is dependant on the thermodynamics (cooling/heating rate). This raised a hypothetical question about how much T_g can be slowed if the rates are slowed. Furthermore, T_g is effected by the crosslink density, by the molecular weight, copolymerization, crystallinity, chemical structure groups, tacticity, and by pressure (97). Therefore, three main theories of glass transitions were proposed to explain at a molecular level, which is outlined in Table 1-3.

Table 1-3: T_g theory with advantages and disadvantages (97).

Theory	Advantage	Disadvantage
Free volume theory	<ol style="list-style-type: none">1. Time and temperature of viscoelastic events related to T_g.2. Coefficients of expansion above and below T_g related	<ol style="list-style-type: none">1. Actual molecular motions poorly defined
Kinetic theory	<ol style="list-style-type: none">1. Shifts in T_g with time frame quantitatively determined2. Heat capacities determined	<ol style="list-style-type: none">1. No T_g predicted at infinite time scales
Thermodynamic theory	<ol style="list-style-type: none">1. Variation of T_g with molecular weight, diluent, and cross-link density predicted2. Predicts true second-order transition temperature	<ol style="list-style-type: none">1. True second-order transition temperature poorly defined

Free volume theory was introduced by Eyring et al primarily states free volume in the form of segmented voids as a vital part for the onset of molecular motion (98). Secondly, it relates the coefficient of expansion above and below the T_g , and third, it relates the viscoelastic motion to the variables of time and temperature.

The kinetic theory defines T_g as the temperature at which the relaxation time for the segmental motions in the main polymer chain is of the same order of magnitude as the time scale of the experiment. The theory approaches the rate of equilibrium of the system accounting for the motion of the voids and molecules. The kinetic theory also provides numerical information about the heat capacities below and above the T_g . There are various models or method postulated pertaining to the kinetic theory such as Vol'kenshtein–Ptitsyn relaxation theory (99), Tool–Narayanaswamy–Moynihan method (100), Kovacs method (101), and Adam–Gibbs theory (102). A comprehensive review of all these theories/models is given by Tropin et al (103). The thermodynamic theory introduces the notion of equilibrium and the requirement for true second-order transition, even at infinitely long scales which was proposed by Gibbs and DiMarzio (104). It successfully predicts the variation of T_g with molecular weight, crosslink density, and diluent content (97).

The free volume needed for calculations in these theories is found by subtracting the occupied volume from the total volume (105). The free volume numbers have different estimations due to different definitions of the occupied volume. Therefore, there are variations in the free volume number fraction. Table 1-4 outlines the various theories that estimate the free volume fraction.

Table 1-4: Summary of free volume numbers from four models (97).

Theory	Free volume fraction	Reference
WLF	0.025	(106)
Hirai and Eyring	0.08	(107)
Miller	0.12	(108)
Simha-Boyer	0.113	(109)

- Glass transition (T_g)

The glass transition is a phenomenon that is observed when an amorphous material is supercooled rapidly (no nucleation or crystallization), the material forms a glass whereby the macroscopic dynamics either ceases or is infinitesimally slower than the characteristics measurement time. The temperature at which this occurs is the T_g (110). The same holds true when heating that the glassy material changes into a rubbery material indicating it is a reversible process. The transition is a kinetic process and the T_g is dependent upon the cooling rate for a given material (111). Faster cooling result in higher T_g and slower cooling result in lower T_g . Figure 1-11 shows the volume changes as a function of temperature. Generally, an amorphous polymer has a single T_g (112). Blends can exhibit one or two T_g depending on their miscibility or immiscibility, which is discussed later (113). T_g is a second-order phase transition, unlike melting, which is a first-order transition whereby latent heat is involved. At T_g , there are changes in derivative thermodynamic properties such as heat capacity, coefficient of thermal expansion, mechanical modulus, and dielectric constant. (114, 115). There are also other physical changes in entropy, rigidity and viscosity (111). As viscosity is one of the indicators, T_g has also been noted as the temperature, at which the shear viscosity is equal to 10^{13} Poise or 10^{12} Pa s (116).

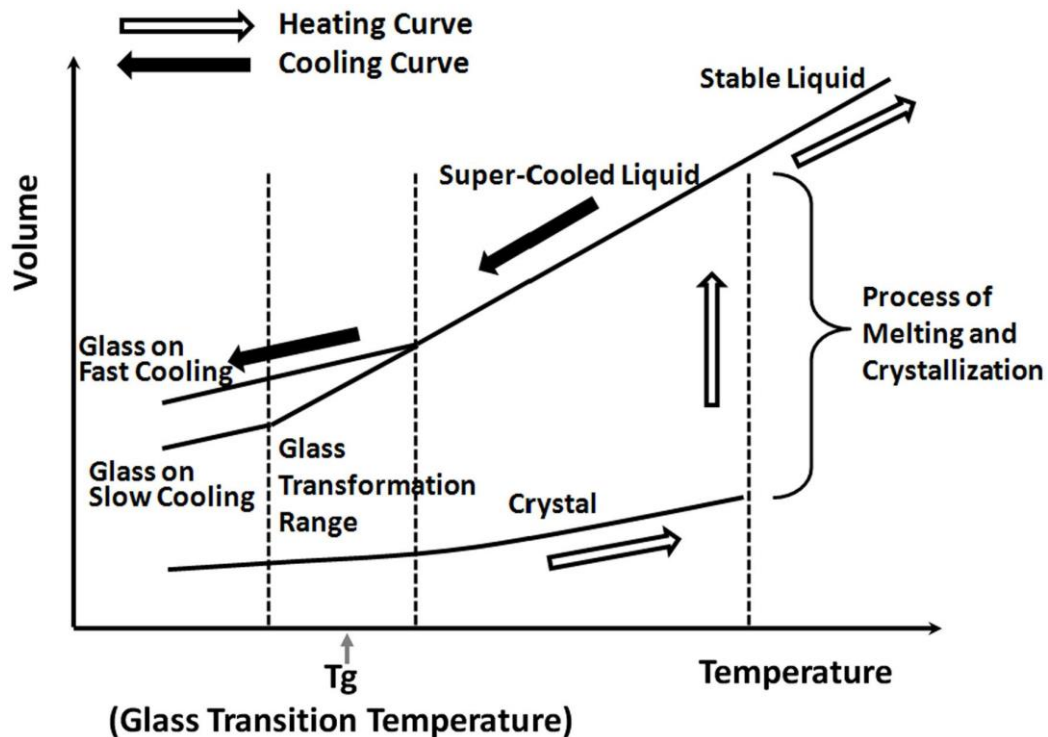


Figure 1-11: Volume of various states of materials as affected by temperature (117).

Based on the derivative thermodynamic property changes mentioned, there are different methods to characterize the T_g of a material. The first is volumetric methods operating based on volume changes using dilatometry and thermal mechanical analysis (118). The second is mechanical or dielectric methods operating based on changes in storage modulus or changes in dielectric loss constant using dynamic mechanical analysis and dielectric analysis (119). The third is a moisture sorption technique operating based on changes in moisture uptake which switches from adsorption to absorption (120). The fourth is thermodynamic analysis operating based on changes in specific heat capacity using a differential scanning calorimetry (121).

- **Glass transition for Blends**

Polymeric blends can have three instances of T_g depending on the miscibility (122). For miscible blends which are a single phase, a single T_g is observed which can be calculated using the Fox equation or Gordon-Taylor equation, shown by equation 1-1 and 1-2 respectively. For immiscible blends, the original two individual T_g of the constituting materials is observed. Thermodynamically, there is always some degree of molecular mixing of one component in another component but this negligible, and therefore still taken as an immiscible blend. For partially miscible blends, there are two separate T_g but both are more shifted toward the T_g of the other polymer (97, 122, 123). The T_g behaviours are shown in Figure 1-12. Such shifted T_g was observed in the works of using epoxy and acrylate polymer in a ratio of 60/40%, weight-wise, where the T_g of pure epoxy was 120°C, which shifted down (inward towards acrylate) to 95°C, while the T_g of pure acrylate was -40°C which shifted up (also inward toward epoxy) to -10°C, indicating a partial blend (often referred as a semi-miscible blend) (124).

Fox Equation
$$\frac{1}{T_g} = \frac{W_1}{T_{g1}} + \frac{W_2}{T_{g2}} \quad (125) \quad \text{Equation 1-1}$$

Gordon-Taylor Equation
$$T_g = \frac{W_1 T_{g1} + k \cdot W_2 \cdot T_{g2}}{W_1 + k \cdot W_2} \quad (121) \quad \text{Equation 1-2}$$

where W_1 is the weight fraction of homopolymer 1, W_2 is the weight fraction of homopolymer 2, T_{g1} and T_{g2} are the individual glass transition of polymer 1 and 2, and k is a fitting parameter.

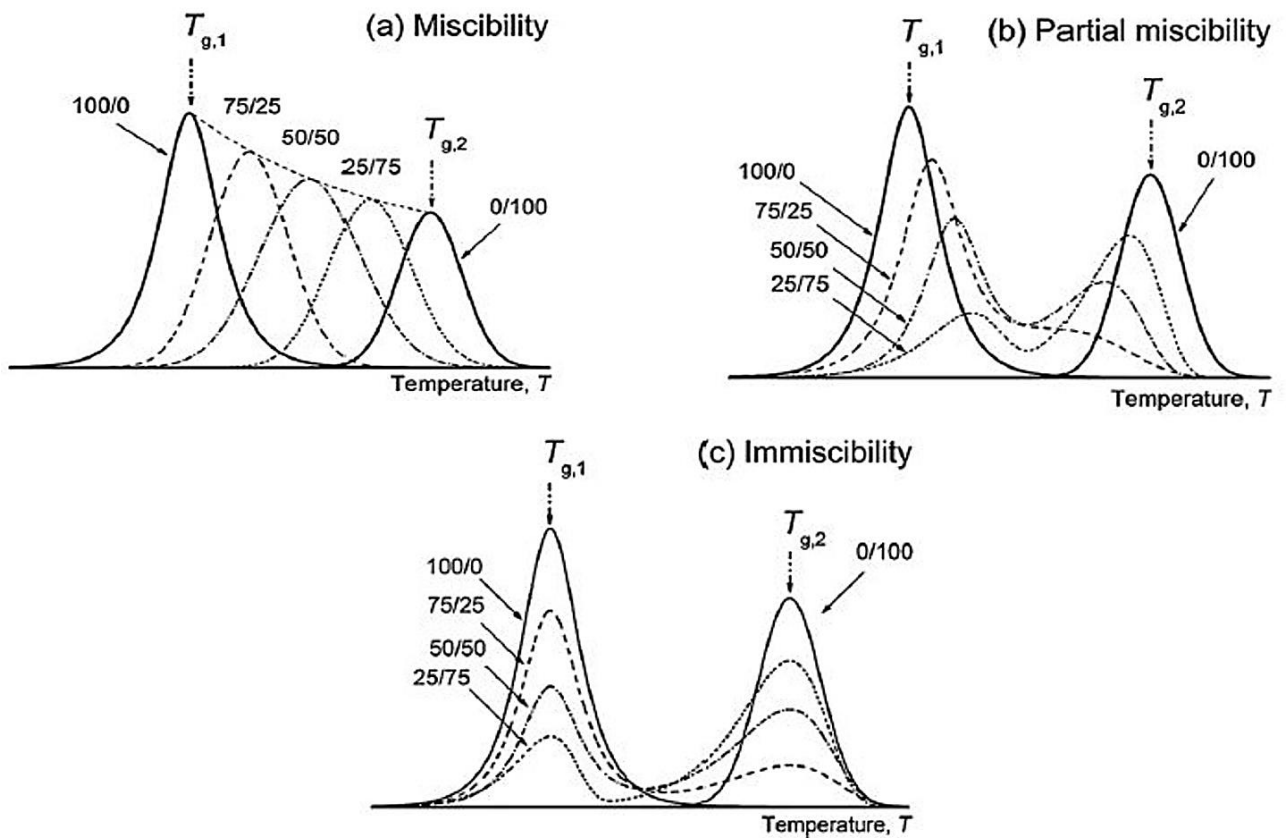


Figure 1-12: Schematic plots of shifts expected in T_g for the three blend scenarios (123).

It is seen that miscibility is an important factor that affects the T_g . In this work, the T_g was used to assess the polymer blends in chapter 4. Two cases of polymer blends were prepared: miscible and semi-miscible blend.

1.2 Main scope of this project

1.2.1 Polymer behaviour in aqueous media

Polymer dissolution is wherein the polymer immersed in a solvent undergoes two transport processes, one being solvent diffusion and the other being chain disentanglement (126). Ueberreiter describes the process being initiated by the solvent as it pushes into the polymer. As the solvent pushes into the polymer, the polymer may or may not swell. In either case, the most outer layer of the polymer is disentangled and flows in the bulk of solvent direction (solution medium). As time passes and the solvent penetrates further, a quasi-stationary equilibrium is reached where the transport rate of polymer into the solvent is balanced by ingress rate of solution into the polymer (127). Ueberreiter also first summarized regions of a glassy swellable polymer based on layering composition shown in Figure 1-13. The infiltration layer, next to the pure polymer, is characterized by many intermolecular spaces through which molecules from the pure

polymer layer can penetrate, starting the diffusion process. The solid swollen layer has been described as a build up layer which is still in the glassy state. The gel layer contains the polymer material that is eroded but held in this state due to the rubbery state of this layer. The final layer before the pure solvent is a liquid layer which encapsulated the entire polymer system (127).

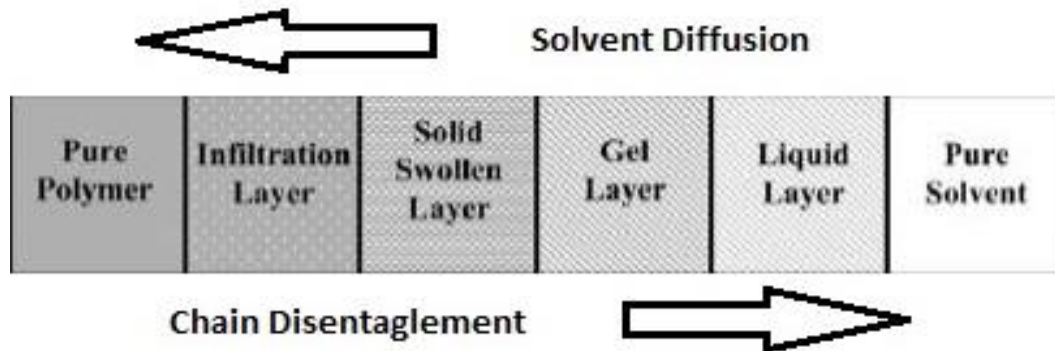


Figure 1-13: Schematic of the surface layer of a polymer during dissolution. The chain disentanglement is in opposite direction to solvent diffusion. Adapted from reference (126).

Factors affecting polymer dissolution can be polymer related or external. Polymer related factors are molecular weight (127), polydispersity (128), structure (129), composition (130), stereochemistry (131), and solvent and additives (132). External factors include agitation (133), temperature (128), and radiation (134).

Regarding molecular weight, the dissolution rate decreases with increasing polymer weight in a nonlinear trend. It was observed that the dissolution rate was inversely related up to a critical molecular weight and thereafter, the dissolution rate plateaus. Below this critical molecular weight, dissolution occurred by stress cracking. Parsonage et al. concluded that the dissolution is controlled by chain disentanglement, which is a function of polymer molecular weight (135). Larger molecular weights yield higher levels of entanglement. Therefore, these molecular weights have a higher degree of swelling before dissolution occurs.

In addition to the molecular weight of the polymer, the dissolution process can also be affected by chain chemistry, composition, and stereochemistry. A polymer dissolves either by exhibiting a thick swollen layer or by undergoing extensive cracking, depending on how fast the osmotic pressure stress that builds up in the polymer matrix is relieved. Therefore, the nature of the polymer's differences in free volume, and segmental stiffness are responsible for behaviour variations from polymer to polymer. It was also found that

the dissolution behaviour is profoundly affected by the tacticity of the polymer (129). Gipstein et al observed variations of dissolution behaviour with stereochemistry in that the solubility rate of isotactic PMMA is much greater than that for the syndiotactic and heterotactic stereo forms (131).

The type of penetrating solvent can also have a profound effect on polymer dissolution. Ouano and Carothers studied the dissolution of PMMA in several solvents and found that crack occurred quicker with the smaller, better solvents than bulky and poorer solvent (129). This was because of higher diffusion rates and swelling power of these solvent molecules. They concluded that if the internal pressure builds up faster than the glassy matrix can relax, through gradual swelling, a fracture can result. It was also pointed out that polymer morphology at the molecular level has a strong influence on the kinematics of dissolution.

External parameters such as agitation and temperature as well as radiation exposure can influence the dissolution process. It was found that the rate of dissolution increases with the agitation and stirring frequency of the solvent due to a decrease of the thickness of the surface layer, and the dissolution rate approaches a limiting value if the pressure of the solvent against the surface of the polymer is increased at all temperatures (127). Drummond et al studied the effects of radiation with samples of P(MMA-co-MAH) with Methyl ethyl ketone, it was shown that the dissolution process is a function of radiation dose (134).

It is noted that the underlying phenomenon of the polymer behaviour can be divided into three processes, which consists of the solvent diffusion (known as hydration), the expansion of polymeric network (known as swelling), and the polymer chain disentanglement into the solvent (known as erosion).

1.2.1.1 Hydration

Hydration refers to the penetration of the solvent into the matrix through the free volume in the material. The rate of penetration of liquid into a porous matrix is driven by the interplay between the capillary forces that promote fluid movement towards the interior and the viscous forces that oppose the liquid movement (136). It was noted that the process of sorption/desorption has been noted to be complex and non-linear

depending on the polymer morphology and chemistry. For example, two distinct hydration profiles were observed for the same polymer by Moy et al (137). The overall response of hydrated polymers is further influenced by factors such as water induced relaxation in the host polymer (138, 139). McBrierty et al summarized the factors that impact hydration of polymers (140). In summary, the behaviour of water is influenced by physical/spatial as well as chemical interactions. Chemical effects include hydrogen bonding to binding sites such as ion clusters, ester, amide, carboxyl and polar sites (141). A hierarchy of interactions has been proposed in order of decreasing energy. They are as such: ion-ion > water-ion > water-polar = polar-polar = water-water > water-hydrophobic (142).

Experimentally, hydration was measured in this work by measuring mass changes. For mass changes to infer hydration, equation 1-3 has been used (143). In this equation, the moisture absorption is simple ratio-wise change equation which describes the absorption as an incremental increase in wet weight (polymer+water) as a ratio to the initial weight in terms of percentage. Other techniques such as NMR and Magnetic Resonance Imaging (MRI) has been used to measure hydration in the event of swelling and erosion occurring simultaneously. NMR has been used to obtain the diffusion coefficient of solvent and NMR imaging has been used to construct a time evolution of hydration (144, 145). Alternative to NMR imaging, once the diffusion coefficients are gathered, substituting into appropriate diffusion equations can produce a time evolution of hydration. The MRI does this by mapping ^1H nuclei associated with mobile water (146).

$$\text{Hydration \%} = \frac{M_t - M_0}{M_0} \times 100 \quad \text{Equation 1-3}$$

where M_0 is the initial mass and M_t is the mass at sample time. In this work, hydration was measured for placebo polymers and formulation using the above equation in chapter 4 and 5.

1.2.1.2 Swelling

There have been multiple theories to describe swelling in polymers. The kinetics of swelling is a continuous process of transition from un-solvated glassy to a relaxed rubbery region. Fick's law of diffusion describes solute transport from polymeric matrices. In rubbery polymers, hydration is described by Fickian transport

and a concentration dependent diffusion coefficient. Fickian transport refers to the solute transport process in which the polymer relaxation time (t_r) is much greater than the solvent diffusion time (147). In glassy polymers, the lagging reorientation of polymer molecules leads to anomalous effects if conducted near or below the T_g .

According to the Bajpai classification, two basic categories arise (148). The first category is the Fickian or Case I transport which appears when the T_g of polymer is well below the ambient temperature. Here, the polymer chains are very mobile and the solvent penetrates easily. The hydration rate, R_{hyd} is slower than the polymer chain relaxation rate, R_{relax} , ($R_{hyd} \ll R_{relax}$), as shown by the first (top) scenario of Figure 1-14.

The second category is non-Fickian diffusion, which occurs when the T_g of the polymer is above the ambient temperature. For non-Fickian diffusion, the polymer chains are less mobile than in Case I transport causing slower hydration into the polymer (149). Two subtypes arise in non-Fickian diffusion, depending on the hydration rates. They are Case II transport and anomalous transport. If the R_{hyd} is much faster than the R_{relax} , Case II transport arises distinguishable by a sharp boundary between the hydrated and non-hydrated parts ($R_{hyd} \gg R_{relax}$). This is shown in the third (bottom) scenario in Figure 1-14. In this case, the drug molecules penetrate the swollen layer much more in the same amount of time compared to Case I transport. In contrast, anomalous transport arises when the hydration rate and relaxation rates are similar ($R_{hyd} \approx R_{relax}$) (143). This is shown in the second (middle) scenario in Figure 1-14.

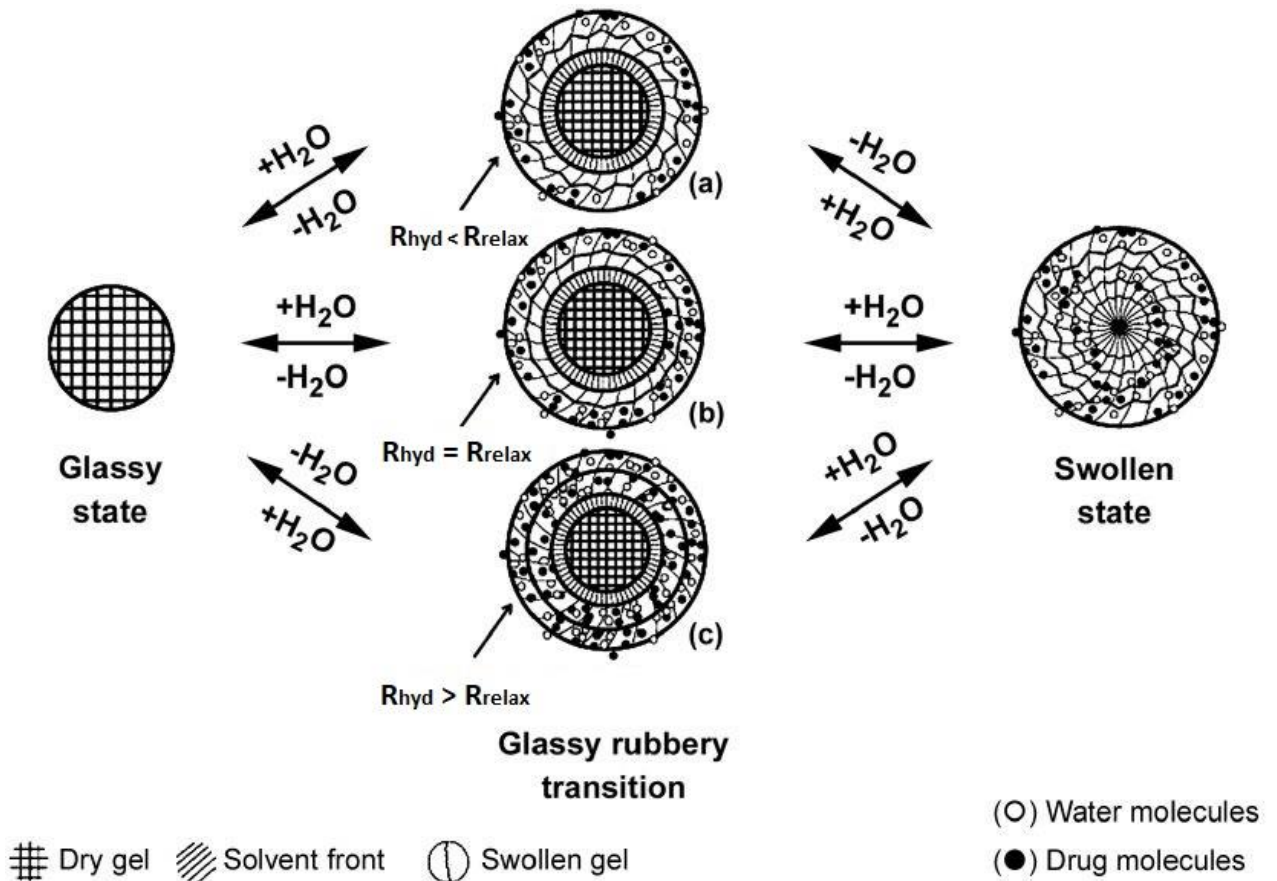


Figure 1-14: Illustrations of swelling cases. The top is Case I transport, the middle is anomalous transport, and the bottom is Case II transport (143).

Experimentally, swelling is measured by volume changes. Ratio-wise percentages volume changes are calculated using Equation 1-4 (150). In this work, the swelling was measured for placebo polymers and formulation using the equation in chapter 4 and 5.

$$\text{Swell \%} = \frac{V_t - V_0}{V_0} \times 100 \quad \text{Equation 1-4}$$

where V_0 is the initial volume and V_t is the volume at sample time.

1.2.1.3 Erosion

Erosion is defined as the loss of mass through the physical dissolution of a polymer. This can result either due to dissolution and diffusion of the polymeric chains or via chain scission, followed by dissolution and diffusion (151). The chain scission is also referred to as chemical degradation that occurs due to hydrolysis for biodegradable polymers (152, 153). This degradation is reflected by loss of molecular weight while erosion is reflected by mass loss (154). In the case of degradation, hydration must occur before hydrolysis can occur. Polymer erosion is a more complex process as it depends on many other processes besides

degradation, such as morphological changes and characteristics of the oligomers formed (155). The resultant oligomers and monomers are more soluble than the polymers. The dissolved products eventually diffuse away from the polymer system shown in Figure 1-15.

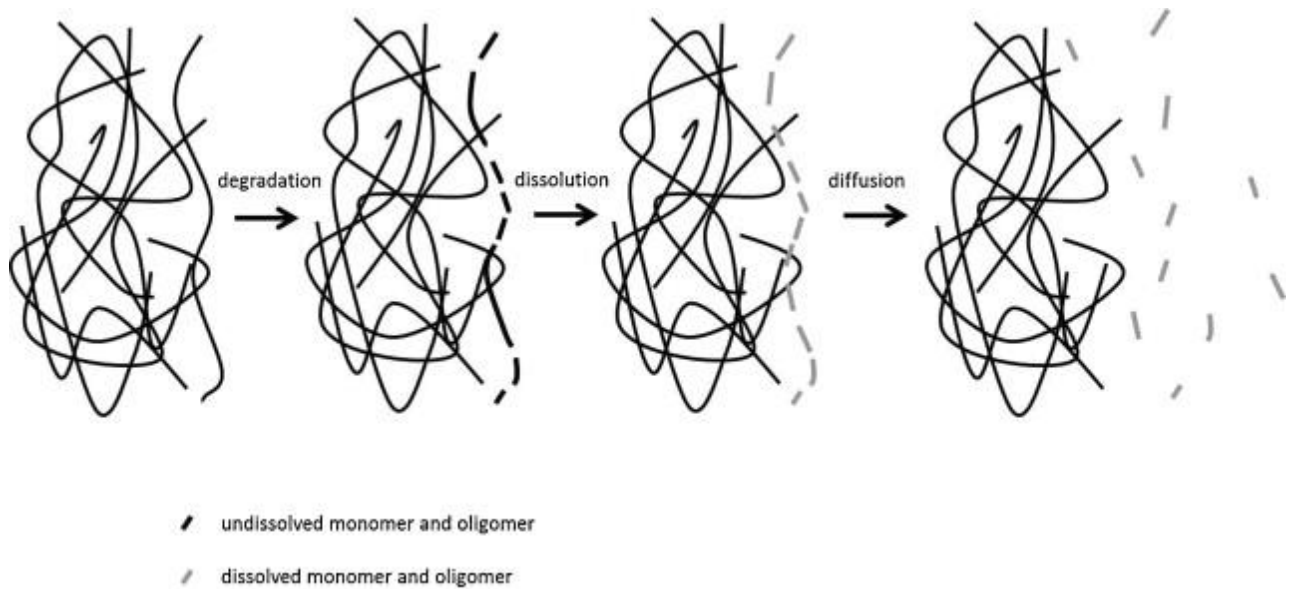


Figure 1-15: The combination of processes leading to erosion (153).

There are two macroscopic mechanisms via which erosion occurs: bulk erosion (homogeneous erosion) or surface erosion (heterogeneous erosion). In bulk erosion, the solvent hydrates (R_{hyd}) into the polymer faster than polymer scission (R_{sci}) causing the polymer to degrade at the same rate throughout the bulk of the system ($R_{hyd} \gg R_{sci}$). Bulk eroding polymer retains the original geometry and size during most of the dissolution process but the chain scission occurs throughout the material. The molecular weight and the mechanical strength of the specimens decrease in time during the erosion process. The decrease in molecular weight occurs essentially from the beginning of the degradation process, whereas loss of mass is much delayed. The external dimensions of the polymer material remain essentially unchanged until the material disintegrates at a critical time point. (156). Conversely, if the polymer scission is faster than the hydration, then erosion only occurs at the areas closest to the surface ($R_{hyd} \ll R_{sci}$). Size and mass of the device decrease in time, whereas molecular weight and mechanical properties of the polymer device remain unchanged. In surface erosion, the rate of mass loss is proportional to the surface area (156, 157). In drug delivery, such polymeric systems are favourable due to the predictability of the erosion process which

can be related to the drug release directly (158). The two mechanisms of erosion along with the loss of mass, molecular weight, and strength are shown of the polymer system are shown in Figure 1-16. In this work, erosion was studied for the placebo polymers in chapters 4 and 5 which include Hypromellose acetate succinate (HPMCAS), Poly-ethylene oxide (PEO), Poly-vinyl alcohol (PVA), Poly-ε-caprolactone (PCL), Poly-(vinylpyrrolidone-co-Vinyl Acetate (PVPVA), Soluplus, and xanthan gum. More details about these polymers are given in chapter 2. Some polymers such as PCL have been well studied to show surface erosion while others cannot be assigned one route exclusively (159, 160).

Whether a polymer undergoes surface or bulk erosion cannot be unequivocally assigned. Erosion model has been prepared by Burkersroda et al using an erosion number (ϵ). Erosion number is an expression which is the ratio between diffusion time and chemical chain scission time. For $\epsilon \gg 1$, surface erosion occurs while for $\epsilon \ll 1$, bulk erosion occurs, and $\epsilon = 1$, prediction cannot be made (161). A list of the driving factors of erosion was stated in the works of Burkersroda et al which are a multifactorial and complex dynamic interplay of degradation, swelling, dissolution, diffusion of oligomers and monomers, and even more factors for electrically erodible polymer or pH changes for pH-sensitive polymers (153, 155). Furthermore, the morphology of the polymer (crystalline vs amorphous) was shown to have different erosion rates (162).

Experimentally, erosion has been measured by dry mass changes shown by Equation 1-5 (163). The difference between hydration and erosion in terms of the sampled weight used is that the hydration measures wet mass including the weight of the solvent and erosion uses dry mass which is the weight material only after drying.

$$Erosion \% = \frac{M_t - M_0}{M_0} \times 100 \quad \text{Equation 1-5}$$

where M_0 is the initial dry mass and M_t is the dry mass at sample time. Predicting polymer dissolution behaviour can be predicted from the measurement of the three factors described which is discussed next.

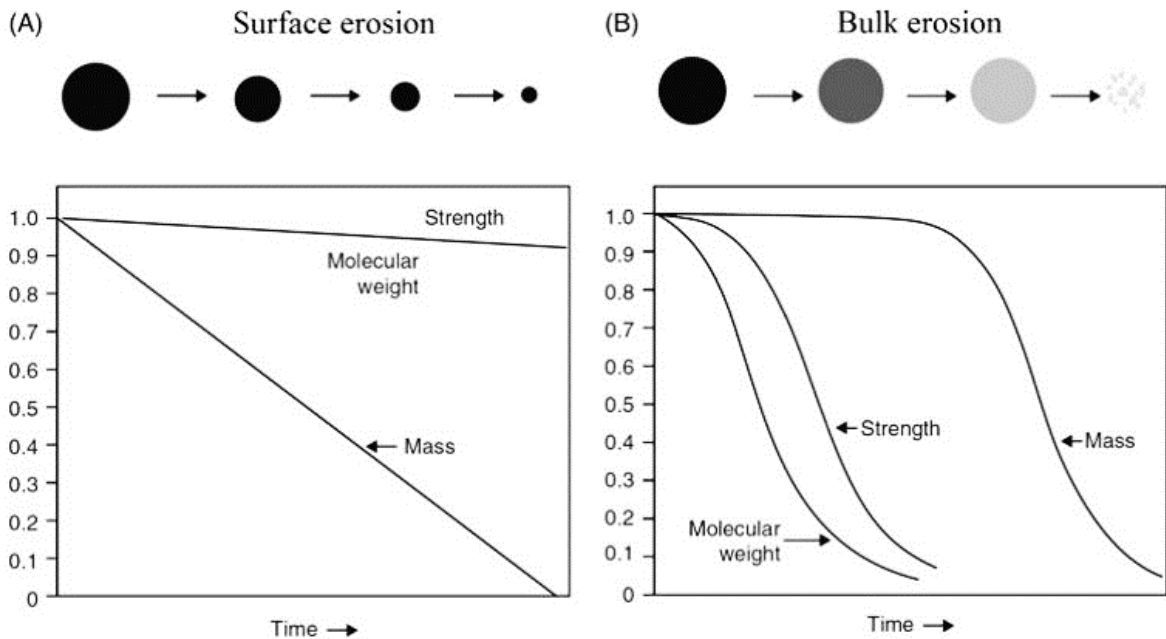


Figure 1-16: A) Surface erosion and (B) Bulk erosion. The strength, mass, and MW due to erosion in both cases are shown (156, 164).

1.2.2 Drug release behaviour of solid dispersions

Drug release is the process in which the drug is released from the polymeric matrix. Polymeric matrices release the drug in one of two ways: diffusion or erosion (151). In the case of diffusion-controlled release, the drug molecules translocate from the initial position in the matrix to the outer surface and onto the solvent through dissolution (165). The drug concentration gradient in the polymer matrix is the driving force for the molecules to diffuse into the surrounding medium. The highest concentration of the drug is in the non-hydrated dry regions of the matrix and the lowest is in the bulk of the solvent (166). The factors that impact the diffusion of a drug molecule is dependent upon the solubility of the drug in the polymer matrix, the concentration of drug in the matrix, and the diffusional pathlength. Many polymeric matrices have drug molecules on the surface of the matrix. Upon immersion into a solvent, the release of these drug molecules is controlled by the rate of diffusion of the drug into the surrounding environment. This can lead to “burst release” phenomenon (167).

For erosion controlled release, the two types of erosion discussed earlier are possible to be exhibited. If water is confined to the surface of the matrix, as in the case of hydrophobic polymers, polymer hydration will occur only on the surface and drug will be released as the surface of the polymer matrix erodes.

Alternatively, if the water penetrates the polymer matrix faster than dissolution at the surface, then erosion will occur throughout the entire material and the drug will be released by bulk erosion (151). Based on the type of controlled release kinetics, three types of drug release model have been formulated. They are as follows (147):

- Diffusion controlled models
- Dissolution based models
- Erosion based models

Diffusions controlled models are derived from Fick's I and II law of diffusion. To predict drug release profiles, the diffusion coefficient of the solute within the polymer matrix should be available, which could be measured by NMR and fluorescence correlation spectroscopy (168). Such models have many assumptions. They assume diffusion takes place only in one dimension, have a constant drug diffusion coefficient for the entire duration, have no matrix swelling or erosion of the bulk material, the drug is initially homogeneously distributed within the matrix, mass transfer resistance due to liquid unstirred boundary layers at the surface of the matrix is negligible compared to mass transfer resistance due to diffusion within the matrix, and drug dissolution is rapid and complete upon exposure to the solvent (147, 169, 170). Examples of diffusion models are the Higuchi model, Noyes-Whitney equation, Nernst-Brunner equation (165, 171). In this work, there are no polymeric matrix formulations that do not erode nor swell. In other words, all matrix formulations either swell or erode. For example, zein formulations used in this work do not erode but do swell significantly. As such, diffusion-controlled models only are not appropriate for describing release kinetics from zein formulations.

The second type of model is dissolution based models. Narasimhan and Peppas developed a model for polymer dissolution based on the molecular mechanism (172). These models assume a constant drug and solvent diffusion coefficient and moving boundaries (147). Moving boundaries indicate volume changes. Such models have shown to successfully capture Fickian and Case II type behaviour in the works of Narasimhan and Peppas wherein release profile of cimetidine hydrochloride from PVA tablet and sodium

diclofenac from a PVA tablet were fitted to the experimental data and the equation (172). Examples of dissolution based model are the Narasimhan-Peppas model and the Gompertz model (172, 173).

The third type of model is erosion based models. Such erosion based models are divided into two main groups based on the approach of erosion evolution. The first group is the diffusion-and-reaction model, which suggests the description of the erosion process as a combination of polymer diffusion and reaction. Majority of models in this group have been used to model bulk eroding process but there is also Monte Carlo technique that has been used for bulk eroding systems (174, 175). The second group is the cellular-automata model, assumes the erosion process as a random event (169). Majority of the second group of models assume the matrix surface detachment is commonly the rate-controlling step, and therefore the models are applied for the surface-eroding system. The erosion models, in general, assume constant material erosion rate and constant surface detachment of drug. Examples of erosion based models are the Weibull model, Hopfenberg model, and Hixson-Crowell model (170, 171, 176).

There are additional numerous empirical models that have been established may help explain the transport mechanism. Examples are Ritger-Peppas, Peppas-Sahlin, and Alfrey equations (147). However, these models do not provide additional insights into a more complex transport mechanism. Furthermore, these models may yield misinformation when there is a need for taking into account specific physicochemical processes (177). For example, Ritger-Peppas and Peppas-Sahlin equations have been applied to describe the release of sodium salicylate from HPMC tablets, indicating a non-Fickian drug release mechanism. The study also revealed that polymer erosion, swelling and dissolution were all involved in the release process and the authors suggested that the conclusion of a non-Fickian drug release mechanism, based on the diffusional exponent (n) of the Peppas models was misleading (178). One particular empirical model, being used frequently, is the Korsmeyer-Peppas model, shown by equation 1-6 (179, 180). Korsmeyer-Peppas has been successful in explaining 60% (or more in some cases) of the drug release profile of formulations that contain soluble and insoluble APIs and poorly soluble polymers. In such cases, significant swelling of the insoluble

polymer occurs after the partial dissolution of polymers and the drug, leading to the quick appearance of pores or even large cavities full of liquid through which the drug diffuses (169). Release from those systems was not well described by any other empirical models (181). Korsmeyer-Peppas has been successfully employed in cases wherein the rate of drug release follows neither the process of diffusion nor that of erosion (182). An exception to the application of this model is for mucoadhesive erodible formulations (183). Since Korsmeyer-Peppas is well suited to fit the drug release profile, this model was used for all the drug release profiles for all the formulations in chapter 3 and 5.

$$\frac{M_t}{M_\infty} = kt^n \quad \text{Equation 1-6}$$

where M_t is mass at time t , M_∞ is the total drug mass at infinite time, k is the drug release constant, and n is the drug release index. These empirical models have been used generally for three major geometries (shown in Figure 1-17) as all geometries can be simplified to three underlying geometries: slabs, spheres, and cylinders (184). Within the matrix system, there exists monolithic solutions and monolithic dispersions. Monolithic dispersions are polymeric matrices where the drug concentration in the matrix is higher than drug solubility. All polymeric matrices in this work were monolithic dispersions and of cylindrical geometry.

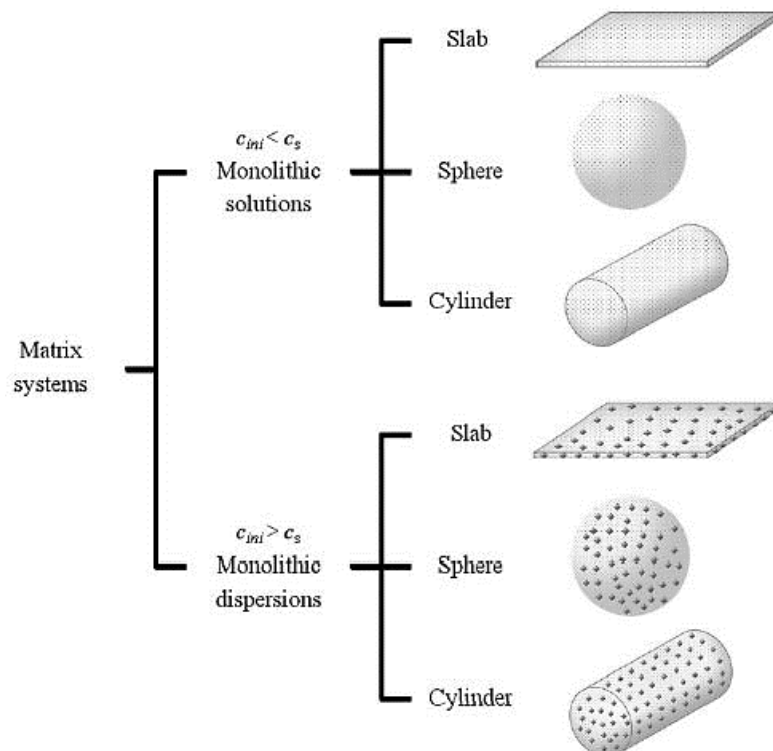


Figure 1-17: Diffusion controlled monolithic geometries. C_{ini} is the initial concentration and C_s is the saturation concentration (184).

1.2.3 Predicting drug release profiles

The aim of controlled release systems in the context of personalized medicine is to achieve a drug release profile that is tailored to the patient's clinical needs. The aim of sustained release, extended release, and immediate release dosage has been explored extensively in pharmaceuticals (44). The factors affecting drug release are the drug, the release medium, and the matrix material. Of the three factors, the drug and release medium is not alterable. The drug is required by the patient and the release medium in the body is fixed to be either in pH 1.2 or 6.8. This leaves only the matrix material alterable. Of the existing works undertaken for controlled release, there is a plethora of literature that focuses on chemical modifications (185-193), and physical modifications (194-197). Such works for chemical modifications have included manipulation of pH-sensitive interactions between polymers by Chen et al to enhance the drug release profile (185) and using different polymer MW by Maggie et al to achieve an altered drug release profile (190), while physical modification includes the creation of pores in the formulation by Ghasemi et al (197). In recent years with the advancement of technology, the mathematical modelling aspect has been witnessed more in pharmaceuticals (161, 170, 198). The benefits of such mathematical modelling with regards to controlled release systems have been discussed. One of the advantages that mathematical models provide is that they yield quantitative information about the system. This characteristics information can be combined with statistics which can give rise to the classification of polymers and drug (199).

An existing commercial software named GastroPlus® aims to be able to simulate a desired drug release profile of the formulated product based on the input information of the excipients used and geometry of the dosage form. The input information for this operation from the user consists of start and end times of the dissolution, the buffer media pH, the paddle speed, and dissolution media volume (200). The drug release profile is generated using one of the three options. The first of these is using the classical Nernst-Brunner model (Equation 1-7) while the second and third options are using the Johnson model (200). Depending on the particle shape, either spherical or cylindrical, the appropriate Johnson-spherical (Equation 1-8) or Johnson-cylindrical (Equation 1-9) model is used, respectively.

$$\frac{dM_U}{dt} = - \left[\frac{3D\gamma}{hr\rho} \left(C_s - \frac{M_D}{V} \right) \right] M_U \quad \text{Equation 1-7}$$

where M_U is the amount of undissolved drug, M_D is the amount of dissolved drug, γ is a unitless calibration constant, V is the volume of dissolution medium, ρ is the density of the drug, D is the diffusion coefficient, h is the diffusion layer thickness, and C_s is the solubility at the particle's surface.

$$\frac{dM_{Ui}}{dt} = - \left[\frac{3D\gamma}{h_i r_{0i} \rho} \left(C_s - \frac{M_{Dt}}{V} \right) \right] (M_{U_{0i}})^{1/3} (M_{Ui})^{1/3} \quad \text{Equation 1-8}$$

where M_{Ui} is the amount undissolved drug of the i th particle, $M_{U_{0i}}$ is the initial amount of undissolved drug, and r_0 is the initial particle radius.

$$\frac{dM_{Ui}}{dt} = - \left[\frac{D\gamma}{h_i r_{0i} \rho} \left(C_s - \frac{M_{Dt}}{V} \right) \right] (M_{U_{0i}})^{1/3} (M_{Ui})^{1/3} \frac{(1 + 2s)}{s} \quad \text{Equation 1-9}$$

where s is the shape factor is (L/D) obtained by dividing L (length) by diameter (D). GastroPlus has been used for a wide variety of pharmacodynamic and pharmacokinetic modelling in humans and animals including the prediction of *in Vitro* drug release profiles for the development of extended release doxazosin tablets (201), correlating *In Vitro* profile with *In Vivo* absorption of efavirenz tablets to develop generic medications (202).

1.2.4 Objectives of the research

FDM 3DP is most commonly advocated for the development of polypills which can be personalized. The method of drug impregnation for drug loading into filament has shown low yielding. Therefore, HME coupled with FDM is an alternate method of filament preparation that allows great flexibility during manufacturing with drug loading, carrier polymer blending, and molecular dispersion of drug. HME, being in the pharmaceutical industry, has been well studied. However, no literature on sources of errors of HME-FDM as a coupled process exists. Therefore, the first objective of this project (Chapter 3) is to probe the sources of errors during a pharmaceutical HME-FDM 3DP coupled process which can then be used to improve the precision when FDM 3DP is used for pharmaceutical applications.

To achieve personalization, precision in drug release from oral dosage is inevitable. Developing a tool to guide the design of the dosage form that can deliver the desired drug release profile to suit each patient will

move the field closer to its intended clinical application. Therefore, understanding the formulation behaviour for polymers and drug is important at the macroscale. Understanding the macroscale behaviour in terms of hydration, swelling, and erosion of the polymer can help predict the drug release for a given class or type of drug in a pre-experiment scenario. Furthermore, the quantitative information deduced from applying the appropriate mathematical model to the appropriate geometry can be combined with statistics to create a classified dataset, which can be the beginnings of a database. This classification can aid in the creation of personalised dosage form that exhibits the desired release profile. Thus, the following specific objectives are the focus of Chapter 4-6:

1. Investigate the predictability of pharmaceutical polymers and polymer blends behaviour (swelling, hydration, and erosion) in aqueous media.
2. Investigate the effects of the key physicochemical properties of the drug on drug release and the significance of the role that the polymer plays in controlling the drug release.
3. Build a classification approach to describe the characteristic drug release profiles of polymeric based dispersions.
4. Use the information generated by the classification approach to build a dataset, with the attempt to enable the guided selection of the appropriate polymer to achieve a desired drug release profile for a given type of drug.

Chapter 2: Materials and Methods

2.1 Introduction

This chapter provides the specific characteristic information of the materials, the working principles, and general methodologies of the processing and characterisation techniques used throughout the project. The materials consist of polymers and drugs. The polymers used in this work were a copolymer of acrylic & methacrylic acid esters & quaternary ammonium groups (Eudragit RS), Xanthan gum, Polycaprolactone (PCL), Poly1-vinylpyrrolidone-co-Vinyl Acetate (PVPVA), Poly(vinyl caprolactam-polyvinyl acetate-polyethylene glycol) graft copolymer (PCL-PVAc-PEG) also known as Soluplus, polyvinyl alcohol (PVA), polyethylene oxide (PEO), Hypromellose acetate succinate (HPMCAS), and purified zein. The model drugs used in this work were paracetamol, lidocaine, and ibuprofen. The reason for using these drugs was that the drugs exhibit different ionized charges at pH 1.2 and pH 6.8 as well as different levels of solubility.

The samples in this work were prepared by hot melt extrusion and/or FDM 3D printing. Once the solid dispersion based filaments or dosages were prepared, characterization was performed to understand their physiochemical properties by using differential scanning calorimetry (DSC), thermogravimetric analysis (TGA), attenuated total reflectance Fourier transform infrared spectroscopy (ATR-FTIR). Ultraviolet spectrometer (UV) was used to evaluate *in vitro* drug release performance. Finally, the statistical techniques used to analyse the data is also discussed in detail in this chapter.

2.2 Materials

2.2.1 Paracetamol (PCM)

Paracetamol, also known as Acetaminophen, is an antipyretic, non-opioid analgesic, and non-steroidal anti-inflammatory drug of Biopharmaceutics Classification System (BCS) class III. The IUPAC name of PCM is *N*-(4-hydroxyphenyl)acetamide (203). PCM used in the thesis was brought from Sigma Aldrich (CAS Number: 103-90-2) with a purity of $\geq 99\%$ (204). The structure and the physical properties are summarised in Table 2-1.

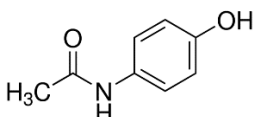
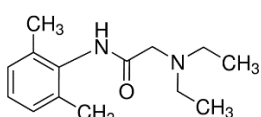
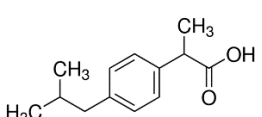
2.2.2 Lidocaine (LID)

Lidocaine, also known as lignocaine, is an amide-type local anaesthetic and Class 1b antiarrhythmic frequently used for its anaesthetic and antiarrhythmic benefits and in the treatment of chronic pain (205, 206). It is of BCS class I. The IUPAC name of lidocaine is 2-(Diethylamino)-N-(2,6-dimethylphenyl)acetamide (207). LID was selected as a model drug due to the positive ionized state in the ranges below PH 7. LID used in the thesis was brought from Sigma Aldrich (Dorset, UK) (CAS Num: 137-58-6) with a purity of $\geq 98\%$ (208). The structure and the physical properties of LID are presented in Table 2-1.

2.2.3 Ibuprofen (IBU)

Ibuprofen is an NSAID with anti-inflammatory, analgesic, and antipyretic properties commonly used to treat fever, pain arising from inflammation and post-surgery, and rheumatoid arthritis (209). It is of BCS class II. The IUPAC name for IBU is 2-(4-isobutylphenyl)propionic acid (210). IBU was selected as an opposing charged API to LID for the anionic charge it poses in the identical pH and its hydrophobic nature (211, 212). IBU, used in the thesis, was brought from Sigma Aldrich (Dorset, UK) (CAS Num: 15687-27-1) with a purity of $\geq 98\%$ (213). The structure and physical properties are enlisted in Table 2-1.

Table 2-1: Physical properties of the three model drugs.

Properties	 Paracetamol	 Lidocaine	 Ibuprofen
Formula	CH ₃ CONHC ₆ H ₄ OH	C ₁₄ H ₂₂ N ₂ O	C ₁₃ H ₁₈ O ₂
Molecular Weight (g/mol)	151.16 (214)	234.34 (208)	206.28 (213)
Solubility (g/L)	17.39 at 30°C (215)	22 at 37°C (216)	0.021 at 25°C (210)
pKa	9.38 (203)	8.01 (207)	5.3 (210)
LogP	0.46 (203)	2.44 (207)	3.97 (210)
Density (g/cm ³)	1.31 (203)	1.01 (217)	1.08 (218)
Glass Transition Temperature (°C)	21.4 (219)	-60 (220)	- 45 (221, 222)

2.2.4 Hypromellose acetate succinate (HPMCAS)

HPMCAS is a pH-responsive cellulose derivative, in particular a cellulose ester, containing acetyl and succinoyl groups (223). Cellulose derivatives are generally categorized into three groups based on pH-responsiveness and chemistry as pH responsiveness, hydrophilicity, and hydrophobicity shown in Figure 2-1.

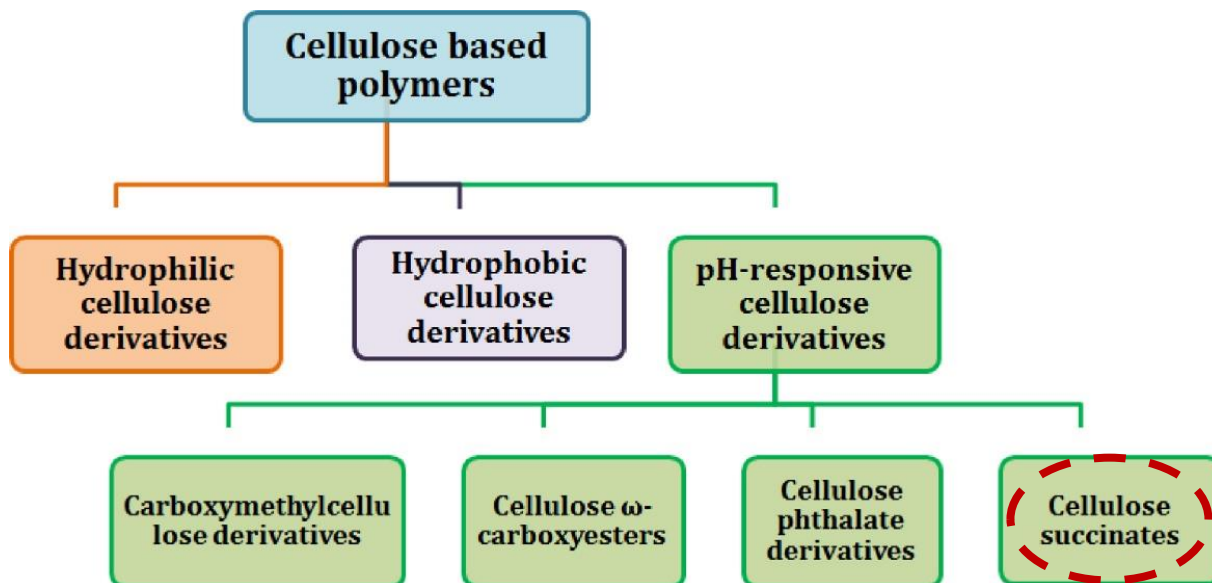


Figure 2-1: The classification of cellulose based polymers. HPMCAS is categorized as cellulose succinate encircled in red (224).

The structure of HPMCAS is shown in Figure 2-2. HPMCAS possesses four types of substituents which are substituted on the hydroxyl groups: methoxy (12%–28%, w/w); hydroxypropyl (4%–23%, w/w); acetate (2%–16%, w/w); and succinate (4%–28%, w/w) (225) making it relatively hydrophobic. Due to the succinate groups, HPMCAS has a pK_a of about 5 (226). Below pH 4, 10% of the polymer ionizes while at least 50% are ionized above pH 5. The pH-dependent solubility can be attributed to the ratio of succinate and acetyl groups. Hence, different grades of HPMCAS have different pH-dependent solubilities, which are summarized in Table 2-2. HPMCAS grades have T_g ranging from 120 °C to 135 °C (227).

Table 2-2: The succinate and acetyl group ratios in different HPMCAS grades and their soluble pH (225, 228).

HPMCAS grade	Succinoyl (%)	Acetyl (%)	Dissolved pH
L-grade	15	8	>5.5
M-grade	11	9	>6.0
H-grade	7	12	>6.5

HPMCAS when partially ionized, minimizes the formation of large polymer aggregates which allows drug/polymer colloids to form. The hydrophobic regions of HPMCAS can interact with insoluble parts of

poorly water-soluble drug molecules, resulting in amorphous drug/polymer complex in solution while the hydrophilic regions can allow the structure to be stable in the aqueous solution (225). The negatively charged succinate groups keep these nanostructures stable, evading the large hydrophobic aggregates of the polymer and drug in solution. HPMCAS used in this work was purchased from Shin-Etsu Chemical Co Ltd. (Niigata, Japan) AS-LF grade with an average molecular weight (MW) of 18000g/mol and white fine powder appearance. By composition, methoxy is 22.3%, hydroxypropoxy is 6.7%, succinoyl is 18.1%, and acetyl is 5.7%. The T_g of this grade is 121°C and the range of solubility of this HPMCAS is pH 5.5 to pH 8 (229).

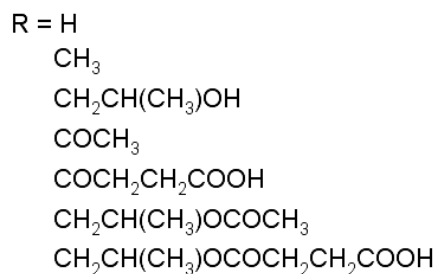
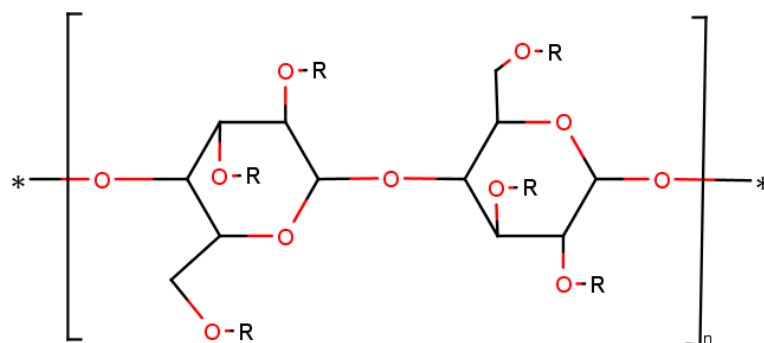


Figure 2-2: HPMCAS structure

2.2.5 Zein

Zein is a major storage protein of corn (230). It is a natural protein located in the endosperm of corn accounting for almost 50% of the total protein content of whole grain of corn (231). Zein is extracted by wet milling from corn gluten meal by solvent extraction using isopropanol (232). Zein is available as a yellow powder whose colour is due to the xanthophylls remaining bound with zein by hydrophobic interaction. Zein is classified as prolamin protein which has high proportions of one of the three constituents or combinations of them; proline and glutamine, all of which are aliphatic amino acid (233). Zein has high proportions of hydrophobic amino acids including 20% of leucine, 10% of proline and 10% of alanine (234, 235). This is the cause of high surface hydrophobicity (236). Zein has been further grouped based on varying

molecular weights (237) and solubility in solutions of 0 to 95% isopropyl alcohol (233). The three major fractions/groups categorized are α -zein (19 and 22 kDa) accounting for 75–80% of total zein, β -zein (17–18 kDa) accounting for 10-15% of total zein, and γ -zein (16 and 27 kDa) accounting for 5–10% of the total zein. With regards to pharmaceutical applications, zein has been used in tablets and caplets as it is a unique matrix former. Zein matrices do not erode (238) but undergo hydration and swelling and can potentially increase by more than 200% of the initial mass (14, 160). Such level of hydration can be compared to hydrophilic matrices (163) and is significantly greater than that of insoluble matrices (239). In addition to this, zein is an excellent candidate due to its natural origin, swelling and self-assembling properties. Purified zein used in this work was purchased from Acros (New Jersey, USA) (CAS #: 9010-66-6) with greater than 91.0% protein content (240). The T_g of pure zein is reported to be approximately 150 °C (241).

2.2.6 Poly (Ethylene Oxide) (PEO)

PEO is a hydrophilic, linear polymer available in several molecular weights ranging from 100,000 to 8,000,000. PEO is a synthetic polymer with the same chemical structure as PEG but higher molecular weight. The structure is shown in Figure 2-3. As unbranched linear macromolecules, the grades of PEO differ with the length of molecular chains. Polymers with molecular weight less than 100,000 are usually called PEGs while higher molecular weight polymers are classified as PEO (242).

PEO can be completely dissolved in both cold and hot water but will precipitate out when the temperature of the solution is close to the boiling point of water, called cloud point. This cloud point is affected by the concentration, the molecular weight of PEO, the concentration of salts, and the pH (243). The dissolution rate of PEO is very slow. The dry powder is easy to be wetted by water, but it tends to form agglomeration and gel if it is not dispersed properly when dissolving into water. The T_g of PEO products ranges from -50°C to -57°C and molecular weight do not have a significant impact on the T_g (243) within the family of products

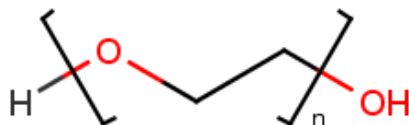


Figure 2-3: PEO structure

PEO has been used for oral dosages taking advantage of the bioadhesive properties (244, 245) and as an osmotic pump tablet (246, 247). The adhesiveness arises due to the long linear chain structure that allows them to form a strong interpenetrating network with the mucus (248). Likewise, the osmotic pump potential arises due to the aqueous solubility and can be used to create high osmotic pressure (249). It is also used as a thickening agent swelling seven times the initial weight (250). PEO used in this work was purchased from Colorcon (Kent, UK) Polyox WSR 301 NF with MW of 4,000,000 (251).

2.2.7 Poly-(Vinyl Alcohol) (PVA)

PVA is a whitish, tasteless, odourless, non-toxic, biocompatible, thermostable, granular or powdered semi-crystalline linear synthetic polymer (252, 253). The monomeric structure of PVA is shown in Figure 2-4. The physicochemical and mechanical attributes of PVA are governed by the number of hydroxyl groups present in the PVA (254). The period length of the saponification reaction determines the degree of hydrolysis of PVA. Based on the degree of hydrolysis and MW, different grades of PVA are available on the market having different characteristics including melting point, viscosity, pH, refractive index, and band gap (255). The effect of variation in vinyl acetate length and degree of hydrolysis under acidic or alkaline conditions results in various congeners of PVA having different flexibility, tensile strength, dispersing power, emulsification index, adhesiveness, and solubility (256).

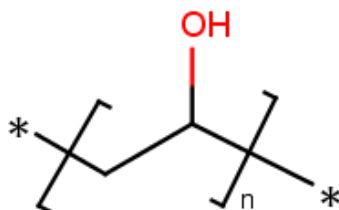


Figure 2-4: PVA structure

PVA has been widely used in the field of 3D printed caplets (46, 257-259). PVA is also well known hydrogel materials and having good biocompatibility has many other applications such as used in contact lenses, implants, drug delivery systems, medical implants and also wound dressing (260). The PVA used in this work was gifted as a sample from Kuraray (Hattersheim, Germany) under the brand name Mowiflex C17 (purity >96%) supplied in the form of pellets. The average MW is 50000 g/mol and T_g of this sample is 60 °C. The indicated melt flow index is 14-20 g/10min (190 °C, 21.6kg) (261).

2.2.8 Poly (ϵ -caprolactone) (PCL)

PCL is a polymer composed of hexanoate repeat units in the class of aliphatic polyesters (262). PCL is a hydrophobic, semi-crystalline polymer with up to 50% crystallinity (263, 264). The crystallinity and molecular weight dictate the physical, thermal, and mechanical properties, and the degradation of PCL (264). PCL structure is shown in Figure 2-5.

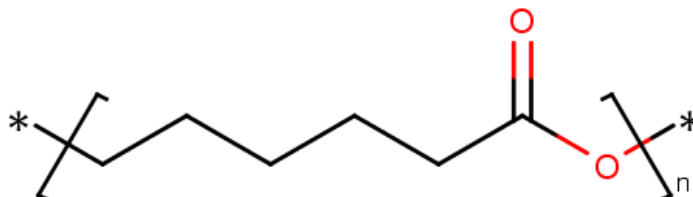


Figure 2-5: PCL structure

PCL has a wide range of applications. The good solubility of PCL, its low melting point and exceptional blend-compatibility has made it a good candidate for research in the biomedical field (265). PCL is used in controlled drug delivery systems due to three factors: 1) due to its permeability ensuring uniform API distribution in the matrix producing a reliable sustained release of the API (266, 267); 2) due to its slow degradation via hydrolysis (268); 3) while undergoing biodegradation, there is a minimal generation of an acidic environment as compared to other polyesters such as PLA and polyglycolic acid (264). The PCL used in this work was purchased from Perstorp (Malmö, Sweden) brand graded as CAPA 6800 (CAS #: 24980-41-4) supplied in granular 3mm pellets. The average MW is 80,000 g/mol, water content of 0.35%, T_g is -61°C, and the melting temperature is 62°C (269). The degree of crystallinity of PCL has been reported to be 67% (270).

2.2.9 Poly (vinylpyrrolidone-co-Vinyl Acetate) (PVPVA)

PVPVA is a copolymer of vinylpyrrolidone and vinyl acetate in a ratio of 6:4 manufactured by polymerization in isopropanol. Since 40% is replaced with lipophilic vinyl acetate functional groups and therefore it is less hygroscopic than the homopolymer system (271). It is very soluble (>10%) in hydrophilic liquids and hydrophobic solvents (272). Commercial PVPVA is yellowish-white in colour with fine particle size (<100µm) and good flow properties (273). The structure of PVPVA is shown in Figure 2-6.

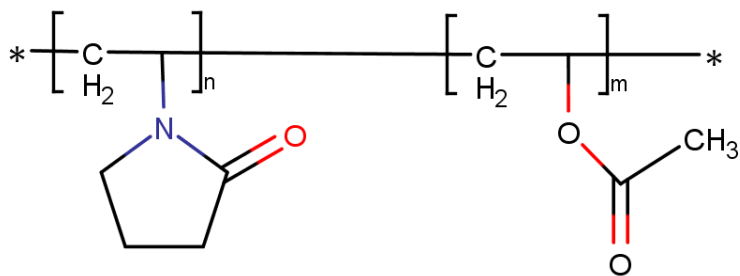


Figure 2-6: PVPVA structure.

PVPVA has a wide range of usages. Usage in oral formulations includes enhancement in solubility and bioavailability of the drug poorly water-soluble drugs like indomethacin, tolbutamide, and nifedipine, (274).

The PVPVA grade used in this work was Kollidon64 from BASF (Ludwigshafen, Germany). This grade of PVPVA has a T_g of 111 °C, T_m of 140 °C, pK_a of -2.5, and solubility of greater than 300g/L (275, 276).

2.2.10 Eudragit® RS 100

Eudragit is the trade name for a common class of polyacrylates and polymethacrylates. Polymethacrylates are synthetic cationic and anionic polymers of dimethylaminoethyl methacrylates, methacrylic acid, and methacrylic acid esters in varying ratios (277). The commonly used Eudragit for the preparation of controlled release solid dispersions is Eudragit L, Eudragit RL, and Eudragit RS, Eudragit RLPO and Eudragit RSPO (272).

Eudragit RS and RSPO are copolymers of ethyl acrylate, methyl methacrylate and low content of methacrylic acid ester with 5% of functional quaternary ammonium groups (272). The MW of this grade is also 32,000 g/mol. Different subgrades of RS exist in different forms. RS100 is granules while RSPO is powder. This grade of Eudragit is insoluble (278). For all works in this thesis, Eudragit RS100 has been used purchased from Evonik (Essen, Germany) supplied as granules, with MW of ≈ 32000 g/mol and T_g of 64 °C (279). The structure of Eudragit RS100 is shown in Figure 2-7.

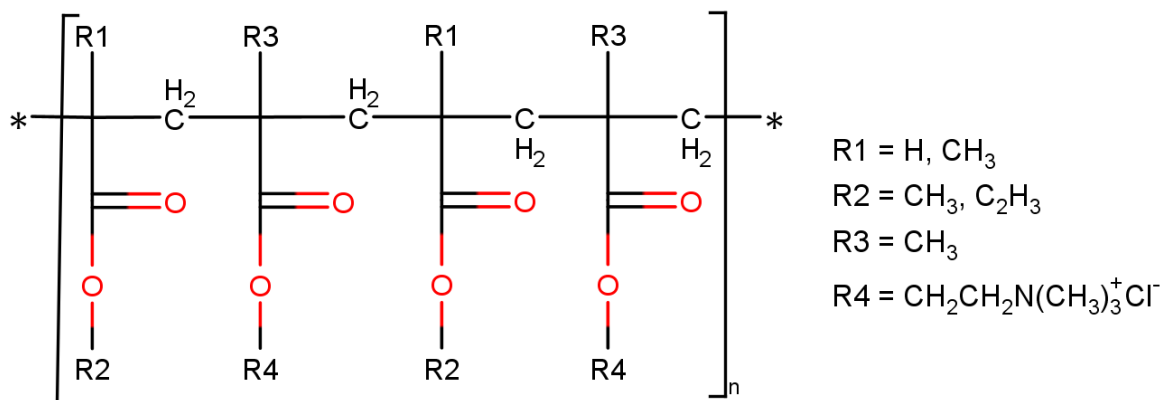


Figure 2-7: Eudragit RS structure. The R groups are from reference (277).

2.2.11 Soluplus®

Soluplus is a graft polymer consisting of polyvinyl caprolactam-polyvinyl acetate polyethylene glycol (PCL-PVAc-PEG). It has been designed for preparing solid solutions of poorly water soluble API by HME due to low T_g of 70 °C and thermal stability at high temperatures (280). The average molecular weight of Soluplus ranges from 90,000 to 140,000 g/mol (281). Soluplus has an amphiphilic structure shown in Figure 2-8 with high aqueous solubility ($\approx 50\%$). Commercial soluplus is a free flowing white-yellowish granule with a faint odour (280). Soluplus used in this work was purchased from BASF (Ludwigshafen, Germany) (CAS #: 402932-23-4) with MW of $\approx 118,000$ g/mol, T_g of 70 °C, and density of 1.082 g/cm³ (282).

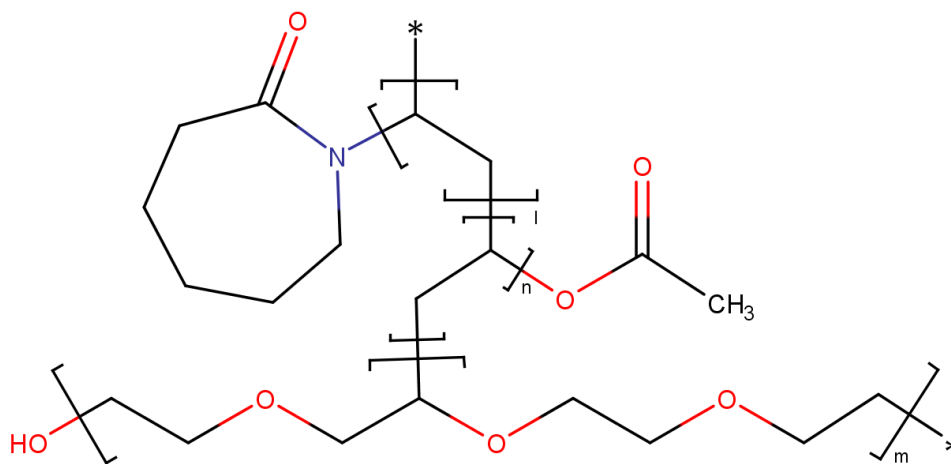


Figure 2-8: Soluplus structure.

2.2.12 Xanthan Gum (XG)

Xanthan gum is an extracellular anionic heteropolysaccharide produced by fermentation of carbohydrates (283). The primary structure of XG consists of repeating pentasaccharide units (284) shown in Figure 2-9. XG has many desirable properties making it of significant industrial interest. One of the characteristics is the

manipulation of the rheology of XG in water systems making it a widely used thickener and stabilizer. The stability is due to two components; primarily the ordered conformation of XG is believed to be responsible for the stability, and secondary is further stabilization by addition of salt. Cations in order $\text{Na}^+ < \text{K}^+ < \text{Ca}^{2+}$, can promote intermolecular cross-linking and strengthening the gel network (285, 286). The resultant of this is XG exhibits pH independent stability which is unaffected over ranges of pH 1 to pH 13 (283, 287) and temperature stability up to 90 °C (288). The XG used in this work was purchased from CPKelco (Leatherhead, UK). The brand name is Xantural 180 (CAS #: 11138-66-2) supplied as a white fine powder with purity greater than 91% (289). The T_g of xanthan gum has been determined to be between -16.4 and -23.3 °C (290).

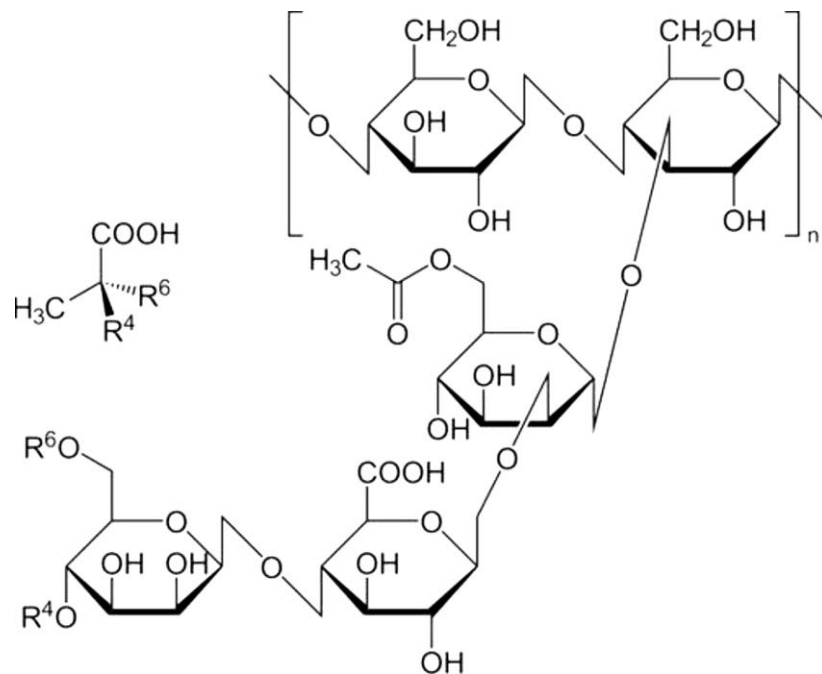


Figure 2-9: XG structure. From reference (291).

2.2.13 Acrylonitrile butadiene styrene (ABS)

ABS is a thermoplastic copolymer whose structures of the monomers are shown in Figure 2-10. The proportions of the monomers typically range from 15% to 35% acrylonitrile, 5% to 30% butadiene and 40% to 60% styrene (292). ABS used in this work was purchased from MakerBot (Brooklyn, USA) as a 3DP filament consisting of ABS resin (CAS #: 9003-56-9) greater than 98% and styrene (CAS #: 100-42-5) less than 0.1% (293) with T_g of 105°C and filament diameter of 1.75 mm (294). ABS was used in this study as a control printed object to the PVA torus printed which is the theme in chapter 3.

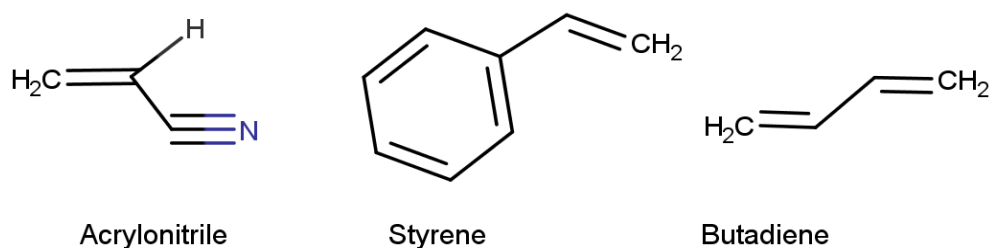


Figure 2-10: Chemical structures of ABS raw materials.

2.3 Processing methods

2.3.1 Hot Melt Extrusion (HME)

The details of the working principle of HME have been discussed in Chapter 1 and therefore, only experimental set up is described here. The raw materials were fed in through the hopper. The hot melt extruder used in this work was twin screw that has co-and counter-rotating twin screw option (Thermo Scientific HAAKE MiniLab II) with a maximum of 5g of material limit at a given time and volume of 7cm³ (295). The extrusion temperature was 30 °C above the T_g or melting point. The screw speed was 100 rpm for all samples. All extrudates were tested in triplicates. HME technique was used to make pure polymer extrudates (studied in Chapter 4) and drug loaded polymeric dispersions (studied in Chapters 3 and 5).

2.3.2 FDM 3D Printing (FDM 3DP)

The FDM 3DP was used in this study to prepare solid dispersions in tori shape in Chapter 3 using PVA with paracetamol as a formulation (PVA-PCM), and ABS as another. Makerbot Replicator 2X desktop 3DP with dual extrusion (MakerBot Industries, LLC) was used with dosages designed in blender software, an open-source 3D computer graphics software used for creating animation, visual effects, and 3D printed models, and finally imported for printing through Makerbot (Brooklyn, USA) Thingiverse software preinstalled on Makerbot (296). The printing temperature for commercial ABS was as per manufacturer recommendation of 220 °C, while for the PVA-PCM formulation was printed at 170°C, 185°C, 185°C, and 190°C. The platform temperature for ABS was 110 °C as per manufacturer recommendation, while 100 °C was used for PVA-PCM filaments. Each formulation was printed in triplicates.

2.4 Material characterisation methods

2.4.1 Differential scanning calorimetry (DSC)

DSC is one of the most common thermoanalysis techniques. DSC is a highly sensitive technique used to determine the thermotropic properties of excipients or actives. The primary function of DSC is to determine the energetics of phase transitions and conformational changes and subsequently quantifying based on the temperature dependence (297). This is achieved by measuring the heat flow difference into the sample and a reference as a function of temperature, while both are maintained at an identical temperature for the duration (298). Using this flow rate difference, it is possible to detect and characterize the melting temperature, the glass transition temperature, the recrystallization temperature, the degradation temperature, and the temperatures of polymorphic formations (299) as well as the degree of purity, the heat of fusion, heat of reactions, and kinetic determination of chemical reactions, such as curing (300, 301). There are two types of commercial DSC; one being powered compensation DSC and the other being heat-flux DSC. The benefit is that both of these DSC cases require minute quantities of a sample between 0.1-10 mg will suffice and operating temperatures range from -180 °C to 700 °C (298). In the heat-flux DSC, a single furnace contains both the sample and the reference pans as shown in Figure 2-11. The pans are put on a heated thermoelectric disk. Attached thermocouples at the bottom of the thermoelectric disk monitor the differential heat flow producing a change in thermocouple signal which is directly proportional to a change in temperature. The heat flow signal is measured as a function of thermal resistance shown by equation 2-1.

$$\frac{dQ}{dt} = \frac{\Delta T}{R} \quad \text{Equation 2-1}$$

Where dQ/dt is the heat flow, ΔT is the temperature difference between the sample and reference, and R is the thermal resistance of the heating disk. This heat flow (dQ/dt) can also be expressed in terms of specific heat capacity (C_p), which is defined as the energy supplied to increase the temperature of a material by one degree Kelvin, as shown by equation 2-2.

$$\frac{dQ}{dt} = C_p \cdot \frac{dT}{dt} + f(T, t) \quad \text{Equation 2-2}$$

where dQ/dt is the heat flow, C_p is the sample specific heat capacity, dT/dt is the heating rate and $f(T,t)$ is the kinetic event that is a function of time at an absolute temperature. The kinetic event can be events such as polymer relaxation, melting, and crystallization. With these two equations, it is possible to combine heat capacity combined with the kinetics of the sample. A resulting DSC thermogram is shown in Figure 2-13.

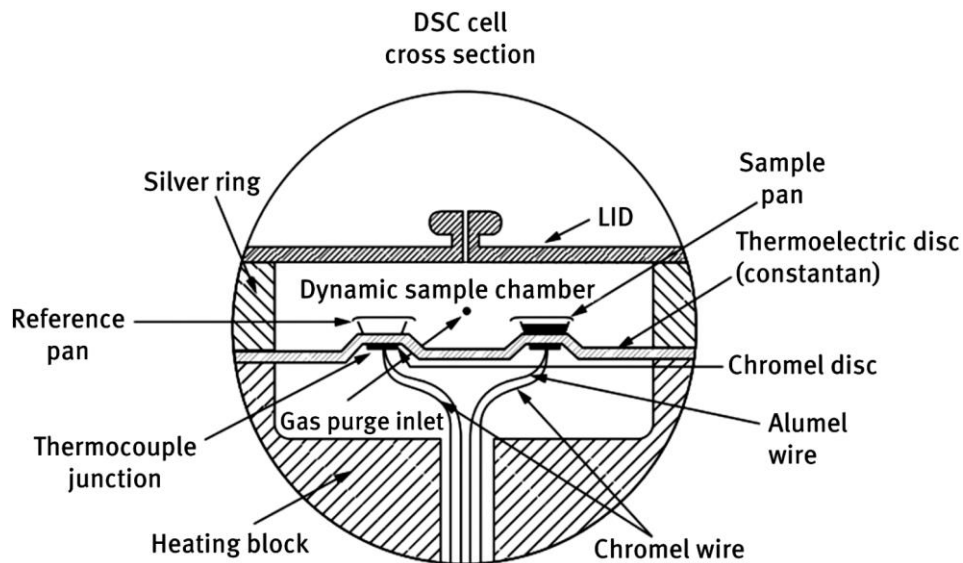


Figure 2-11: Schematic of the furnace interior of a heat flux DSC (298).

In a power compensated DSC, two separate heating elements are used: one for the sample and one for the reference. The sample and reference stay at the same temperature and any change in the temperature between the sample and the reference acts as a signal to “turn on” one of the heaters. When any chemical or physical changes such as reaction, phase change, or glass transition occur in the sample, there is a difference in temperature of the sample and reference. This leads to extra power to be directed to the cell at the lower temperature to heat it to keep the temperature of the sample and the reference cells as constant ($\Delta T = 0$) throughout the experiment. In this way, the power and the temperatures of the sample and reference are measured accurately and continuously using Pt resistance sensors (shown in Figure 2-12).

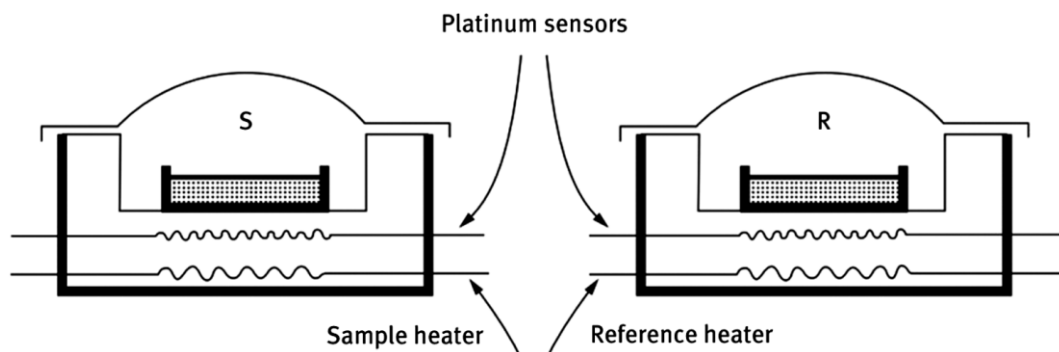


Figure 2-12: Schematics of power compensated DSC (298).

The DSC used in this work was A Q-2000 (TA Instruments, Newcastle, DE, USA), which is a heat flux DSC, to characterise the polymers powders/pellets, the APIs powder, and the formulation extrudates and 3D printed solid dispersions. All samples were weighed up to 3 mg and TA standard aluminium crimped pans were used. The standard procedure was to heat at rates of 10 °C/min in the range between -50 to 240 °C followed by cooling at 10 °C/min to the starting temperature and reheat at 10 °C/min for all samples. A constant nitrogen purge was applied at the 50 mL/min. Samples were tested in triplicate.

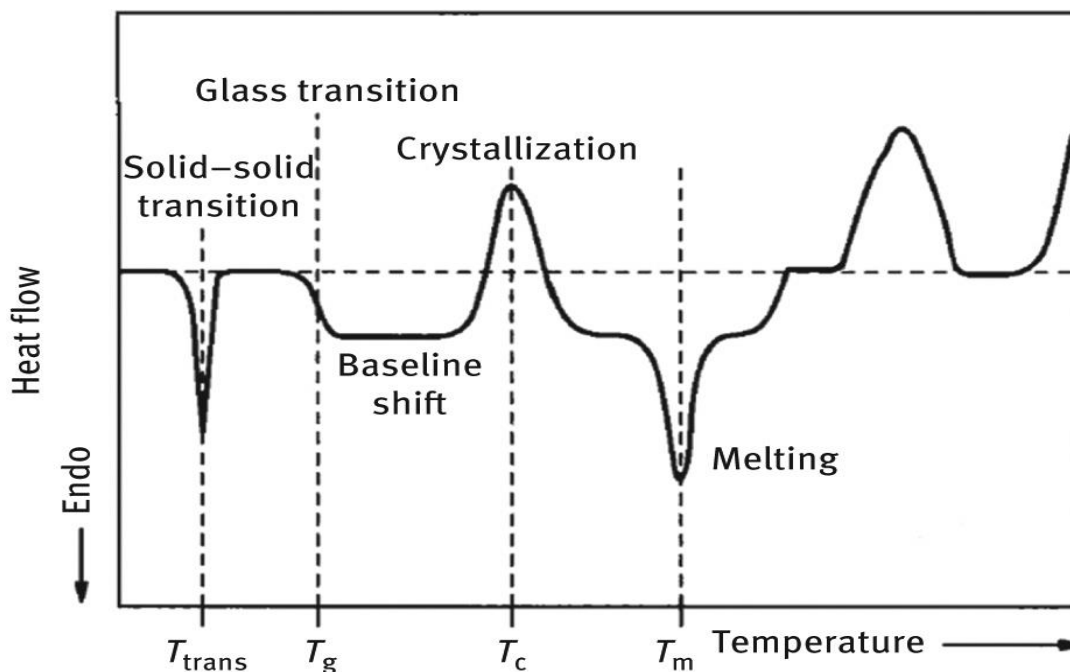


Figure 2-13: DSC thermogram showing thermal kinetic events. The area under the curve can be calculated to give the enthalpy of the event (298).

2.4.2 Thermogravimetric Analysis (TGA)

TGA is a widely used technique for characterising a system by measuring changes in physicochemical properties at elevated temperatures either as a function of increasing temperature or time (302). Results from such analysis are used to determine the thermal and oxidation stability of materials. It also provides information about the components of a material, decomposition kinetics, moisture and volatile content of materials (303). Weight loss during analysis is usually an indication of decomposition, evaporation, reduction or desorption. On the other hand, weight gain indicates oxidation or absorption. The basic operation for TGA is a precision balance is used to weight the sample and placed in a furnace that is programmed for a linear rise of temperature with time (302). The resulting graph can have three features; a plateau implying constant weight, a curve implying the rate of weight loss, and an inflexion, at which the

weight change is minimum but not zero, implying the formation of an intermediate compound (302, 304). The TGA used in this study was TGA Q5000 (TA Instruments, Newcastle, USA) for evaluating the thermal stability of polymers, APIs, formulation, and physical mixtures. The standard procedure was to heat at rates of 10°C/min from 25 °C to 400 °C. All samples were done in triplicates.

2.4.3 Fourier transform infrared (FTIR)

FTIR has a wide range of applications from analysis of small molecules or molecular complexes to the analysis of cells or tissues (305). In the case of pharmaceuticals, it is used for the former two cases. The IR region is beyond 700 nm (the ending of visible wavelength) and the classical IR region extends from 200 to 4000 cm^{-1} . Within this region, subdivisions have been made; Far infrared (400–10 cm^{-1}), mid-infrared (4,000–400 cm^{-1}), and near-infrared (13,000–4,000 cm^{-1}) (306). The energies associated in this region are low enough to suffice molecules to vibrate but not to cause electron transitions. This leads to the basic operating principle of FTIR which is probing molecular vibrations. The IR band absorbed correspond with the vibration of certain functional groups (307). The FTIR measurement can be carried out in the modality of transmission or reflectance. An IR spectrum is obtained by determining what fraction of the incident IR is absorbed or reflected at a particular frequency. Therefore, IR spectroscopy can decipher the molecular structure as the spectra contain vibrations uniquely dependant on atomic masses, bond strengths, and intra-and intermolecular interactions (306).

The hardware of FTIR consists of an interferometer and the schematic of a two beam Michelson interferometer is shown in Figure 2-14 which consists of a fixed and a moveable perpendicular mirror. Thereafter Fourier transformation is used to convert the interferogram to a spectrum via a computer program. When this is done in the absence of any sample, it results in the base spectrum and when done in the presence of a sample, it produces the sample spectrum (306).

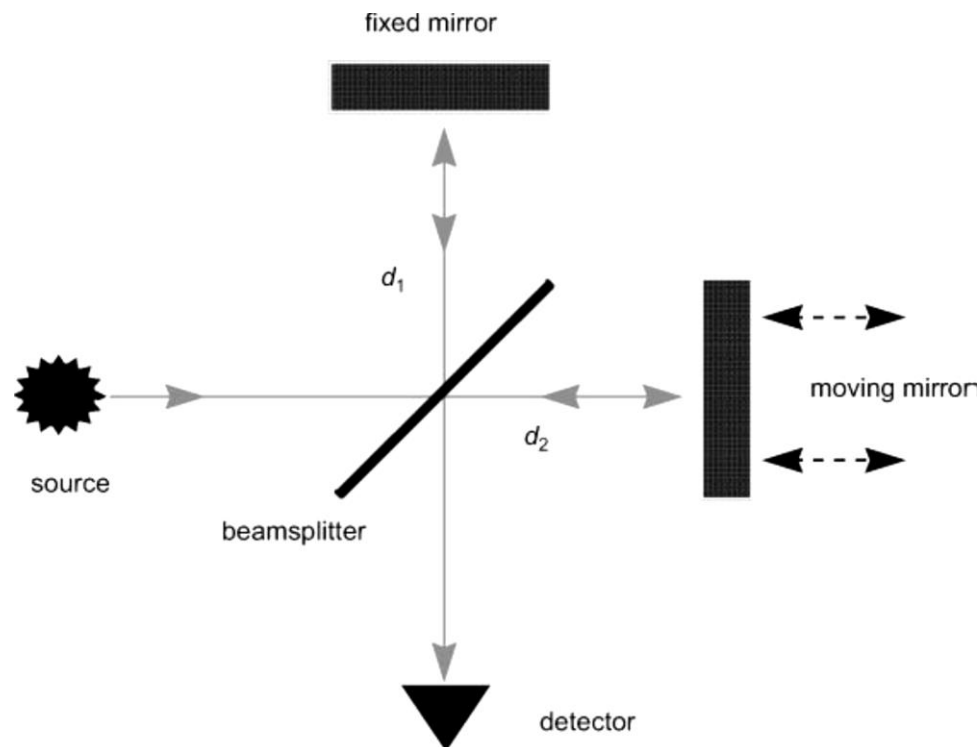


Figure 2-14: Schematic of a Michelson interferometer (306).

There are two modalities of FTIR operation which are transmittance and reflection. In transmission, the IR source illuminates the sample and the detector is placed behind the sample to acquire the fraction of light transmitted through the sample. In such cases, the sample must be at partly transparent. Transmission mode has been used to analyze thin samples such as films (308) or tissues (309) but it is not possible with thicker tablets. In contrast, for reflection, the detector is placed on the same side of the sample as the source to record the signal reflected by the sample. The two types of reflection measurement commonly used in the characterisation of pharmaceutical materials are attenuated total reflection (ATR) and diffuse reflection (DRIFTS) (306).

In ATR, the sample is placed in optical contact against a special crystal, termed the *ATR crystal*, which is composed of a material with a high index of refraction. The IR beam is focused onto the bevelled edge of the ATR element by a set of mirrors which is reflected through the crystal, and then directed to the detector by another set of mirrors while in DRIFTS, the IR beam interacts with the sample and is scattered by interaction with the particles. A fraction of this beam is reflected by the sample and recorded by the detector. The two methods of measurements are shown in Figure 2-15.

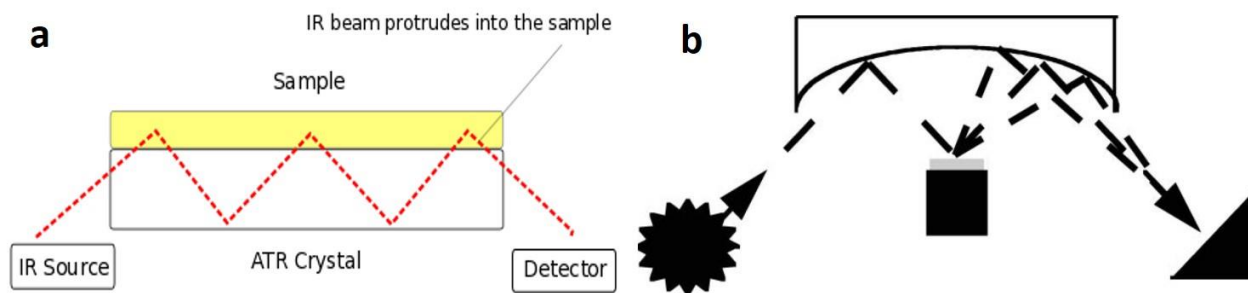


Figure 2-15: a) ATR crystal schematic. b) DRIFTS measurement schematic. Adapted from (306, 310)

In this study, FTIR was used to characterise the samples and to study the interactions between drug and polymers in the formulations for chapters 4 and 5. IFS 66/S spectrometer (Bruker Optics Ltd., Coventry, U.K.) equipped with a Golden Gate heated top plate attenuated total reflectance accessory (Specac Ltd., Orpington, U.K) was used to perform the IR spectroscopic studies. The spectrum reading was taken between 4000 and 550 cm^{-1} with 2.0 cm^{-1} resolution and 32 scans. All samples were examined in triplicate. OPUS software version 7.8 was used to analyse ATR-FTIR spectra.

2.4.4 Ultraviolet Spectrophotometry (UV-vis)

UV-vis uses ultraviolet light which is ranges from 800 - 200 nm and is based on Beer-Lambert law (Equation 2-3) which states that the absorbance of a solution is directly proportional to the concentration of the absorbing species in the solution and path length. Hence, if the path length is fixed, it can be used to determine the concentration from the absorbance in a solution.

$$A = \epsilon \ell c \quad \text{Equation 2-3}$$

where A is absorbance, ϵ is molar absorption coefficient, ℓ is the optical path length, and c is the molar concentration. The principle of UV-vis is that molecule or ion will exhibit absorption in the visible or ultraviolet region when radiation causes an electronic transition within its structure. Thus, the absorption of light by a sample in the ultraviolet or visible region is accompanied by a change in the electronic state of the molecules in the sample. The energy supplied by the light will promote electrons from their ground state orbital to higher energy, excited state orbital or anti-bonding orbital (311). Since each electron in a molecule has a unique ground state energy, and because the discrete levels to which it may jump are also unique, any absorbed energy will correspond to a specific wavelength. The specific wavelength at which the absorption

occurred can be plotted spatially along with any absorption data at wavelengths over the UV region creating the UV absorption spectrum (312). The schematic of the UV procedure is shown in Figure 2-16.

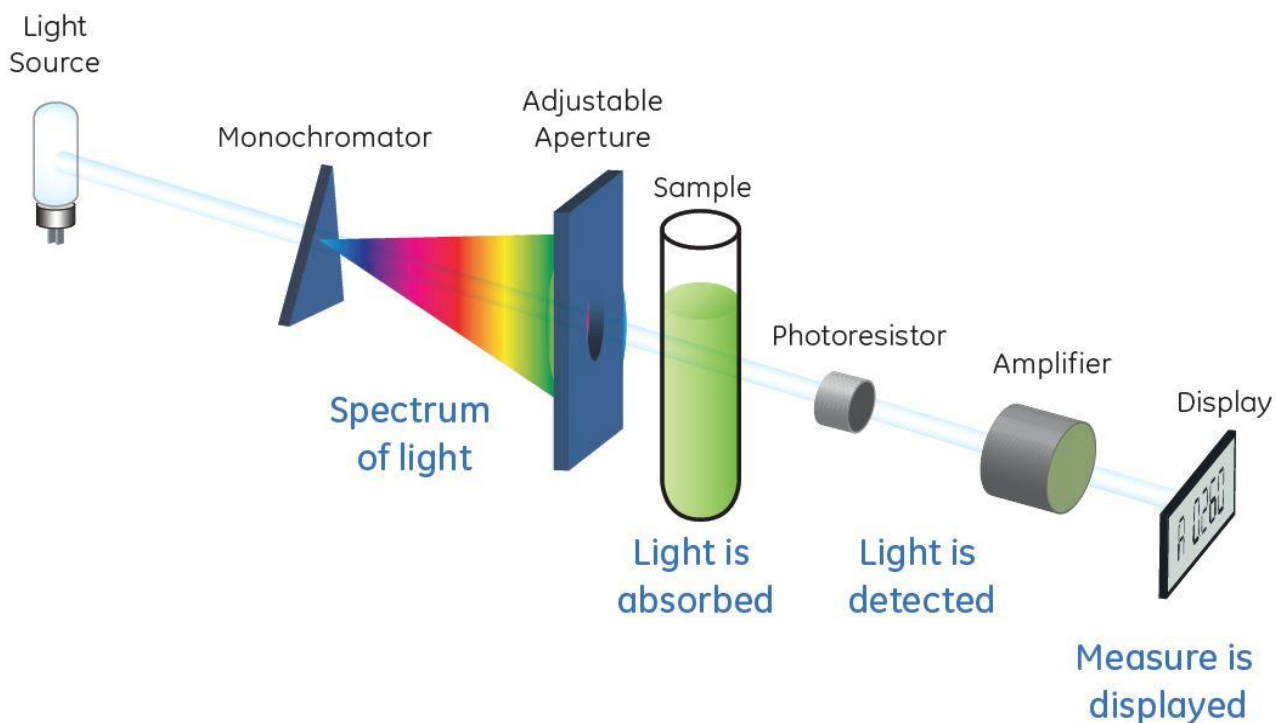


Figure 2-16: UV data capture process (313).

In this study, UV-vis was used to evaluate the drug release concentrations of lidocaine, ibuprofen, and paracetamol formulations in chapters 5 and chapter 3 (paracetamol only) as a part of the in vitro studies. The UV-vis (PerkinElmer Lambda 35, Llantrisant, UK) was used with ranges from 190–1100 nm and the resulting spectrum was analysed on UV Winlab software (version 2.85.04) supplied by PerkinElmer (314).

2.4.5 Drug Loading Efficiency

The amount of drug loaded in the HME extrudates which consisted of paracetamol and PVA in Chapter 3, lidocaine within zein, HPMCAS, and PEO, ibuprofen within zein, HPMCAS, and PEO, and paracetamol within zein, HPMCAS, and PEO matrices in Chapter 5 were measured by dissolving the solid dispersion samples in a beaker containing 250 ml of buffer pH 1.2 and ethanol (organic solvent) and measuring the UV absorbance of the solution. A similar procedure was followed for measuring drug efficiency in pH 6.8 where the extrudates were dissolved in a beaker containing 250 ml of buffer pH 6.8 and ethanol. After complete dissolution, 5 ml samples were withdrawn and filtered using 0.45 μm pore size (Minisart NML single use syringe, Sartorius, UK). The filtered samples then scanned for their content of the API (lidocaine, ibuprofen,

and paracetamol) using a UV–VIS at the max peak wavelength (λ_{\max}) 220 nm, 264 nm, and 243 nm for lidocaine, ibuprofen, and paracetamol, respectively. The max peak wavelength of each drug was obtained by screening across the full spectrum of each sample. The loading efficiency was measured in triplicates.

2.4.6 In vitro dissolution studies

In vitro dissolution study is the core of and the final parameter to be measured that allows for the bridging of further data analysis and the culminating aspect (drug release) of all the previous steps carried out, which included all the preformulation work and formulation work. The dissolution test is carried out in a dissolution apparatus according to official pharmacopoeia for reasons of evaluating drug release quantitatively in terms of kinetic parameters from formulations (315). This is done for quality control and research and development to check if drug content uniformity is within acceptable limits (316). According to USP recommendations, there are four official USP apparatus; USP apparatus I (Basket), USP apparatus II (Paddle), USP apparatus III (Reciprocating Cylinder), and USP apparatus IV (Flow Through Cell) (317).

In this study, USP apparatus II (Copley CIS 8000, Copley Scientific Ltd., Nottingham, U.K.) was used as shown in Figure 2-17. The experiments were performed at $37\text{ }^{\circ}\text{C} \pm 0.5\text{ }^{\circ}\text{C}$ with a paddle speed rotation of 100 rpm in 900 ml of pH 1.2 and pH 6.8, under sink conditions, for all HME polymer placebo extrudates in chapter 4, HME formulation extrudates in chapter 5, and FDM 3D printed formulation in chapter 3. The justification of performing in sink conditions is that all dissolution models, which were discussed in section 1.2.3, are valid in sink conditions. The media was sampled at times of predetermined times and filtered through an $0.45\text{ }\mu\text{m}$ filter. The drug concentration was measured by UV-Vis spectroscopy at the sampled time intervals. The *in vitro* drug release studies were done in triplicates.

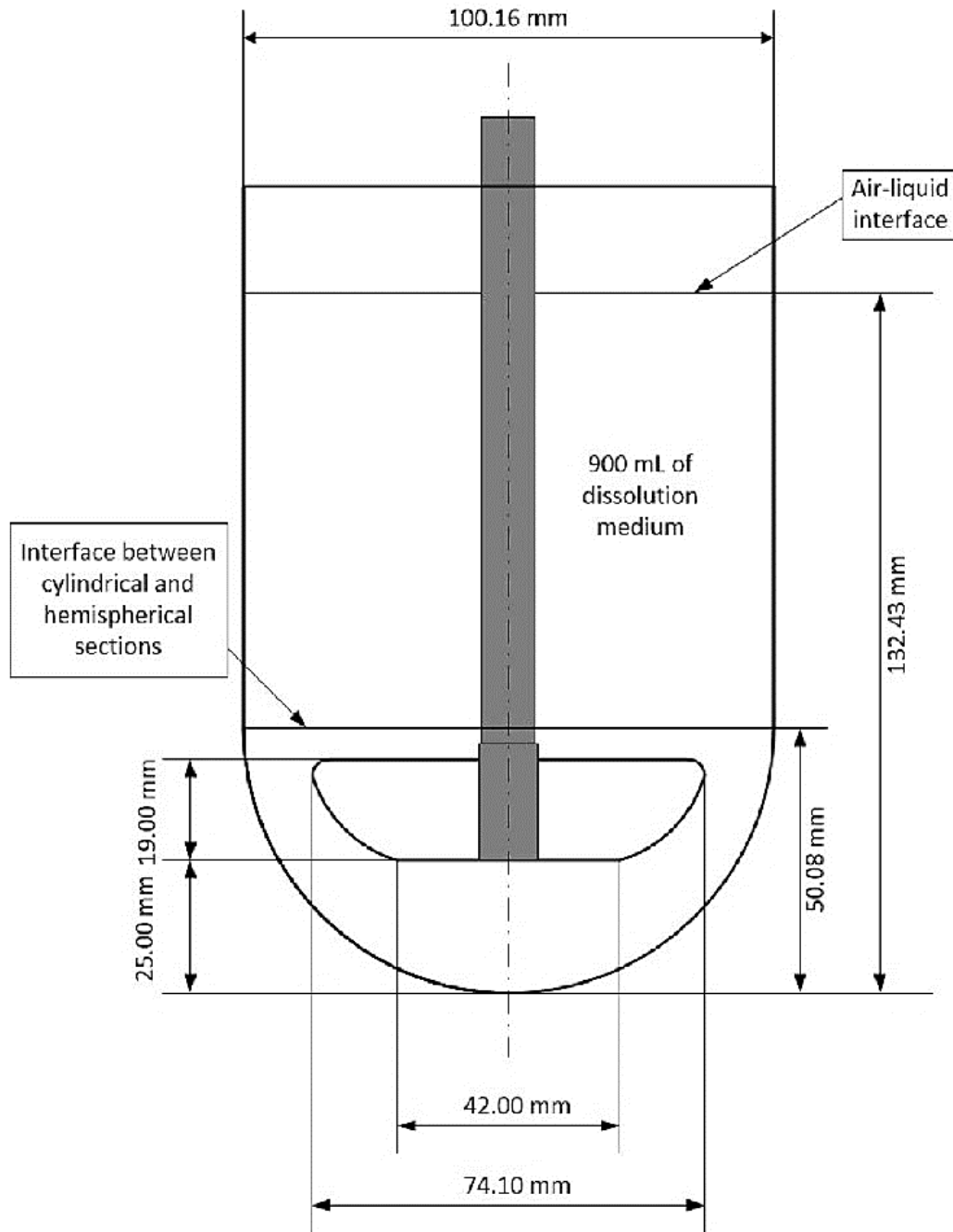


Figure 2-17: USP Apparatus II as described by USP standards (318).

2.5 Advanced Statistical Methods

In this section, the advanced statistical methods used in analysing the data will be discussed. These include classification schemes such as K-means, prediction schemes such as artificial neural network, and dimension reduction technique such as principal component analysis which are used in Chapter 6. The first of these methods to appear chronologically in Chapter 6 is K-means clustering which is discussed next. All analysis was performed on SPSS (statistical software package) from IBM version 25.

2.5.1 K-means Clustering

K-means clustering is a common clustering technique. K-means clustering consists of four steps. The first step is termed 'initialization' wherein cluster points (k points) are randomly generated in the space, which are used as initial centroids. The second step is termed 'classification' wherein the distances from all the objects (data points) to all the centroids (cluster mean point) are calculated and each object is assigned to its closest centroid. The third step is termed 'centroid calculation' wherein new centroids are calculated using the mean value of the objects that belong to each cluster. This is iterated until the fourth step is reached, which is 'convergence' wherein no object migrations from one cluster to another is possible due to absolute minimization of distance calculation that has been achieved (319). Therefore, the algorithm has reached equilibrium and terminates with the output of clusters graphically generated. This process is summarized in Figure 2-18.

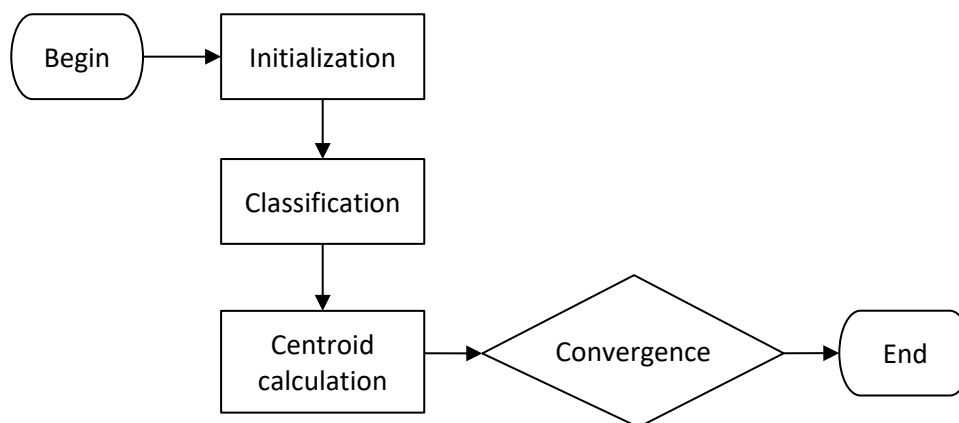


Figure 2-18: Standard K-means algorithm (319).

In this study, K-means clustering was performed on the dataset of polymer placebo behaviours and formulation drug release parameters in chapter 6 to obtain the centroid value of each cluster. The number of clusters was determined to be four clusters in the case of polymers and two or three clusters for formulations. The basis for the number of clusters is discussed more in chapter 6.

2.5.2 Principal Component Analysis (PCA)

PCA is a multivariate dimension reduction technique that is used to reduce complicated sets of data containing possibly correlated variables (320). PCA method of reduction is preferred because the systematic variation of a single variable is desired in scientific study. However, in sciences, researchers frequently

collect measurements on several variables simultaneously which are mostly exhibiting some degree of correlation. Therefore, it is inherent that PCA must reduce large datasets in an adaptive and insightful way and assumes that the phenomena of interest can be explained by the variances and covariances between the variables in the original dataset (321).

Mathematically, PCA reduces the dimensionality by taking interrelated variables, x_1, x_2, \dots, x_p , and finding combinations of these based upon variances to produce a transformed set of variables, z_1, z_2, \dots, z_p , that are uncorrelated. The indices z_i are called the principal components (PC) (321). The resultant graph is termed loading plot and an example of a PCA transformed loading plot is shown in Figure 2-19.

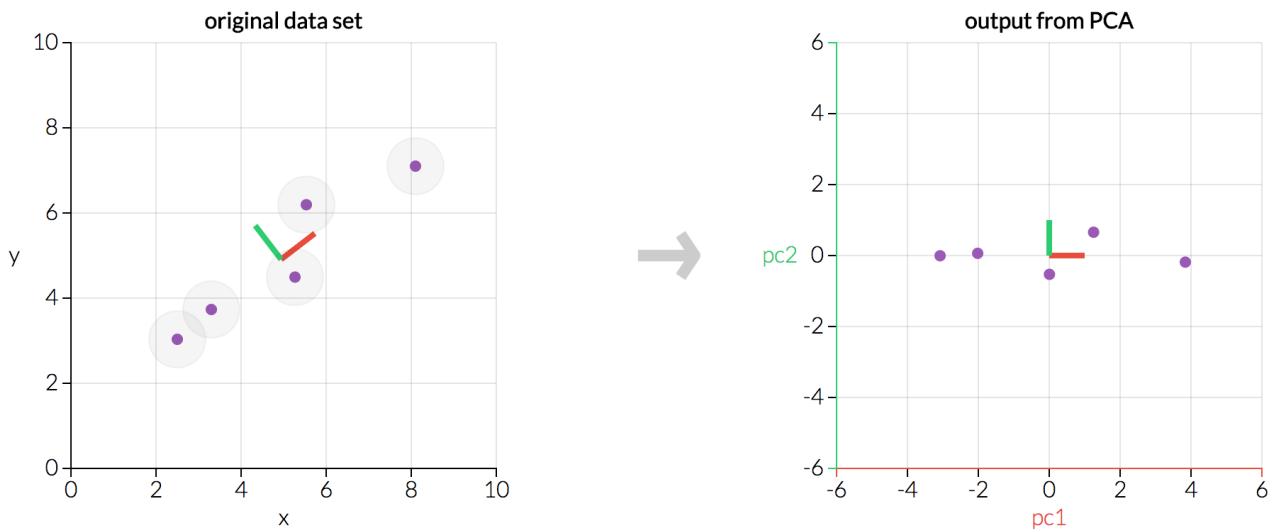


Figure 2-19: Original data in cartesian coordinates on the left and the output on the right after PCA is performed. The transformed coordinates are in term of PC1 and PC2, which are the two axes (322).

The number of PC that most efficiently explains the data is a key step and is achieved by a scree test or scree plot which involves eigenanalysis (323, 324). Eigen analysis forms from finding the eigenvectors and eigenvalues of the covariance matrix. In a scree plot, the x-axis is the number of eigenvalues determined. The eigenvalues are ordered from the strongest to weakest in terms of the effect on the dataset. The y-axis gives the magnitude of the eigenvalues from the covariance matrix diagonalization. Based on the scree plot, two methods exist in literature to choose the number of PC for analysis. The first is eigenvalue one criterion wherein the choice of the number of PC is based on the number of components with eigenvalues higher

than the value of 1 while the second is by the amount of variance explained wherein the chosen numbers of PC should explain 70 to 80% of data variance (325). An example scree plot is shown in Figure 2-20.

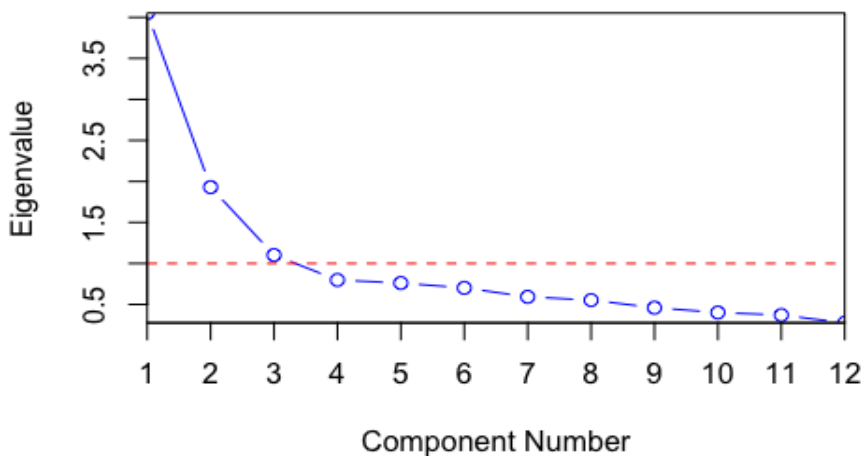


Figure 2-20: Scree plot of 12 components. The red dashed line indicates the threshold for retention. Three of the components have eigenvalues greater than 1 and are therefore retained for analysis. This means the creation of loading plots, in this case, will be with three axes, PC1, PC2, and PC3.

In this study, PCA was used to create loading plots of polymer behaviours (swelling, erosion, and hydration) and drug release profiles in order to observe trends of the behaviour. The number of principal components was chosen based on the number of components that had eigenvalue higher than 1.

2.5.3 Artificial Neural Network (ANN)

The research of neural network ANN has attracted great attention in recent years. ANN is a computational structure modelled loosely on biological processes (326). The concept of ANN originated from the study of mammal's brain wherein researchers noticed that the brain consists of billions of interconnected neurons and can deal with computationally complex demanding tasks such as face recognition, body motion planning, and muscles locomotion control (327). From this concept, ANN aims to be able to emulate the learning ability of biological systems (328, 329). Therefore, it is important to emphasize that ANN relies on learning strategies. Figure 2-21 illustrates the similarities between ANN and the mammalian brain.

The basics of ANN operations consists of three layers which in order of operations are an input layer, hidden layer, and an output layer very similar to the neuron of the mammalian brain (330). The input layer accepts signals from the outside world and redistributes these signals to all neurons in the hidden layer where the weights of the neurons represent the features in the input patterns. As a result, the output pattern of the

entire network is established by the output layer (331). The data flowing from input to the output layer requires transfer function, also known as activity functions, which determine the relationship between inputs and outputs of a node and a network (332). Thereafter, the learning process comes into effect. More than a hundred learning algorithms are available. The greatest advantage of ANN is that it consists of many nodes operating in parallel and can communicate with each other through connecting synapses yielding to the testing of numerous outcomes (333). Meanwhile, the disadvantage is that a large number of sample size is required to learn and validate. Only thereafter can prediction for untested data be considered as a correct and reliable output (334).

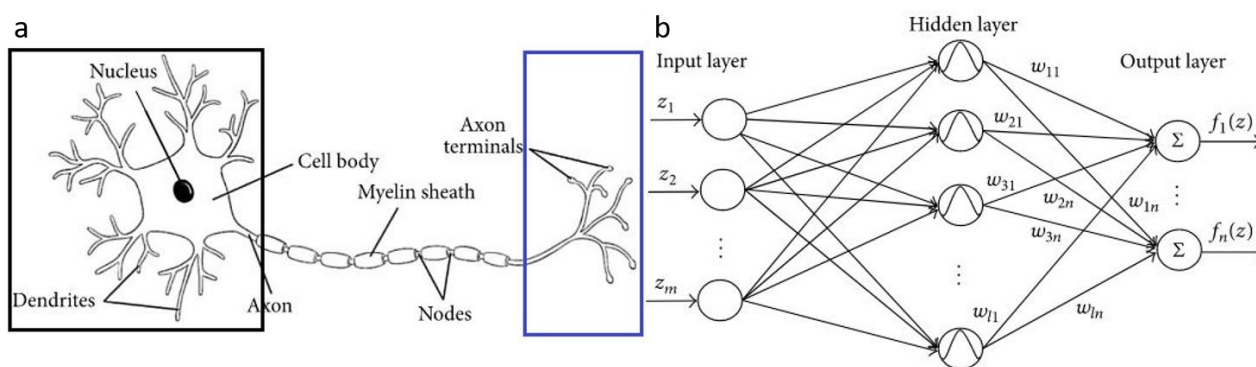


Figure 2-21: a) A mammalian neuron. The black rectangle signifies the input layer while the blue signifies the output. The nodes and sheath are the hidden layer. (b) ANN computational structure Z_m is the input, W_{im} is the weighting of features, and $f_n(z)$ is the output. Adapted from reference (327)

ANN has been used in diverse areas including in pharmaceuticals (335). In pharmaceuticals, ANN has been used to predict the effect of formulation and process variables (336), prediction of in vitro dissolution profiles (337), prediction of drug permeability (338), optimizing emulsion formulation (339), determination of factors controlling the particle size of nanoparticles (340), investigate the effects of process variables on derived properties of spray dried solid dispersions (341), and validation of pharmaceutical processes (342). In this study, ANN has been used to investigate the importance of factors relating to formulation dissolution profile to predict the drug release profile in chapter 6.

Chapter 3: Investigation into the origins of errors in drug release measurements of polymeric solid dispersions prepared by FDM 3D printing

3.1 Introduction

A key focus of this project is to first understand, then attempt to predict the drug release behaviour of polymeric based solid dispersions prepared by extrusion-based methods including hot melt extrusion (HME) and subsequent FDM 3D printing for the potential applications such as personalised medicine. It is important to first establish the reliability and reproducibility of the manufacturing process and the measurements of *in vitro* drug release data. In this chapter, the solid dispersions were prepared using a two-step coupled process of HME and FDM 3D printing. The experimental research was to account for errors that are generated in the due process. All errors from sample preparation to *in vitro* dissolution tests analysis, following the flowchart illustrated in Figure 3-1, were examined to gain insights into the origins of the errors that were observed in the final *in vitro* drug release data. For any scientific experiments, no physical quantity can be measured with perfect certainty thereby making errors unavoidable. This implies repeated measurements of a quantity will certainly yield varying values and a range within which the true value lies with a specified likelihood. The scientific study of measurement is known as metrology (343). Two fundamentals, accuracy and precision are explained in the following section.

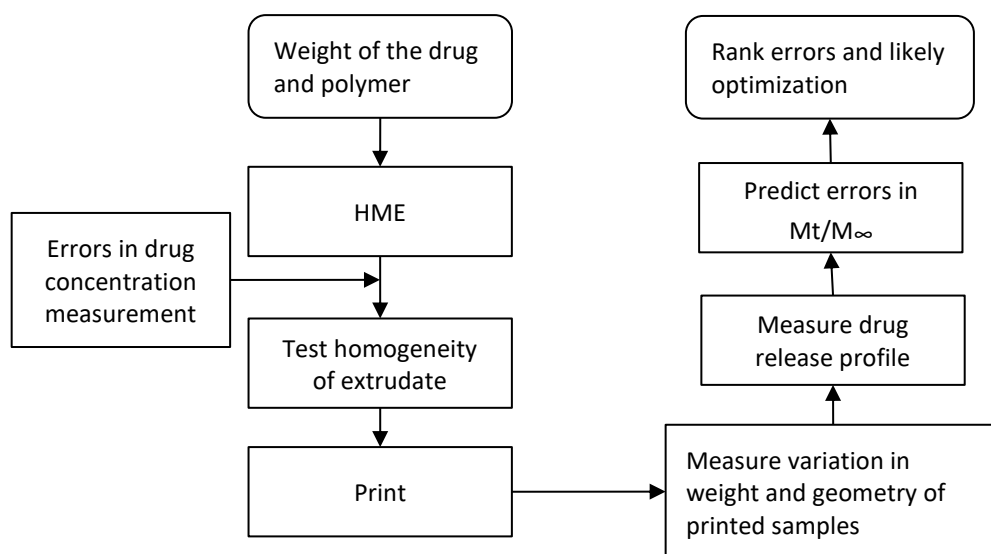


Figure 3-1: Mapping the error process pathway of drug release and optimization

3.1.1 Accuracy vs Precision

Experimental error, itself, is measured by its accuracy and precision. Accuracy measures how close a measured value is to the true value. Since the true value for a physical quantity may be unknown, it is sometimes not possible to determine the accuracy of a measurement. Precision measures how closely two or more measurements agree with others. Precision is referred to as repeatability or reproducibility. A highly reproducible measurement tends to give values which are very close to each other (344). Figure 3-2 illustrates the difference between precision and accuracy.

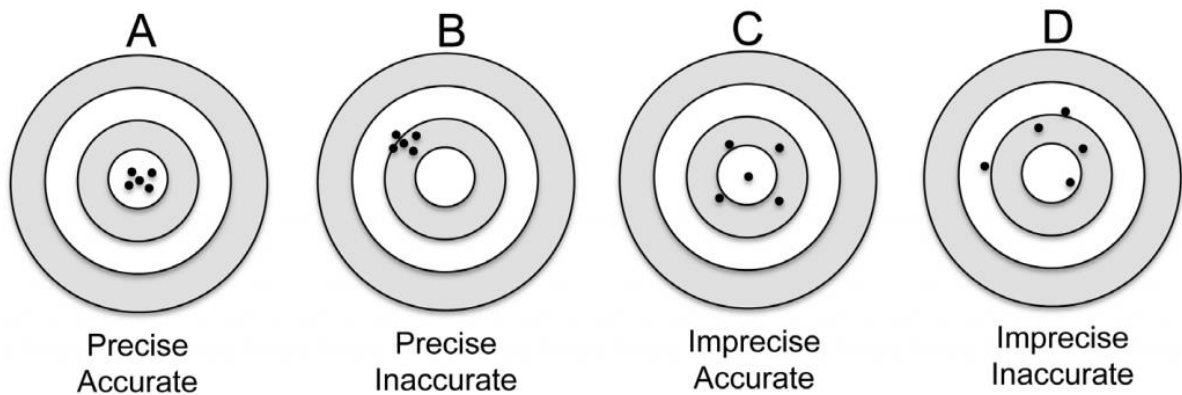


Figure 3-2: The four outcomes of varying accuracy and precision

3.1.2 Types of errors

The true value is the value that is unique and expected from measurements in the absence of any errors (4). Three error types exist in measurement theory. They are systematic, random, and gross errors. Gross errors arise due to humans which can be eliminated by a careful recording of the data (343). Examples of gross errors include instrument reading before a steady state is reached or parallax error (perceived shift in an object's position as it is viewed from different angles) in reading a measurement. Systematic error is hard to detect but once detected, is correctable. Systematic error is either constant or proportional to the measurement. Systematic errors influence the accuracy of measurement (345). Examples of systematic error are imperfect instrument calibration.

Random errors are two-sided errors as the variation in measurement occur unpredictably above or lower than the measured mean value or the true value (3). Random errors can be easily detected and can be reduced by repeating the measurement or by refining the measurement method. Random errors directly

affect the precision of a measurement. The smaller the random error, the more the precision (345, 346). Common sources of random errors are problems estimating a quantity that lies between the graduations on an instrument and the inability to read an instrument because the reading fluctuates while measuring.

Figure 3-3 shows the Gaussian distribution of probability curves. The systematic and random errors are visualizable from this illustration. The systematic error is the difference between the true mean (theoretical value) and the experimental (EXP) measured mean. The systematic error can be either positive or negative relative to the true value but often cited as an absolute value (modulus). The random error can be calculated with many models but most commonly estimated by the standard deviation (347).

In this chapter, the aim is to assess the errors of drug release measurement from the HME-FDM continuous process. The systematic and random errors for HME, 3DP, and UV will be investigated, ranked, and optimized to achieve more accurate and predictable drug release.

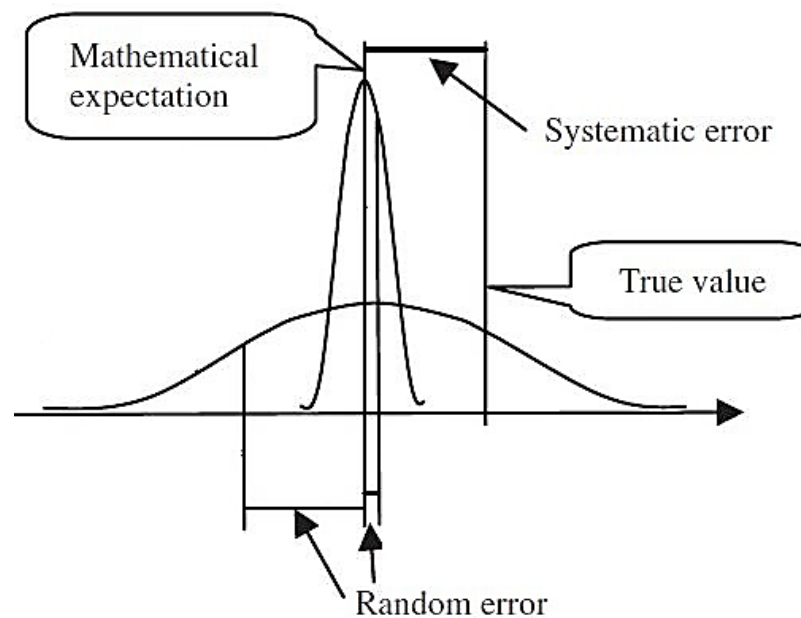


Figure 3-3: Measurement concept of errors from probability curves. Adapted from reference (343).

3.2 Materials

PVA was obtained from Kuraray (Germany) under the trade name Mowiflex C17 as pellets. The melt flow index (MFI) is (190 °C, 21,6kg) [17g/10min], $T_m \approx 180 - 200$ °C, and the T_g is 60 °C (261). The model drug chosen was paracetamol (PCM) bought from Sigma Aldrich (CAS Number: 103-90-2) with a purity of $\geq 99\%$

(204). ABS bought from Makerbot, is an amorphous thermoplastic polymer which is used for manufacturing multiple household products and is a commonly used in 3D printing has been used as a controlled polymer to PVA with (MFI) is (200 °C, 5kg) [5.5g/10min] and T_g of 105 °C (294, 348). Samples were prepared using different combination of polymer and drugs or polymer only placebo for the different stages of error study and is summarized in Table 3-1.

Table 3-1: Materials used as per error study aspects summarized.

Experiment stage	Material
Drug uniformity by HME	PCM loaded PVA extrudates
Printing reproducibility by FDM printing	PVA and ABS torus
Weight uniformity by FDM printing	PVA and ABS torus
In Vitro drug release quantification by UV Spec	PCM loaded PVA extrudates

3.3 Methods

3.3.1 Hot melt extrusion (HME)

A Thermofisher HAAKE Minilab II with twin co-rotating screws was used for the preparation of the filaments for measuring drug content homogeneity. During the preparation of samples, the screw speed was set to a standard 100 rpm. The processing temperature was 10–20 °C higher than the melting temperature (T_m) of the polymers. The samples were prepared in two separate batches: one with a residence time of five minutes and another with ten minutes. Four different extrusion temperatures for preparation of filament were used.

3.3.1.1 Drug content uniformity of the HME extrudates

Mowiflex (PVA) mixed with 10% PCM were fed into the extruder. Four filaments were made by HME at temperatures of 170°C, 180°C, 185°C, 190°C. Six pieces with a length of 1.5 cm were cut at 5 cm interval from each filament to produce six random samples per filament. The cut samples were weighed, and their dimensions measured via a digital caliper. All filaments per temperature were done in triplicates. The sample illustration is shown in Figure 3-4.

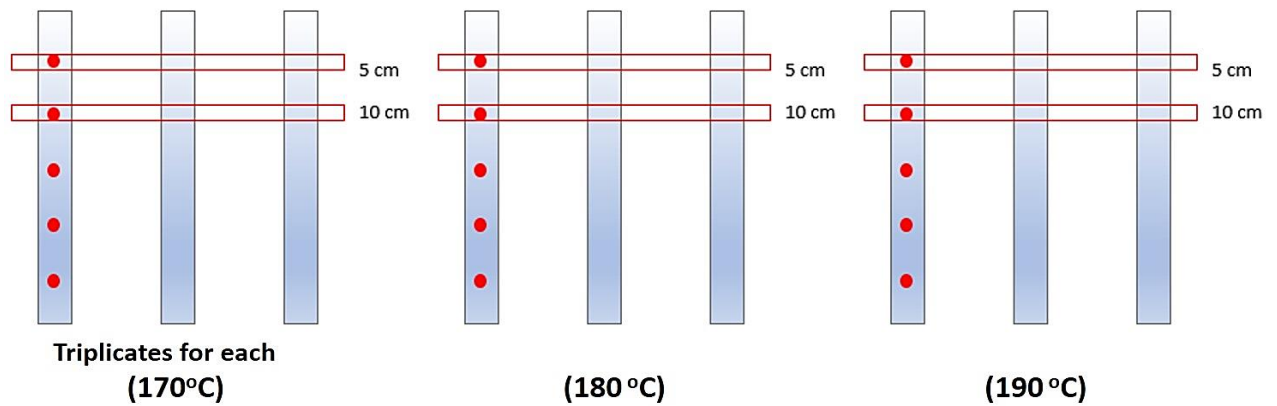


Figure 3-4: Schematic of filament sampling. Red dots indicate 1cm (not shown in triplicates) samples taken at 5cm interval indicated by the red rectangle across the filaments.

The weight uniformity is presented as drug weight per polymer weight. Due to the filament flattening under gravity when exiting the die from HME, the geometry of the solidified filament is an elliptical cylinder shown in Figure 3-5. The volume of an elliptical cylinder is given by $V = \pi \times a \times b \times L$, where a is the major radius, b is the minor radius, and L is the length, all in centimetres.

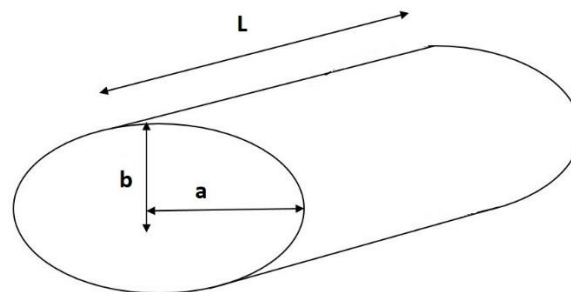


Figure 3-5: Elliptical cylinder where a is the semi-major axis; b is the semi-minor axis, and L is the length

3.3.2 FDM 3D Printing

The FDM 3DP is the subsequent step after filament production through HME and was used to print oral dosage to investigate printing accuracy and precision of the printing process. MakerBot Replicator 2X consisting of dual extrusion print nozzles was used. It has a maximum print volume of 15 X 16 X 24.9 cm³, nozzle diameter of 1.75mm, and an exit tip diameter of 400 microns (349). The printer has three print settings from low to medium to high quality printing whereby the extrusion speed decreases with each higher print quality. The printed oral dosage was in the shape of a torus (plural: tori). A torus geometry has a mathematical advantage over other geometries in drug release studies. Other geometries as pyramid, cube, sphere, and slabs, all of which were considered in the preliminary phase as a validation of the work performed by Goyanes et al (350). First, the surface area (SA) to volume (V) ratio can be increased or

decreased in a manner that allows either surface area or volume to be constant while altering the other parameter. The surface area to volume ratio (calculated: SA/V) is an important indicator of the drug release with the torus exhibiting the faster dissolution rate of all (350, 351). Second, the drug release flux can be assumed in one direction outward (radially) in polar or spherical coordinates (352). Third, the torus is a cylinder wherein the boundaries are adjoined together, effectively postulating it as an infinite cylinder illustrated in Figure 3-6. Thus, the equations of a cylinder can be applied in a simpler form where any API diffusion at the ends can be neglected, in turn making computations less intensive and less time consuming.

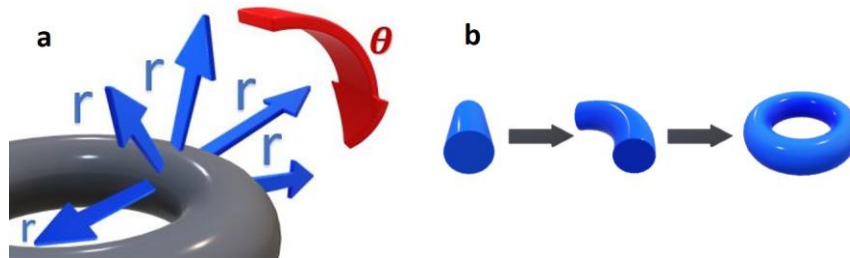


Figure 3-6: **a)** In polar coordinates, the diffusion occurs in one dimension in the radial direction (r) indicated by the blue arrows while θ is the angle at which the radial diffusion takes place. **b)** The starting cylinder if curved and joined end to end forms a torus which is effectively an infinite cylinder.

3.3.2.1 Reproducibility of 3DP torus

The reproducibility of the FDM 3DP was investigated by observing any difference in physical dimensions between the designed and printed specifications of the torus. The dimensions refer to the diameter and the annulus, which were measured using a digital caliper. Figure 3-7 shows these two parameters of the torus that was measured. The radius was obtained by halving the diameter values. Twenty tori were printed from two filaments of two polymers. Ten tori were prepared in each batch. One batch was using the commercial filament ABS while the other was using PVA via HME process. The PVA with PCM filament was prepared at HME processing temperature of 190 °C and residence time of five minutes. The printing temperatures for PVA formulation were 200 °C and 230 °C for ABS. The selected design specification was a torus diameter of 14mm and an annulus of 2mm. For a torus, the annulus is equal to the width which is also equal to the height. For calculations of the volume of the torus and surface area, equations 3-1 and 3-2 can be used, respectively. The null hypothesis (H_0) is that no volume difference will be observed.

$$V(r,R) = \frac{1}{4}\pi^2(r+R)(R-r)^2 \quad \text{Equation 3-1}$$

$$SA = \pi^2(R^2 - r^2)$$

Equation 3-2

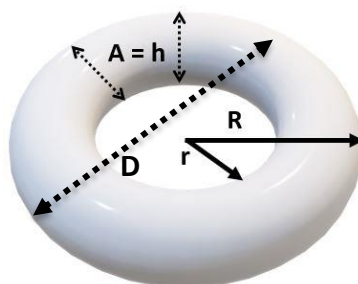


Figure 3-7: Inner radius (r) and outer radius (R) for torus V and SA calculation. A is the annulus (the diameter of the ring) and is equal to the height (h). D is the diameter of the torus.

3.3.2.2 Weight uniformity

The FDM 3DP tori were weighed using analytical mass balance. It is expected samples of each batch are identical and as such, should, therefore, exhibit no weight difference, which is the H_0 .

3.3.2.3 In vitro drug release studies

In vitro drug release studies were carried out in dissolution testing apparatus (Caleva, Germany) using British Pharmacopeia (BP) apparatus 2 paddle method. A paddle rotation speed of 100 rpm and 900 ml of Milli-Q deionized water were used with a temperature of $37^\circ\text{C} \pm 0.5^\circ\text{C}$. During dissolution, at predetermined time intervals, 5 mL samples were taken and replaced by 5 ml fresh water. The samples were collected through filtration membrane of $0.45\mu\text{m}$ pore size (minisart NML disposable syringes, UK) before UV measurements. The sampling times were every three minutes up till fifteen minutes, every thirty minutes thereafter, and every hour beyond three hours (3min, 6, 9, 12, 15, 30, 60, ..., 180, 240, ..., End). All samples were tested using the above *in vitro* method three times.

3.3.2.4 Calculation of cumulative error in drug release data

For the cumulative error in drug release, three tori were prepared using PCM and PVA by using HME-FDM. The mean weights and volume of these tori were 0.130 ± 0.041 g and a volume of 117.1 ± 3.4 mm³. The aim for investigating cumulative errors in drug release is to be able to predict the variations that will result from using drug release models. The drug release model used is the Korsmeyer-Peppas equation which is used to analyze both Fickian and non-Fickian drug release from swelling and non-swelling polymeric delivery systems of cylindrical geometries, shown in equation 3-3. The aspect ratio (n) indicates the mechanism of release.

$$\frac{M_t}{M_0} = kt^n \quad \text{Equation 3-3}$$

$0.45 < n = \text{Fickian}$, $0.45 < n < 0.89 = \text{Anomalous}$, $n > 0.89 = \text{Case II transport}$

where $\frac{M_t}{M_0}$ is the drug fraction, K is the release rate constant, and n is the aspect ratio. The term anomalous refers to non Fickian diffusion which is driven by micro-instabilities obstructing a laminar flow or laminar diffusion. The above equation has only one variable: time (t). The other two are constants that can be found from curve fitting. Since this equation parametrises the drug release profile, using partial differentials, the absolute error for the drug release profile can be estimated. The generic error of a function of n variables $f(x,y,\dots, i)$ using partial differentials is given by equation 3-4 (353).

$$\Delta f = \frac{\partial f}{\partial x} \delta x + \frac{\partial f}{\partial y} \delta y + \dots + \frac{\partial f}{\partial i} \delta i \quad \text{Equation 3-4}$$

Where δf is absolute error in f , $\frac{\partial f}{\partial i}$ = partial derivative of f with respect to i , and δi is error in i . This drug release absolute error is given by equation 3-5. The error in sampled drug mass (δM_t) value is obtained experimentally from UV, thus UV errors (E_{UV}) can substitute the right side expression of equation 3-5. This is discussed on the next page where the Beer-Lambert law is introduced.

$$\delta M_t = (M_0 k n t^{n-1}) \delta t = E_{UV} \quad \text{Equation 3-5}$$

In the above equation, δt (the time in error sampling) is negligible, especially for automatic dissolution machine. In equation 3-5, M_0 is taken as a constant and thus error-free but in reality, is an averaged value. There are two approaches to obtaining the error in M_0 . The first approach is to measure it directly using a UV-Vis spec. The second approach is to estimate it from the process steps involved. An error in initial drug mass (δM_0) exists which arise from the processing steps involved (from HME to 3DP, then to UV). Therefore, predicting δM_0 requires an estimation of the error in each step. In section 3.3.1.1, the drug content uniformity is investigated. From this, the initial drug mass error in HME (δM_{HME}) arises. For 3DP, there are two approaches to deducing δM_0 . Both of these approaches are investigated. The errors in 3DP arise in volume and weights. The error in volume (δV_{3DP}) is estimated by equation 3-6 and drug mass error in 3DP (δM_{3DP}) is directly from weighing after printing. This δM_{3DP} is a direct approach to get δM_0 . In the case the

oral dosage is not weighed, the other approach involves δV_{3DP} . Knowing the δV_{3DP} and the density of the drug, δM_{3DP} can be found using $m = DV$. For example, -20% δV_{3DP} indicates δM_{3DP} is also less by 20% since density is constant.

The UV spectrometer relies on the Beer-Lambert law (equation 3-7) containing one variable concentration (c). The UV spectrometer error can be subdivided into three types: calibration curve errors, instrumental errors, and sampling errors. To deduce calibration curve errors, three calibration curves were prepared for PCM in deionized water. The resulting variation will quantify the errors due to calibration curves. To deduce instrumental error, the absorbance of one diluted sample was repeatedly obtained. Ten repeat readings were done. The sample concentration was 15 μ g/ml. To deduce sampling error, the absorbance of PCM released from ten tori samples were measured at using the mean calibration curve found in the investigation of calibration errors. Since the cumulative averaged concentration of the tori can fluctuate based on the number of samples, any variations in absorbance is due to sampling error. The cumulative averaged concentration converges to a number as the sample size grows larger. This convergence occurs because of the sensitivity of random difference in the concentration among each sample diminishes with a larger size. The time point chosen for sampling was 3 mins. The three errors combined will give the total error in absorbance (δA). The δA is given by equation 3-8. Rearranging equation 3-8, δc can be gathered. The error in drug mass from UV (δM_{UV}) is deduced from the c using $\delta m = \delta CV$, with a volume of 900mL. As the experiment is under sink conditions, the volume of the solution can be taken as a constant without any errors.

$$\partial V = \frac{\partial V}{\partial r} \delta r + \frac{\partial V}{\partial R} \delta R = \frac{\pi^2(3r^2 - 2rR - R^2)}{4} \delta r + \frac{\pi^2(3R^2 - 2rR - r^2)}{4} \delta R \quad \text{Equation 3-6}$$

$$A = \epsilon \ell c \quad \text{Equation 3-7}$$

$$\delta A = \epsilon \ell \delta c \quad \text{Equation 3-8}$$

Where δr is the error in inner radius, δR is the error in outer radius measurements, ϵ is the molar absorption coefficient, ℓ is the path length, c is the concentration of the solution, δA is the absorbance absolute error and δc is the concentration error. Expressions of cumulative error can be formulated for drug

release which includes both M_t (error in sampled mass) as well as M_0 (error in initial mass). M_t is indicative of UV error while M_0 is indicative of HME-FDM production steps. The δM_t , in terms of UV, is by combining equation 3-5 and equation 3-8 with $\delta m = \delta CV$, is given by equation 3-9. δM_0 from 3DP is given by equation 3-10. In case the oral dosage is not weighed after 3DP, δM_0 is given by equation 3-11, where δM_{3DP} is in terms of density and volume ($D\delta V_{3DP}$). Lastly, combining equations 3-9 and 3-11, with non-constant M_0 , gives the drug release error in terms of the manufacturing processes, which given by equation 3-12, where the left side is δM_t (left side of equation 3-9) and δM_0 (right side of equation 3-12) is the right side of equation 3-11.

$$\delta M_t \equiv \frac{V\delta A_1}{\varepsilon\ell} \quad \text{Equation 3-9}$$

$$\delta M_0 = \delta M_{3DP} \quad \text{Equation 3-10}$$

$$\delta M_0 \equiv \frac{V\delta A_2}{\varepsilon\ell} = \left(\frac{\pi^2(3r^2 - 2rR - R^2)}{4} \delta r + \frac{\pi^2(3R^2 - 2rR - r^2)}{4} \delta R \right) D \quad \text{Equation 3-11}$$

$$\frac{V\delta A_1}{\varepsilon\ell} = \left[\frac{\pi^2(3r^2 - 2rR - R^2)}{4} \delta r + \frac{\pi^2(3R^2 - 2rR - r^2)}{4} \delta R \right] D \quad \text{Equation 3-12}$$

where V is the volume which in this case is 900mL, A_1 is the dissolution sampled absorbance, A_2 is the initial sample absorbance, and D is the density.

3.4 Results and discussion

3.4.1 Characterization of samples

The characterization of the formulations has been presented in the appendix. The DSC thermograms shown in Appendix Figure 1. The 10% drug loading showed a plasticizing effect of the PVA and in amorphous form.

3.4.2 In vitro drug release studies

In this section, the error in UV measurement was deduced. Three sources of error arise in measurement by using the UV spectrometer (δA_{UV}) which consist of calibration error (δA_c), equipment error (δA_e), and sampling error (δA_s). the first of these presented is the δA_c . The average of three calibration curves for PCM are shown in Table 3-2. The total error was calculated using the following equation: $E_T = (E_s^2 + E_r^2)^{1/2}$ where E_T , E_s , and E_r are total error, systematic error, and random error respectively (354, 355). The standard deviation was used to represent the random error. The E_s depends on comparing the

difference in measurement between the averaged experimental value and the true expected value. The true value cannot be determined as the ϵ (the molar absorption coefficient) in equation 3-7 is a value that is derived from the absorbance, concentration, and length ($\epsilon=A/\ell c$) of which, concentration and absorbance, vary simultaneously. However, since the E_s is constant and present in every process step, the source of error that affects in practice is the E_r . Therefore, for δA_c , the E_r is 1.1×10^{-3} , and thus the E_T is 1.1×10^{-3} .

Table 3-2: The variations of calibration and the goodness of fit (R^2) measuring the three curves in deionized water. y is the absorbance and x is the corresponding concentration obtained from best fits.

Trials	Equation	R^2
Calibration Curve 1	$y = 0.0617x$	0.999
Calibration Curve 2	$y = 0.0596x$	0.992
Calibration Curve 3	$y = 0.0604x$	0.997
Average	$y = 0.0606x$	0.996
Standard Deviation	± 0.0011	-

The equipment error (δA_e) was quantified by repeated measurement of absorbance of one of the diluted samples. The sample concentration was $15 \mu\text{g/ml}$ and the mean measured absorbance was 0.95520 AU. Based on the ten repeated absorbance measurements, the E_r of δA_e was 1.37×10^{-4} absorbance units (AU), and E_T of 1.37×10^{-4} AU. Figure 3-8 shows the absorbance frequency distribution for repeated measurement.

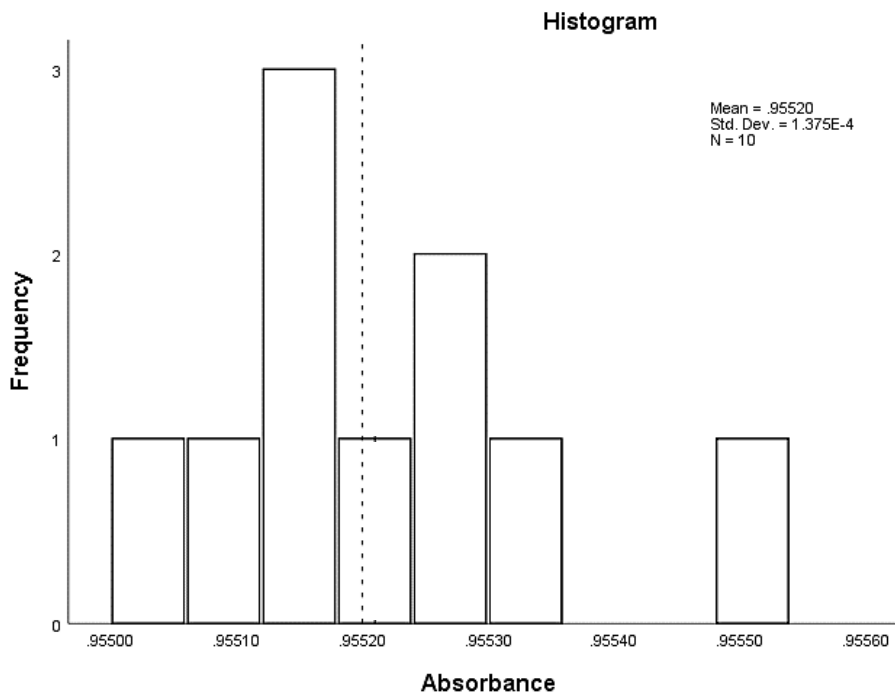


Figure 3-8: UV absorbance distribution for $15 \mu\text{g/ml}$ sample over ten repeated measurements. The dotted line is the measured mean.

The δA_s (from sampling) was deduced from the UV absorbance of ten 3DP tori, which is shown in Figure 3-9.

The δA_s exhibited an E_r was 0.12 AU equating to an E_T of 0.12 AU.

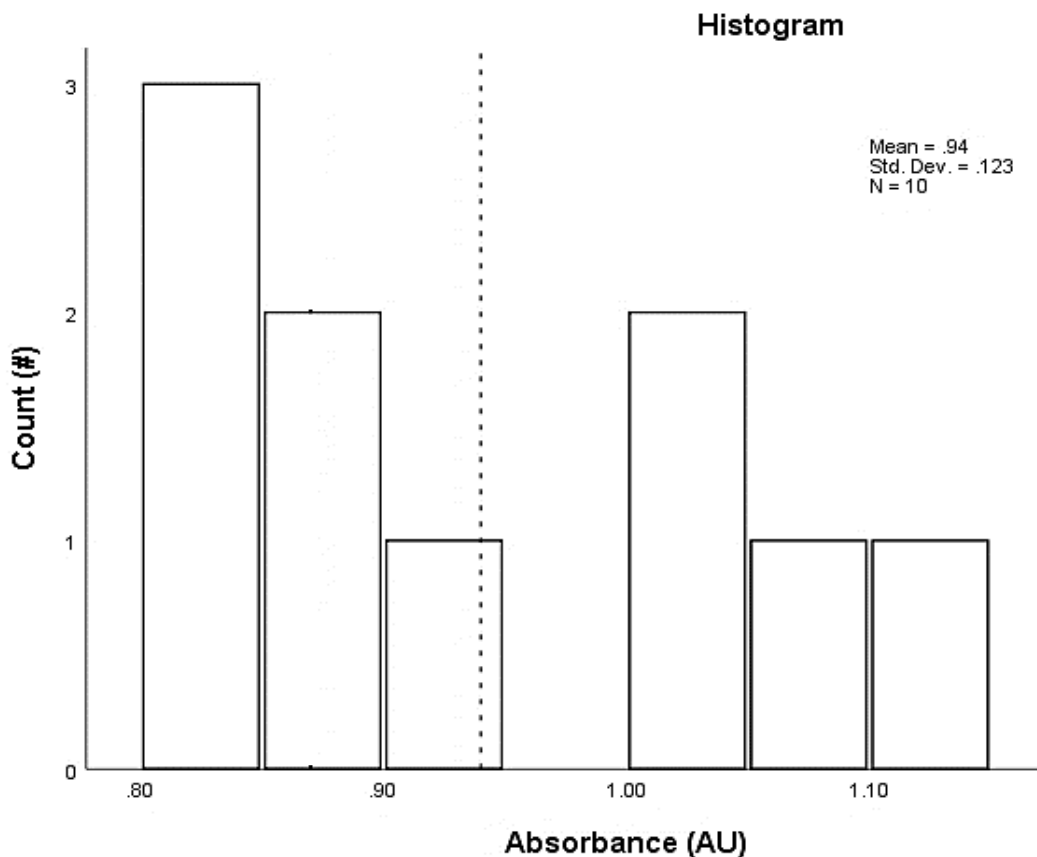


Figure 3-9: UV absorbance distribution of ten samples. The dotted line is the measured mean.

The δA_{UV} is a linear combination of calibration error (δA_c), equipment error (δA_e), and sampling error (δA_s) ($\delta A_{UV} = \delta A_c + \delta A_e + \delta A_s$). Figure 3-10 illustrates the contribution, percentwise. The total δA_{UV} is 0.121 AU. Percentwise ranking shows $\delta A_s > \delta A_c > \delta A_e$. Lowest contribution from δA_e is as expected due to instruments undergoing quality control testing for many aspects including accuracy and precision before being commercialized (356). The highest δA_{UV} error from sampling was also expected. Two explanations can be proposed. First, sampling in UV is the last step in the pipeline of HME-FDM continuous process of oral dosage manufacture. This implies, that each of the ten samples has varying errors present; that have propagated from earlier manufacture steps. Second, the average sampling error of all the samples and sample size have an inversely correlated relationship (357). As the sample size increases, the sampling error is lower. A sample size of ten is still low with a high margin of error. Statistical approaches such as Monte Carlo simulations have been applied to reduce the sampling error (358, 359). Anderson demonstrated the

importance of small sample size affecting sampling error in MC simulations. Due to the small sample size, the goodness of fit (R^2) was highly sensitive of any outliers compared to larger sample sizes with outliers. Smaller sample sizes led to sampling distributions of the likelihood ratio test statistic that were different from the corresponding theoretical chi-square distribution (360).

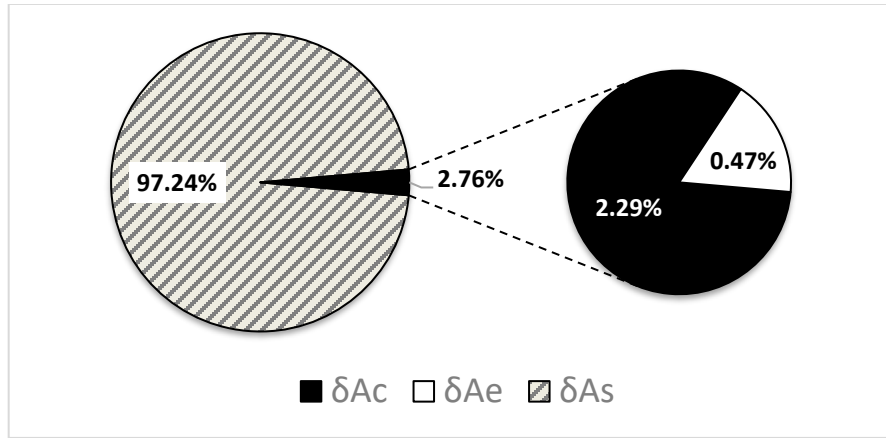


Figure 3-10: A percentwise in terms of the that affects the UV spectrometer. Ae is equipment error replaced

Furthermore, the convergence of random error with increasing sample size can be deduced from the central limit theorem (CLT) (358, 361). Figure 3-11 shows the convergence of δA_s for the ten replicates. The variance in δA_s , found from standard deviation (random error in δA_s), for ten samples was scaled to 100,000 samples. Beyond 100,000, the effect of sample size diminishes. According to CLT, the central value (mean) that will be attained when the sample size is large enough is 0.94 AU. The sample size at which this occurs was found out to be 99,995th sample, the random error in δA_s is zero.

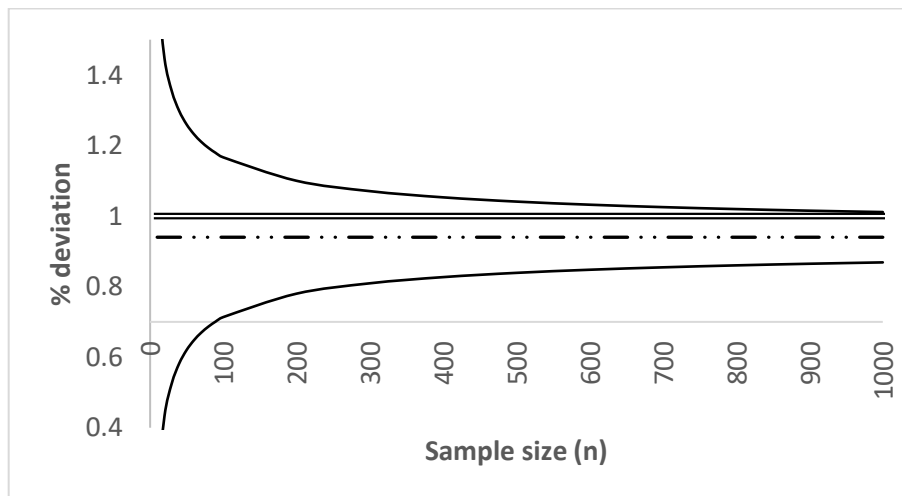


Figure 3-11: Convergence of δA_s . The solid curve represents the maximum and minimum absorbance ($A \pm \delta A$) at various sample sizes. The dotted-dashed line represents the mean absorbance that is reached at large sample sizes. The double line is the UV absorbance limit at 1AU. The scope of the graph has been cut to 1000 samples. Beyond this, the graph is asymptotic and the change is gradual.

3.4.3 HME Studies

3.4.3.1 Measuring drug content uniformity of HME

With a drug loading of 10%, the weight of the drug per weight of the polymer (mg/g) of the six filament samples for the four temperatures is shown in Table 3-3. At residence time of five minutes, the average drug homogeneity (column) does show a difference for inter-filament at different processing temperature but not significantly different in the case between 170°C and 180°C. The processing temperature of 190°C is significantly more homogenous than 170°C or 180°C. It was expected that the standard deviation of weight homogeneity for intra-filament would decrease with increasing processing temperature as the melt viscosity decreases above the melting of the drug. The T_m of PCM form I is 169°C (203). A decrease in melt viscosity allows a smoother flow of the material in the HME barrel. The variance decreased for identical processing temperatures of ten minutes of residence. The residence time characterizes the heat energy produced over a specific period during the material shear (362). Due to the increased holdup time in time in the HME barrel, more homogenous mixing of the API can occur. Li et al reported that the short residence time of materials in the extruder is not sufficient to achieve complete API dissolution in the matrix (363). However, numerous literature cites prolonged residence times as the cause of drug degradation, which suggests the effect of residence time may be parabolic on drug content (362-364).

Table 3-3: Drug w/w of filament cut samples at the two residence times and various temperatures.

Intervals (cm)	5 minutes of residence				10 minutes of residence			
	Temperature (°C)							
	170	180	185	190	170	180	185	190
	Drug weight per polymer weight (mg/g)							
5	90.88	59.90	73.44	92.12	73.81	96.14	105.64	96.90
10	90.13	82.76	78.67	98.65	77.99	93.51	94.43	104.36
15	116.29	117.20	106.55	103.07	77.46	105.19	85.65	92.24
20	91.91	141.98	74.48	99.56	74.20	119.98	87.54	98.65
25	86.18	118.26	53.75	104.86	96.19	122.92	117.49	77.65
30	161.77	120.31	97.88	100.68	96.16	127.82	119.32	104.34
Average ± SD:	<u>106.19</u> ±29.28	<u>106.74</u> ±29.79	<u>80.80</u> ±18.89	<u>99.82</u> ±4.41	<u>82.64</u> ±14.51	<u>110.93</u> ±10.30	<u>101.68</u> ±14.74	<u>95.69</u> ±9.98

Censi et al have reviewed the factors that can be optimized for HME process (365). The focus here is to assess the errors in weight uniformity of the HME process. Therefore, it is important to discern the two

types of errors quantitatively in the HME. Since each processing temperature is a different population, the errors will also be different for each temperature. As an example, the measurement concept of weight uniformity for HME processing temperature at 170°C is shown in Figure 3-12.

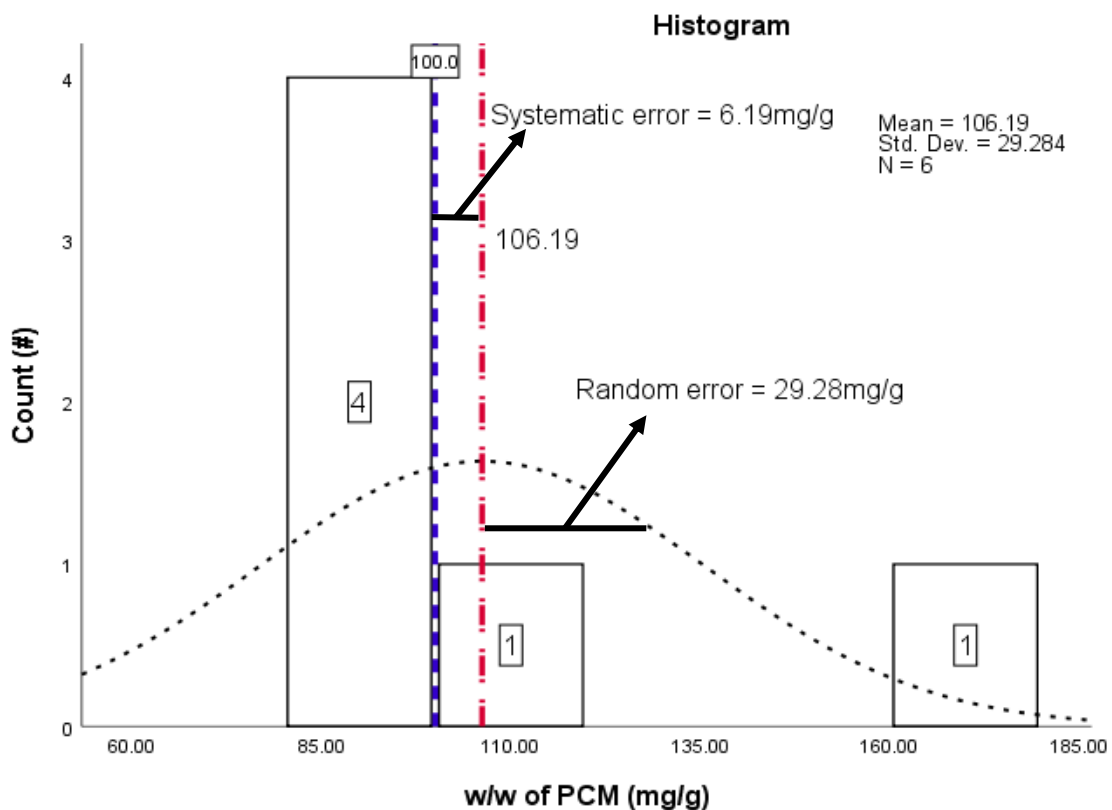


Figure 3-12: Measurement concept for HME weight uniformity at 170°C. Blue dashed line marks the true (target) value that is theoretically expected. The red dashed line is the EXP mean. The black dashed curve is the probability distribution curve.

The two errors types for each temperature are presented in Figure 3-13. A trend in E_T exists of improved drug concentration uniformity with increasing HME processing temperature and residence times. Extrapolating to where the $E_T = 0$ by fitted to a quadratic equation, yields HME processing temperatures of 161 °C or 191 °C for 5min residence time and no solution for 10 min residence time. The former temperature 161°C is below the T_m of PCM and therefore excluded. The latter temperature is suitable for HME. This processing temperature was performed but the error was not eliminated. Additionally, the onset of PCM degradation is 240 °C from TGA (366). The FDM printing temperature ranges about 20 to 50°C above the HME processing temperature (25). Mackay et al reported the minimum printing temperature required for amorphous polymers is $T_g+78^\circ\text{C}$ (367, 368). Therefore, an HME processing temperature of 191°C implies a print temperature range of 211°C or 241 °C, the higher range of which is sufficient to degrade PCM.

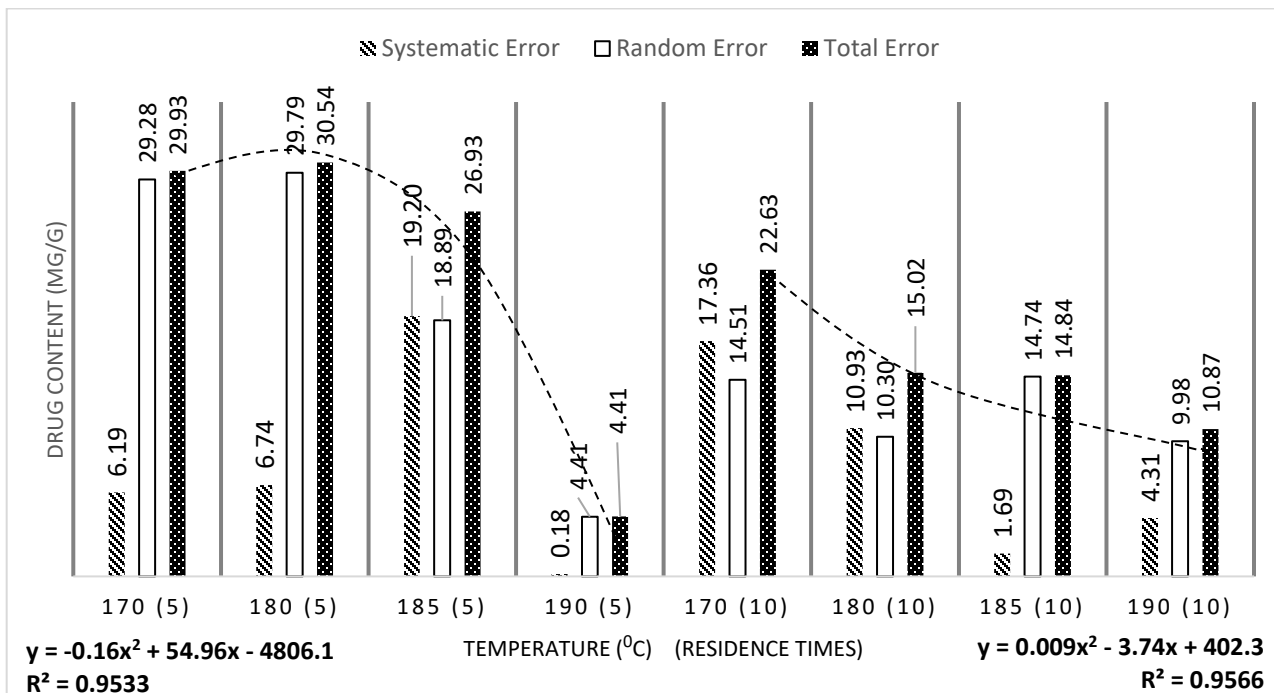


Figure 3-13: Error subtypes for HME processing temperature. The 5 or 10 in brackets beside temperature indicate the residence time. The trendline fitted to 5 minutes is shown on the bottom left while the trendline for 10 minutes is on the bottom right.

3.4.4 FDM 3DP studies

3.4.4.1 Reproducibility of FDM 3DP object dimension

The comparison of twenty tori dimension is shown in Table 3-4. It was observed that a significant deviation for diameter exists from the theoretical (THRY) specification. The expected lower bound for diameter from THRY due to printer reproducibility error is 13.89mm (14.00-0.11 from column 1 and row 1 or table 3-3) but instead was lower for both polymers. Upper bound diameter from experimental (EXP) measurements also fails to attain the lower bound diameter of the THRY specification. This can signify issues for the printer in controlling the nozzle over the x-y plane. However, the annulus measurement (also x-y plane) was within the THRY specification.

Table 3-4: Tori dimension comparison. THRY denotes design specification while EXP denotes experimental measurement.

	PVA			ABS		
	Diameter	Annulus	Height	Diameter	Annulus	Height
THRY (mm)	14.00 ± 0.11	2.00 ± 0.11	2.000 ± 0.003	14.00 ± 0.11	2.00 ± 0.11	2.000 ± 0.003
EXP (mm)	13.65 ± 0.07	2.02 ± 0.04	1.99 ± 0.09	13.78 ± 0.09	2.02 ± 0.03	1.98 ± 0.04

One possible explanation for this is shrinking of the sides of the printed layers. During solidification, cooling takes place due to the temperature gradient between the oral dosage and the surrounding. As stated in chapter 1, cooling occurs by conduction within the layers and by convection at the interfaces between air

and object. Ceteris paribus, convection of heat is faster than conduction (369). Due to the position of 3DP design, the air at the bottom near the platform and air at the top near the nozzle tip is hotter than the region between the two parts. Therefore, the lateral sides of the oral dosage are in contact with cooler air. The fastest rate of cooling happens in this direction and hence the fastest rate of solidification and accounting for fastest shrinkage. The bottom plate would be the subsequent slower rate of cooling due to the slightly lower temperature gradient. The surface layer is in closest proximity to the heated nozzle and is always subjected to the most recent deposited layer which is always hotter the layers beneath. Therefore, the solidification rate is the slowest in this direction. This phenomenon is shown in Figure 3-14. A temperature reading at any point in time during 3DP would show a ranking of $T_a < T_b < T_n$.

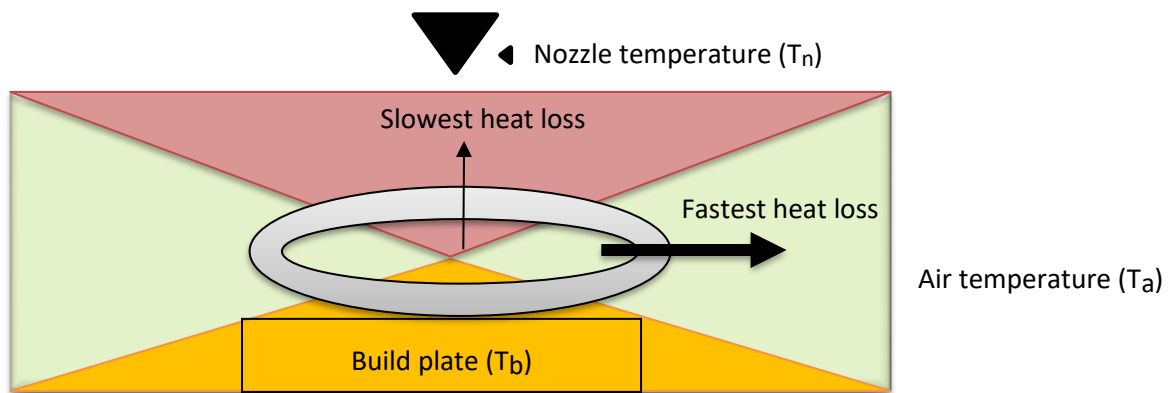


Figure 3-14: Cooling gradient from the object (black torus shape) while successive layers are being deposited. The arrows represent outgoing convection. A greater thickness of the arrow represents higher heat flux. The lateral side will always shrink the fastest and prone to have the highest deviation. Red region shows the most heated area while the yellow region shows the cooler moderate region and the green region shows the lowest heated area.

In the case of height, which operates in the z plane, the EXP error range ($\pm 0.09\text{mm}$ for PVA and $\pm 0.04\text{mm}$ for ABS) was greater than the theoretical error range of $\pm 0.01\text{mm}$. This is most likely due to a 'double printing effect' that is observed on all the tori. This seems an unavoidable issue for the printing of torus geometry. For such geometries where the initial deposition conjoins with final deposition, the strands (printed filament) overlap after deposition on the same point of the platform causing an abrupt increase in height, which is usually reflected as a variance/error in the z plane. Figure 3-15 illustrates this issue for one of the ABS torus printed of the ten tori samples.

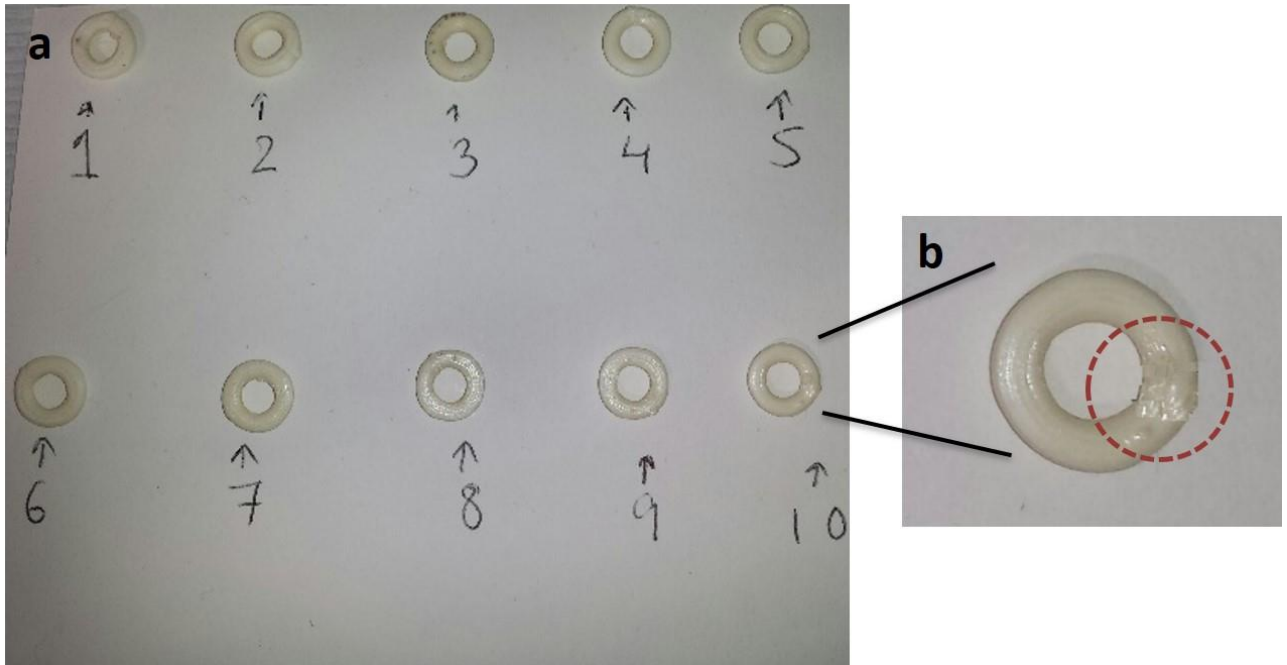


Figure 3-15: a) Ten ABS tori. b) A closeup of torus # 10 showing the double printing effect upon solidification.

Overall, experimental results showed that the range of error was lower for the commercial filament ABS than PVA (except for diameter). In chapter 1, the phases of FDM 3DP was divided into three aspects: feeding, deposition, and solidification. Any error due to the feeding phase can be eliminated as the oral dosage has successfully printed. Solidification accounted for the shrinkage. Therefore, since both polymer oral dosage exhibits constantly lower error ranges (indicating a systematic error), a contributing factor can be rheological properties during deposition. Wang et al states Melt Flow Index (MFI), crystallinity, and plasticization are important for successful 3DP (370). The MFI of PVA is 17g/10min at 190 °C and the MFI of ABS is 5.5 g/10min at 200 °C (261, 348). The PVA flows better at lower temperatures. Accounting for the external printer factor, Alhijaj et al concluded the printing speed will have a greater contribution than printing temperature (48). However, the printing speed was identical for both polymers. Therefore, the printing temperature may be an issue. The printing temperatures of 200 °C for PVA and 230 °C for ABS indicate that PVA will flow better due to the MFI difference. This may be the cause of higher error range for PVA as the better flow can lead to uncontrolled smearing on the platform before the solidification occurs. However, this does not explain the higher error range for ABS (± 0.09) than PVA (± 0.07). This most likely is a random error as this is not constantly reproducible in other dimensions and relative minuscule compared to each other (± 0.02).

The systematic and random error in terms of resolution (in x, y, and z plane) for ABS and PVA geometries by FDM 3DP are presented in Figure 3-17. As an example, the distribution curve for PVA torus diameter is shown in Figure 3-16. The diameter indicates the error in the x-y direction resolution of the 3DP. The systemic error for the diameter is 0.35mm (14.00mm –13.65mm). The random error is estimated by using the standard deviation found to be 0.072mm.

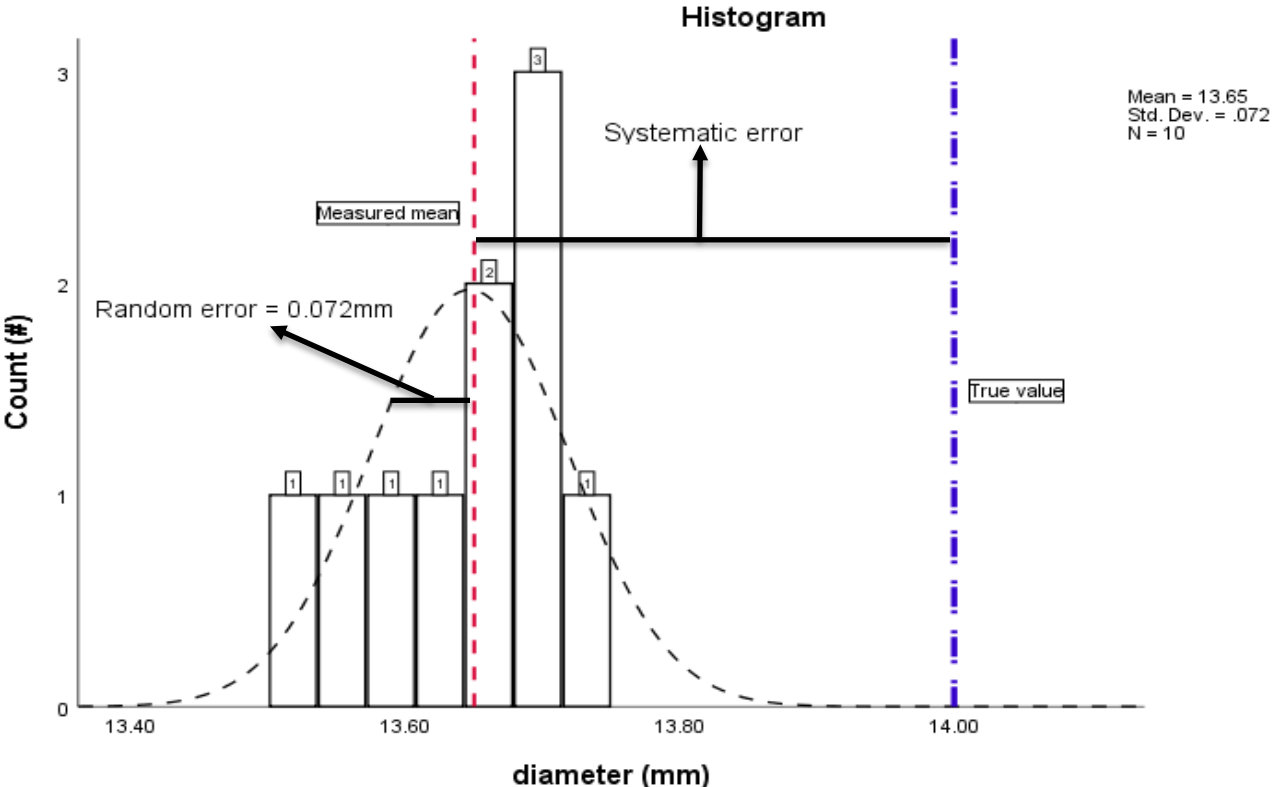


Figure 3-16: Measurement concept for the diameter of PVA. The blue dashed line marks the true value expected from THRY specification. The red dashed line is the EXP mean. The black dashed curve is the probability distribution curve.

It was observed in both cases, the ABS showed higher errors, which was unexpected. ABS is a commercial filament with uniform filament thickness and hence consistent feeding into the 3DP. Additionally, the rheological and thermal properties required for smoother deposition and solidification respectively for ABS is likely optimized. Moreover, it was surprising to observe that the random error in the height of printed ABS torus was reasonably similar to the systematic error of ABS height. Although this can make the reproducibility of the height a serious technical problem, it should be noted that this random error (0.09mm) is identical to the random error in printed PVA torus (0.09mm) and therefore consistent. Yet, the systematic error varied by six times (0.12mm/0.02mm) for the height of the two polymers. This is most likely due to the double printing effect prominently observed with ABS height but not in PVA height.

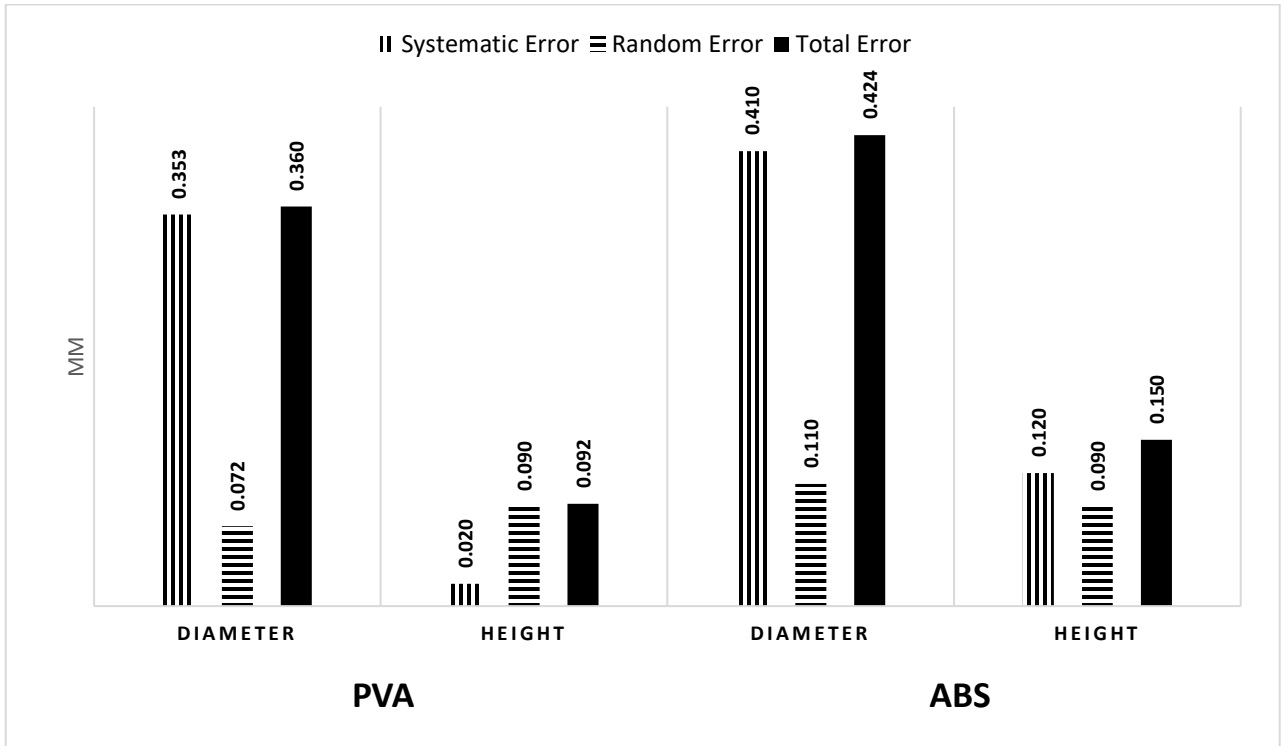


Figure 3-17: Error types categorized for 3DP resolution in x, y, and z directions.

Using equation 3-1, the volume of tori can be calculated. The error in the radius for volume is given by equation 3-6. The total error found for the diameter of PVA and ABS, after dividing by 2 ($R = D/2$), is taken to be the error in major radius (δR). The minor radius (δr) is found by subtracting the annulus from the diameter and halving the value. The errors in the volume are discussed in section 3.4.5.1 Case I: δM_0 from 3DP tori volume measurements).

3.4.4.2 Weight uniformity

Figure 3-18 depicts the weight per volume distribution. The theoretical weight for the formulation was deduced by accounting 90% polymer weight and 10% PCM. The ABS theoretical weight was deduced by using theoretical volume with density. The density of ABS is 1.07g/cm^3 (371), PVA is 1.25g/cm^3 (261), and PCM is 1.31g/cm^3 (203). It can be observed that weight uniformity is more precise and accurate for ABS. In contrast, PVA weight uniformity was relatively less accurate and highly imprecise, as expected. ABS being a commercial filament should have more homogenous distribution in the filament. Knowing the systematic error of printing resolution to be less than the true value, a lower volume than true volume was expected for both ABS and PVA, which was observed. As mentioned earlier, if the weight of the object is measured post-printing, the total error in weight for drug is directly from this measurement, which is the δM_{3DP} . The

true M_{3DP} of the torus is 0.015g (0.15g/10). The total experimental δM_{3DP} of the ten tori is 0.0081g with a random error of 0.0078mg and a systematic error of 0.0025g.

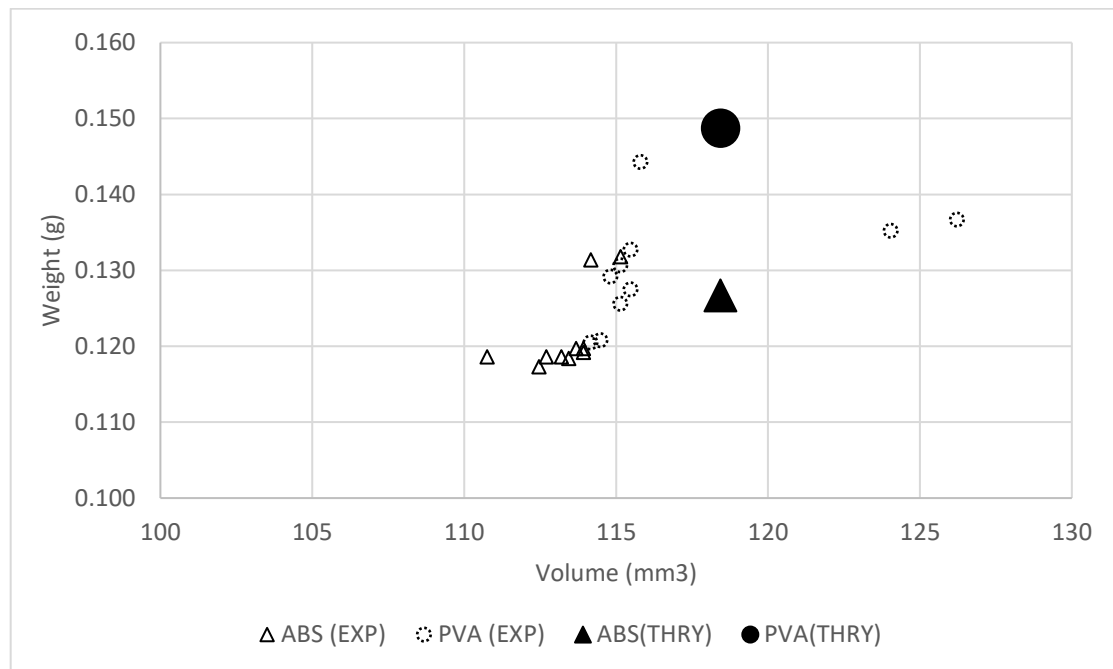


Figure 3-18: Weight vs volume distribution of the printed tori from the two polymers.

Skewness is a measure of how much the data is nonsymmetric. For the application of any parametric tests to the data group, the skewness has to be within ± 3 ; else the results are invalid (372). The PVA with PCM loaded filament was prepared at 190 °C via HME. The skewness for the drug weight uniformity ($\mu\text{g}/\text{mm}^3$) at 190 °C is 0.715 (from analyzing Table 3-3 190 °C in SPSS). The printing temperature was 200°C and the skewness of the PCM concentration at 200 °C for 3DP is 1.531. As the skewness for both was within ± 3 , any parametric test is valid. For successful printing, the weight of PCM should not significantly differ between HME and FDM. Statistically significant lower drug weight indicates drug degradation. Paired sample T-test (a parametric test) was used to compare the means of two dependent groups before and after an event was employed for the PCM weights (373). The event, in this case, is the printing. The PCM mean drug weight from HME process is $131.36 \mu\text{g}/\text{mm}^3$ and the PCM mean drug weight from 3DP process is $123.58 \mu\text{g}/\text{mm}^3$. The significance level of the paired T-test was 0.105 for the 95% confidence interval. This is greater than the significance level of 0.050 and hence H_0 of no difference between the sample is statistically significant. In other words, the PCM concentration in the two samples was not altered before and after printing.

3.4.5 Cumulative error in drug release

The left side of equation 3-11 is a measure of the drug mass release during dissolution obtained from the UV spectrometer. The δA_{UV} is affected by δA_c , δA_t , and δA_s . In the case of the cumulative error in drug release, two scenarios exist. First, the δM_0 is derived from volume calculation in the 3DP process step. Second, the δM_0 is calculated directly from the weight of the printed oral dosage.

3.4.5.1 Case I: δM_0 from 3DP tori volume measurements

Equation 3-12 outlines the possible error from volume measurements. The drug release is expressed as a percentage. The % relative error for a function (f) is given by $\frac{\delta f}{f} \times 100$ (353). The % relative error for drug release is given by rearranging in the form of equation 3-13. δA is the total δA_{UV} excluding the systematic error which is 0.121 AU. The reason for excluding the systematic error is that the drug release profile does not include any systematic error. The systematic error that exists in the oral dosage, appear in both M_t and M_0 . For example, an oral dosage can have systematically 50% of the mass compared to theoretical specification. This 50% is reflected equally in δM_t . Thus, the % relative error is more accurate if the systematic error is excluded.

$$\frac{\delta \left(\frac{M_t}{M_0} \right)}{\frac{M_t}{M_0}} \times 100 = \frac{\frac{V \delta A}{\varepsilon \ell}}{\left[\frac{\pi^2(9r^2 - 2rR - R)}{4} \delta r + \frac{\pi^2(3R^2 - 2rR - r^2)}{4} \delta R \right] D} \times 100 \quad \text{Equation 3-13}$$

$$\frac{VA}{\varepsilon \ell} \frac{1}{\frac{1}{4} \pi^2 (r + R)(R - r)^2 (D)}$$

Where A_1 is the sample absorbance. Since these parameters are constant for any absorbance and radius values of triplicate sample size, error bound for the oral dosage profile can be found. With the appropriate δr and δR of 0.36mm, and δA of 0.12 AU, the % relative error according to equation 3-13 is $\pm 56\%$. This has been illustrated in Figure 3-19 for a drug release profile. The red curve shows the absolute error bounds. It is observed that random error from the experiment is within the absolute error bound. When the upper bound of the curve goes above fractional drug release of 100%, the increasing portion of the curve thereafter can be taken as a constant valued at 100%. This is because the fractional drug release more than 100% does not have any physical interpretation.

3.4.5.2 Case II: δM_0 from 3DP tori mass measurements

If the oral dosage weight is measured, the δM_{3DP} is directly from the weight measurements. The resulting left side of equation 3-10 is simply the δM_{3DP} . Equation 3-14 shows the resulting relative percentage error form by dividing equation 3-9 by equation 3-10.

$$\frac{\delta \left(\frac{M_t}{M_0} \right)}{\frac{M_t}{M_0}} \times 100 = \frac{\frac{V \delta A}{\varepsilon \ell}}{\frac{\delta M_{3DP}}{VA}} \times 100 \quad \text{Equation 3-14}$$

$$\frac{\delta \left(\frac{M_t}{M_0} \right)}{\frac{M_t}{M_0}} \times 100 = \frac{\frac{V \delta A}{\varepsilon \ell}}{\frac{\varepsilon \ell}{M_{3DP}}} \times 100$$

The δM_{3DP} for the ten tori was 7.8mg. This δM_{3DP} is equated to be the δM_0 . δA_{UV} is 0.12AU which equates to a δM_t of 1.69mg. This produces a % relative error of $\pm 22\%$ shown in Figure 3-19. It is observed that many of the random error at sample time points are not within the error bound derived by this method. This indicates that the total error estimation from the mass measurement may underrepresent the experimental errors. This can be because of the number of variables used in calculating the relative error in the two cases. The estimation of absolute error from volume calculation (Equation 3-13) is less precise due to more error-prone variable present in the calculation (3 in total: δA , δr , and δR) vs two in total (δA and δM_{3DP}) for direct weight measurements. The less precision allows more variance of drug release, allowing for more experimental error and in this case encompasses the experimental random error.

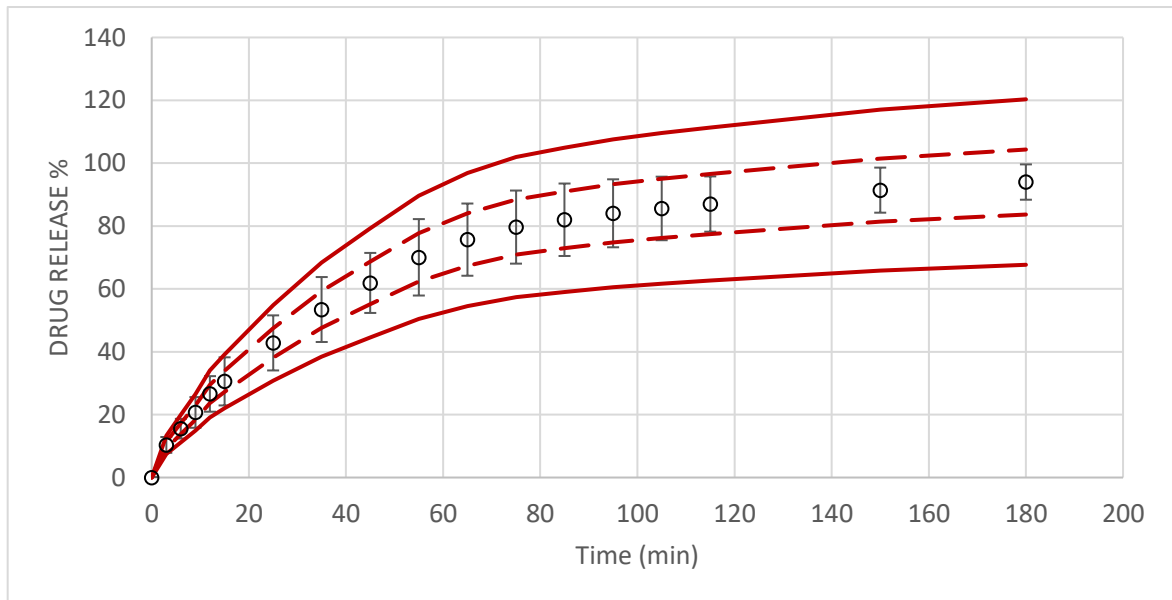


Figure 3-19: The absolute error in drug release attainable at each sample time point. The red solid curve represents absolute error from the volume calculations of 3DP oral dosage while the red dashed line represents absolute error from the mass calculations from 3DP oral dosage.

3.4.6 Process Optimization

Knowing the error from each of the processes, it is possible to minimize the cumulative error in drug release. For HME, the optimization of HME weight homogeneity is attainable through longer residence times. For 3DP, the printing temperature can have an effect which for the formulation was 200°C. For the UV spectrometer, creation of more calibration curves can reduce the random error. Bigger sample sizes also improve the error. Lower error in drug release leads to a better approximation of the parameters (k and n) on the right side in the Peppas equation (equation 3-3). Therefore, *in vitro* dissolution studies of a torus processed optimally with 10% PCM has been used to validate minimization of errors. In the previous section, drug release for the torus undergoing 5min residence time in the HME process was shown. From Figure 3-13, it was observed that higher HME processing temperature had more homogeneous drug distribution. A higher printing temperature of 210°C was used. Five calibration curves were utilized, and the experiment was replicated in quintuplicates. The cumulative error in drug release was found using equation 3-12. δA was 0.11AU. δr and δR are both 0.31mm. Figure 3-20 shows the resultant drug release profile with a relative error of $\pm 17\%$. As expected, the EXP error decreased and possible error bounds were narrower.

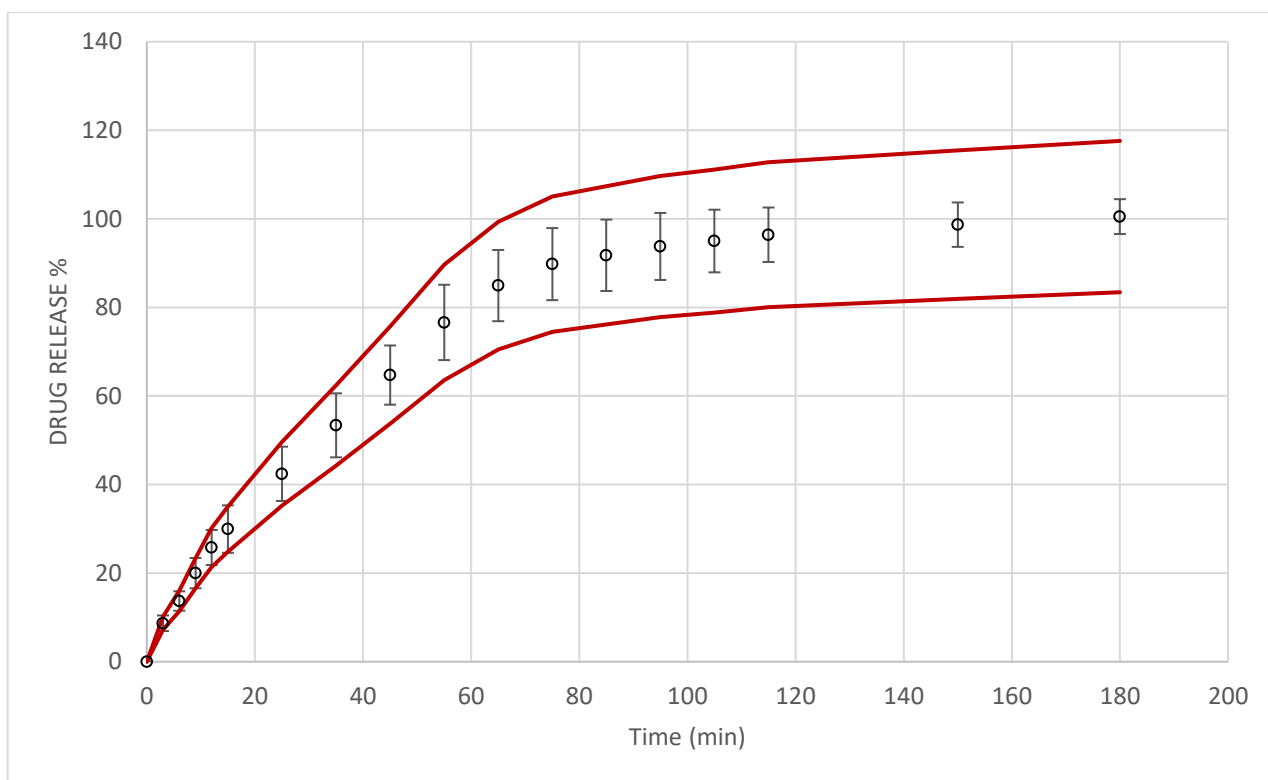


Figure 3-20: drug release of PCM under optimized manufacture process condition. The red curve is the possible error bound for this drug release profile.

The parameters of Peppas equation can be estimated from the two bounds. It can be seen that the aspect ratio which indicates the underlying transport mechanism does not alter significantly that can indicate a different mechanism. An aspect ratio of 0.45 to 0.89 is anomalous transport. This is shown in Table 3-5.

Table 3-5: Curve fitted parameters using Peppas model for drug release profile

	Release constant (k)	Aspect Ratio (n)
Lower estimate (Experimental)	9.39	0.56
Averaged estimate (Experimental)	10.13	0.51
Upper estimate (Experimental)	10.88	0.47

3.5 Limitations

Limitations exist that can hinder the use of such error cumulations to be generic for all drugs. The error in the drug release profile is essentially cumulative random error exhibited from all the manufacturing process. The random error will vary for different equipment and alterable process parameter. For example, a different hot melt extruder will have different δA_e and varying the process parameter like screw speed will affect the weight homogeneity. The same reasoning holds for the 3DP and UV spectrometer. The systematic error will also be minimized by using newer improved equipment.

The limitations to generalizing the drug release from the dosage also stem from the materials itself. A different drug or polymer will have a different melt viscosity. The drug loading will influence the drug release. A higher drug loading or a hydrophilic drug will likely exhibit faster dissolution rates. The choice of drug or polymer will alter the rheological and thermal properties of the formulation which will cause changes to the printing resolution and thereby the associated 3DP error (δM_{3DP} and δV_{3DP}). This in practice will be demonstrated by shrinking during solidification and in the deposition phase.

Lastly, gross error and analytical errors are not emphasized in this chapter. This is because gross errors can be eliminated, and analytical errors cannot be quantified for every step of the process. Due to the fact, that all possible errors cannot be always quantified for an experiment, the concept of triplicate repeats exists as this gives the random probability of errors possible across all the analytical steps (374).

3.6 Conclusion

In this chapter, the error for the manufacture of oral dosage via HME-FDM continuous process method was investigated. The systematic, random, and total error for each of the process was deduced. Based, on the random error from each manufacturing process, the cumulative error in the drug release profile was produced. This helps in ascertaining the highest margins of error possible for the given formulation in the current manufacture process pipeline. Thereafter, based on the findings, five tori under optimum processing condition were prepared. The drug release profile for these tori was compared wherein the random error of the quintuplicate was found to be lower compared to sub-optimum processing conditions. Unfortunately, although the error propagation concept can be generalized for any formulation, the error values obtained here cannot be applied to any generic formulation. Furthermore, the error values ascertained cannot be deduced in a pre-experiment case due to numerous limitations.

Chapter 4: Characterisation of the polymers and polymer blends behaviour in aqueous media

4.1 Introduction

Polymers are often used as the carriers in the solid dispersions based dosage forms manufactured using FDM 3D printing (368, 375). A limited number of pharmaceutical grade polymers can be directly printed using FDM and in most cases, additional excipients such as plasticizers or blending with other polymers are needed to achieve the thermoplasticity required for FDM printing (368, 376). Examples of such polymers include HPC (377), Eudragit EPO (378), PEO/PEG (47), PVA (379), PLA (380), and PCL (381). In general, polymers used in pharmaceutical solid dispersions can be differentiated into hydrophobic and hydrophilic matrix formers. Examples of hydrophobic polymers include ethylcellulose (382), Eudragit (383), PLA (384), and PCL (268) while hydrophilic ones such as PEO (385), PEG (386), and PVA (387). Depending on the solubility of one polymer in the other, blends of polymers can be classified as miscible, semi-miscible and immiscible. Therefore, the resultant blend can be a single phase or a phase-separated system. This aspect is important in formulations as phase phenomenon governs the behaviour of the blend and their performance (such as physical stability and drug release pattern) when used as a drug delivery vehicle.

In order to understand and subsequently predict the drug release behaviour of a polymeric based solid dispersion system, it is important to have a thorough understanding of the behaviour of the polymeric matrix in aqueous media in the first instance (388, 389). In this chapter, a systematic study of a group of commonly used pharmaceutical polymers for hot melt extrusion (HME) and FDM 3D printing was performed in order to parametrise the hydration, swelling and erosion behaviour of the polymers and polymer blends in aqueous environments. The kinetics of these three processes of each polymer in the aqueous media were measured. In addition, the behaviour of miscible and semi-miscible polymeric blends was studied. All experiments were carried out in pH 1.2 (gastric pH) and pH 6.8 PBS (intestine pH). These kinetics parameters along with other intrinsic characteristics of the polymer were used to form a dataset that was used by later chapters to categorise the polymers based on their behaviour in the aqueous media.

4.2 Materials and Methods

The materials used in this chapter are HPMCAS LF, PCL CAPA 6800, PEO WSR N10 LEO, purified zein, Eudragit RS100, Xanthan Xantural 180, Soluplus, PVPVA Kollidion, Moweiflex PVA. The product details and their physicochemical properties are described in chapter 2.

4.2.1 Preparation of Filaments

Filaments were prepared using HME method. The standard procedure mentioned in section 1.1.2.1 and 2.3.1 of preparing filaments was used. The feeding batch size was 7g in all cases. The extrusion temperatures for the polymers and their behaviors are listed in Figure 4-1. Xanthan gum extrudate was prepared by adding 10% MilliQ water and gently stirring the mixture for 10 to 15 mins. The addition of water is necessary to facilitate extrusion at a temperature of 70 °C. Zein extrudates were prepared by adding 10% MilliQ water to powdered zein and mixing in a ceramic mortar and pestle to facilitate HME with an extrusion temperature of 80 °C. The screw speed in all cases was 100 rpm. For the polymer blends, the default polymer mix ratio was 50/50% as per the weight of two polymers. The miscible blend was composed of HPMCAS/Soluplus while the semi-miscible blend was composed of HPMCAS/PEO. The filament extruded was cut into an equal length of 2cms.

Table 4-1: Polymer extrudates at their temperatures with behaviors observed

Polymer	Extrusion temperature (°C)	Polymer characteristics
HPMCAS	160	Swell, hydrate, and erode in pH 6.8
PCL	100	Insoluble/very low solubility
PEO	120	Swell, hydrate, and erode in both pH
Eudragit	160	Insoluble/ very low solubility
Soluplus	110	Hydrate and erode in both pH
PVPVA	160	Erode in both pH
PVA	190	Hydrate and erode in both pH
Xanthan gum	70	Swell, hydrate, and erode in both pH
Zein	80	Hydrate and swell but non-eroding
HPMCAS/Soluplus (miscible blend)	150	Hydrate and erode in pH 6.8
HPMCAS/PEO (Semi-miscible blend)	150	Swell, hydrate, and erode in both pH

4.2.2 Measurement of Polymer behaviour

Three polymer behaviours were studied in this chapter. They were hydration, erosion, and swelling in aqueous media which were parametrised. The parametrisation allowed comparison of the polymers in terms of the three behaviours. For polymer blends, these parametrised values of the individual polymer were used to emulate the behaviour of the blend, accounting for the 50% mass of individual polymers. During each sampling point, these three measurements were done.

The **hydration** was measured by recording the wet weight of the polymer at the sampling time points by using an analytical balance. The increased wet weight measured compared to the initial dry weight which signifies the additional weight due to hydration (water intake) The normalised hydration is given by the left side of Equation 4-1. The right side of the equation is the Vangernaud model used for fitting to hydration curve (390). K_H is the hydration constant. The hydration index (n_H) is an indicator of the diffusion mechanism for the material. For cylindrical shapes, $n < 0.55$ and corresponds to Fickian diffusion whereas $0.50 < n < 1.0$ indicates that diffusion is non-Fickian diffusion (391).

$$H_{\%} = \frac{w(\text{wet})_t - w(\text{dry})_0}{w(\text{dry})_0} \times 100 = K_H t^{n_H} \quad \text{Equation 4-1}$$

where W_t is weight at time t , W_0 is weight at time 0 min, K_H is hydration constant, and n_H is hydration index.

The **swelling** was measured by using a digital caliper. The volume was measured at the sampling times. The radius (from the diameter) and length of the filament were used to calculate the volume of the cylindrical filament shown in Figure 4-1. Equation 4-2 shows the volume calculation of cylindrical geometry. The left side of Equation 4-3 shows the swell ratio calculation while the right side is an empirical equation, used for parametrising the swelling curve. All readings were done in triplicates.

$$V = \pi \times r^2 \times l \quad \text{where } r^2 = \frac{d}{2} \quad \text{Equation 4-2}$$

$$S_{\%} = \frac{V_t - V_0}{V_0} \times 100 = K_S t^{n_S} \quad \text{Equation 4-3}$$

where l is length, d is diameter, r is the radius, $S_{\%}$ is the swell percentage, V_t is the volume at time t , V_0 is the initial volume, K_S is a swelling constant and n_S is swelling index.

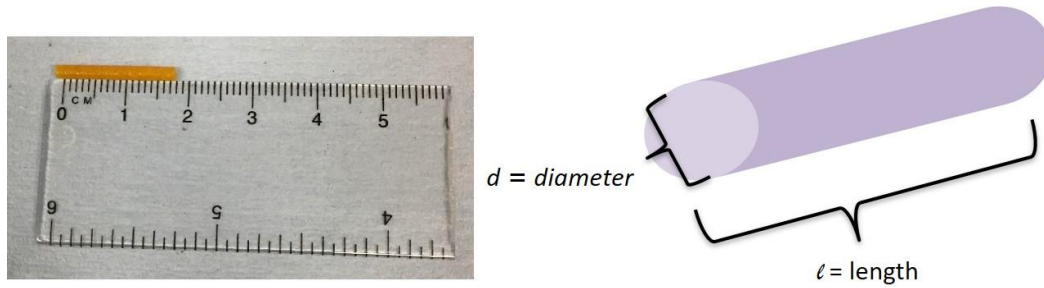


Figure 4-1: The filament cross-section in 3D perspective. Length is denoted by (l) while the diameter is denoted by (d)

The **erosion** was calculated by measuring the dry weight change of the polymers at every sampling time and comparing to the initial weight. This procedure is as follows. First, an equal number of filament samples were made to the number of sampling times. For example, sampling times of 5 mins, 10 mins, 15 mins and 30 mins would mean four sampling times. As such, four filament samples can be made. Next, all four filament samples are put in one dissolution vessel. Thereafter, at a sampling point, one of the samples would be taken and dried before the weight was measured. This sample would then not be put back in the vessel. This meant there are only three samples left in this with three more sampling times. Eventually, all samples were measured by the end of the dissolution sampling times and all the dry weights were referring to the weight of the samples after complete drying at each time point. This differential weight is calculated using the left side of the Equation 4-4. There are reports that polymer erosion has been fitted to linear regression models (zero order) as well as exponential decay (first order) (392, 393). Gaillard et al investigated polymer erosion and concluded that first order fitting provided higher accuracy (394). Therefore, the first order model was used for fitting. This is illustrated by the right side of Equation 4-4. These measurements were done for samples in pH 1.2 and pH 6.8 in triplicates.

$$E_{\%} = \frac{w(\text{dry})_t - w(\text{dry})_0}{w(\text{dry})_0} \times 100 = W_{(\text{dry})_0} e^{-E_K t} \quad \text{Equation 4-4}$$

where $W(\text{dry})_t$ is the dry weight at sample time, $W(\text{dry})_0$ is the initial dry weight and E_K is erosion constant.

4.2.3 Characterization of polymer blends

The pure polymers chosen were HPMCAS, PCL, PEO, Eudragit, Xanthan, Soluplus, PVA, PVPVA, and Zein. The blends were chosen to represent miscible and semi-miscible blends. HPMCAS/Soluplus was the miscible blend and HPMCAS/PEO was the semi-miscible blend. The miscibility of polymer blends was determined by the glass transition temperature (T_g) of the resulting mixture compared to the single polymers. The T_g was

gathered by using differential scanning calorimetry (DSC). The T_g of a miscible blend should exhibit a single T_g between the T_g 's of the component. The miscible blend in this work is HPMCAS/Soluplus. The T_g can be calculated by using the Flory-Fox equation, shown in equation 4-5 (125). A semi-miscible blend will show two separate T_g between the range of the individual components (122). The semi-miscible blend in this work is HPMCAS/PEO. Both miscible and semi-miscible polymer blends had a 50/50 weight ratio of the individual polymers. For semi-crystalline PEO, the recrystallization enthalpy was used to estimate the amount of crystalline PEO.

$$\frac{1}{T_g} = \frac{W_1}{T_{g1}} + \frac{W_2}{T_{g2}} \quad \text{Equation 4-5}$$

4.3 Results and Discussion

4.3.1 Overview of polymer behaviour in aqueous media

The summary of the kinetics of the behaviour of the polymers is given in Figure 4-2 for pH 1.2 and in Figure 4-3 for pH 6.8 excluding the insoluble polymers that do not any physical changes in the media. It is observed that for all polymers plotted, there is a simultaneous activity of the three aspects except for zein which does not exhibit any erosion. Since the polymers, excluding zein and insoluble polymers, are eroding and hydrating simultaneously, it is not possible to identify the effect of hydration alone. However, it is possible to distinguish the mechanism of transport from the shape of the curve and the effect of erosion individually. Since some polymers swell and some erode without swelling from the beginning of the experiment, it is possible to categorize them as swellable or erodible polymers. The swellable polymers consist of PEO, Xanthan gum, zein, and soluplus for pH 1.2 and pH 6.8. Meanwhile, the erodible polymers consist of PVPVA, PVA in pH 1.2 and HPMCAS, PVPVA, and PVA in pH 6.8. PCL (not shown in Figure 4-2) is also an eroding polymer in both pH but the progression of erosion is longer than the experiment duration. PCL erosion time has been reported to be two to four years (395). Such polymers that erode without swelling have a negative ratio in terms of volume on the plots as the volume decreases compared to initial volume. As an example, this is observed with PVPVA and PVA.

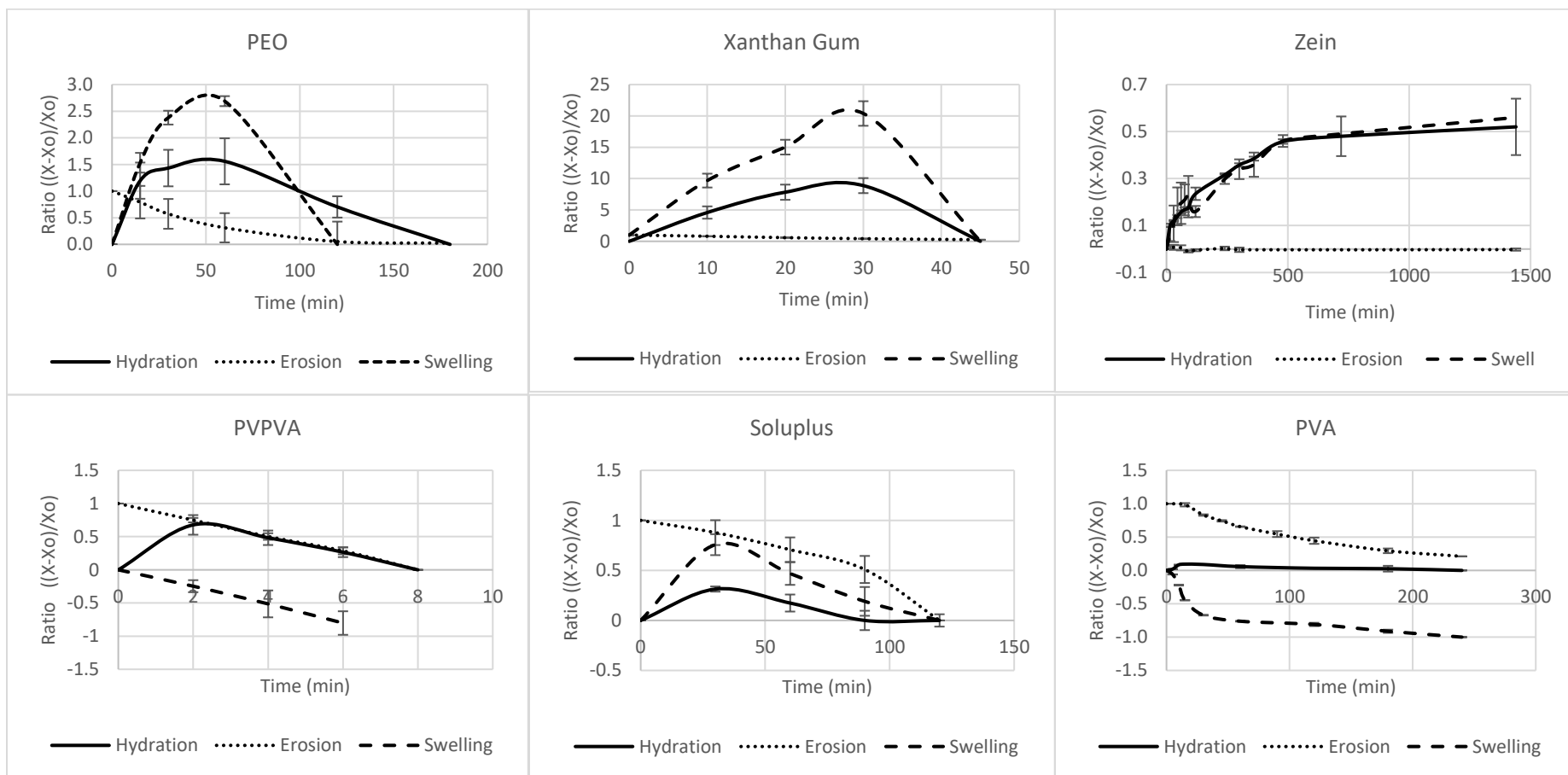


Figure 4-2: Mass and volume changes with the time of polymers in pH 1.2. The polymers that do not show any changes are omitted (PCL, Eudragit, and HPMCAS). The axis for all graphs has been replaced with a generic $(X-X_o)/X_o$. For hydration, the generic $(X-X_o)/X_o$ is $(M_t-M_o)/M_o$ where the M has been stated in equation 4-1. For volume, the generic $(X-X_o)/X_o$ is $(V_t-V_o)/V_o$ where the V parameters have been stated equation 4-3. For erosion, the generic $(X-X_o)/X_o$ is $(M_t-M_o)/M_o$ where the M has been stated in equation 4-4. Erosion is plotted in reverse from a ratio of 1 eroding to a final ratio of 0. The solid lines/dashed line presented here are only connecting data points.

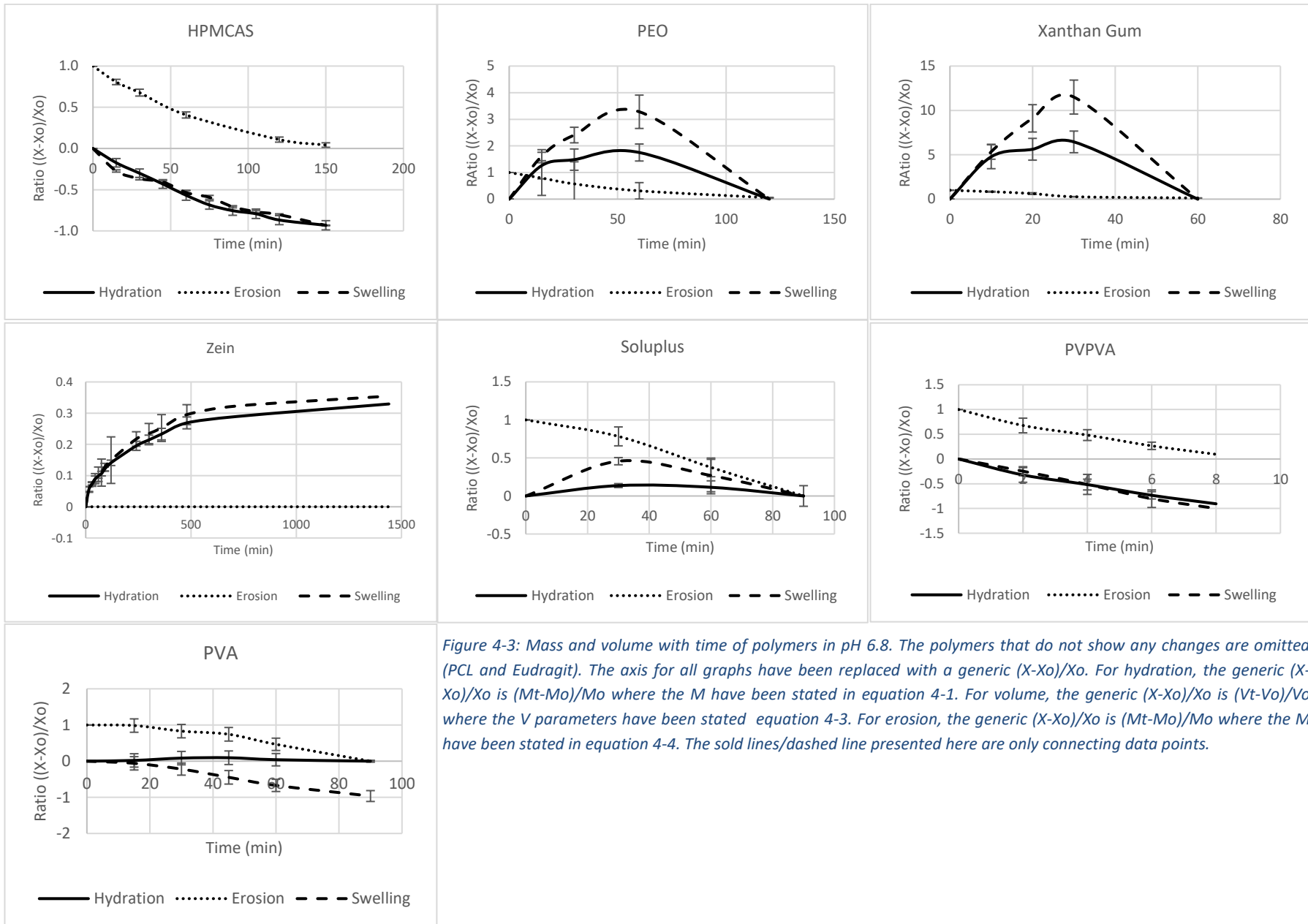


Figure 4-3: Mass and volume with time of polymers in pH 6.8. The polymers that do not show any changes are omitted (PCL and Eudragit). The axis for all graphs have been replaced with a generic $(X-X_o)/X_o$. For hydration, the generic $(X-X_o)/X_o$ is $(M_t-M_o)/M_o$ where the M have been stated in equation 4-1. For volume, the generic $(X-X_o)/X_o$ is $(V_t-V_o)/V_o$ where the V parameters have been stated equation 4-3. For erosion, the generic $(X-X_o)/X_o$ is $(M_t-M_o)/M_o$ where the M have been stated in equation 4-4. The solid lines/dashed line presented here are only connecting data points.

4.3.2 Hydration behaviour

The first parameter measured was the differential wet weight signifying the hydration. The hydration ratio for all the polymers in pH 1.2 and pH 6.8 is presented in Figure 4-4. At both pH, there are two groups of polymers. The first group are hydratable polymers which exhibit net positive hydration. Net positive hydration is when there is an increase in the wet mass during the experiment. All hydratable polymers have been plotted up to the maximum hydration timepoint. After this point, erosion is more dominant in polymer behaviour. The second group are non-hydratable or minimally hydratable polymers. Polymers that maintain 95% of the initial mass for the duration of the experiment are considered in the second group of non-hydratable polymers. The first group of polymers include Xanthan gum, PEO, zein, and PVA (only pH 1.2). Two of the four polymers are superabsorbent polymers (SAPs). SAPs have three factors contributing to water absorption. They are the density of cross-linking, the affinity between polymer and solvent, osmotic pressure caused by polyelectrolyte counter ions. Xanthan gum, a hydrophilic polymer, has a high affinity to water (396). It is also stable over ranges of pH 1 to pH 11 (283). This indicates the properties it shares for water as super absorbent are also unchanged over the range of pH wherein it is stable. As such, it expands in water and other solvents. This generates a wider surface area upon which the polymeric chain molecules can interact with the solvent attracting more solvent molecules in close proximity. Furthermore, the conformation of xanthan gum is responsible for the stability which is due to the presence of salt. The cation (Na⁺, K⁺, or Ca²⁺) promote the intermolecular cross-linking strengthening the gel network (397, 398).

PEO, a hydrophilic polymer, is a linear polymer but upon contact with water, rapidly hydrates due to its high solubility and forms a hydrogel which is seen in both pH. When PEO come into contact with water, forces of attraction (chiefly hydrogen bonding) start acting between polymer and water. Due to the high water-affinity of the polymer, these forces are likely to be preferred over polymer-polymer interactions (190). The structure of PEO (-O-CH₂-CH₂-)_nOH is likely to hydrogen bond. It has also been reported that such gels have high osmotic activity (193). This, for a hydrophilic polymer, causes the crosslinked network to expand

outward as polymeric material tends to flow outward due to the high affinity for the solvent and solvent to penetrate to balance the pressure leading to greater hydration which is a property of SAPs.

PVA is a water-soluble synthetic polymer but the physicochemical and mechanical attributes of PVA are dictated by the number of hydroxyl groups. PVA comes in varying hydrolysis percentages. With higher hydrolysis, there is an abundance of vinyl alcohol units, which are distributed within PVA, disrupting the crystalline phase of the PVA. This makes the polymer very hydrophilic and water-soluble with a high capacity for hydrogen bonding (399). In this case, with the 98-99% hydrolysis (261), the PVA chains disperse in a short time and tend to form hydrogen bonds with the solvent.

For zein, it was reported that the hydration can be contributed to the charge. Bouman et al mention osmotic pressure is increased at pH 1.2 as there are more counter ions present due to positively charged zein coming from the predominant α helix zein with an isoelectric point of pI 6.8 (14). In addition, the expansion of the network structure was stated likely due to the de-amidation of the glutamine and asparagine amino acids of the zein (14). Although swelling was the result of this, for the volume to expand, it indicates the free space is filled up by the solvent.

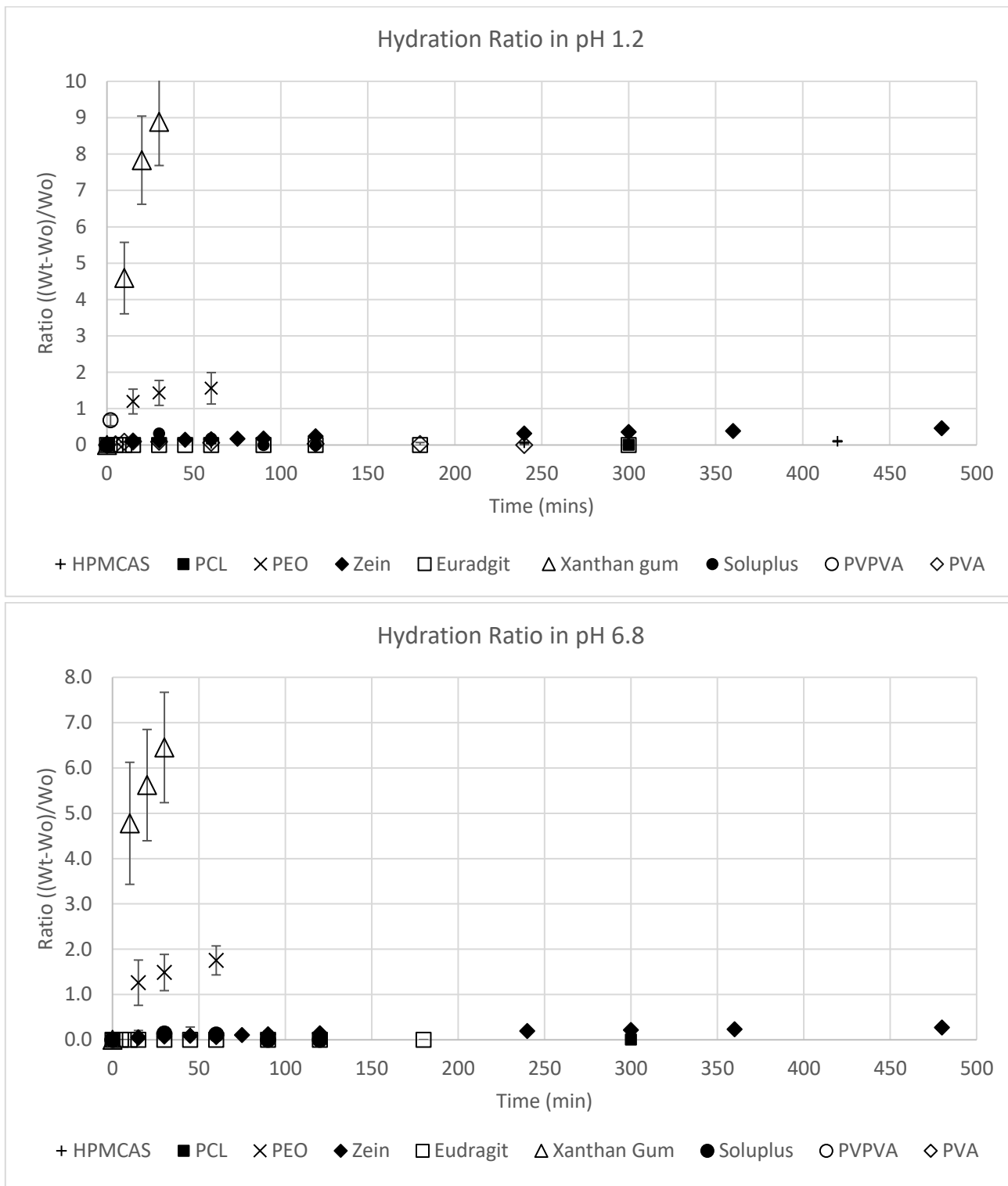


Figure 4-4: Top) The hydration ratio all the nine polymers in pH 1.2. Bottom) The hydration ratio all the nine polymers in pH 6.8. The timescale for non-hydratable polymers have been shortened.

The second group of polymers in Figure 4-4 include Euradgit, PCL, PVPVA, and HPMCAS which are non-hydratable polymers or exhibit minimal hydration. Euradgit RS100 is a copolymer of ethyl acrylate, methyl methacrylate and low content of methacrylic acid ester with quaternary ammonium side groups. The ammonium groups are ionisable (277). This insolubility arises from the side groups. The side chain of

Eudragit RS consists of groups of R1:H, CH₃, R2: CH₃, C₂H₃, R3: CH₃, R4: CH₂CH₂N(CH₃)⁺ Cl⁻ (277, 278) of which non-polar CH₃ in major proportion are hydrophobic and impart low solubility even though Cl⁻ is hydrophilic (400). The hydration observed for PCL can be due to the fact it is a hydrophobic semi-crystalline polymer. The degree of crystallinity hinders diffusion of solvent molecules. It is also noted that with the increase of molecular weight, the crystallinity decreases. HPMCAS lack of hydration could be due to the unionised state in the buffer. HPMCAS has four types of substituents on the hydroxyls. The first is methoxy with a mass content of 12–28%, second is hydroxypropyl with a mass content of 4–23%, third is acetate with a mass content of 2–16%, and fourth is succinate, with a mass content of 4–28% (225). This succinate group has a pK_a of 5. This means HPMCAS is 10% ionised at most at pH ranges less than pH 4 and at least 50% ionised at pH values of about 5 and higher. Therefore, HPMCAS is insoluble and not significantly ionised at pH 1.2 with the presence of hydrophobic methoxy and acetate substituents. At pH 6.8, there is more solubility due to the higher ionisation, making HPMCAS a pH responsive polymer.

Table 4-2 shows the fitting to Vangernaud model which is a semi-empirical model similar to the Korsmeyer-Peppas model. For Xanthan gum and PEO, the hydration constant is higher than all the other polymers in both pH indicating a higher rate of solvent ingress. The explanation for this can be gathered from the hydration index. The hydration index indicates the mechanism of transport is Fickian diffusion, which is commonly referred to as Fickian or case I diffusion in literature. According to Singh, the shape of the hydration curve can yield about the mechanism of transport (401). However, an issue exists that the shape of the curve is not an unambiguous criterion for distinguishing Fickian II from Fickian I transport. In such cases, it is important to know whether the boundary moves. If the boundary moves (i.e. volume changes) and the gel remains rubbery throughout swelling or collapse after, the transport is called Fickian I. Since the boundary moves for zein, PEO, and Xanthan gum, they exhibit Fickian I transport. Additionally, the molecular relaxation may be either much faster than diffusion ($T > T_g$) or extremely slow ($T < T_g$) (401). The T_g of PEO (-57 °C) and Xanthan gum (-23 °C) are both below the dissolution temperature of 37°C which indicates faster molecular relaxation compared to diffusion. Hence the higher solvent ingress and the higher

hydration ratio. The T_g of zein (150 °C) is higher than dissolution temperature indicating very slow molecular relaxation. Hence the lower solvent penetration and the lower hydration ratio.

Table 4-2: Vangernaud model fitted to hydratable polymers.

<i>pH</i>	1.2			6.8		
	<i>k_H</i>	<i>n_H</i>	<i>R</i> ²	<i>k_H</i>	<i>n_H</i>	<i>R</i> ²
PVA	0.04 ± 0.01	0.61 ± 0.03	0.99	-	-	-
Xanthan gum	1.31 ± 0.70	0.52 ± 0.01	0.98	2.51 ± 0.83	0.27 ± 0.04	0.99
PEO	0.73 ± 0.12	0.18 ± 0.02	0.99	0.66 ± 0.12	0.23 ± 0.05	0.99
Zein	0.03 ± 0.01	0.37 ± 0.09	0.95	0.02 ± 0.01	0.37 ± 0.02	0.97

4.3.3 Swelling behaviour

The anatomy of a swelling tablet is shown in the top left of Figure 4-5. The swelling front is the boundary between the glassy region (circle A) and the rubbery gel region (circle B) of the polymer marked as r_A (179). The diffusion front indicates the boundary between the undissolved and dissolved polymer in the gel layer marked as r_B . The erosion front is the most outer fringe of the tablet or polymer extrudate identifying the boundary between the matrix (circle C) and the dissolution medium marked as r_C . This was observed for some polymers such as PEO while not observed for others such as Xanthan gum (shown at the bottom of Figure 4-5). In both cases, the erosion front was the limit of measurement for matrix edge.

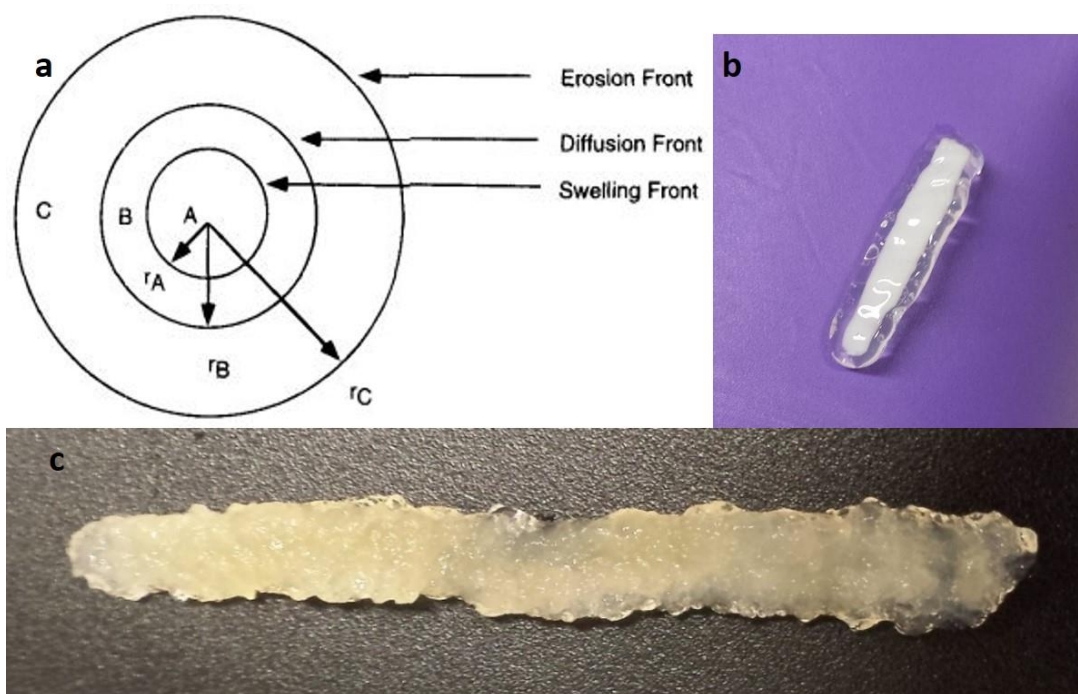


Figure 4-5: a) Schematic representation of diffusion, erosion and swelling fronts and different layers of swelling dosage (179). (b) PEO exhibiting swelling front and erosion front. (c) Xanthan gum without a clear swelling front.

The swelling ratios of the polymers are shown in Figure 4-6. It can be seen that the two highest swelling polymers are SAP. Zein also does swell but a lower ratio. There are distinctly two groups of polymers where swelling is observed and where swelling does not occur. The non-swelling polymers (PCL, HPMCAS, Eudragit, PVPVA, Soluplus and PVA) have a combination of insoluble and soluble polymers. For insoluble polymers, there is no hydration and hence no causation for swelling. For soluble polymers, if the hydration ratio of the solvent was faster than the molecular relaxation rate of the polymer, swelling was observed. Conversely, swelling was not observed if diffusion was slower than molecular relaxation.

Furthermore, it is seen that the swelling ratios are not proportional to the hydration ratios for the same swellable polymer. In pH 1.2, Xanthan gum had a maximum hydrated ratio of $\approx 10X$ while the swelling ratio was $\approx 20X$. PEO in pH 1.2 had a maximum hydrated ratio of $\approx 1.8X$ and swell ratio of $\approx 3.6X$. The similar case for both polymers in pH 6.8. This behaviour is not seen with zein. In pH 1.2, zein at 30 minutes exhibited a hydrated ratio of 0.12X (12%) and a swollen ratio of 1.11X (11%); at 300 minutes (5 hours) exhibited a hydrated ratio of 1.36X (36%) and a swollen ratio of 1.34X (34%); at 1440 minutes (24 hours) exhibited a hydrated ratio of 1.49X (49%) with a swollen ratio of 1.48X (48%).

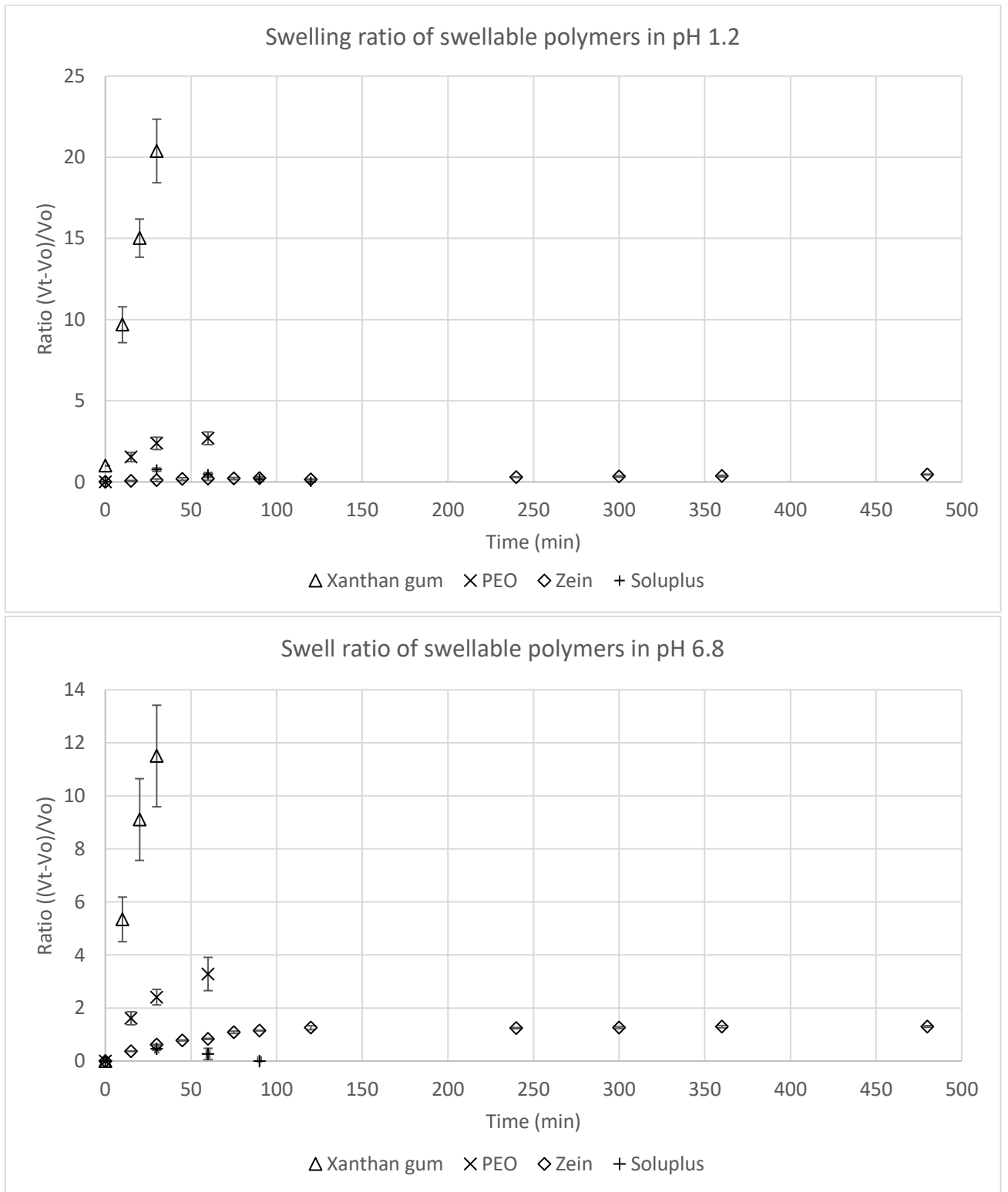


Figure 4-6: The swelling ratios of swellable polymers in pH 1.2 on top and pH 6.8 at the bottom.

Using equation 4-3, the swelling constant and swelling index is shown in Table 4-3. The high K_s values of PEO, Xanthan gum, and soluplus compared to zein indicate burst swelling kinetics. Zein shows no burst swelling consistent with the much lower value of 0.04. Higher K_s gives a steeper gradient which gives faster release initially and such formulations are known to have a burst release (147).

Table 4-3: The swollen polymers fitted to the generalized model and their goodness of fit (R^2). K_s is the swelling constant and n is the swelling index.

Polymer	pH 1.2			pH 6.8		
	K_s	n_s	R^2	K_s	n_s	R^2
Xanthan gum	1.54 ± 0.13	0.74 ± 0.03	0.99	1.15 ± 0.27	0.68 ± 0.08	0.99
PEO	0.46 ± 0.11	0.42 ± 0.10	0.99	0.43 ± 0.18	0.49 ± 0.07	0.99
Zein	0.04 ± 0.01	0.37 ± 0.08	0.98	0.09 ± 0.01	0.18 ± 0.03	0.95
Soluplus	0.51 ± 0.08	0.05 ± 0.01	0.98	0.31 ± 0.01	0.05 ± 0.01	0.91

4.3.4 Erosion behaviour

The erosion ratios of erodible polymers are presented below in Figure 4-7. It can be seen that other than PVPVA, the SAP have high erosion rates. However, very high erosion rates of PVPVA might be contributed to the unit composition of PVPVA. The unit composition is 6:4 of PVP:VA in PVPVA chain with the aim was of increased solubility (192). Without swelling, erosion is the only dominant process for PVPVA, which occurs rapidly. Furthermore, it can be argued that the zero order model might be a better fit for PVPVA. From chapter 1, zero order polymer mass loss is expected for surface erosion polymers.

The erosion rate found from equation 4-4 is presented in Table 4-4 suggests that the first order model is in good agreement with the data denoted by R^2 . Ranking the erosion ratios show a similar trend for both pH medium (PVPVA < Xanthan gum < PEO < Soluplus < PVA). The exception is with pH 6.8, where HPMCAS erodes and the descending erosion ratios are PVPVA < Xanthan gum < PEO < HPMCAS < Soluplus < PVA.

Table 4-4: The erosion rates of erodible polymers in both pH fitted to exponential decay.

Polymer	pH 1.2		pH 6.8	
	E_k	R^2	E_k	R^2
PVPVA	19.15 ± 0.10	0.99	17.34 ± 0.12	0.97
Xanthan Gum	2.77 ± 0.03	0.99	3.07 ± 0.09	0.94
PEO	1.91 ± 0.02	0.99	1.90 ± 0.03	0.99
PVA	0.66 ± 0.02	0.98	0.83 ± 0.02	0.98
Soluplus	1.21 ± 0.04	0.95	1.30 ± 0.10	0.91
HPMCAS	-	-	1.56 ± 0.04	0.99

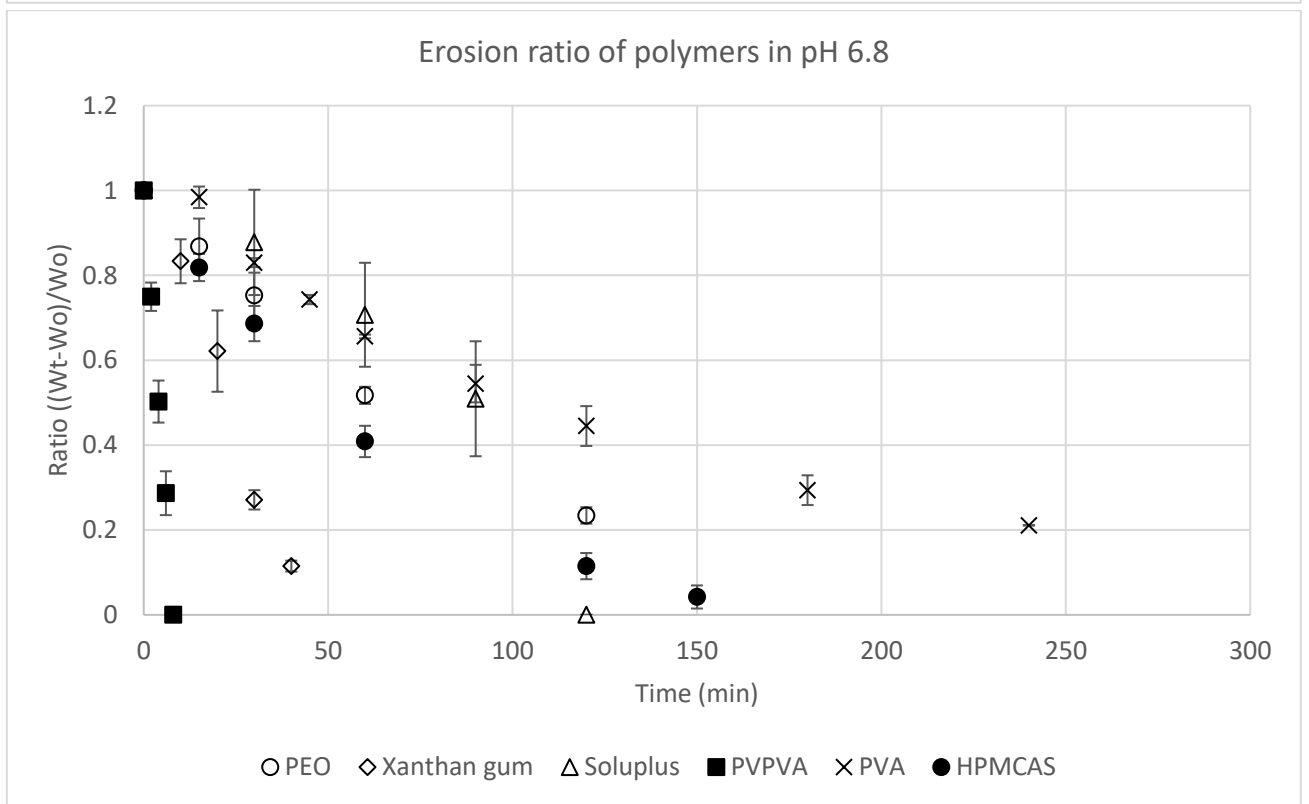
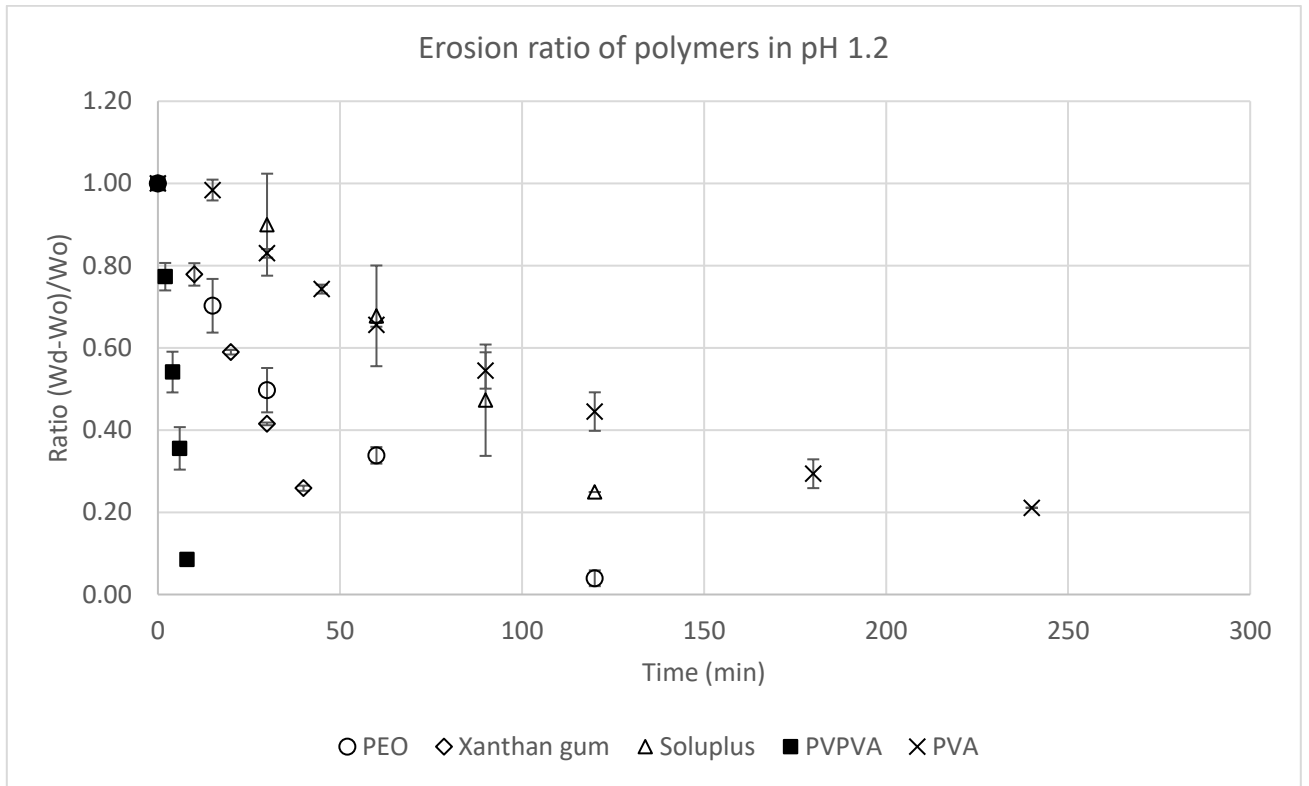


Figure 4-7: Top) The erosion ratio of eroding polymers in pH 1.2. Bottom) the erosion ratio of erodible polymers in pH 6.8

4.3.5 Characterization of blends

The DSC thermogram of the miscible HPMCAS-Soluplus is shown in Figure 4-8. A single T_g is observed for the HPMCAS-Soluplus between the pure HPMCAS and pure soluplus at 95.81 °C, which agrees with a T_g of 96.75 °C obtained from the Flory-Fox equation (equation 4-5) for a 50/50 blend, indicating a miscible blend (125).

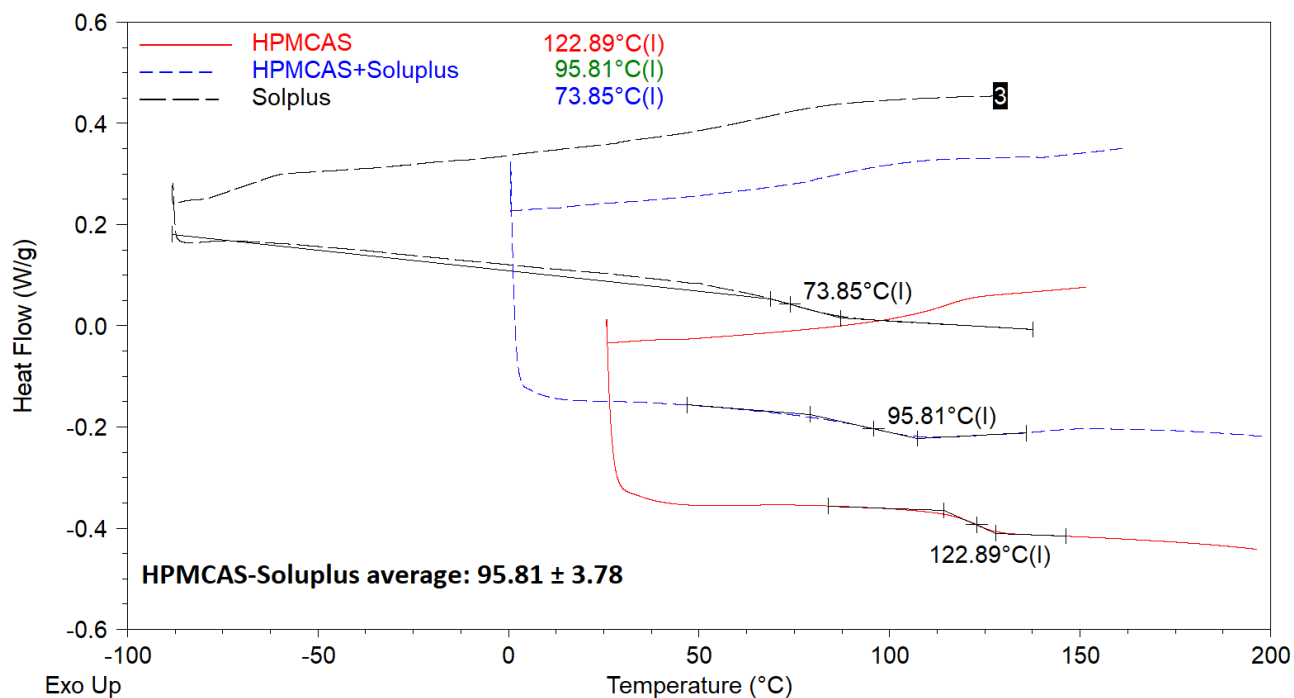


Figure 4-8: DSC thermogram of the HPMCAS (red), Soluplus (black), and HPMCAS-Soluplus 50/50 blend (blue). The T_g is shown on the thermogram, and with the corresponding polymer colours.

In the case of HPMCAS-PEO, the PEO T_g has been reported to be -62 °C to -67 °C (402-405). This well-established value of -62 °C will be taken as the T_g of PEO. Rather, the recrystallization and melting enthalpies are taken into account. The thermogram is shown in Figure 4-9. It can be seen that for pure PEO, the recrystallization enthalpy is 189.4 J/g. After accounting for the quantity of PEO in the blend, the enthalpy calculated is 88.83 J/g. The recrystallization enthalpy of the blend is 38.53 J/g which is about 2.3 times lower than 88.8 J/g. This means 43% of PEO is crystalline after heating and 57% is amorphous in the blend.

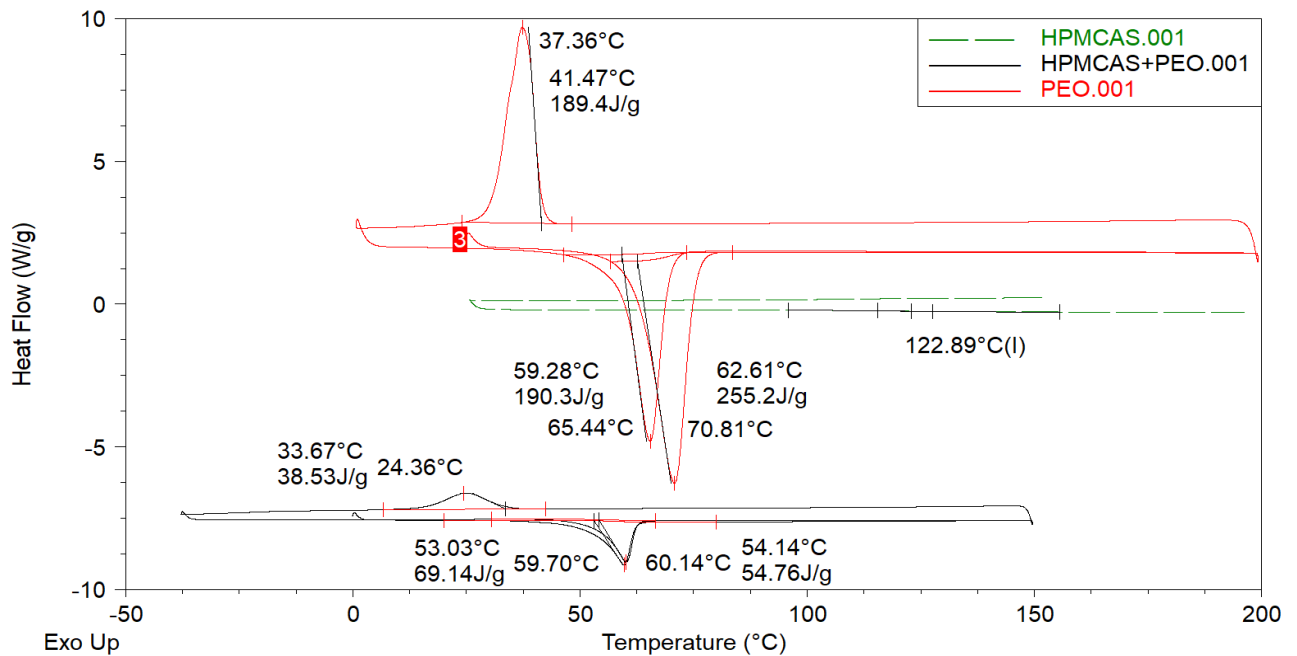


Figure 4-9: DSC of HPMCAS (green dash), PEO (red line), and HPMCAS-PEO 50/50 blend (black line). The melting and recrystallization temperatures and the corresponding enthalpies are given (J/g) while the T_g for HPMCAS is given.

4.3.6 Miscible and semi-miscible blend behaviour

The hydration ratios of the miscible blend are shown in the top left of Figure 4-10. In pH 6.8, there is not positive hydration but rather, negative hydration (erosion) and as such, has been omitted. The blend appears to exhibit characteristics of both polymers. While HPMCAS is insoluble at pH 1.2 and soluplus hydrates to a maximum of 1.31X (31%) at 60 minutes, the blend hydrates to the same ratio of soluplus but at a delayed time of 420 minutes (7 hours). The duration of hydration is 7 folds slower compared to soluplus. It can be seen that if one is an insoluble polymer and the other is hydratable, the net effect is slower hydration. The hydration ratio of the semi-miscible blend has been shown in the top right of Figure 4-10. In the case of the semi-miscible blend, the hydration time is faster than the pure PEO but a point to note is that that behaviour kinetics of the blends are different than the constituents when compared to miscible blend. For the fully miscible blend, the hydration profile is in between the two polymer profiles while for the semi-miscible blend, the hydration profile is outside the region of the two constituting polymer profiles. One reason for this could be due to the fact this is not a single phase system. Since the HPMCAS is 10% ionised at this pH, this can increase the osmotic activity in the matrix thereby increasing the affinity of the solvent. The hydration parameters are presented in Table 4-5. Work done Mudassir et al on hydrogels shows that the mechanism changes with pH and polymer blend composition degree (406). The penetrant

transport from the matrix system is governed by diffusion, so determining the diffusion coefficient of the hydrogel is essential.

The swelling ratio shown in the bottom left of Figure 4-10 shows the miscible blend swelling does occur at pH 1.2. The swelling profile of the miscible blend is also between the constituting polymers as opposed to the semi-miscible blend. The swelling constants for the miscible blend (Table 4-6) indicate that at pH 1.2, there is a significant decrease in the swelling ratio due to the addition of HPMCAS. The swelling mechanism is still hydration dominated but shows this faded about two-folds, explainable by the insoluble HPMCAS slowing hydration; not necessarily increasing diffusion. At pH 6.8, as soluplus swelling constant is lower with HPMCAS eroding, no swelling is observed compared to pH 1.2. In contrast, the semi-miscible blend swelling constant showed a smaller decrease from K_s 0.46 to 0.31 at pH 1.2 due to retaining of more individual blend properties and some conversion of PEO to amorphous form. The value of index change is greater for the HPMCAS/PEO is 1.5X greater than PEO. This can account of some portion of two-fold slowdown by the addition of HPMCAS. However, the increased rate in hydration is due to some of the PEO becoming amorphous which is in agreement with roughly the amount of amorphous PEO. The erosion ratios for the miscible are shown in Figure 4-11. The erosion ratios exhibit first order mass loss in the cases of all blends in all medium. As before, the erosion ratios for the miscible blend is between the two constituent polymers. This is expected as both polymers aggregately contribute to faster erosion than either of the one polymer. An exception emerges for the semi-miscible blend eroding in pH 1.2. HPMCAS/PEO erosion is between the two constituent polymers while it was expected to be outside of the region of two polymers erosion profile. This can be intuitive as PEO is soluble while HPMCAS is not. It is expected that HPMCAS will slow down the erosion causing the profile to be between the two constituting polymers. This is due to the insoluble HPMCAS polymer slowing down erosion. However even in the blend, only the PEO composition erodes and thereafter, erosion is halted. The erosion ratios are shown in Table 4-7.

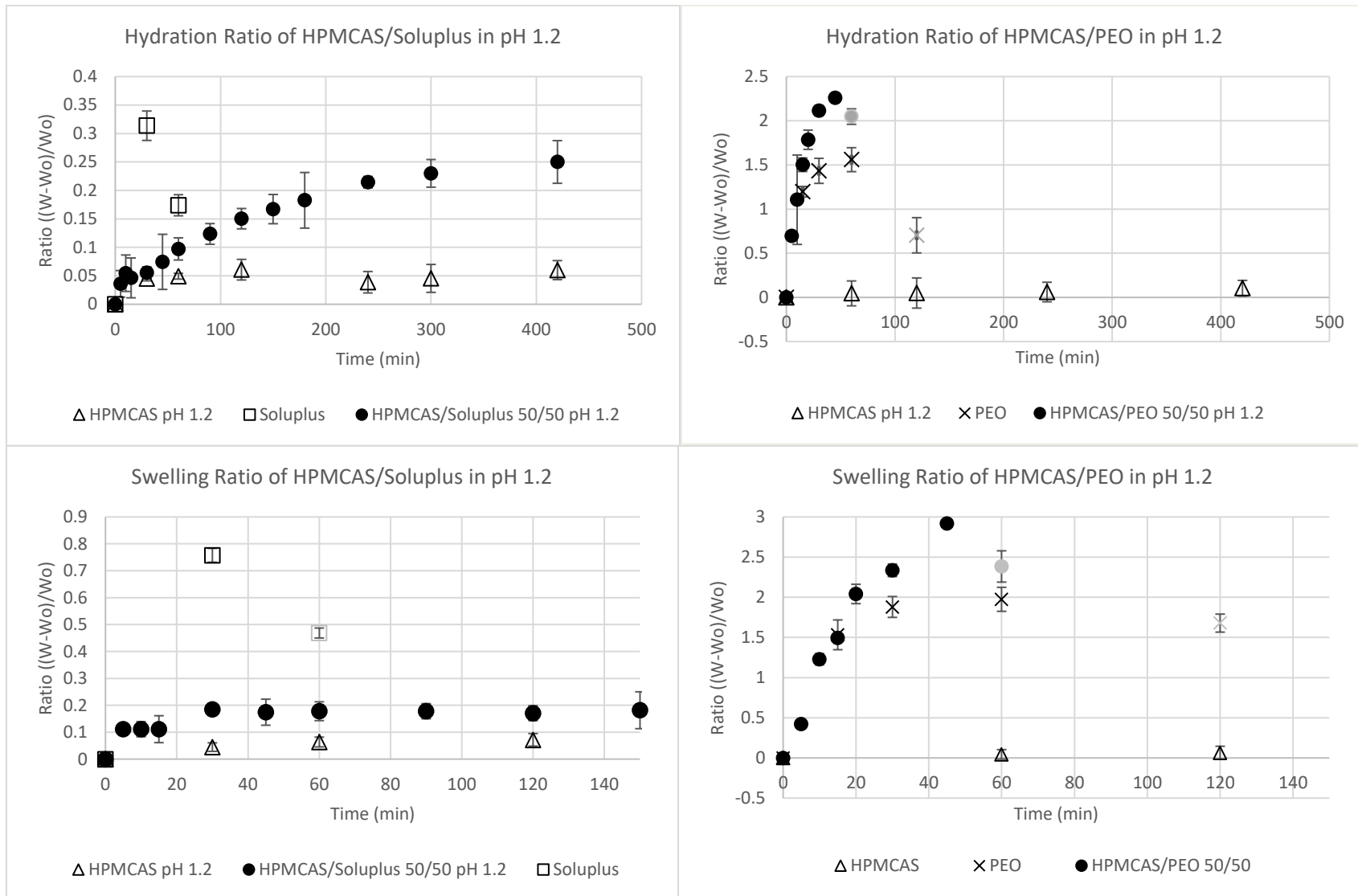


Figure 4-10: **Top left)** Hydration ratios of HPMCAS/Soluplus compared to pure polymers in pH 1.2. **Top right)** Hydration ratios of HPMCAS/PEO and pure polymer in pH 1.2. **Bottom left)** Swelling ratios of HPMCAS/Soluplus and pure polymer in pH 1.2. **Bottom right)** Swelling ratios of HPMCAS/PEO and pure polymer in pH 1.2. pH 6.8 exhibits negative hydration (erosion) for the blends and have been omitted here. The grey last data point for some polymers indicates the beginning of erosion. HPMCAS, being insoluble has data over longer duration but this has been omitted as it is constant at a ratio of zero.

Table 4-5: Hydration parameters fitted to the Vangernaud model in pH 1.2. (*) indicates the error here is omitted as it is too small.

Polymer blend	K_H	n_H	R^2
HPMCAS/Soluplus 50/50	0.01*	0.55 ± 0.07	0.99
HPMCAS/PEO 50/50	0.39 ± 0.09	0.48 ± 0.04	0.98

Table 4-6: swelling constant (S_k) and swelling mechanism for the blends in both pH. Cases of no swelling are denoted by -.

Polymer	pH 1.2			pH 6.8		
	K_S	n_S	R^2	K_S	n_S	R^2
HPMCAS	-	-	-	-	-	-
PEO	0.46 ± 0.11	0.42 ± 0.10	0.996	0.43 ± 0.18	0.49 ± 0.07	0.999
Soluplus	0.51 ± 0.08	0.05 ± 0.01	0.983	0.31 ± 0.01	0.05 ± 0.01	0.812
HPMCAS/Soluplus	0.09 ± 0.02	0.12 ± 0.03	0.947	-	-	-
HPMCAS/PEO	0.31 ± 0.16	0.61 ± 0.08	0.956	-	-	-

Table 4-7: The erosion constant of the polymers and blends in both pH and the goodness of fit

Polymer	E_K		R^2	
	pH 1.2	pH 6.8	pH 1.2	pH 6.8
HPMCAS	-	1.56 ± 0.34	0.97	0.99
PEO	1.91 ± 0.92	1.90 ± 0.23	0.99	0.99
Soluplus	1.21 ± 0.04	1.30 ± 0.10	0.95	0.91
HPMCAS/Soluplus	0.44 ± 0.08	3.51 ± 1.91	0.95	0.99
HPMCAS/PEO	2.95 ± 0.57	3.27 ± 1.81	0.97	0.96

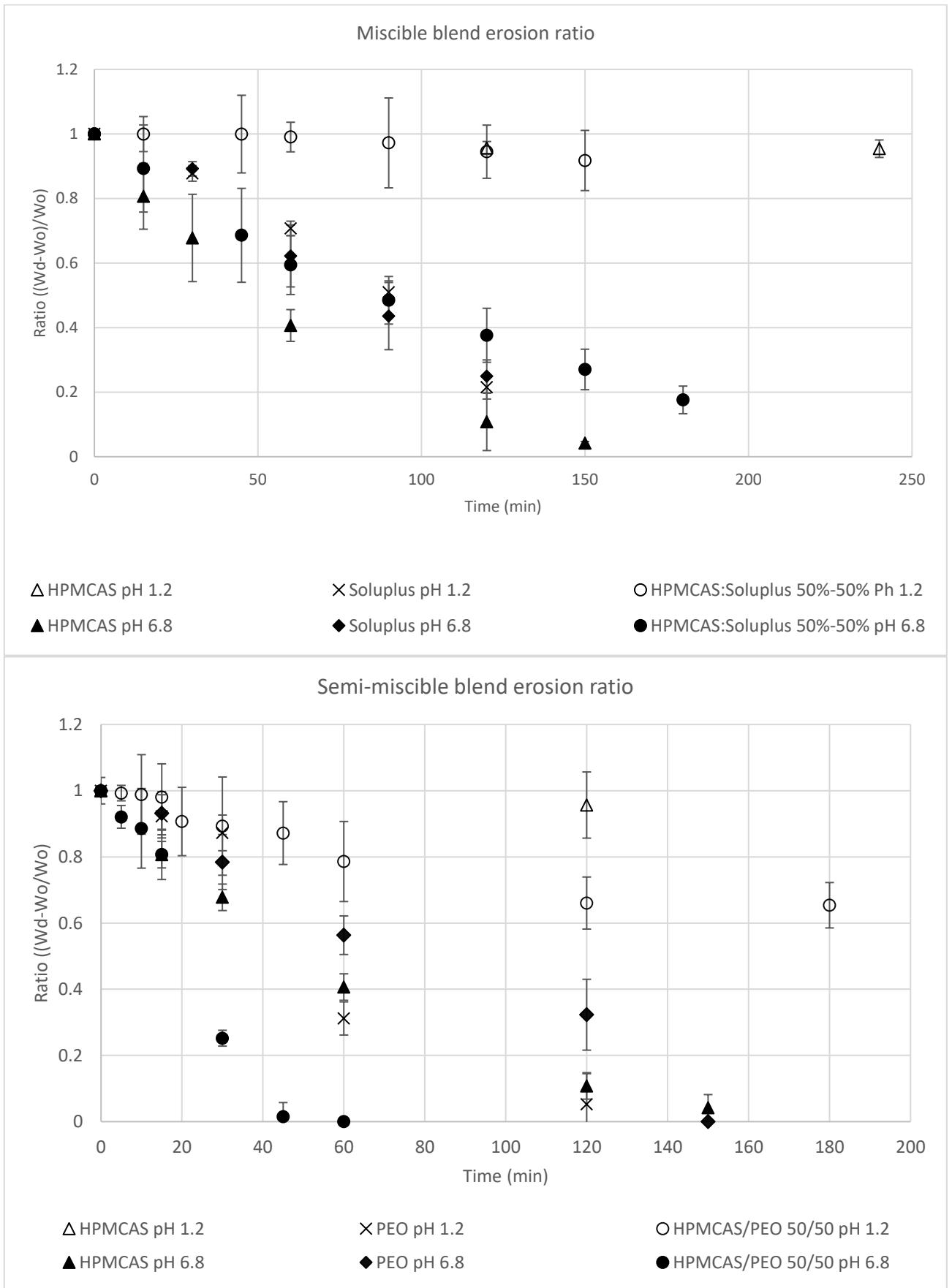


Figure 4-11: The erosion ratios for miscible HPMCAS/soluplus 50/50 in pH 1.2 (red) and pH 6.8 (blue) and the polymers individually.

4.3.7 Towards predicting polymer blend behaviour in aqueous media

One initial approach is to inspect if the prediction of polymer blend as an ideal solution yields accurate prediction. Prediction refers to applying the information deduced about the polymer to another blend in a pre-tested stage. Since the blends are 50/50% weight, the predicting profile would result from summing 50% of the weight data at each time point. The resultant for hydration and swelling of HPMCAS/Soluplus is presented in Figure 4-12. It can be seen that hydration and swelling ratios in pH 1.2 has been overpredicted by the calculated profile. This is due to the fact pure soluplus hydrates and swells more than the blend. The effect of an insoluble blend has affected this behaviour by more than half for the 50% of the blend. It is interesting to note that curve fitting of the calculated profile yielded the transport mechanism to be borderline Fickian and anomalous with a n_H of 0.55 ± 0.03 while experimental data curve fitting yielded n_H of 0.55 ± 0.07 , indicating the transport mechanism was not mis-deduced. The calculated profile is based on a prediction case while the experimental curve fitting is based on the actual data. Meanwhile, the hydration constant was lower for the experimental data. In pH 6.8, the model was able to better predict the blend behaviour kinetics but still produced inaccurate results. In the case of semi-miscible HPMCAS/PEO blend (Figure 4-13), both ratios were underpredicted by the calculated profile. This is because of pure PEO, which hydrates and swells less than the blend. Moreover, the prediction was erroneous. The fitting of calculated profile yielded anomalous transport mechanism ($n_H = 0.70 \pm 0.07$) which is significantly different from the experimental profile which yielded Fickian transport ($n_H = 0.48 \pm 0.04$). In pH 6.8, the calculated profile over predicted the blend behaviour for hydration and swelling. This is because pure PEO hydrates while pure HPMCAS erodes slowly. Comparing identical sampling times, the hydration ratio of PEO is higher than the negative hydration ratio (effectively erosion ratio) of HPMCAS. For example, a sampling time point of 15 minutes at pH 1.2, the PEO hydration ratio is 1.26 times while the HPMCAS hydration ratio is 0.86 times (Figure 4-4). The difference in PEO is 26% increase while the difference in HPMCAS is 14% decrease. The faster ratio increase due to PEO causes the cumulative ratio of calculated blend hydration ratio to be higher than the experimental ratio. Similar reasoning for swelling in pH 6.8 applies.

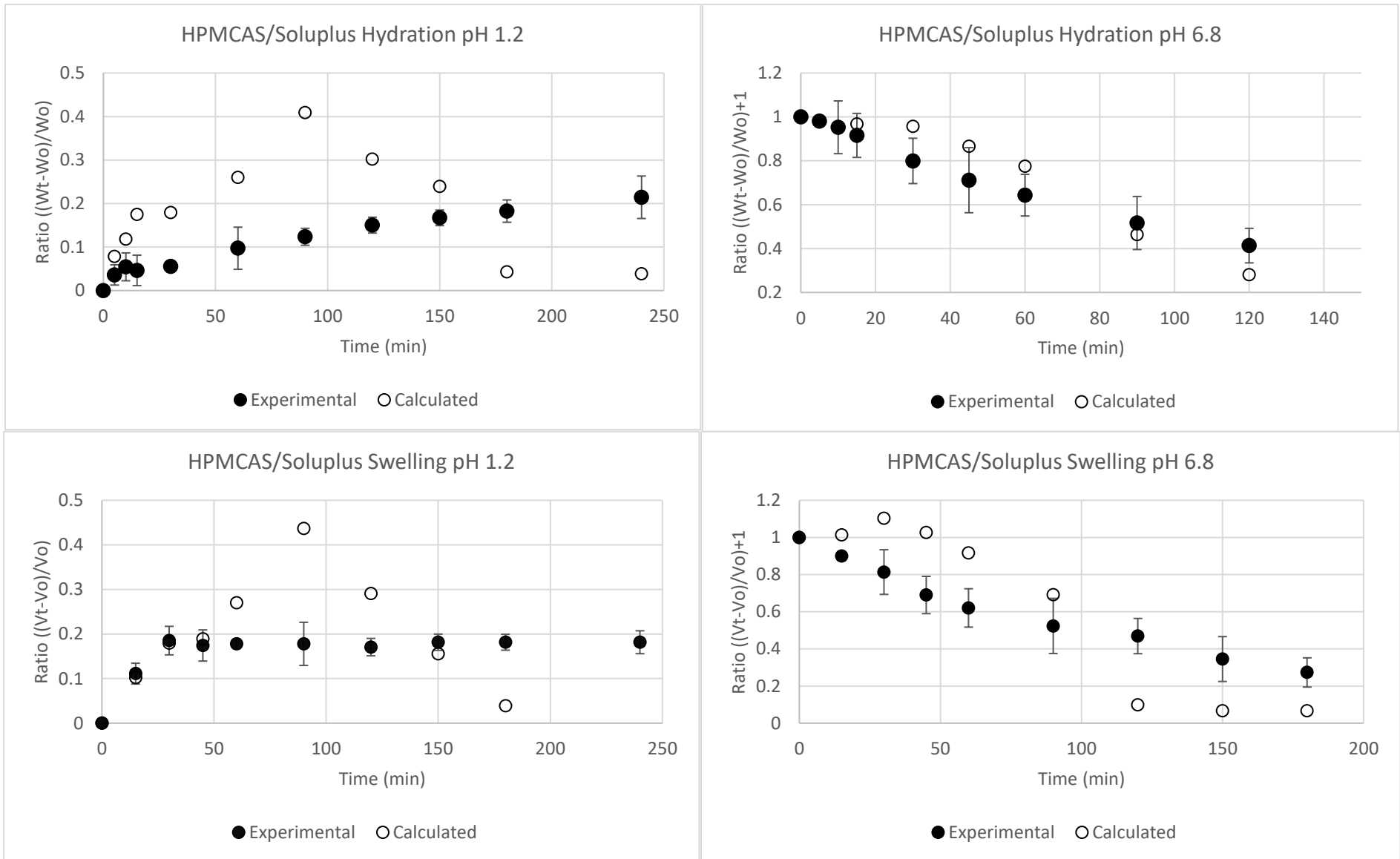


Figure 4-12: HPMCAS/Soluplus experimental vs calculated hydration and swelling ratios in pH 1.2 and 6.8

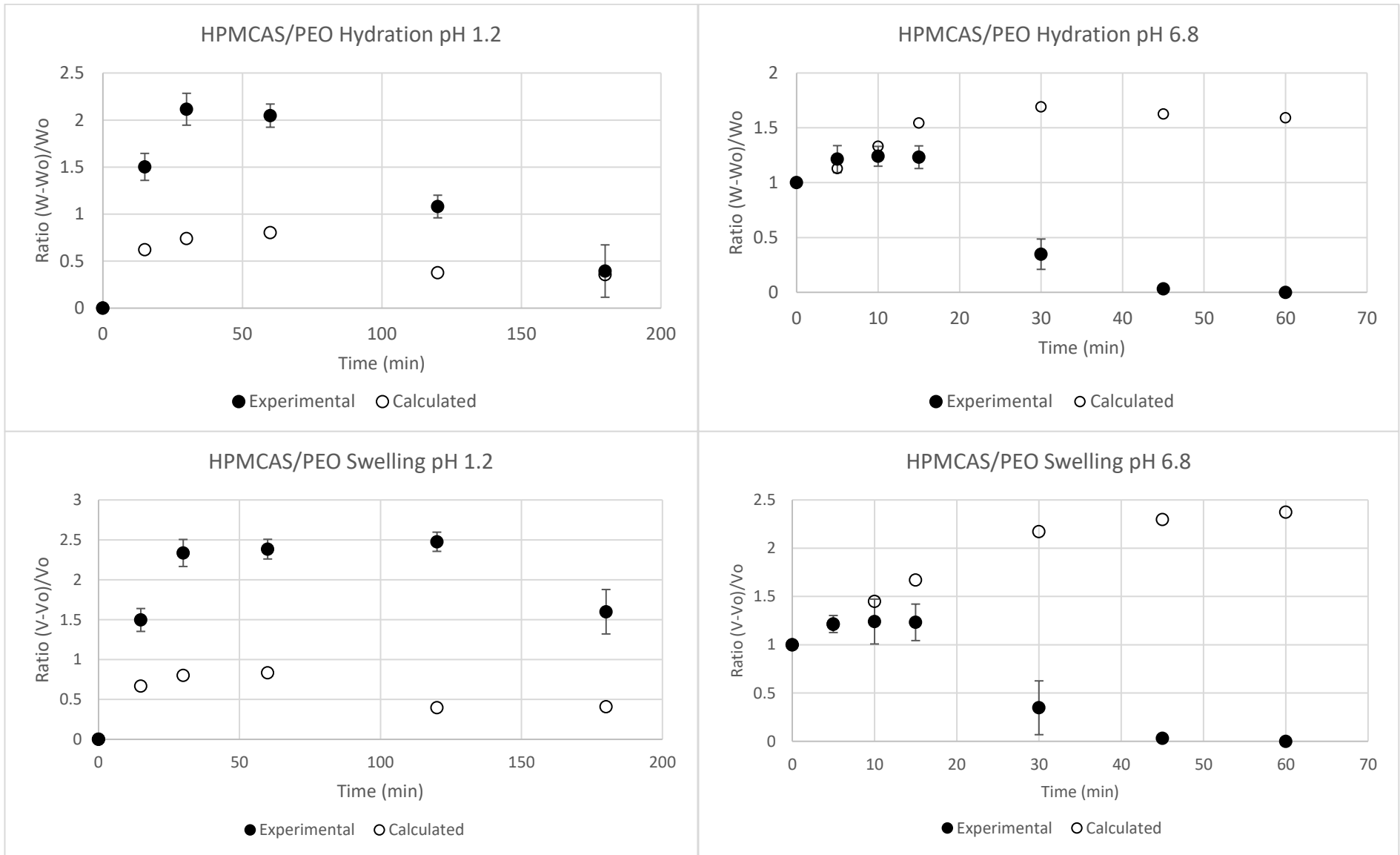


Figure 4-13: HPMCAS/PEO experimental vs calculated hydration and swelling ratios in pH 1.2 and 6.8

Comparing the erosion ratios of both blends in pH 1.2 yields similarly inaccurate blend profile prediction as shown in Figure 4-14. The insolubility of HPMCAS in pH 1.2 slows erosion of the blend causing lower than observed values. However, the prediction was more accurate for pH 6.8 but still significantly different for many of the sampled time points. A trend seems to emerge when investigating the constituting polymers and their respective blends. The ideal polymer mixture seems to hold in certain circumstances. If the polymers both exhibit the same properties (i.e.: both swell or both erode), then the ideal polymer mixture scenario appears to be able to predict with better accuracy compared to when the properties of the polymers differ, shown in Table 4-8. When they differ, the application of ideal polymer mixture calculation is most likely to be invalid. For example, in pH 1.2, HPMCAS does not erode (✖) while PEO erodes (✓) causing the resultant blend calculation to be invalid (✖). The calculations hold valid in pH 6.8; when HPMCAS erodes (✓) as well as PEO (✓) erode resulting in the blend to be accurately predicted (✓). Ideal solutions form from the random mixing of molecules with the same size and shape wherein the intermolecular forces between pairs of like segments and unlike segments are all equivalent (407). The molar volume of HPMCAS is 14,008 cm³/mol (229, 408) while PEO is 3,571,429 cm³/mol (409), and soluplus is 109,225 cm³/mol (409). Since the molecule sizes are not the same, the agreement to ideal solution laws is surprising.

Table 4-8: Blend and polymer kinetics. The (✖) indicates no while the (✓) indicates yes for the category of the row.

pH 1.2	Soluplus	HPMCAS	PEO	HPMCAS/Soluplus	HPMCAS/PEO
Hydration (positive ratio)	✓	✖	✓	✖	✖
Swell	✓	✖	✓	✖	✖
Erosion (negative ratio)	✓	✖	✓	✖	✖
pH 6.8	Soluplus	HPMCAS	PEO	HPMCAS/Soluplus	HPMCAS/PEO
Hydration (positive ratio)	✓	✖	✓	✖	✖
Swell	✓	✖	✓	✖	✖
Erosion (negative ratio)	✓	✓	✓	✓	✓

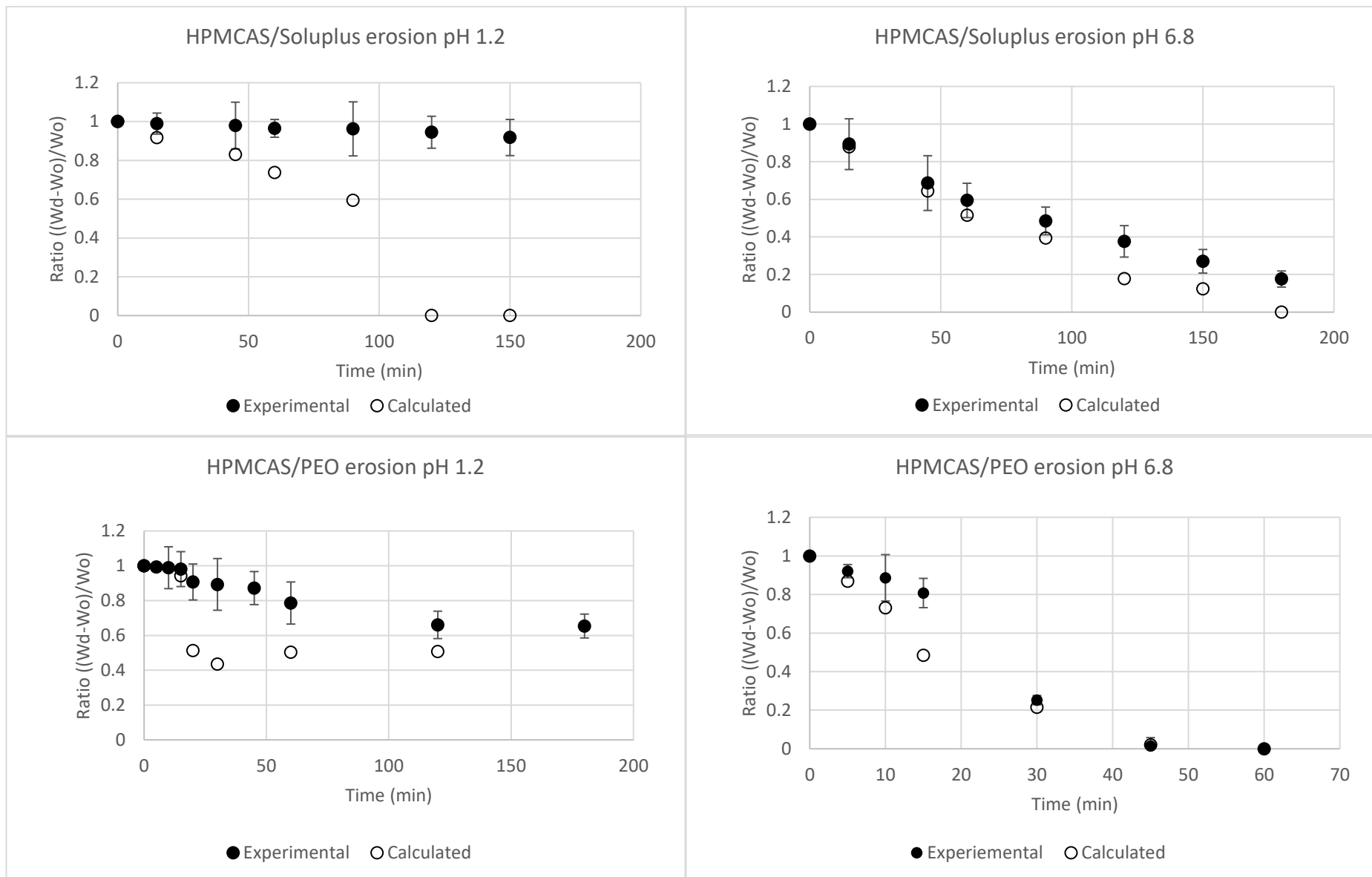


Figure 4-14: Experimental and calculated erosion ratios of HPMCAS/Soluplus and HPMCAS/PEO in pH 1.2 and pH 6.8

For more accurate prediction than the ideal polymer mixture, other approaches can be applied. The critical aspect of blends is the miscibility of the constituents leading to the stability of the system. The stability of polymer mixtures can be predicted from knowledge of the solubility parameters and hydrogen-bonding tendencies of the components. However, these predictions are not always very accurate as the model is oversimplified. More sophisticated solution theories do not perform any better prediction (410). They contain parameters that can only be determined by analysis of particular mixtures, and it is not possible to characterize individual components a priori. Numerous attempts have been made to improve the predictive ability of the solubility parameter method. These generally proceed on the recognition that intermolecular forces can involve dispersion, dipole-dipole, dipole-induced dipole, or acid-base interactions. The most promising has been proposed by Hansen and often known as the Hansen solubility parameters which relies on contributions due to dispersion forces, polar forces, and hydrogen-bonding (410).

Other approaches have dealt with determining the miscibility of polymer blends wherein the analysis is depended on the Random Phase Approximation (RPA) theory and the classical Flory–Huggins (F-H) theory (411). In the framework of the F-H theory, the interaction parameter (χ) is dependent on temperature, pressure, composition. The polymer kinetics will differ with different composition. The χ can give the energy difference of the molecules of the polymer and the solvent (412). The smaller the value of χ , the greater the rate at which the free energy of the solution decreases with the addition of solvent. Consequently, liquids with the smallest χ 's are usually the best solvents for a polymer. Negative values of χ often indicate strong polar attractions between polymer and solvent, thus increasing miscibility (413).

4.3.8 Categorization summary

In this section, a table was constructed enlisting the parameters measured for the polymer and blends. The table has been split into three tables. The first, Table 4-9 represents the solubility and swellability of the polymers. The second, Table 4-10, represents the time points at which the maximum hydration ratios ($t_{H_{max}}$) and maximum hydration ratios ($t_{S_{max}}$) were attained. The third, Table 4-11, shows the hydration, swelling, and erosion parametrization of the polymer and blends done in this chapter.

Table 4-9: Polymer swelling and solubility in pH 1.2 and pH 6.8 given by yes (Y) or no (N).

Polymer	Soluble (Y/N)		Swell (Y/N)	
	pH 1.2	pH 6.8	pH 1.2	pH 6.8
HPMCAS	N	N	N	N
PEO	Y	Y	Y	Y
Zein	N	Y	Y	Y
Xanthan Gum	Y	Y	Y	Y
PCL	Y	N	N	N
Eudragit	N	N	N	N
PVPVA	Y	N	N	N
PVA	Y	N	N	N
Soluplus	Y	Y	Y	Y
HPMCAS/PEO (50/50)	Y	Y	Y	N
HPMCAS/Soluplus (50/50)	Y	Y	Y	N

Table 4-10: The peak hydration and swelling times of the polymer and blend in pH 1.2 and pH 6.8.

Polymer	t H _{max}		t S _{max}	
	pH 1.2	pH 6.8	pH 1.2	pH 6.8
HPMCAS	-	-	-	-
PEO	60	60	60	60
Zein	2880	2880	2880	2880
Xanthan Gum	30	30	30	30
PCL	-	-	-	-
Eudragit	-	-	-	-
PVPVA	-	-	-	-
PVA	10	10	-	-
Soluplus	30	30	30	30
HPMCAS/PEO (50/50)	45	-	45	-
HPMCAS/Soluplus (50/50)	420	-	30	-

Table 4-11: Polymer kinetics dataset of hydration, swelling, and erosion in pH 1.2 and pH 6.8

Polymer	Hydration constant		Transport mechanism		Swell constant		Swelling Index		Erosion constant	
	pH 1.2	pH 6.8	pH 1.2	pH 6.8	pH 1.2	pH 6.8	pH 1.2	pH 6.8	pH 1.2	pH 6.8
HPMCAS	-	-	-	-	-	-	-	-	-	1.56 ±0.34
PEO	0.73 ±0.12	0.66 ±0.12	0.18 ±0.02	0.23 ±0.05	0.46 ±0.11	0.43 ±0.18	0.42 ±0.10	0.49 ±0.07	1.91 ±0.92	1.90 ±0.23
Zein	0.03 ±0.01	0.02 ±0.01	0.37 ±0.09	0.37 ±0.02	0.04 ±0.01	0.09 ±0.01	0.37 ±0.08	0.18 ±0.03	-	-
Xanthan Gum	1.31 ±0.70	2.51± 0.83	0.52 ±0.01	0.27 ±0.04	1.54 ±0.13	1.15 ±0.27	0.74 ±0.03	0.68 ±0.08	2.77 ±0.03	3.07 ±0.09
PCL	-	-	-	-	-	-	-	-	-	-
Eudragit	-	-	-	-	-	-	-	-	-	-
PVPVA	-	-	-	-	19.15 ± 3.23	-	-	-	19.15 ±0.10	17.34 ±0.12
PVA	0.04 ±0.01	-	0.61 ±0.21	-	0.66 ±	-	-	-	0.66 ±0.02	0.83 ±0.02
Soluplus	-	-	-	-	0.51 ±0.08	0.31 ±0.01	0.05 ±0.01	0.05 ±0.01	1.21 ±0.04	1.30 ±0.10
HPMCAS/PEO (50/50)	0.39 ±0.09	-	0.48 ±0.04	-	0.31 ±0.16	-	0.12 ±0.03	-	2.95 ±0.57	3.27 ±1.81
HPMCAS/Soluplus (50/50)	0.01	-	0.55 ±0.07	-	0.09 ±0.02	-	0.61 ±0.08	-	0.44 ±0.08	3.51 ±1.91

4.4 Limitations of the study

In this chapter, only a fixed polymer ratio was investigated. Earlier studies confirm that polymer behaviour kinetics differ with differing polymer blend ratios. Since a generic set of rules could not be gathered by adding the individual constituting polymer behaviours, except where the polymer behaviour kinetics are identical, a database would need to include a certain number of ratios that may be used widely (thus saving from investigating every varying degree of composition) such as HPMCAS/soluplus 10/90, 20/80, 30/70, 70/30, 50/50, 25/75, 75/25, 10/90, and other polymer combinations.

Further, molecular level interactions are not investigated in this work but proposed such as the Hansen solubility parameter and Flory Huggins theory. Based on these theories, more differences observed among the blends may be more accurately described such as the hydrated or swelling ratios observed which differ from the calculated profile of the blends. It may also describe the inter-pH differences observed between pure polymers such as hydration ratio of 9 times for Xanthan gum in pH 1.2 vs a ratio of 6.5 times in pH 6.8.

4.5 Conclusion

In this chapter, the factors affecting the kinetics of the polymer behaviour were studied by investigating the hydration, swelling and erosion ratios in the two buffers of pH 1.2 and pH 6.8. The use of Vangernaud model was used to fit the hydration ratios while a power law empirical model was used for fitting the swelling ratios. Both were chosen over simple fits as they encompass the initial to plateau better shown by R^2 values. The erosion ratios exhibited inverse first order and were fitted to first order decaying models.

In addition, an identical approach was used for the blend. The blends in some cases exhibited complex multiphase profiles which were time dependant of the composite's polymer properties such as maximum hydration time and/or maximum swell. At these maximum points, the dominant mechanism would change for the blend. The application of ideal polymer mixtures accounting for 50% weight of the constituting polymer to create the blend profiles yielded only reasonably good agreement when both effects were common in the constituting polymers such as both eroding. This has rendered the deduction of a generic

equation unattainable for blends which do not exhibit commonly shared behaviour in the media such as one constituent being a swelling polymer and the other a non-swelling polymer or likewise one hydrating polymer and the other a non-hydrating polymer.

Lastly, a dataset, with the gathered data of polymers, was constructed to help in modelling the behaviour of the drug loaded formulation using the polymer/blend bringing one step closer to being able to achieve a desired drug release profile and choosing an appropriate formulation.

Chapter 5: Categorizing the effect of drug types on polymer behaviour

5.1 Introduction

In the previous chapter, the factors affecting the kinetics of the behaviour of pharmaceutical polymers (hydration, swelling and erosion) used in 3D printing were investigated. The cornerstone of polymer choice in oral dosages is to attain drug release in a desired pattern in order to achieve the optimal absorption and therapeutic outcome (414, 415). There have been several drugs reported being made solid dispersions using FDM 3D printing such as acetaminophen (49), indomethacin (368), warfarin (378), carvedilol (375), theophylline (47), puerarin (416), gentamicin sulfate (25), felodipine (52), haloperidol (417), ciprofloxacin hydrochloride (418), domperidone (377), prednisolone (419), dipyridamole (53). As reported widely in the solid dispersions research, the physicochemical properties of the drug and the polymer-drug interactions can have profound impacts on the properties of the formed solid dispersions (420, 421). Therefore, it is important to investigate systematically how different types of drugs can interact with polymers to influence the polymer behaviour and drug release.

In this chapter, the drug release behaviour of the solid dispersions formed by three model polymers and three model drugs were carried out. The model drugs were chosen to present positively charged, negatively charged or neutral in pH 1.2 or 6.8. The data generated were used to build a dataset that was later used in building the classification approach to facilitate the choosing the appropriate polymer or combination of polymers for a given drug.

5.2 Materials and methods

The polymers used in this chapter were purified zein, Hypromellose acetate succinate (HPMCAS) AS-LF, and Poly-(Ethylene Oxide) (PEO) WSR N10 LEO and their physicochemical properties are described in section 2.2.4 to 2.2.6 of chapter 2. The three drugs used were lidocaine, ibuprofen, and paracetamol and their physicochemical properties are described in section 2.2.1 to 2.2.3 of chapter 2.

5.2.1 Preparation of filaments

The procedure mentioned in section 4.2.1 of preparing filament using HME technique was used. However, in this case, the addition of drug loadings of 10% and 30% by weight in two different batches were prepared. The extruded filament was then cut into 2cm pieces for *in vitro* studies.

5.2.2 Measurement of factors

The measured factors of the formulation were hydration, swelling, and erosion in pH 1.2 and pH 6.8. The methods of measurement were as per the outlined procedure of hydration, swelling, and erosion in section 4.2.2 of chapter 4. An additional procedure was to measure the drug release of the formulations. The drug release was measured by UV spectroscopy at wavelengths of 220nm, 264nm, and 243nm for lidocaine, ibuprofen, and paracetamol respectively using the procedures described in section 2.4.4 of chapter 2.

5.2.3 Choice of polymers and drugs

The choice of polymers here was to investigate the difference between a polysaccharide (HPMCAS), a protein (zein) and superabsorbent polymer (PEO), in the presence of a positively charged, a negatively charged, and a neutral drug. Most molecules contain some specific functional groups likely to lose or gain proton(s) under specific circumstances. Each equilibrium between the protonated and deprotonated forms of the molecule can be described with a constant value called K_a . The log of this value is known as pK_a . The charge of the drug can be deduced from the species distribution diagram of the drug in the buffer (422). The species distribution diagram was calculated using MarvinSketch software (423). The pK_a plugin calculates the pK_a values of the molecule based on its partial charged species distribution. The reported pK_a values for lidocaine, ibuprofen, and paracetamol is 7.8, 4.5, and 9.5 respectively (207, 210, 424). The percentages of charged species are shown in Table 5-1. The charged form (column 2) indicates the charge that is possessed by the percentage fraction in pH 1.2 (column 4) and pH 6.8 (column 6). For example, in pH 6.8, lidocaine is 90.01% positively charged while ibuprofen is 98.89% negatively charged. It is hypothesized that lidocaine, which is ionic in both pH, is soluble and has a higher osmolarity than neutral drug and will cause higher hydration, swelling, and erosion in the formulation compared to placebo. Two sets of drug loading with each polymer were chosen for the studies: 10% and 30% drug loading. It is hypothesized that higher ionic

drug loading should cause higher and faster hydration, swelling, and erosion due to the fact higher quantity should amplify the osmolarity compared to the 10% drug loaded formulations.

Table 5-1: The % of charged species of the drugs in the buffers. The charged form of the drug in the buffer is given by column 3.

	pK _a	Charged form	Neutral (%)	Charged (%)	Neutral (%)	Charged (%)
Drug			pH 1.2		pH 6.8	
<i>Lidocaine</i>	7.9	+	0	100	9.99	90.01
<i>Ibuprofen</i>	4.4	-	99.98	0.02	1.11	98.89
<i>Paracetamol</i>	9.5	-	100	0	99.78	1.22

5.3 Results and Discussion

The characterisation of the formulations are presented in the appendix. The presentation of results is divided into eight sections. Prior to all the sections, the results of polymer behaviours and drug release is presented for all the formulations. HPMCAS formulations results are presented in Figure 5-1 for HPMCAS/lidocaine, in Figure 5-2 for HPMCAS/ibuprofen, and in Figure 5-3 for HPMCAS/ paracetamol. Zein formulation results are presented in Figure 5-4 for zein/lidocaine, in Figure 5-5 for zein/ibuprofen, and in Figure 5-6 for zein/paracetamol. PEO formulations results are presented in Figure 5-7 for PEO/lidocaine, in Figure 5-8 for PEO/ibuprofen, and in Figure 5-9 for PEO/paracetamol. In each section, the effect on the individual polymer with regards to hydration, swelling, and erosion with the different drugs is presented. The first section (section 5.3.1) presents drug release cases. The first case, in no particular order, is drug release driven only by diffusion. In this case, the diffusion is due to hydration. The second case is the diffusion is accompanied by simultaneous swelling or erosion. In this case, there are two polymer behaviour exhibited. The third case is when all three of the behaviour occur. Thereafter, the individual polymer behaviour will be investigated to understand the different cases of drug release from formulation. Three cases of polymer behaviour arise for drug release. The second section (section 5.3.2) report effect of charge state on polymer hydration. The third section (section 5.3.3) presents the effect of drug loading on hydration. The fourth section (section 5.3.4) presents the effect of charge state on polymer swelling, while the fifth section (section 5.3.5) presents the effect of drug loading on swelling. The sixth section (section 5.3.6) presents the effect of charge state on polymer erosion and the last section (section 5.3.7) summarizes the effect of charge state to overall polymer behaviour.

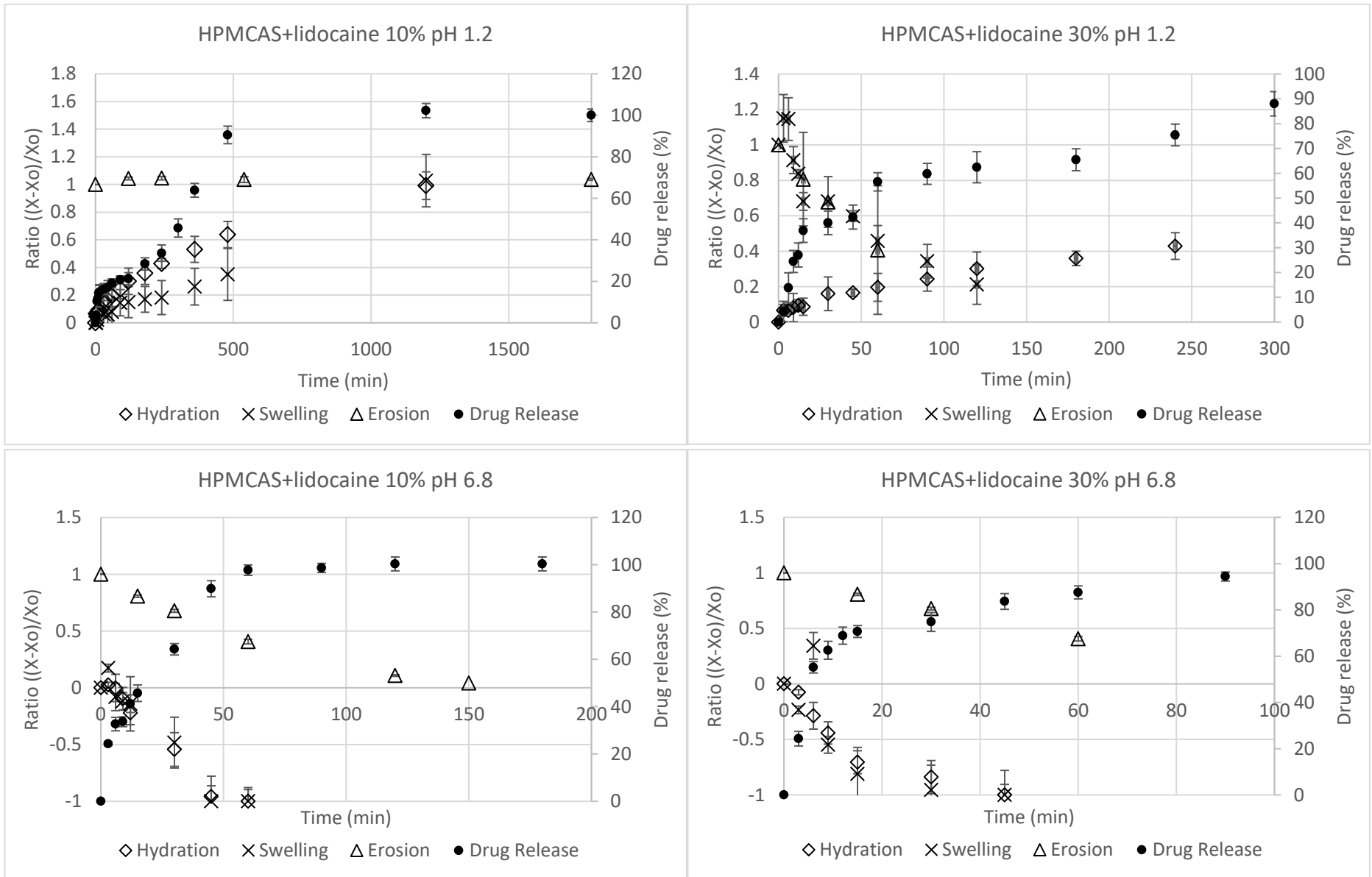


Figure 5-1: Drug release and HPMCAS behaviour for lidocaine formulations. The generic ratio $((X-X_o)/X_o)$ has been presented, which can be substituted by wet mass in the case of hydration, volume in the case of swelling, and dry mass in the case of erosion. the drug release is plotted on the secondary y-axis. Erosion is always plotted in inverse increasing from an initial ratio of 1.

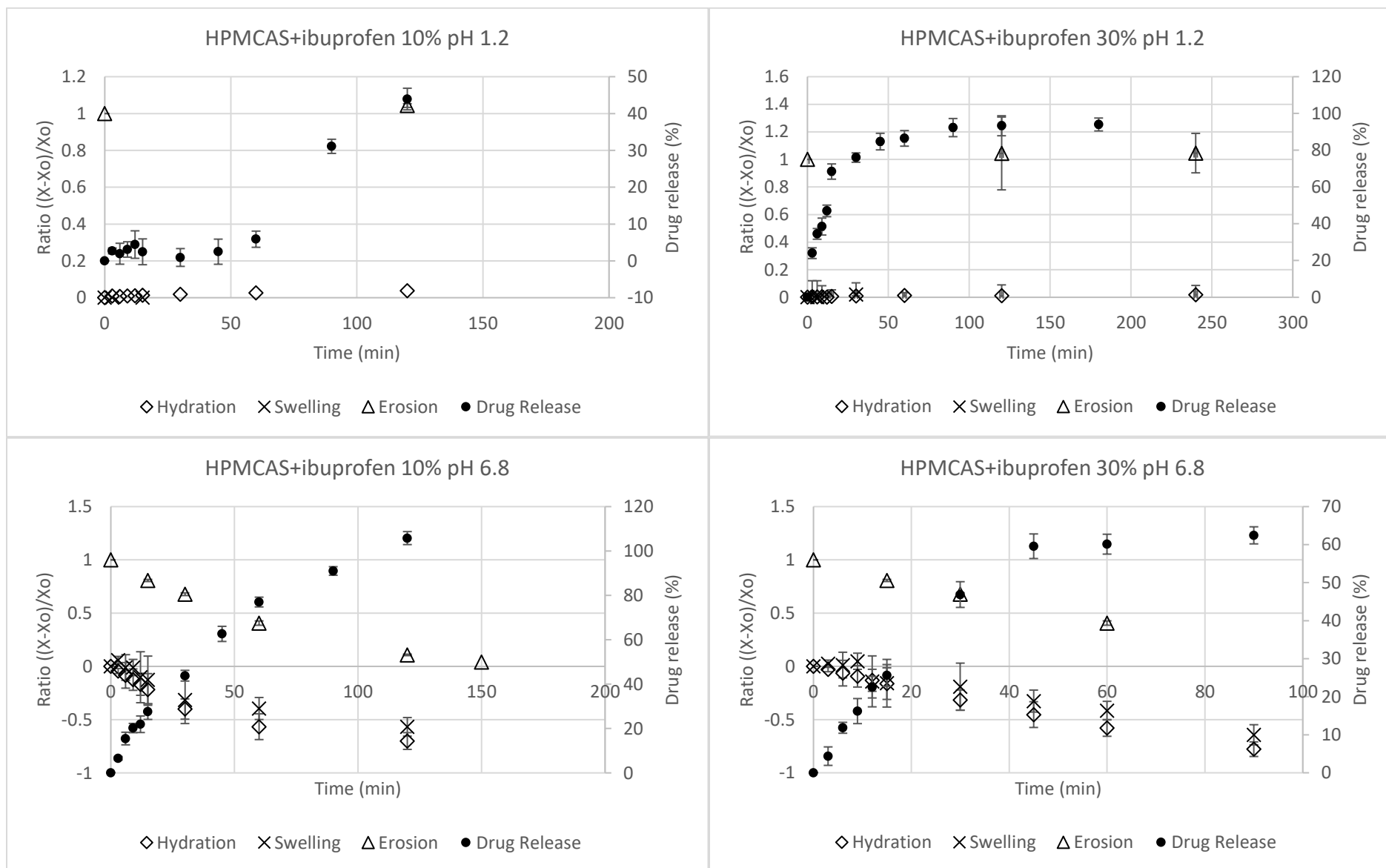


Figure 5-2: Drug release and HPMCAS behaviour for ibuprofen formulations. The generic ratio $((X-X_o)/X_o)$ has been presented, which can be substituted by wet mass in the case of hydration, volume in the case of swelling, and dry mass in the case of erosion. the drug release is plotted on the secondary y-axis. Erosion is always plotted in inverse increasing from an initial ratio of 1.

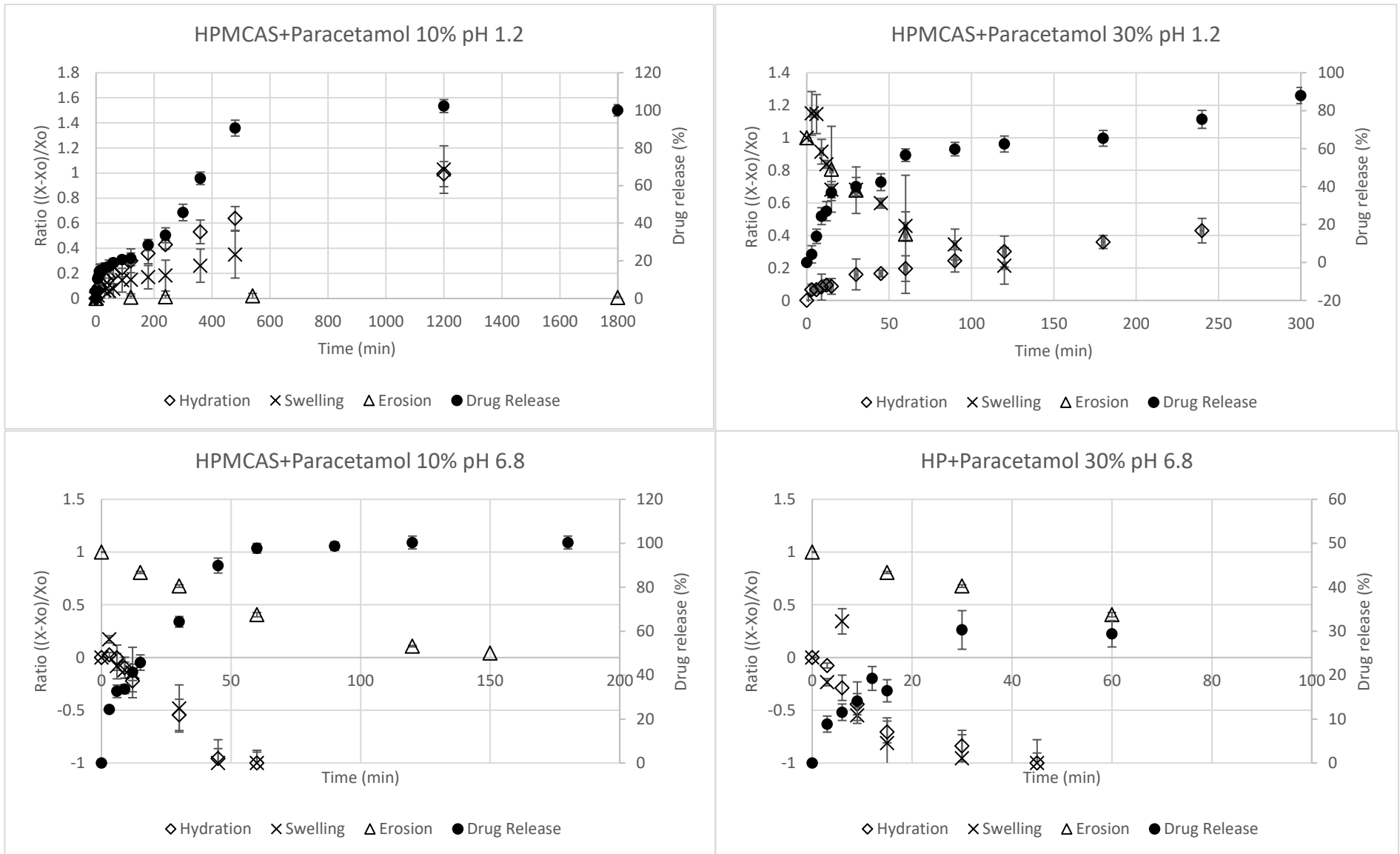


Figure 5-3: Drug release and HPMCAS behaviour for paracetamol formulations. The generic ratio $((X-X_o)/X_o)$ has been presented, which can be substituted by wet mass in the case of hydration, volume in the case of swelling, and dry mass in the case of erosion. the drug release is plotted on the secondary y-axis. Erosion is always plotted in inverse increasing from an initial ratio of 1.

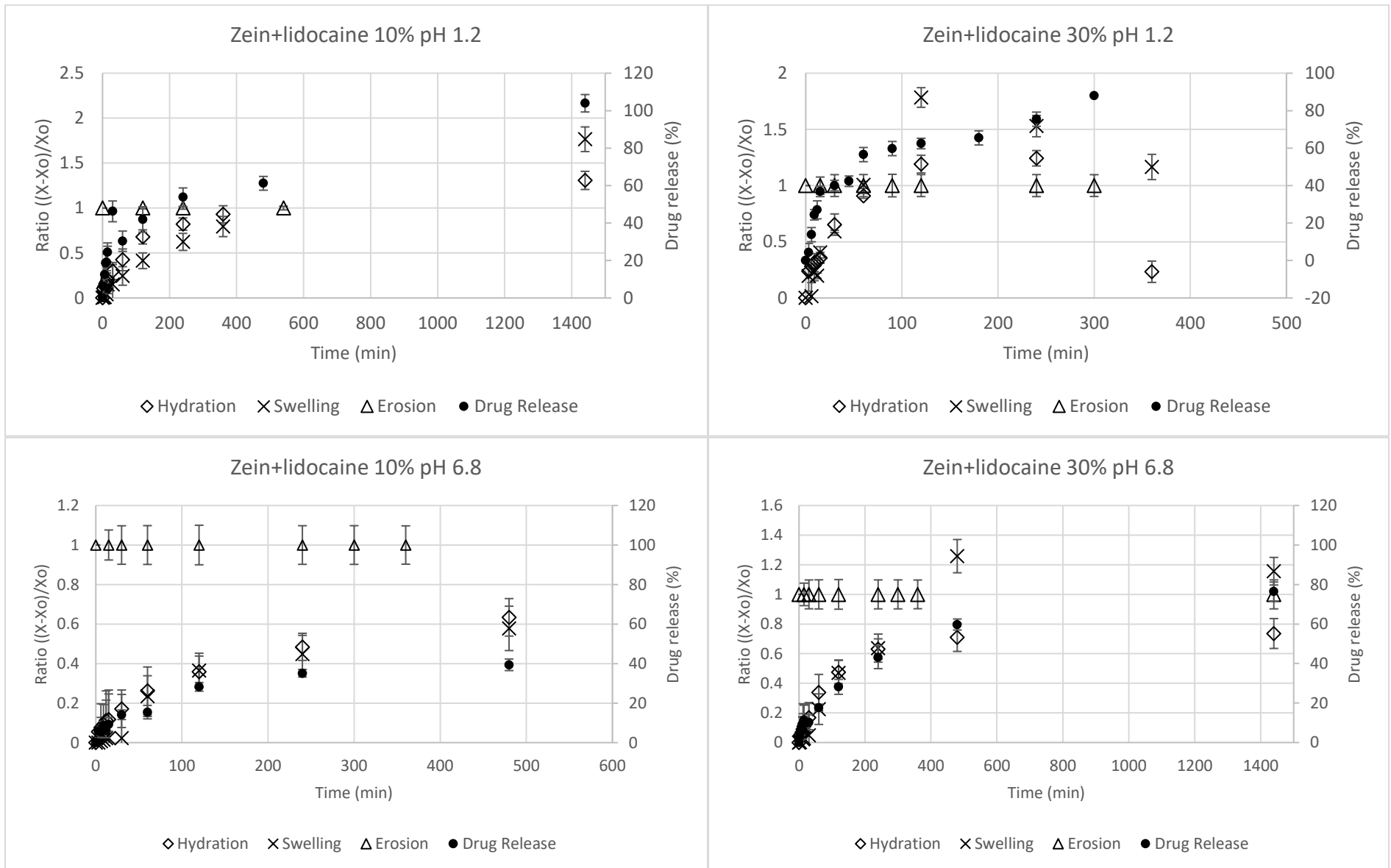


Figure 5-4: Drug release and zein behaviour for lidocaine formulations. The generic ratio $((X-X_o)/X_o)$ has been presented, which can be substituted by wet mass in the case of hydration, volume in the case of swelling, and dry mass in the case of erosion. the drug release is plotted on the secondary y-axis. Erosion is always plotted in inverse increasing from an initial ratio of 1.

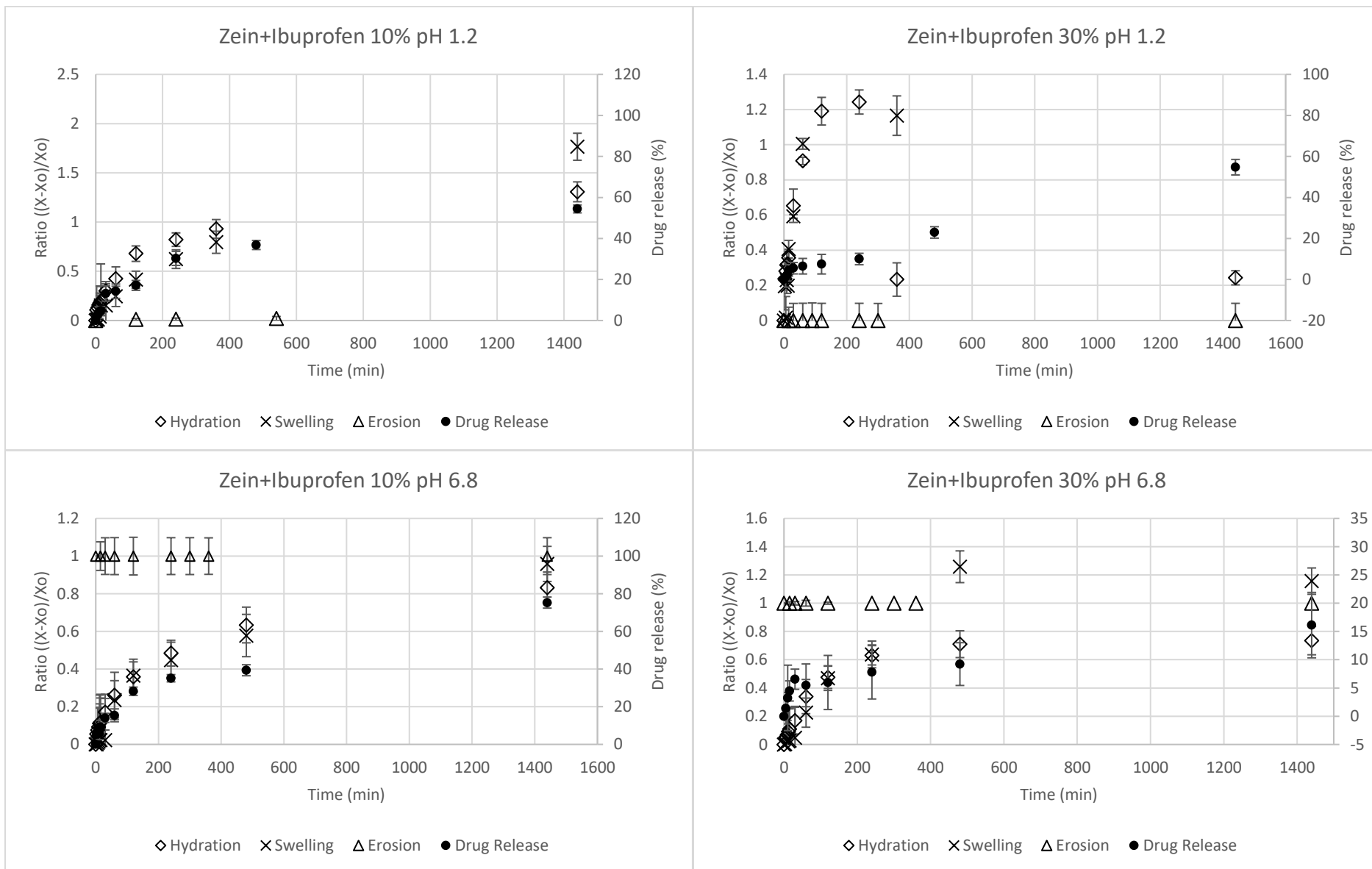


Figure 5-5: Drug release and zein behaviour for ibuprofen formulations. The generic ratio $((X-X_o)/X_o)$ has been presented, which can be substituted by wet mass in the case of hydration, volume in the case of swelling, and dry mass in the case of erosion. the drug release is plotted on the secondary y-axis. Erosion is always plotted in inverse increasing from an initial ratio of 1.

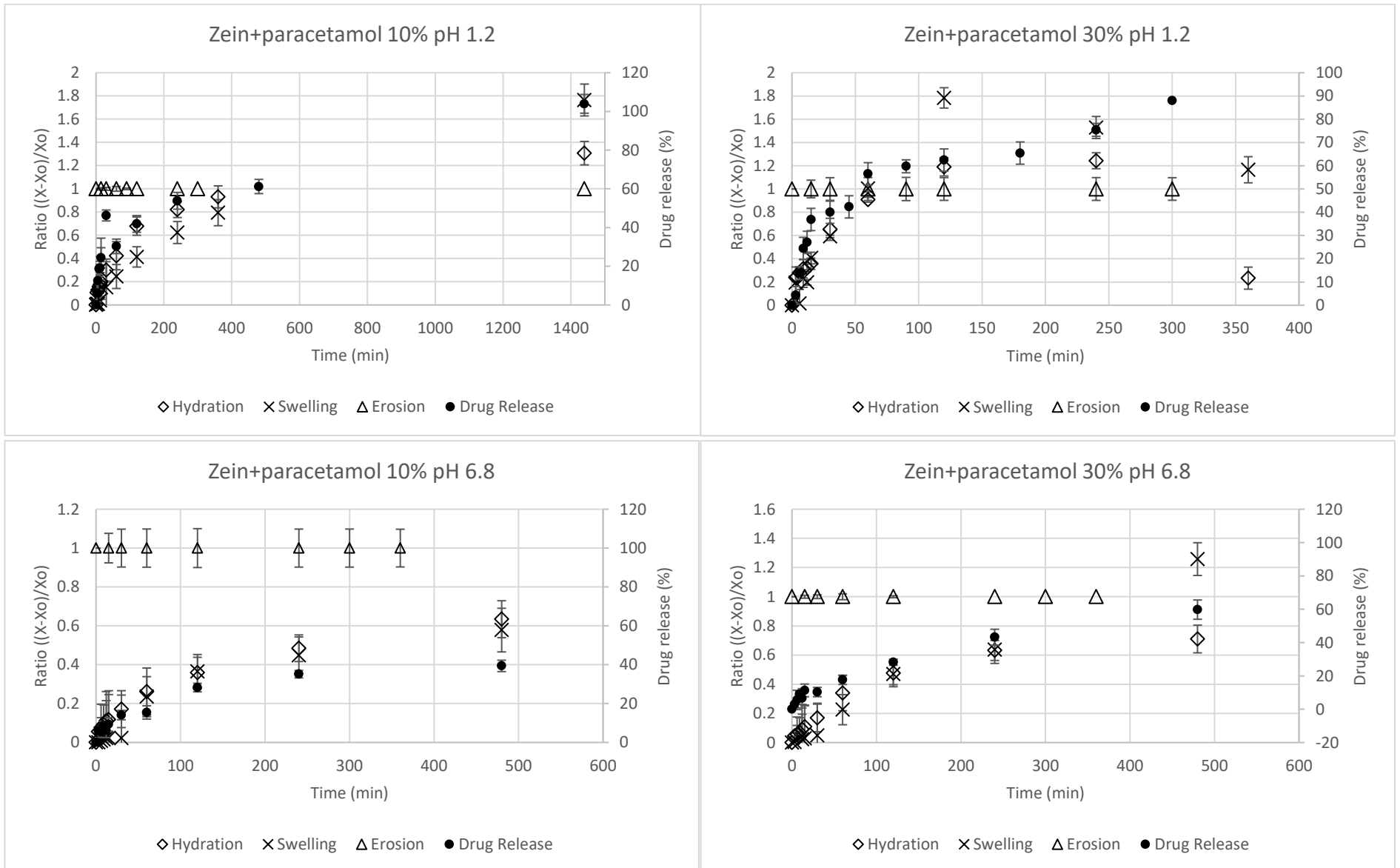


Figure 5-6: Drug release and zein behaviour for paracetamol formulations. The generic ratio $((X-X_o)/X_o)$ has been presented, which can be substituted by wet mass in the case of hydration, volume in the case of swelling, and dry mass in the case of erosion. the drug release is plotted on the secondary y-axis. Erosion is always plotted in inverse increasing from an initial ratio of 1.

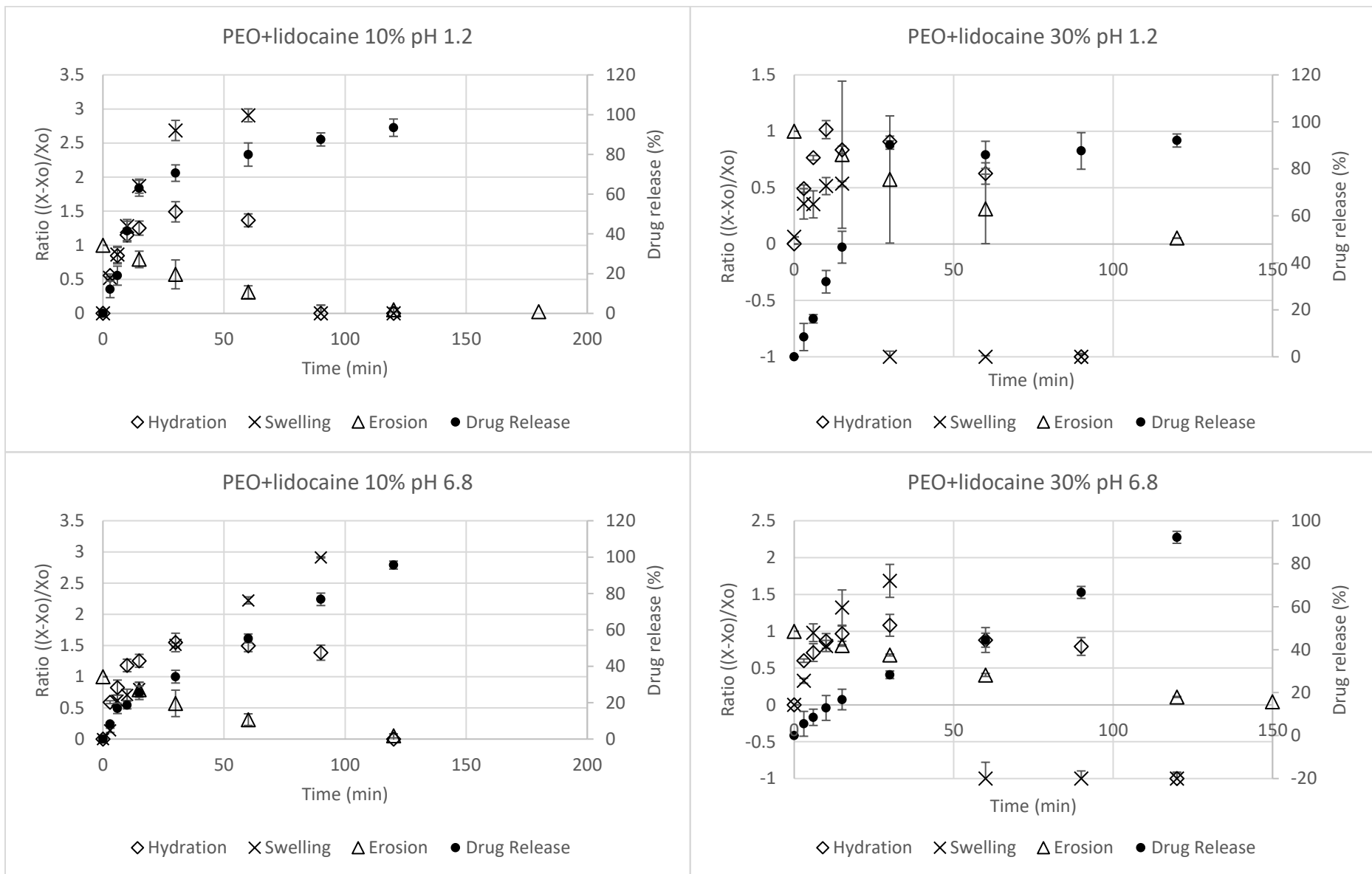


Figure 5-7: Drug release and PEO behaviour for lidocaine formulations. The generic ratio $((X-X_o)/X_o)$ has been presented, which can be substituted by wet mass in the case of hydration, volume in the case of swelling, and dry mass in the case of erosion. the drug release is plotted on the secondary y-axis. Erosion is always plotted in inverse increasing from an initial ratio of 1.

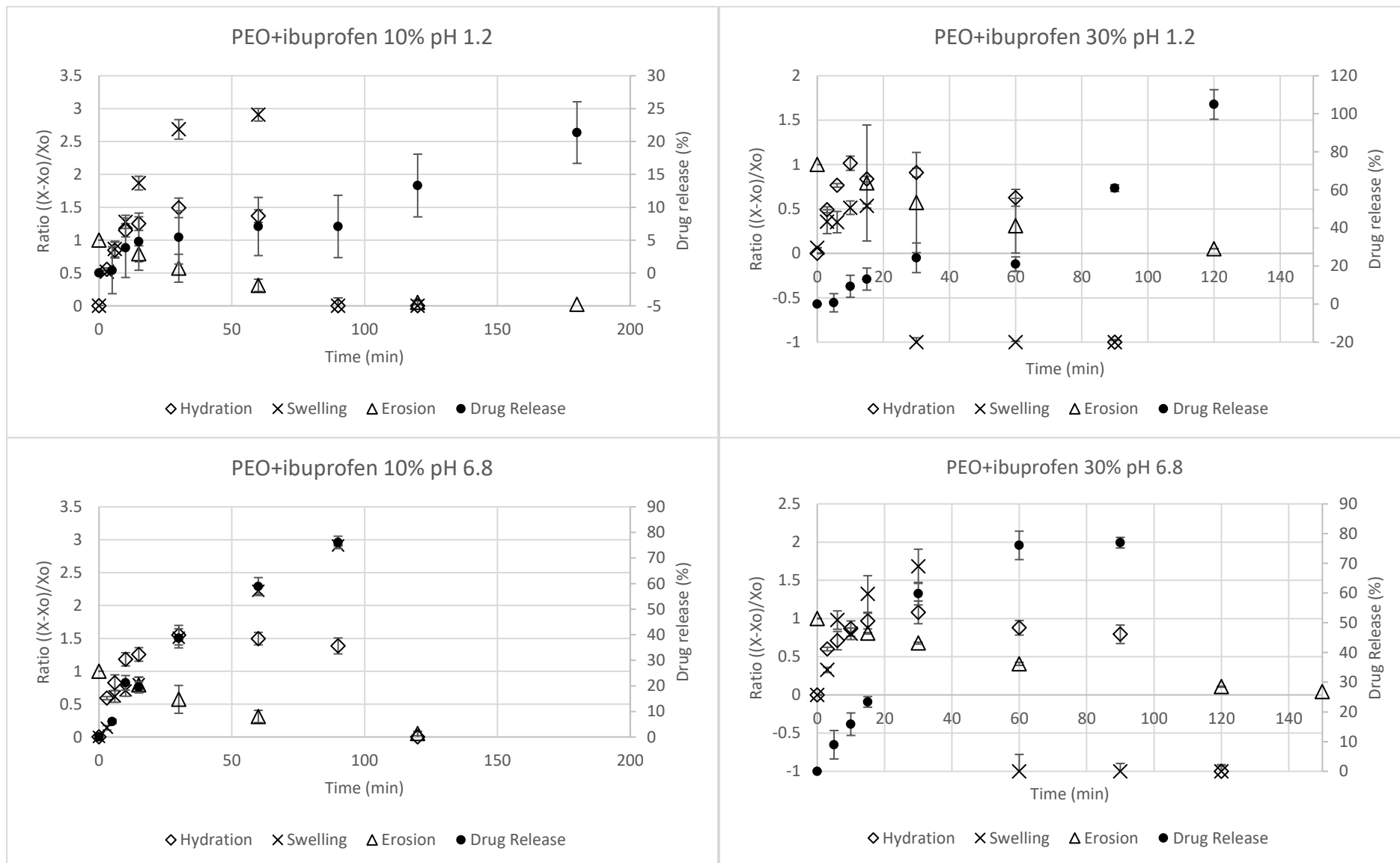


Figure 5-8: Drug release and PEO behaviour for ibuprofen formulations. The generic ratio $((X-X_o)/X_o)$ has been presented, which can be substituted by wet mass in the case of hydration, volume in the case of swelling, and dry mass in the case of erosion. the drug release is plotted on the secondary y-axis. Erosion is always plotted in inverse increasing from an initial ratio of 1.

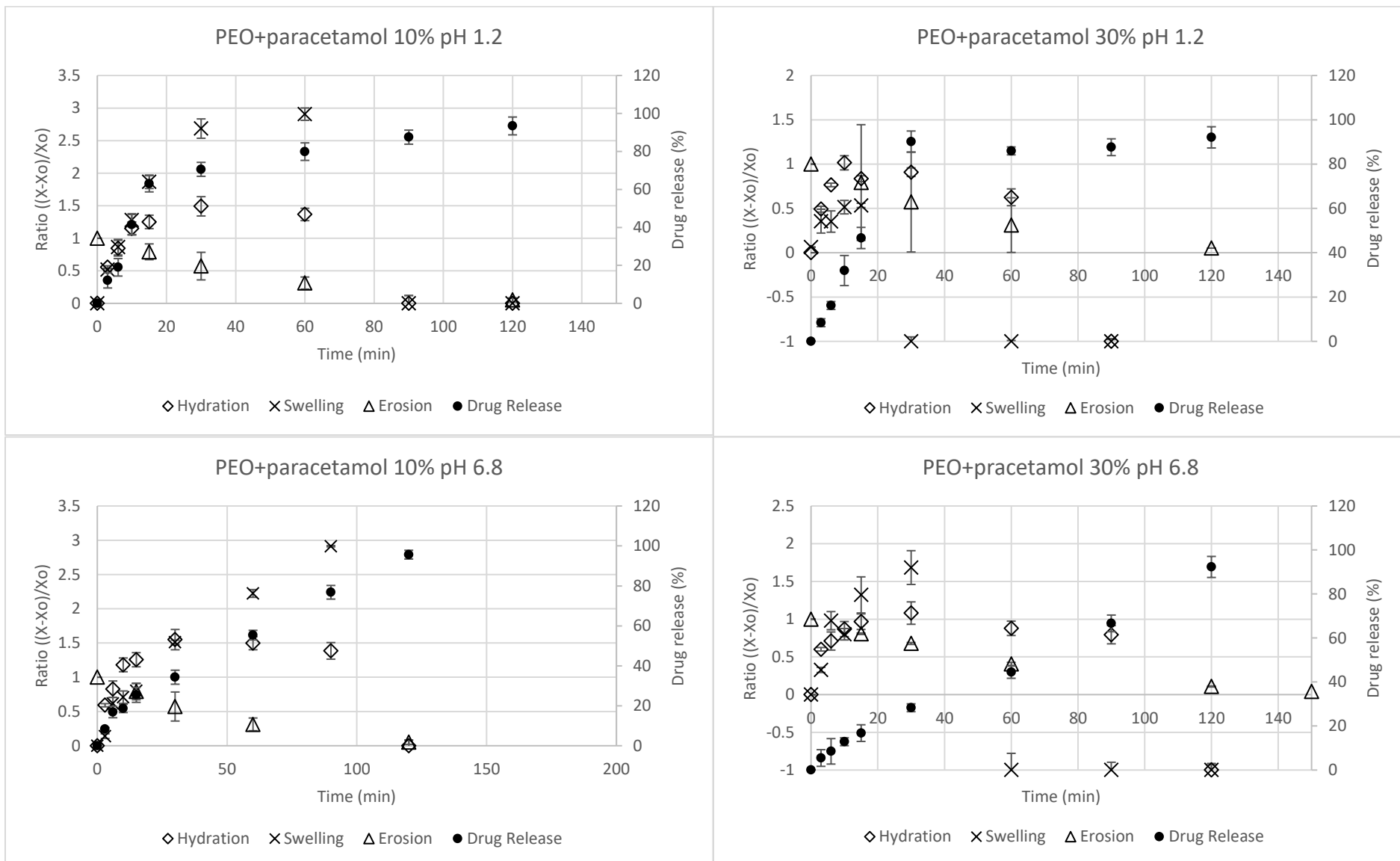


Figure 5-9: Drug release and PEO behaviour for paracetamol formulations. The generic ratio $((X-X_o)/X_o)$ has been presented, which can be substituted by wet mass in the case of hydration, volume in the case of swelling, and dry mass in the case of erosion. the drug release is plotted on the secondary y-axis. Erosion is always plotted in inverse increasing from an initial ratio of 1.

5.3.1 Effect of Ionisation state of the model drug on drug release of solid dispersions

In this section, the drug release profile and polymer behaviour will be presented. As mentioned previously, three cases of polymer behaviour arise for drug release. The first case is drug release driven only by diffusion which is due to hydration. The second case is the diffusion is accompanied by simultaneous swelling or erosion and the third case is when all three of the behaviour occur. Additionally, the drug release constant (K_D), release mechanism (n), and the t_{50} (drug release half-life) will be useful in comparing the formulations.

5.3.1.1 Case I

In case I, the drug release is driven only by diffusion which is due to hydration. The first case is seen with HPMCAS formulations in pH 1.2. HPMCAS, in pH 1.2, is insoluble. The addition of a hydrophilic drug increases the osmotic gradient. This drives the diffusion of the solvent into the matrix which becomes entrapped causing a density reduction in the matrix while allowing the hydrophilic drugs to dissolve into the solvent. At 30% lidocaine loading for HPMCAS, the quantity of lidocaine is sufficient to exhibit a disintegrant effect in the matrix. The duration of complete drug release was much shorter than 10% lidocaine loaded HPMCAS. Hydrophobic ibuprofen slowed the diffusion significantly. Additionally, HPMCAS, in pH 1.2, showed a low K_D and a long (t_{50}) duration compared to other formulations, shown in Table 5-2. Lidocaine t_{50} was lower than paracetamol t_{50} as expected while ibuprofen had a higher t_{50} which is expected for a hydrophobic drug. For both paracetamol and ibuprofen at lower drug loadings, the mechanism or release was Fickian diffusion ($n < 0.45$) and becomes anomalous transport ($0.45 < n < 0.89$) at higher drug loading. As mentioned in chapter 1, Fickian diffusion occurs when the polymer relaxation time is much greater than the solvent diffusion time. At 10% drug loading, diffusion becomes the only mechanism and thus the t_{50} is slow, but at 30% loading, majority of the formulation composition is more hydrophilic, the diffusion rate becomes equal to the polymer relaxation and hence the increase of n values for all lidocaine and paracetamol formulations in pH 1.2. By comparing the drug release of lidocaine, which is charged, to ibuprofen, it can be noted that solubility is a more dominant factor of determining drug release than ionisation.

5.3.1.2 Case II

In this case, the diffusion is accompanied by either swelling or erosion. In such cases, the density of the polymer at the matrix interface is quite low so that the polymer chains along with drug molecules dissolve into the solvent. In such cases, the higher the ratio of swelling or erosion, the lower the density of the matrix will become at the interface. This will drive the drug release to be greater compared to a less swelling or eroding polymer. This behaviour can be seen with all zein formulations, shown in Figure 5-4, Figure 5-5, and Figure 5-6. The parametrized values of fitting of zein formulations are shown in Table 5-2. Zein does not erode in either pH. Zein is positively charged in pH 1.2. Paracetamol and lidocaine release did not show any significant difference for t_{50} , K_D , or n . Zein exhibited an intermediate t_{50} between HPMCAS and PEO. Zein with 30% ibuprofen loading had release mechanism value of 0.99 indicates case II transport whereby the movement of molecules in the matrix is influenced by polymer relaxation and associated with state transition (glass-to-gel transition). As such the gelling layer of zein gradually becomes thicker and therefore the drug concentration gradient along the diffusional pathlength is decreased. The gradually decreased drug concentration gradient results in progressively slower drug release rates as evidenced by very low K_D (0.04) for this formulation. Ibuprofen is neutral like paracetamol but showed significant difference reasoning that solubility is a factor, not ionisation. In pH 6.8, Zein is neutrally charged and exhibits longer t_{50} for lidocaine and paracetamol formulations. Bouman et al observed that charge difference between zein and indomethacin retarded the drug release and like charges accelerated the drug release (14). The charges for zein, lidocaine, and ibuprofen are shown in Figure 5-10. This still does not explain the reason for zein (neutral) and ibuprofen (negative) fast drug release times. One possible explanation for this might be that the hydrophobic drug diffuses through the hydrophobic zein matrix faster than the hydrophilic drug (425). This may indicate that intermolecular forces have a more dominant role compared to ionisation. However, if ibuprofen is charged it is behaving as weak acid. This may lead to certain local regions where the pH is reduced. Once water is absorbed, the system becomes more heterogeneous and the behaviour could be highly complex.

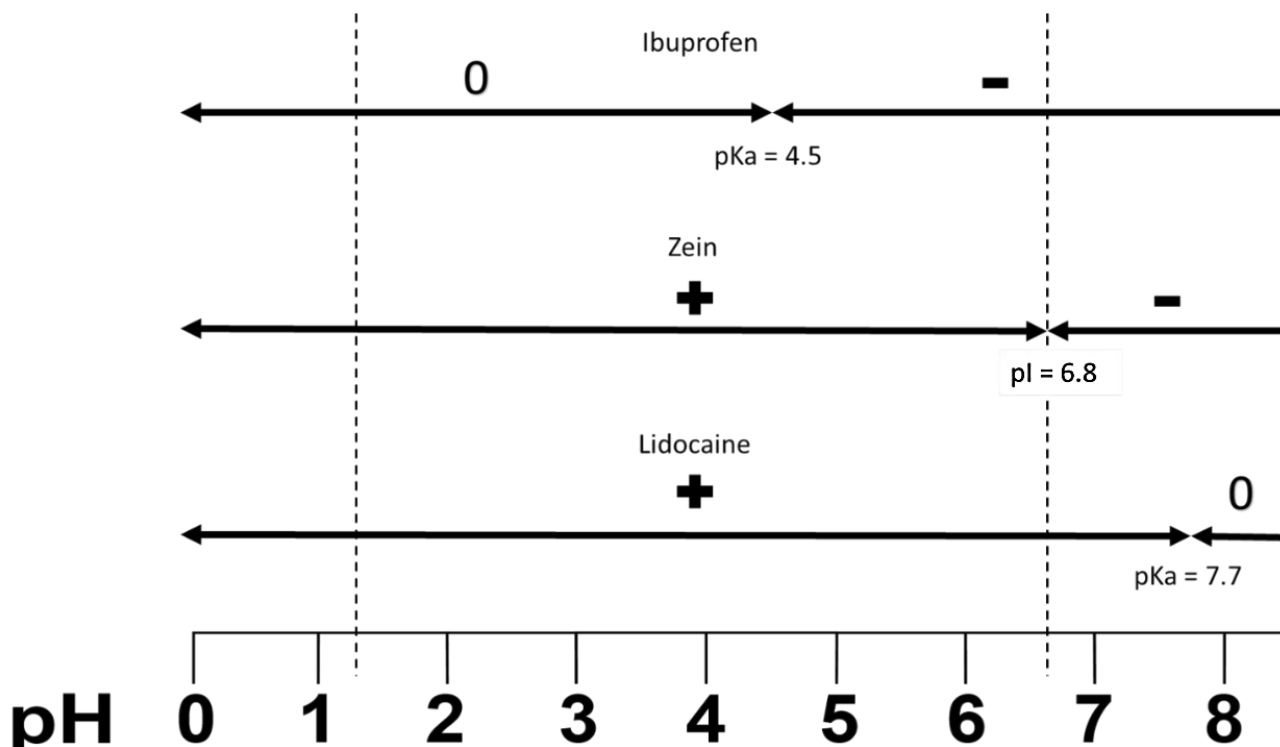


Figure 5-10: Schematic overview of the charge of zein, lidocaine, and ibuprofen. The pH scale has only been shown until pH 8. Beyond this, any charge attained was not part of the experimental pH. Paracetamol was omitted as it is neutral in all pH. The dashed line shows the two pH at which studies were performed.

5.3.1.3 Case III

The third case is wherein diffusion, swelling, and erosion occur simultaneously. This is observed for PEO formulations shown in Figure 5-7, Figure 5-8, and Figure 5-9. PEO exhibited the shortest t_{50} and high K_D values as a superabsorbent polymer. However, in both pH, there was no significant difference among the drug release parameters. In the case of 30% ibuprofen loading in pH 1.2, case II transport was seen with a significantly prolonged t_{50} of 88 minutes (5.5X slower than other PEO formulation which is slowed 1.3X). In general, ibuprofen loadings retarded t_{50} due to the hydrophobic nature of the drug. This reaffirms the ionisation played a minor role for drug release.

Table 5-2: Drug release constant (K_D) \pm SD and the mechanism of release of the formulations in pH 1.2 and pH 6.8. t_{50} is the half release time that allows for comparison.

Formulation	pH 1.2				pH 6.8			
	$K_D \pm SD$	n_d	R^2	t_{50} (min)	$K_D \pm SD$	n_d	R^2	t_{50} (min)
HPMCAS+Lidocaine 10%	5.93 \pm 1.98	0.29	0.91	325	16.79 \pm 6.91	0.39	0.95	26
HPMCAS+Lidocaine 30%	1.46 \pm 0.88	0.59	0.98	50	13.60 \pm 0.38	0.23	0.98	20
HPMCAS+Ibuprofen 10%	-	-	-	-	3.58 \pm 1.41	0.75	0.99	36
HPMCAS+Ibuprofen 30%	15.69 \pm 14.43	0.46	0.84	14	2.93 \pm 1.76	0.80	0.99	28
HPMCAS+Paracetamol 10%	4.87 \pm 1.54	0.37	0.93	539	11.28 \pm 3.49	0.43	0.94	48
HPMCAS+Paracetamol 30%	2.12 \pm 1.15	0.64	0.92	88	14.83 \pm 2.38	0.32	0.98	36
Zein+lidocaine 10%	8.84 \pm 2.04	0.33	0.97	220	2.91 \pm 1.59	0.44	0.99	680
Zein+lidocaine 30%	7.22 \pm 3.31	0.35	0.96	120	4.26 \pm 1.25	0.41	0.98	340
Zein+Ibuprofen 10%	1.62 \pm 0.47	0.51	0.98	120	1.98 \pm 0.34	0.61	0.87	12
Zein+Ibuprofen 30%	0.04 \pm 0.29	0.99	0.98	120	1.99 \pm 0.98	0.25	0.91	15
Zein+Paracetamol 10%	6.78 \pm 1.69	0.38	0.96	190	2.18 \pm 1.93	0.39	0.98	760
Zein+Paracetamol 30%	7.45 \pm 1.56	0.34	0.95	120	4.12 \pm 1.34	0.52	0.97	634
PEO+lidocaine 10%	13.22 \pm 8.38	0.46	0.93	10	4.22 \pm 2.47	0.64	0.99	10
PEO+lidocaine 30%	8.85 \pm 4.43	0.58	0.91	13	2.56 \pm 0.41	0.72	0.99	14
PEO+Ibuprofen 10%	2.95 \pm 1.21	0.24	0.94	16	3.51 \pm 2.25	0.68	0.98	33
PEO+Ibuprofen 30%	0.74 \pm 0.45	0.99	0.91	84	3.44 \pm 1.38	0.77	0.95	21
PEO+Paracetamol 10%	9.48 \pm 4.34	0.53	0.94	14	3.98 \pm 2.08	0.68	0.98	18
PEO+Paracetamol 30%	12.38 \pm 3.23	0.58	0.97	14	3.49 \pm 1.87	0.68	0.98	24

5.3.2 Effect of ionisation state of the model drug on polymer hydration (positive weight change)

A note about the word hydration used in this work needs to be mentioned. When measuring the wet weight of the extrudate, there is a simultaneous activity of water ingress and erosion is taking place. The hydration ratio of pure HPMCAS and HPMCAS formulation is presented in Figure 5-11. Hydration ratio is taken as a positive ratio. As such, hydration of HPMCAS formulation occurs only in pH 1.2. The hydration ratio was higher for lidocaine than the other two drugs. Lidocaine is a hydrophilic drug which is fully positively charged in pH 1.2. As the formulation is immersed in the solvent, the charged drug molecule in the matrix modifies the wettability of the formulation interface (426). In this case, the wettability is increased resulting in an increased solvent uptake. Ibuprofen and paracetamol, meanwhile, are neutral in this pH and does not increase osmolarity as does lidocaine.

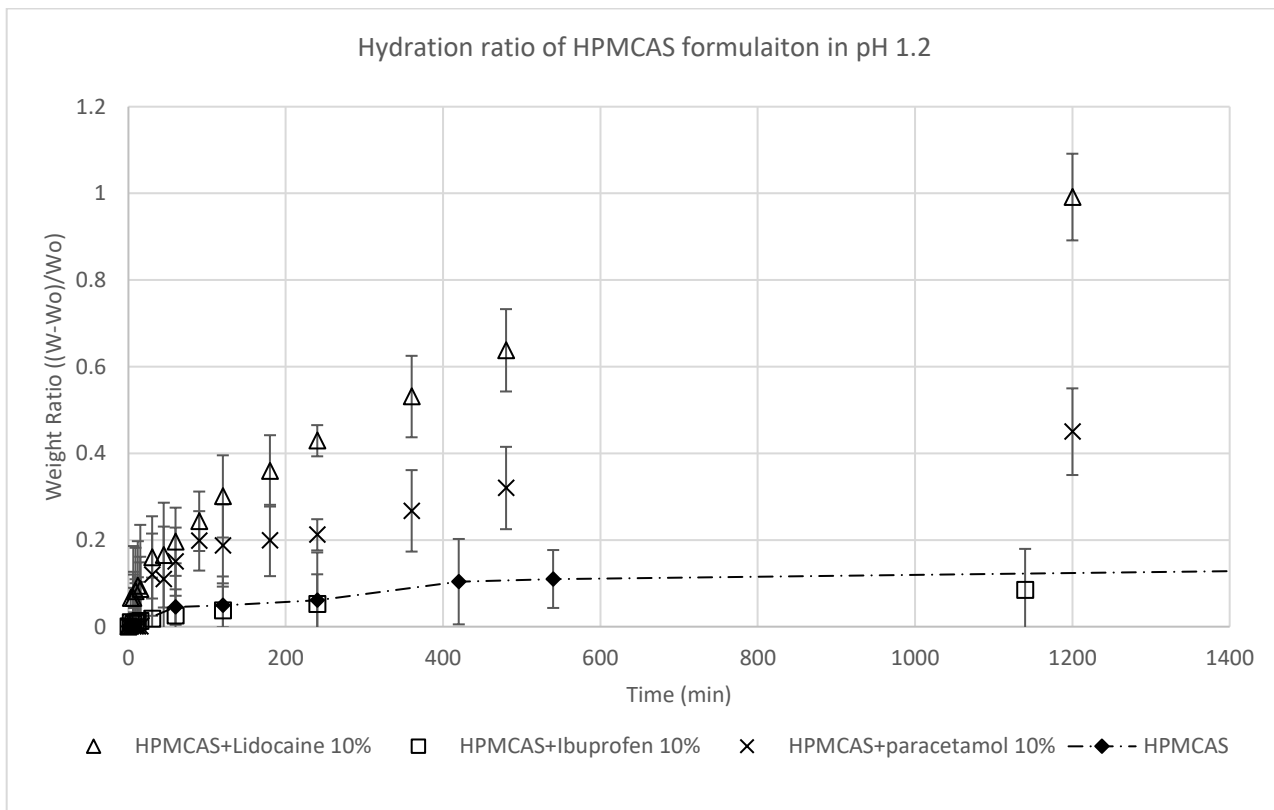


Figure 5-11: HPMCAS hydration ratio and HPMCAS formulation hydration ratios in pH 1.2.

However, although paracetamol is also neutral, there is a difference in the hydration ratio between ibuprofen and paracetamol loaded formulations. This greater solubility of paracetamol (21 mg/mL in pH 1.2) than ibuprofen (0.06 mg/mL in pH 1.2) results in higher hydration in pH 1.2 (427). Hence, in the case of an insoluble polymer (HPMCAS) which acts as a non-interacting carrier, the true effect of the drug can be investigated. The driving force for hydration is likely the solubility of the drug.

The PEO loaded formulation hydration is shown in Figure 5-12. In the case of PEO, the effect of the ionised state of the drug is less obvious due to PEO being a super-absorbent polymer (SAP). Such SAP can retain a large percentage of solvent, relative to its weight, within their structure (143). Lidocaine loaded PEO had an initial high hydration ratio but plateaued earlier than the two other formulations. This may be because lidocaine was released earlier within the first ten minutes when the hydration ratio was higher. The drug release to hydration will be compared later on. At pH 6.8, the two hydrophilic drugs, of which lidocaine is 90.01% positively charged and paracetamol is 99.78% neutral, did not show any significant variation of hydration ratio from the pure PEO itself. Ibuprofen, which was 98.89% negatively charged exhibited a

slowdown. Ionisation will increase the osmolarity and therefore the driving force for water ingress. This can explain the decrease the wettability of the surface of ibuprofen loaded formulations leading to less amount of solvent ingress.

The zein formulation hydration ratios are shown in Figure 5-13. Lidocaine loaded zein formulations were observed to show a higher hydration ratio in both pH. A factor for this could be the electrostatic interaction between the drugs and the zein matrix. Bouman et al observed the drug release was faster when the carrier and drug were identically charged and release was slower when they were oppositely charged (14). The same reasoning could hold in the case of hydration. In pH 1.2, zein and lidocaine are positively charged while ibuprofen and paracetamol are neutral. This can explain the higher hydration ratio observed for zein and lidocaine. Lidocaine is positively charged and ibuprofen is negatively charged while paracetamol is neutral. This can explain the higher hydration ratio observed for zein and lidocaine (both +) and lower hydration ratio for zein and ibuprofen (+ and -). Figure 5-10 illustrated this, however, it is more likely that solubility is the explaining factor.

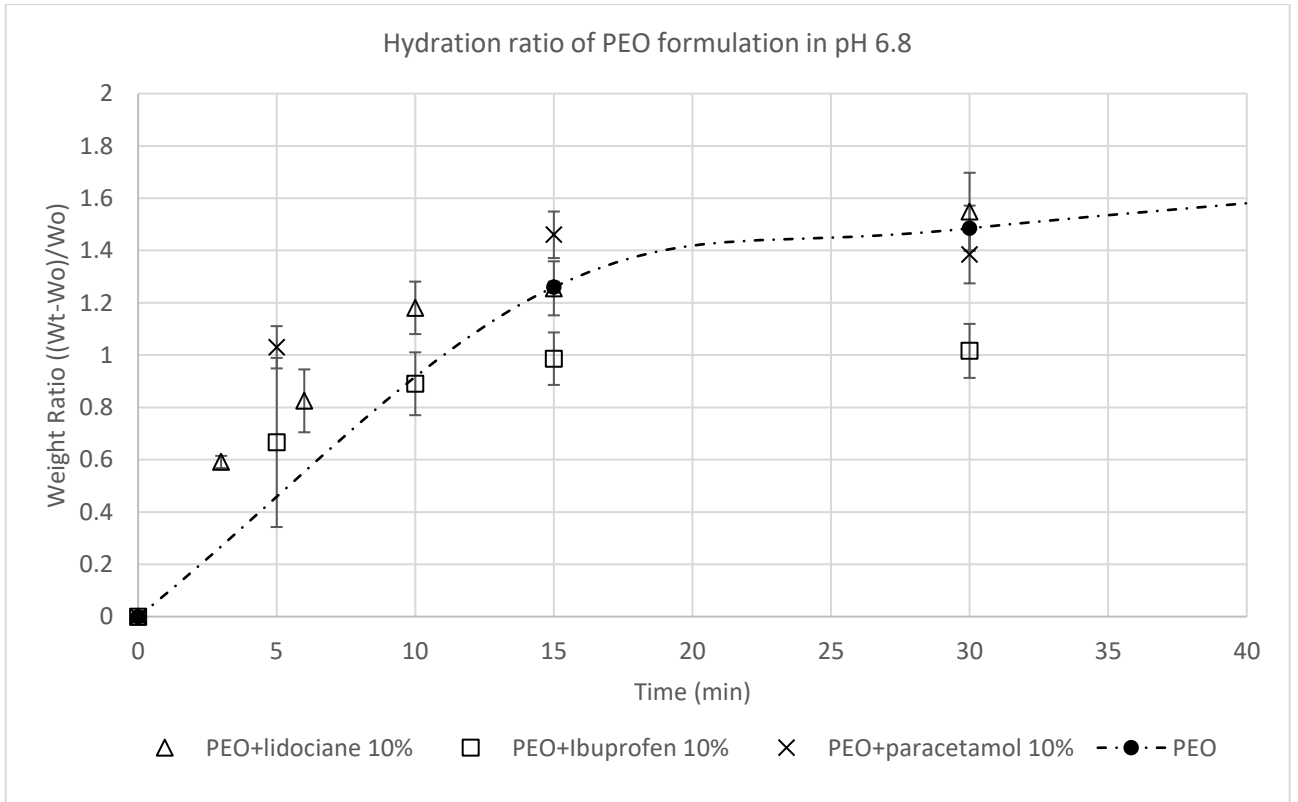
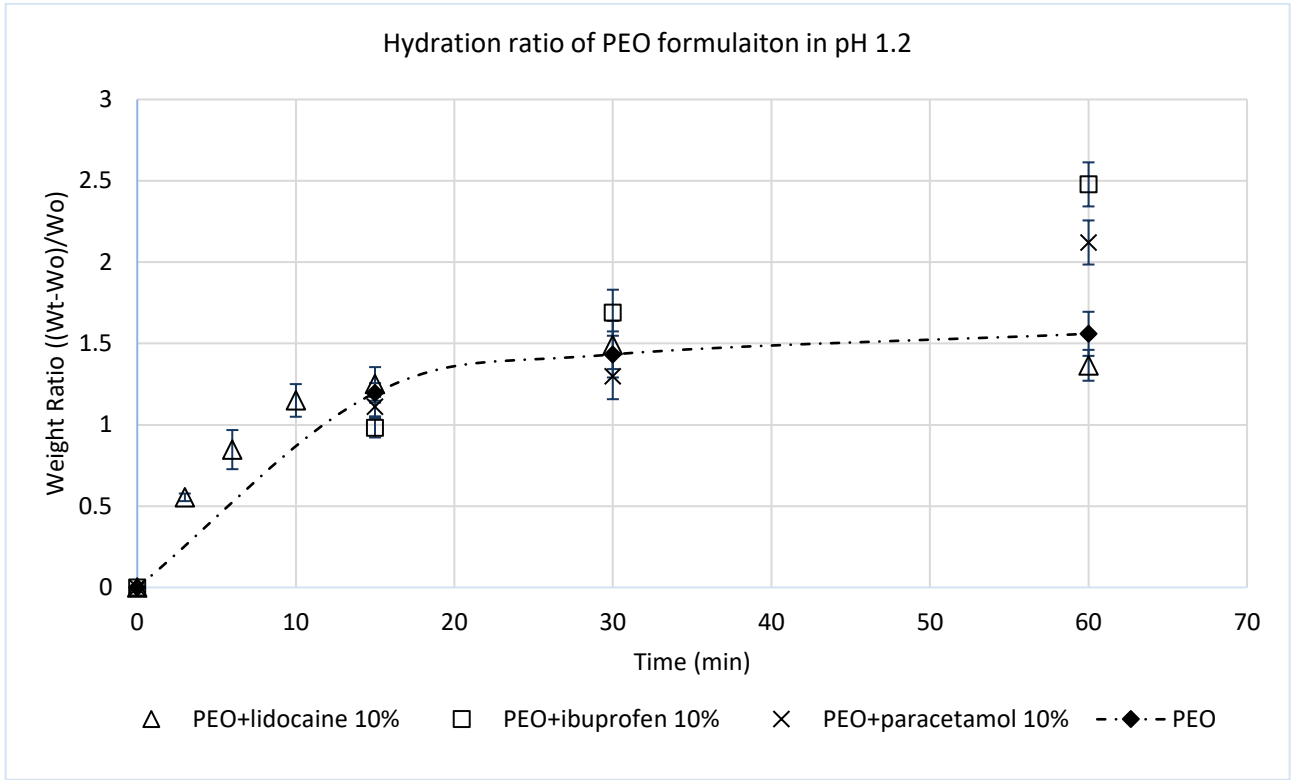


Figure 5-12: Top) PEO hydration ratio and PEO formulation ratios in pH 1.2. Bottom) PEO hydration ratio and PEO formulation hydration ratio in pH 6.8.

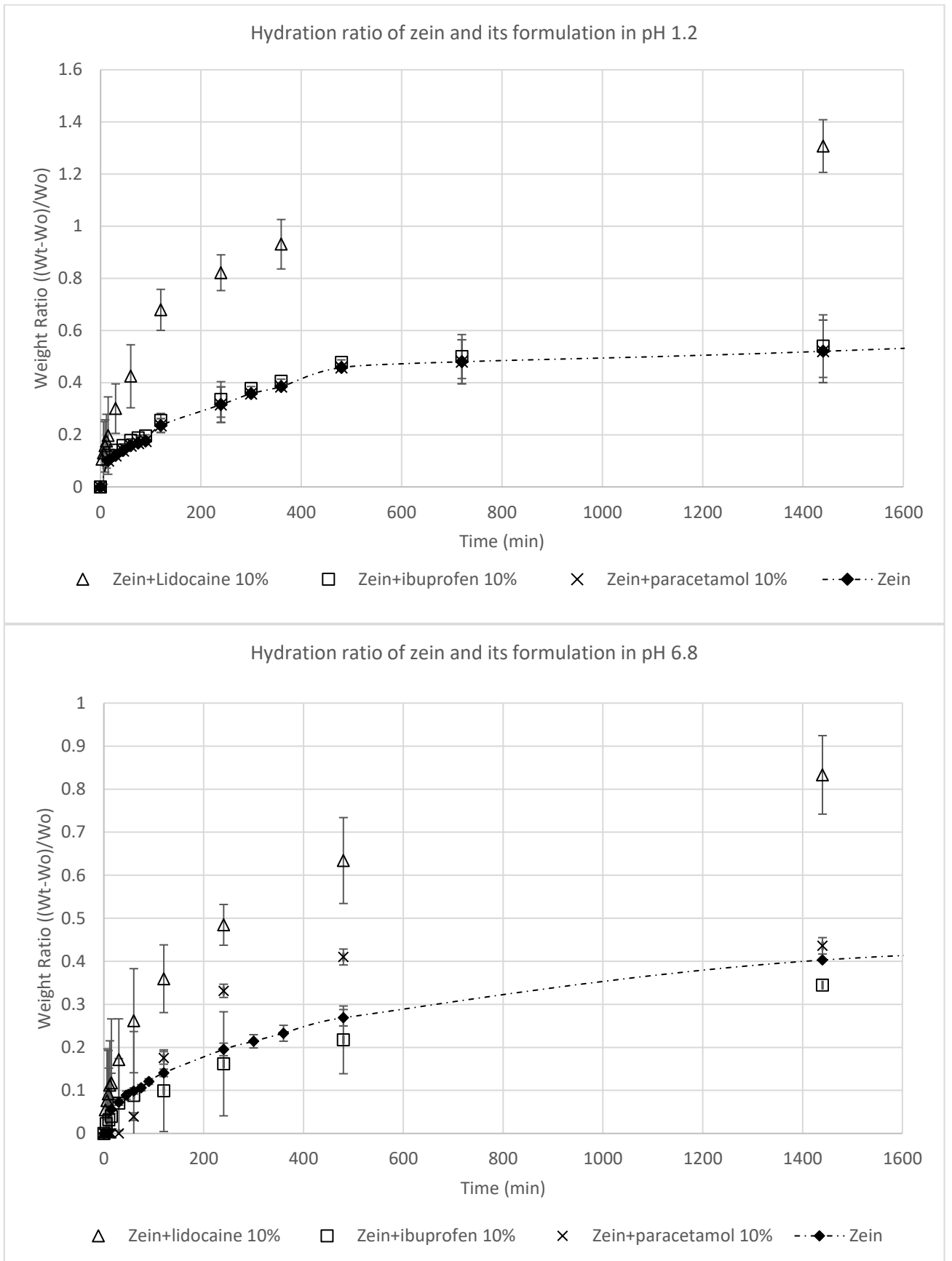


Figure 5-13: Top) zein hydration ratio and zein formulation ratios in pH 1.2. Bottom) Zein hydration ratio and zein formulation hydration ratios in pH 6.8.

5.3.3 Effect of drug loading on polymer hydration

An interesting case arose with 30% lidocaine loaded HPMCAS. The tendency of lidocaine to dissolve is much greater than at 10% lidocaine loading that it causes erosion (negative hydration) for the insoluble HPMCAS polymeric matrix. Hydration ratio is taken when the wet formulation to dry formulation ratio is positive but this formulation was included in the hydration ratio as this is an exception. As the surface of the matrix erodes, this causes the solvent to percolate to the inner layers causing more wetting and erosion. In pH 1.2, the solvent limits ionisation of HPMCAS chain to 10% at most. Due to this, the dissolved chain remains in a compact folded state. As the chains are hydrophobic when unionised in a poor solvent, HPMCAS/lidocaine 30% formulation collapses into globules. The addition of lidocaine in high quantities has made the drug act as a super disintegrant and although paracetamol loading of 30% with HPMCAS did not exhibit this behaviour, it is believed that higher loading of paracetamol will cause the same eroding behaviour of HPMCAS formulation to occur in pH 1.2 (428). The hydration ratios of HPMCAS formulation in pH 1.2 is shown in Figure 5-14.

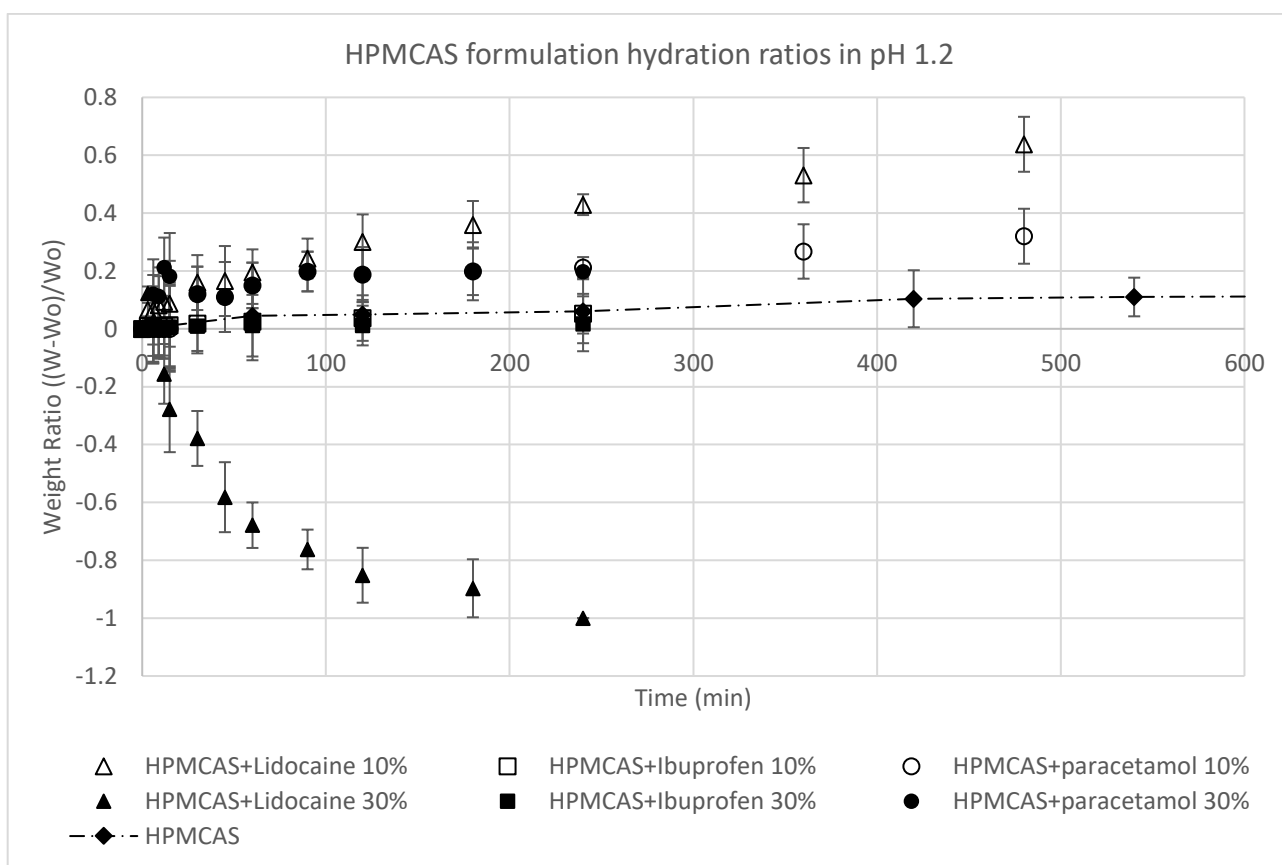


Figure 5-14: HPMCAS formulation hydration ratio in pH 1.2. Hydration ratios are not shown for pH 6.8 as no hydration but erosion takes place of the formulation.

The compared ratio of hydration at different drug loadings is shown in Figure 5-15. The hydrated ratio (plotted on the primary axis) was derived by dividing the maximum hydrated ratio at 30% by the maximum hydrated ratio at 10% (i.e. $\text{Formulation}_{30\%}/\text{Formulation}_{10\%}$). A value, greater than one would indicate higher hydration for the 30% formulation as the numerator is increasing faster than the denominator. A value between zero and one would indicate slower hydration for the 30% drug loaded formulation relative to the 10% drug loaded formulation. A negative ratio indicates erosion. Erosion is not included in this plot. The only exception was the case of HPMCAS loaded with 30% lidocaine at pH 1.2. This was included for comparison as the 10% lidocaine loaded did not show any erosion but 30% lidocaine loaded HMCAS formulation did.

The time ratio (secondary axis) indicates how fast the higher drug loading caused the formulation to reach the maximum hydrated ratio where the hydration ratio was compared on the primary axis. A value of one indicates the time taken was the same for both formulations while a value lower than one indicate a shorter time. Therefore, it can be seen that for the HPMCAS lidocaine formulation, the addition of higher drug loading caused erosion and the time taken to was faster at a ratio of 0.1 (a tenth of the time). For most formulations, the higher drug loading caused slower hydration. Zein loaded with ibuprofen had value just above one (1.08) but this can not be taken to be significant due to the variation overserved on the triplicates. The time ratio for most of them is the same which allows for a comparison of the hydration ratios at identical times ratio. Some formulations such as PEO with lidocaine and PEO with paracetamol in pH 1.2 and PEO with ibuprofen at pH 6.8 showed lower hydration but at a much shorter time. This seems to be an observation with PEO which is prone to absorbing high quantities of solvent but also undergoing erosion. Since the hydration ratio is lower but the time is shorter, it could be the rate of solvent ingress is faster due to the increased affinity of the matrix from higher drug loading causing most of the drug to be released faster, but also increasing erosion.

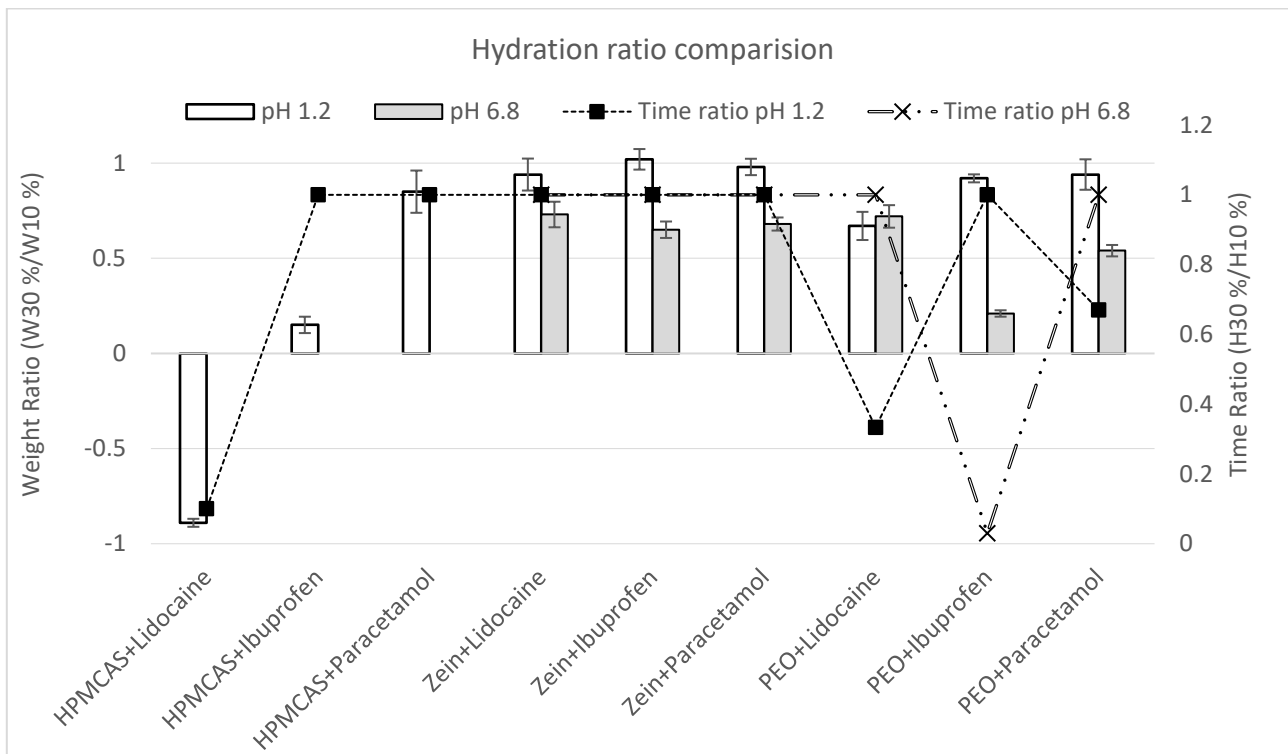


Figure 5-15: Formulation hydration ratio and time to reach hydration ratio comparison. A weight ratio above 1 indicates faster hydration while between 0 and 1 indicates slower hydration. Negative ratio is indicating erosion. The time ratio (secondary axis) indicates how fast the higher drug loading caused the formulation to reach the maximum hydrated ratio. The time ratio (H30%/H10%) is the time of maximum hydration ratio at 30% drug loading divided over maximum hydration ratio at 10% drug loading. A value of less than 1 indicates faster swelling for the 30% formulation.

5.3.4 Effect of ionisation on polymer swelling

The swelling ratios of zein formulations are shown in Figure 5-16. The addition of hydrophilic charged drug increased the swelling ratio in both pH. This is to be expected based on the hydration ratio that was observed. As more of the solvent ingresses, more of the polymer free volume is occupied causing the polymer to undergo relaxation. Ibuprofen caused less swelling due to the drug hydrophobicity. The addition of hydrophobic drugs to the zein matrix makes the combined system more hydrophobic. It has been known that upon contact with the solvent, five steps occur in sequence (165). First, the solvent diffuses into the matrix. Then, the solvent acts as a plasticizer, lowering the polymer glass transition temperature, T_g , causing the glass-rubber transition, the gel formation, and polymer swelling. At this point, the soluble drug dissolves and diffuses through the gel layer. If the drug is hydrophilic, it will accelerate the diffusion as the molecularly dispersed hydrophilic drug particles in the matrix enhance affinity for the solvent particles. If the drug is hydrophobic, the particles will decelerate the diffusion of solvent by acting as a repulsive the solvent particles. This is the most probable cause for a difference between the lidocaine and ibuprofen.

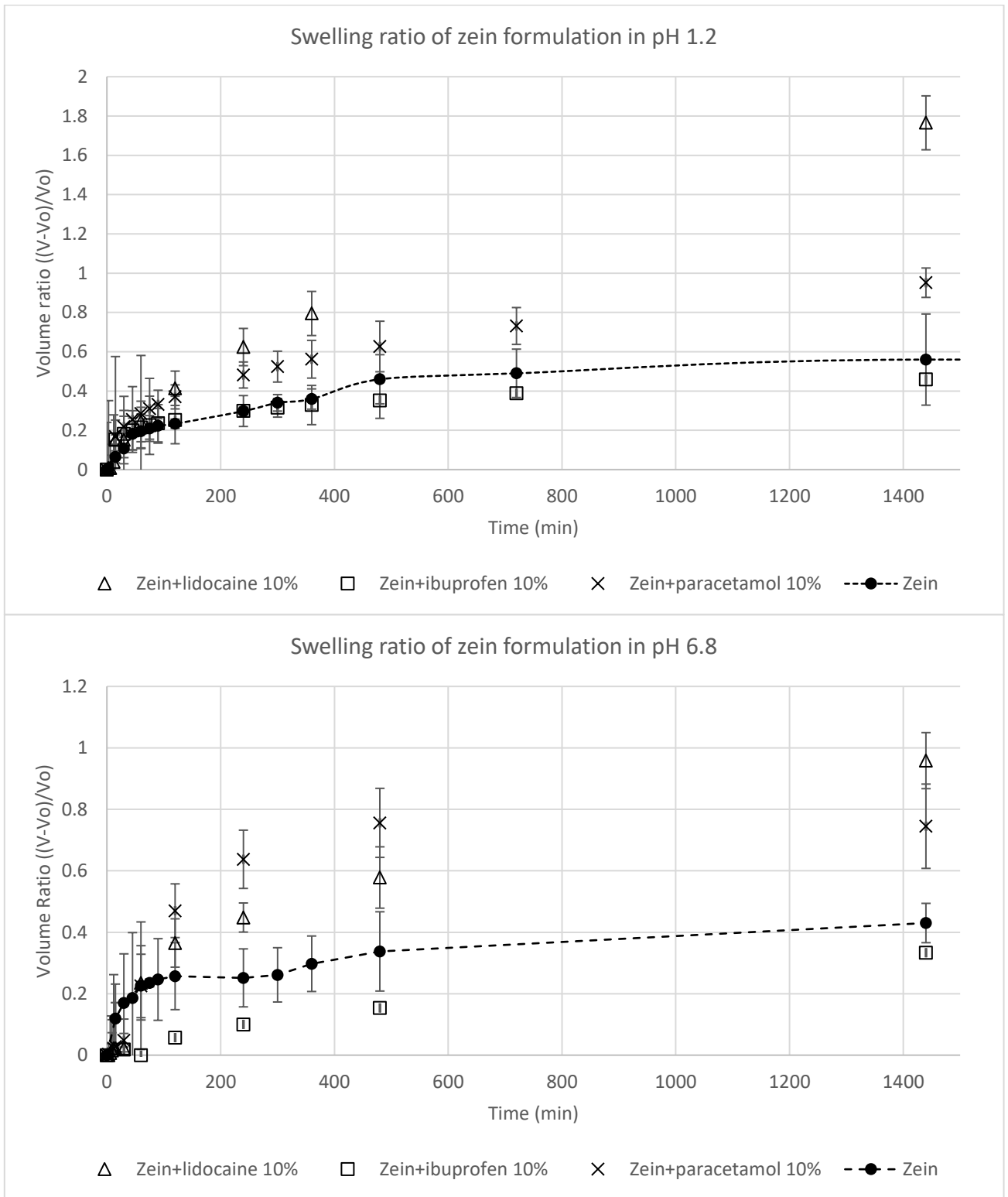


Figure 5-16: Top) Zein and zein formulation swelling ratios in pH 1.2. Bottom) Zein and zein formulation swelling ratios in pH 6.8

In the case of PEO formulations, lidocaine loaded formulation did show higher swelling than ibuprofen. While, in pH 6.8, the swelling ratio for both drugs is lower than the pure PEO. Rowell and Banks describe that moisture control can be subcategorized as water repellents and dimensional stabilizers. While water repellents control the rate of water sorption, dimensional stabilizers control affect swelling requiring

chemical modifications (429). The reason ibuprofen loading could lower the swelling ratio is that ibuprofen is negatively charged while the hydroxyl in PEO is also negatively charged leading repelling which cause less solvent uptake and in turn less swelling. Lidocaine is positively charged in this pH and the increase in positive charge while the reduction in OH⁻ could lead to less solvent uptake and therefore less swelling too.

The PEO formulation swelling ratio is shown in Figure 5-17.

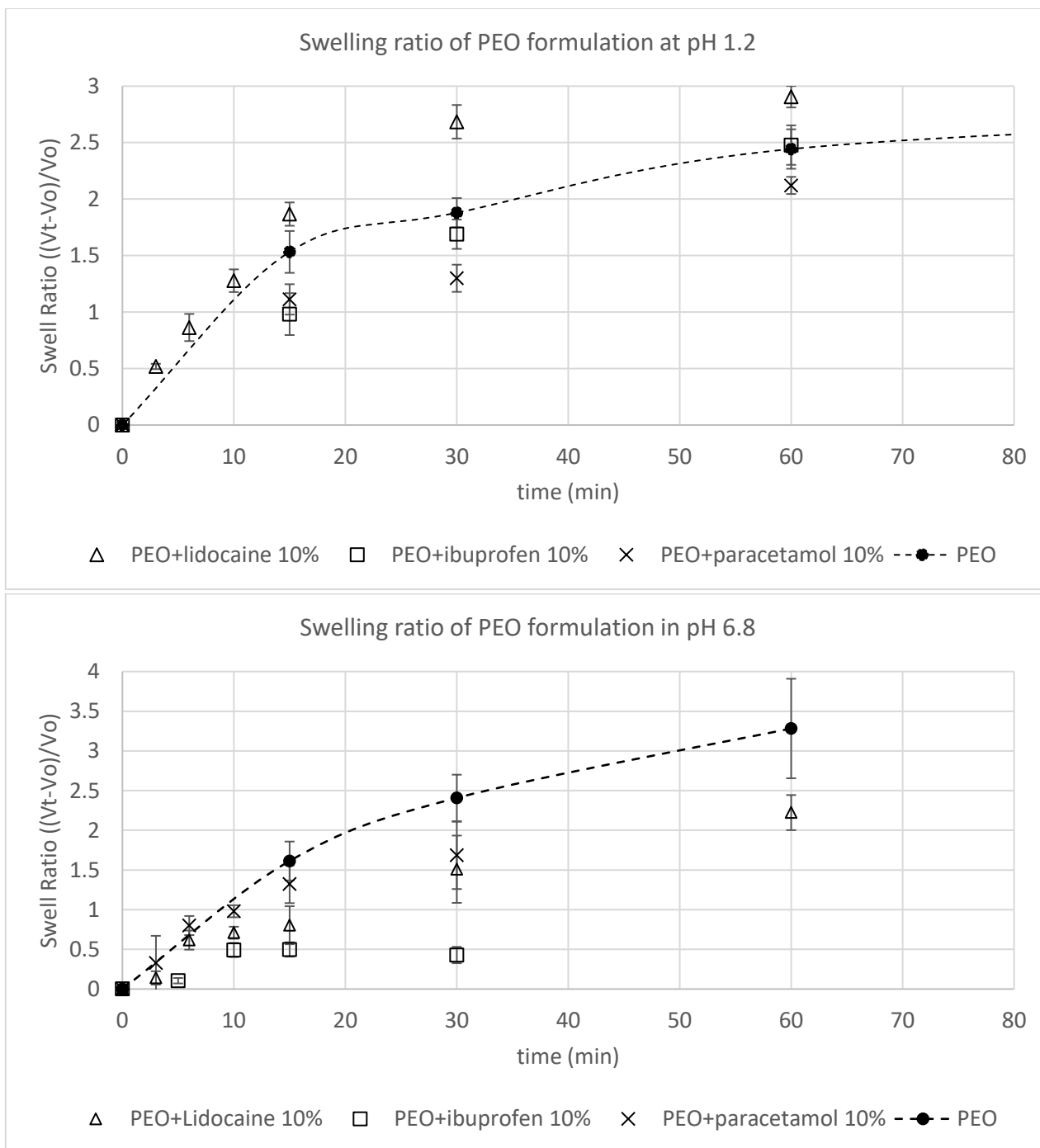


Figure 5-17: Top) PEO and PEO formulation swelling ratios in pH 1.2. Bottom) PEO and PEO formulation swelling ratios in pH 6.8

5.3.5 Effect of drug loading on polymer swelling

It appears the swelling was reduced in pH 1.2 but not significantly as the ratio is close to one but in the range of 0.9 to 1 except for 30% lidocaine loaded PEO formulation. The swelling rate increased for this formulation as the value is close to 0.2 (value on the secondary axis for the dashed line), indicating swelling was five times faster with three times the drug load. The swelling rate increased for all PEO formulations in pH 1.2 with the highest increase being for lidocaine followed by ibuprofen and then paracetamol. The compared ratio of swelling at different drug loadings are shown in Figure 5-18. In pH 6.8, the swelling increased for both zein and PEO by the addition of higher quantities of hydrophobic ibuprofen. The swelling rate decreased for all formulations with the addition of higher drug loading as all values are less than 1. Moreover, it can be observed that the swelling rates exhibited the fastest increase for lidocaine formulations and slowest increase for paracetamol for both formulations. According to obstruction theories (430-432), which focus on sieve effect in the polymeric network, the addition of more hydrophobic drug particles should make the network more impenetrable elongating the path length for solvent molecules to diffuse in and drug molecules to diffuse out. Conversely, the addition of more hydrophilic lidocaine should make the network more impenetrable but to a lesser degree than hydrophobic ibuprofen. The swelling profile fitted to the semiempirical power model is presented in Table 5-3.

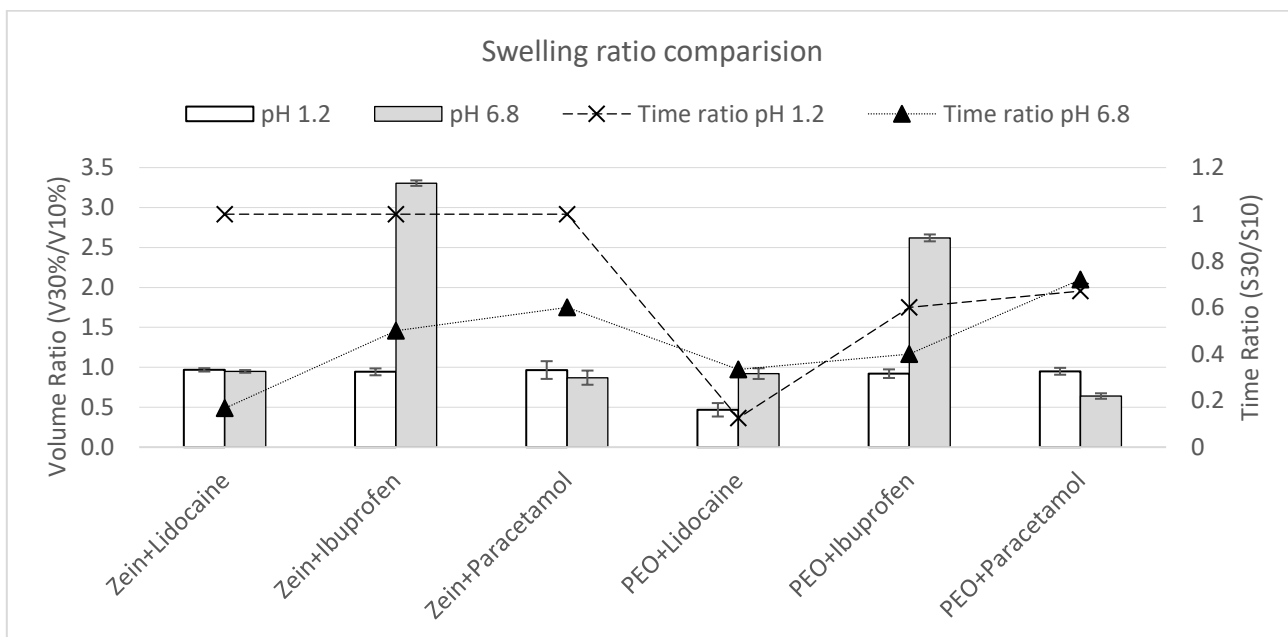


Figure 5-18: Swelling ratio comparison for swellable formulations. The time ratio (secondary axis) indicates how fast the higher drug loading caused the formulation to reach the maximum swelling ratio. A volume ratio above 1 indicates faster swelling while between 0 and 1 indicates slower swelling.

Table 5-3: The swelling constant (K_s), the swell index(n_s), and their goodness of fit (R^2) for polymers and drug loadings in pH 1.2 and pH 6.8.

Formulation	pH 1.2			pH 6.8		
	K_s	n_s	R^2	K_s	n_s	R^2
Zein*	0.04 ± 0.01	0.37 ± 0.08	0.99	0.09 ± 0.01	0.18 ± 0.03	0.99
PEO*	0.46 ± 0.11	0.42 ± 0.10	0.99	0.43 ± 0.18	0.49 ± 0.07	0.99
Zein+lidocaine 10%	0.04 ± .001	0.48 ± 0.06	0.96	0.02 ± 0.01	0.52 ± 0.16	0.95
Zein+lidocaine 30%	0.21 ± 0.04	0.38 ± 0.12	0.91	0.01 ± .008	0.68 ± 0.24	0.98
PEO+lidocaine 10%	0.59 ± 0.08	0.37 ± 0.09	0.94	0.45 ± 0.14	0.55 ± 0.17	0.99
PEO+lidocaine 30%	0.24 ± 0.06	0.31 ± 0.12	0.94	0.29 ± 0.16	0.52 ± 0.18	0.92
Zein+Ibuprofen 10%	0.08 ± 0.01	0.34 ± 0.08	0.97	0.07 ± .006	0.23 ± 0.08	0.96
Zein+Ibuprofen 30%	0.02 ± 0.01	0.26 ± 0.05	0.96	0.01 ± .008	0.49 ± 0.14	0.93
PEO+Ibuprofen 10%	0.38 ± 0.08	0.23 ± 0.04	0.98	0.16 ± 0.08	0.35 ± 0.10	0.70
PEO+Ibuprofen 30%	0.25 ± 0.04	0.37 ± 0.13	0.98	0.09 ± 0.02	0.53 ± 0.09	0.99
Zein+Paracetamol 10%	0.06 ± 0.01	0.42 ± 0.08	0.97	0.05 ± .008	0.56 ± 0.16	0.99
Zein+Paracetamol 30%	0.17 ± 0.02	0.54 ± 0.07	0.98	0.03 ± .009	0.61 ± 0.21	0.99
PEO+Paracetamol 10%	0.43 ± 0.24	0.26 ± 0.03	0.96	0.13 ± 0.08	0.49 ± 0.14	0.95
PEO+Paracetamol 30%	0.37 ± 0.16	0.28 ± 0.11	0.97	0.23 ± 0.10	0.54 ± 0.19	0.94

5.3.6 Effect of ionisation state of the model drug on polymer erosion

The erosion rates of the formulations fitted to exponential decay are presented in Table 5-4. There is a significant increase in erosion rates with the addition of drugs for all formulations except zein. Zein is a non-eroding polymer. HPMCAS is insoluble in pH 1.2 while 30% lidocaine HPMCAS loading exhibited a disintegrating effect. The likely explanation for this is the quantity of the hydrophilic drug. Lidocaine is hydrophilic and upon contact with the solvent, the hydrostatic pressure in the formulation is increased (433). The pressure is increased either by water/solvent wicking into the plug or swelling phenomena. The latter effect is not observed. This wicking promotes de-aggregation of the plug particles (434). Since the majority of the constituent is the insoluble polymer, the plugs particles are all drug particles. As these particles are dissolved, microscopic channels are created through which percolation of the solvent occurs. The surface layer breaks at some point when a critical osmotic pressure builds up inside the matrix due to the accumulation of solvent (161). Such effect is not seen with paracetamol 30% HPMCAS loading but it is suspected that with higher paracetamol loading, this phenomenon will be observed.

The type of bond within the polymer backbone mainly that determines the rate of hydrolysis, degradation, and subsequent erosion. In the case of PEO, the C-O-C backbone of PEO gives unmatched hydrophilicity

compared to carbon based backbone (435). The increase in erosion of PEO formulation relative to pure PEO is due to the addition of the lidocaine and the decrease is due to the addition of ibuprofen. Generally increasing net solubility gives rise to hydrophilicity and erosion. By the same token, PEO/ibuprofen loadings were observed to have lower erosion ratio than lidocaine as ibuprofen has two atoms available for hydrogen bonding. However, this does not fully explain for differences in solubilities between lidocaine and ibuprofen. Based on solubility theory, factors such as temperature, pressure, density and concentration of the solvent, intramolecular attractive forces, and polarity affect the solubility of the solute (drug) (436, 437). Furthermore, hydrate theory, and theories of dissociation and molecular association advance the study of the solubility of solvents. Since the dissolution of a particle of a solute in a liquid is due to (i) the attraction exercised by the molecules of the solvent (ii) the attraction exercised by the molecules of solute already in solution, the variance in erosion ratios between lidocaine and ibuprofen can reducibly be explained by this variance of attraction due to all the solubility factors mentioned above.

In pH 6.8, the erosion ratio for PEO was lower than pH 1.2 but all PEO formulations exhibited a higher erosion rate. Kavangh et al showed that an increase in ionic strength of polymer to a decrease in matrix erosion rate (438) implying reverse is also true. The decrease in erosion rates as the ionic strength increased was attributed to the “salting out” of the polymer by the organic ions present in the dissolution media. However, PEO is a non-ionizable polymer and pH insensitive polymer (243). Additionally, Kofi also showed the model drugs used showed that despite HPMC being a non-ionic polymer, the medium ionic composition can influence its behaviour (438, 439). Similarly, HPMCAS (pH responsive) formulations exhibited erosion (higher erosion rate for HPMCAS-lidocaine 30%) in this pH. In the previous chapter, the pH responsiveness of HPMCAS has been discussed. HPMCAS polymer chains, which are ionised in pH 6.8, expands due to the repulsion between charges on the polymer chain allowing for the dissolution of the chain and subsequently undergoes erosion. In contrast, in pH 1.2, the solvent prevents ionisation of HPMCAS chain, the dissolved chain remains in a compact, folded state. Since the chains are hydrophobic when unionised in a poor solvent, they collapse into globules which were precisely observed for HPMCAS-lidocaine 30% in pH 1.2.

With regards to the ionisation of drugs, there was not a significant difference between HPMCAS-lidocaine (+) and HPMCAS-paracetamol (neutral). This reflects a similar result trend obtained by Rania et al where the dissolution behaviour of carvedilol was investigated. They found that although carvedilol was 100% ionised from pH 1.2 to 90% ionised at pH 6.8, the dissolution behaviour and erosion was unaffected and only changed when the ionic strength of the medium was altered by adding salts which varied the solubility from 2398.6 µg/ml in pH 1.2 to 31.3 µg/ml in pH 6.8 (440). Thus, the erosion variance between ibuprofen and lidocaine/paracetamol can be explained by the difference in their solubilities in the medium; not by the ionisation which if true, would exhibit a difference in pH 1.2.

Table 5-4: Erosion rates ($E_k \pm SD$) of polymers and formulations in pH 1.2 and pH 6.8.

Formulation	pH 1.2		pH 6.8	
	E_k	R^2	E_k	R^2
HPMCAS	-	-	0.64 ± 0.23	0.98
Zein	-	-	-	-
PEO	0.79 ± 1.32	0.94	0.58 ± 0.12	0.98
HPMCAS+Lidocaine 10%	-	-	2.24 ± 0.12	0.98
HPMCAS+Lidocaine 30%	1.19 ± 0.23	0.91	4.91 ± 0.63	0.98
Zein+lidocaine 10%	-	-	-	-
Zein+lidocaine 30%	-	-	-	-
PEO+lidocaine 10%	7.91 ± 1.09	0.95	8.11 ± 1.43	0.95
PEO+lidocaine 30%	3.11 ± 0.87	0.85	5.05 ± 1.56	0.96
HPMCAS+Ibuprofen 10%	-	-	1.63 ± 0.42	0.96
HPMCAS+Ibuprofen 30%	-	-	0.86 ± 0.52	0.97
Zein+Ibuprofen 10%	-	-	-	-
Zein+Ibuprofen 30%	-	-	-	-
PEO+Ibuprofen 10%	3.87 ± 1.34	0.94	5.89 ± 1.18	0.96
PEO+Ibuprofen 30%	2.54 ± 1.23	0.93	4.72 ± 0.92	0.98
HPMCAS+Paracetamol 10%	-	-	1.81 ± 0.83	0.97
HPMCAS+Paracetamol 30%	-	-	3.82 ± 1.19	0.98
Zein+Paracetamol 10%	-	-	-	-
Zein+Paracetamol 30%	-	-	-	-
PEO+Paracetamol 10%	5.33 ± 1.67	0.96	8.08 ± 1.07	0.98
PEO+Paracetamol 30%	4.72 ± 0.84	0.98	7.03 ± 1.15	0.99

5.3.7 Effect of ionisation on overall polymer behaviour

In the preceding sections, the overall effects of the ionisation of the drugs on polymer behaviours were investigated. The dynamics of polymer behaviour and drug release is complex. The ionisation of the drug

affects the drug release of the matrix system compared to the placebo polymer. However, it is more likely that solubility plays a more dominant role than ionisation. The effect of ionisation on polymer behaviour compared to the placebo is summarized in Table 5-5.

5.4 Conclusion

In this chapter, four major parameters were investigated relating to the dissolution behaviour of the formulation in pH 1.2 and pH 6.8. They were hydration, swelling, erosion, and drug release. Three different carrier classes were investigated with three different drugs. The aim was to investigate whether the ionisation of drugs contributed to a difference in the four parameters. It was found that formulations showed differences in hydration ratio and a clear trend based on ionisation was not shown. Higher drug loading increased hydration ratios in some cases. However, the solubility of the drug had a more dominant role. For swelling, the SAPs have the highest swell as well as their formulations. The difference in this swelling behaviour can define a distinguishing criterion for different classes of carriers which is discussed more in detail in the next chapter. The swelling increased for ibuprofen as expected compared to lidocaine. The mechanism of swelling also changed with the drugs (indirectly loss of polymer). Higher loading of hydrophilic drugs caused more anomalous transport. With regards to erosion, solubility seems to be the driving factor for erosion rates with the pH be one of the factors that can alter solubilities of the formulation. It was also observed that very high quantities of hydrophilic drugs can act as a disintegrant.

Variations in drug loadings cause a change of release mechanisms. Addition of higher hydrophobic drug quantities equates to more diffusion controlled release while the addition of hydrophilic drugs leads to more anomalous controlled release. The addition of some hydrophobic drugs to a formulation can give rise to case II transport. In terms of duration of release, SAPs are the fastest and proteins are the slowest. pH responsive formulations are very versatile in this regard. It was also confirmed that if the polymer and drug have identical charges, this accelerates drug release while if they have non-identical charges, this decelerates drug release.

Table 5-5: Polymer behaviour compared for ionised drug loadings. The arrows indicate if the factor is increasing or decreasing as a result. The = sign denotes change of the same magnitude. N/A is noted when the specific factor does not apply to the polymer.

	pH 1.2						pH 6.8					
HPMCAS												
	Hydration		Swelling		Erosion		Hydration		Swelling		Erosion	
Charge	Ratio	Time	Ratio	Time	Ratio	Time	Ratio	Time	Ratio	Time	Ratio	Time
+	↓	↑	N/A	N/A	↑	↑	N/A	N/A	N/A	N/A	↑	↑
-	↓	=	N/A	N/A	N/A	N/A	N/A	N/A	N/A	N/A	↑	↓
0	↓	=	N/A	N/A	N/A	N/A	N/A	N/A	N/A	N/A	↑	↑
Zein												
	Hydration		Swelling		Erosion		Hydration		Swelling		Erosion	
Charge	Ratio	Time	Ratio	Time	Ratio	Time	Ratio	Time	Ratio	Time	Ratio	Time
+	=	=	=	=	N/A	N/A	↓	=	=	↑	N/A	N/A
-	=	=	=	=	N/A	N/A	↓	=	↑	↑	N/A	N/A
0	=	=	=	=	N/A	N/A	↓	=	↑	↑	N/A	N/A
PEO												
	Hydration		Swelling		Erosion		Hydration		Swelling		Erosion	
Charge	Ratio	Time	Ratio	Time	Ratio	Time	Ratio	Time	Ratio	Time	Ratio	Time
+	↓	↑	=	↑	↑	↑	↓	=	=	↑	↑	=
-	↓	=	=	↑	↓	↓	=	↑	↑	↑	↑	=
0	=	↑	=	↑	↑	↑	↑	=	↓	↑	↑	=

Chapter 6: Classification of drug release profiles

6.1 Introduction

In this chapter, the aim is to utilize statistical approaches to analyse the correlations between polymer behaviour and drug release kinetics with an attempt to use such knowledge to develop a prediction tool to aid the development of solid dispersion formulations. The polymer behaviours data gathered in chapter 4 are classified using *K*-mean clustering while the drug release profiles gathered in chapter 5 are first reduced using principal component analysis (PCA) to create a reduced model of drug release profiles followed by *K*-means clustering. This allows the creation of a classified library (shown in the top panel of Figure 6-1). Thereafter, the scenario of achieving a desired drug release profile is investigated where the drug and the drug release duration is known (shown in the bottom panel of Figure 6-1).

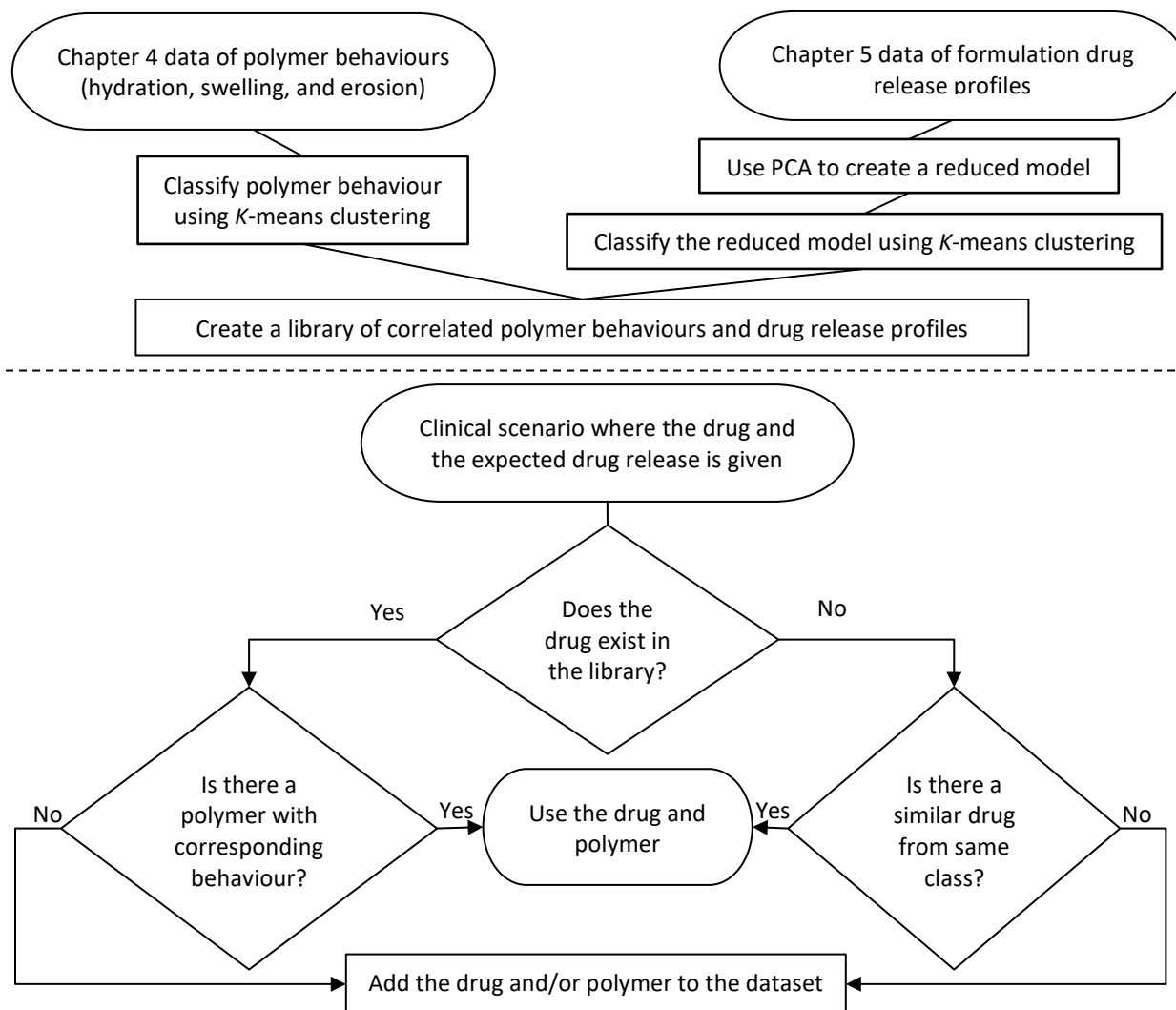


Figure 6-1: Top) The integration of chapter 4 and chapter 5 data to classify the data. The dashed line indicates separation. Bottom) The logical pathway of investigation when the drug and drug release duration is provided for achieving a desired drug release profile.

6.2 Methods

6.2.1 Clustering

K-means clustering, being linear, is faster computational clustering method but and only reduces in speed for a much larger dataset and hence not a problem for the dataset being analysed here (441). Background to *K*-means clustering technique has been discussed in chapter 2. *K*-mean clustering was used on the polymer dataset for all the factors that were measured. The cluster distinguishing criteria was chosen based on the data. The cluster centres gave the value of the factor that is common characteristics of the cluster, which was also obtained from *K*-means clustering. Clustering was performed on SPSS software.

6.2.2 Principal component analysis (PCA)

PCA is a dimension reduction technique that was performed on all the drug release profiles (known as the full model) to create a reduced model. This type of PCA is known as functional PCA (442). Details of the PCA technique has been discussed in chapter 2. The creation of the reduced model is mathematically complex but in a simplified step is given below:

1. All drug release profiles are passed as a data matrix
2. The mean and variance of all the profiles are computed in the matrix
3. Eigenvalue decomposition of the matrix is computed which gives eigenvalues and eigenvectors
 - The eigenvectors are the principal components (PC)
4. The significance of the PC is observed (variation as a probability that is accounted by each PC)
5. The PCs are plotted as profiles. These plotted PC profiles are termed as 'reduced curves'

These reduced curves are important as it gives the underlying most distinct curves that account for most of the variation of all drug release profiles in the full model. Separate PCA was performed for drug release profiles for pH 1.2 and pH 6.8. The number of components for PCA was chosen based on eigenvalues that have a value greater than the value of 1.

A different type of PCA, known as simplified PCA, was used to deduce any difference of any underlying behaviour that distinguishes all the drug release profiles (442). Simplified PCA gives the best possible

representation of a p -dimensional dataset in q dimensions ($q < p$) while being able to account for maximizing variance in q dimensions. Rotations of axis are used to find the best suited axis for q dimensions that minimize the distance to all data points thereby accounting for maximum variance among all the data points. In this case, Varimax rotation was used on the drug release profiles. Loading plots (mentioned in chapter 2 Figure 2-20) created from this PCA, on which further K-means clustering was performed to classify any groups of observations.

6.2.3 Artificial neural network (ANN)

ANN was used on the polymer and formulation dataset. Chapter 2 outlines the details of ANN in general. The input for ANN were all the factors measured and the output was chosen to be t_{50} (half drug release time) in the first scenario and t_{100} (complete drug release time) in the second scenario. ANN procedure resulted in the ranking of the importance of individual factors. This ranking is useful in understanding the effect of each factor in achieving the output (t_{50} and t_{100}). This means that given this ranked list, the most important factor can be varied to have the highest variation of the output. Likewise, the second most important factor has the second most variation on the output. ANN was performed on SPSS software V25.

6.3 Result and discussion

6.3.1 Polymers classification

Polymers behaviours were classified using K-means clustering for hydration, swelling, and erosion. As a reminder, the term hydration is used to describe weight gain and only positive weight gain of the polymer. The aspect on which these behaviours were classified was with respect to the half-life (t_{50}) of the behaviour. Four cluster categories were chosen with each of them representing a different t_{50} interval. Cluster #1 represents no t_{50} of hydration for polymers. Cluster #2 represents short t_{50} (low value) of hydration for polymers. Cluster #3 represents intermediate t_{50} of hydration for polymers and cluster #4 represents long t_{50} (high value) of hydration for polymers. The intervals of clusters are relative to the data available. Since the cluster intervals (high or low or intermediate) are relative to the data, the cluster boundary does not imply an absolute physical interpretation and subject to users' choice of the number of subdivisions such as very low, low, high, and very high t_{50} etc. For example, the boundary between no t_{50} and low t_{50} for

hydration is a value of five minutes. Values greater than five minutes lie within the cluster#2 (no t_{50}) whereas values less than five minutes lie within cluster#1 (low t_{50}). The clusters are shown in Table 6-1 through to Table 6-3 below.

Table 6-1: Hydration t_{50} of polymers

Case	Clusters (pH 1.2)	Clusters (pH 6.8)
1:HPMCAS	1	1
2:PEO	2	3
3:Zein	4	4
4:XG	2	2
5:PCL	1	1
6:Eudragit	1	1
7:PVPVA	1	1
8:PVA	2	2
9:Soluplus	2	2
10:HP/PEO	2	1
11:HP/Sol	3	1

Table 6-2: Swelling t_{50} of polymers

Case	Clusters (pH 1.2)	Clusters (pH 6.8)
1:HPMCAS	1	1
2:PEO	3	3
3:Zein	4	4
4:XG	2	2
5:PCL	1	1
6:Eudragit	1	1
7:PVPVA	1	1
8:PVA	1	1
9:Soluplus	2	2
10:HP/PEO	2	1
11:HP/Sol	2	1

Table 6-3: Erosion t_{50} of polymers

Case	Clusters (pH 1.2)	Clusters (pH 6.8)
1:HPMCAS	1	2
2:PEO	3	3
3:Zein	1	1
4:XG	3	3
5:PCL	1	1
6:Eudragit	1	1
7:PVPVA	4	4
8:PVA	2	2
9:Soluplus	2	2
10:HP/PEO	2	2
11:HP/Sol	1	2

The cumulative classified clusters of all polymer behaviours are presented in Table 6-4 for pH 1.2 and in Table 6-5 for pH 6.8. In both tables, the column denotes the clusters, and the cluster category denotes the characteristics of the cluster. The two tables represent the library of polymer behaviours in the two pH.

Table 6-4: Clusters of all factors for pH 1.2. Polymers of the factors clustered are displayed in the cell unit. The cluster category row indicates the interpretation of each cluster for the preceding factor in the row.

pH 1.2	Clusters			
Factor	1	2	3	4
Hydration	HPMCAS, PCL, Eudragit,	PVA, Xanthan gum, Soluplus PEO, HP/PEO	HP/Sol	Zein
Cluster category	No hydration	Low t_{50}	Intermediate t_{50}	high t_{50}
Swelling	HPMCAS, PCL, Eudragit, PVPVA, PVA	Soluplus, HP/Sol, HP/PEO Xanthan gum	PEO	Zein
Cluster category	No swelling	Low t_{50}	Intermediate t_{50}	high t_{50}
Erosion	HPMCAS, Zein, PCL, Eudragit, HP/Sol	HP/PEO, Soluplus, PVA	PEO Xanthan Gum	PVPVA
Cluster category	No erosion	High t_{50}	Intermediate t_{50}	Low t_{50}

Table 6-5: Clusters of all factors for pH 6.8. Polymers of the factors clustered are displayed in the cell unit. The cluster category row indicates the interpretation of each cluster for the preceding factor.

pH 6.8	Clusters			
Factor	1	2	3	4
Hydration	HPMCAS, PCL, Eudragit, PVPVA, PVA, HP/Sol, HP/PEO	Xanthan gum, soluplus, PEO	PVA	Zein
Cluster category	No hydration	Low t ₅₀	Intermediate t ₅₀	high t ₅₀
Swelling	HPMCAS, Zein, PCL, Eudragit, PVPVA, PVA, HP/PEO, HP/PEO	Xanthan gum, Soluplus	PEO	Zein
Cluster category	No swelling	Low t ₅₀	Intermediate t ₅₀	high t ₅₀
Erosion	Zein, PCL, Eudragit	PVA, HPMCAS HP/PEO, HP/Sol, Soluplus	PEO Xanthan Gum	PVPVA
Cluster category	No erosion	High t ₅₀	Intermediate t ₅₀	Low t ₅₀

6.3.2 Drug release curves classification

The drug release curves of all the formulations are shown in the top left and top right of Figure 6-2 for the two pH. Functional PCA performed on the full model in each pH yielded the most underlying curves that explain most of the variation. The number of components in PCA was chosen to be three as they explained most of the variance in observance. The bottom left of Figure 6-2 shows the reduced curves in pH 1.2. In pH 1.2, Component #1 explained 88.1% of the variance, while component #2 explained 8.8% of the variance, and component #3 explained 1.8% of the variance for a cumulative of 98.7% of the total variation explained. The similarity of the rotated curves to a formulation is given by the coefficient of the rotated component matrix. Only the highest similarity of the generated curve to a formulation is stated here. The curve generated by component #1 is 93.5% similar to HPMCAS loaded with 10% lidocaine. The curve generated by component #2 is 93.7% similar to PEO loaded with 10% ibuprofen. The curve generated by component #3 is 57.7% similar to HPMCAS loaded with 30% ibuprofen. The bottom right of Figure 6-2 shows the reduced curves for pH 6.8. In pH 6.8, Component #1 explained 55.7% of the variance, while component #2 explained 39.4% of the variance, and component #3 explained 3.3% of the variance for a cumulative of 98.4% of the total variation explained. The curve generated by component #1 is 92.9% similar to PEO loaded with 10% lidocaine. The curve generated by component #2 is 95.2% similar to zein loaded with 10% lidocaine. The curve generated by component #3 is 26.7% similar to PEO loaded with 30% ibuprofen. It is observed that even with the number of PCA components chosen to be three, two components explain most of the variance sufficiently reasonably. The drugs which appear in both pH are lidocaine and ibuprofen. Looking at

the coefficient of the rotated component matrix shown in Table 6-6 for pH 1.2 and in Table 6-7 for pH 6.8, the coefficient (values) of paracetamol formulations are close to the lidocaine curves indicating most of the characteristics of the paracetamol formulation can be explained by the lidocaine formulations. Therefore, all the drug release profiles can be explained as a linear combination of ibuprofen and lidocaine, which also explains paracetamol, accounting for 98.7% and 98.4% of the variance in pH 1.2 and pH 6.8, respectively.

Next, the polymers in terms of drug release can be classified by combining PCA and K-means clustering. The number of components was determined using the eigenvalue cut-off approach (eigenvalue >1) which led to two PCA components. In the loading plot that is constructed from the PCA, the components appear as component #1 and component #2, not what the components are. The interpretation of the component is subject to the user's perception of the commonalities that might be shared by the data that lie highly correlated on that specific component axis. From loading plot, component #1 (x-axis) can be interpreted to be the drug release times and component #2 (y-axis) can be taken to be release amount. The loading plot (also known as component plot) of the formulations in pH 1.2 is shown in Figure 6-3.

Table 6-6: Component matrix in pH 1.2

Component Matrix in pH 1.2					
	Component			Component	
	1	2		1	2
HPLido10	0.902	-0.417	HPPara10	0.913	-0.383
HPLido30	0.981	0.134	HPPara30	0.964	-0.254
ZeinLido10	0.963	-0.217	ZeinPara10	0.999	-0.004
ZeinLido30	0.986	-0.155	ZeinPara30	0.986	-0.156
PEOLido10	0.900	0.406	PEOPara10	0.888	0.433
PEOLido30	0.918	0.385	PEOPara30	0.928	0.357
HPIbu10	0.977	-0.130			
HPIbu30	0.979	-0.131			
ZeinIbu10	0.960	-0.261			
ZeinIbu30	0.994	0.081			
PEOIbu10	0.943	0.066			
PEOIbu30	0.924	0.313			

Table 6-7: Component matrix in pH 6.8

Component Matrix in pH 6.8					
	Component			Component	
	1	2		1	2
HPLido10	0.953	-0.291	HPPara10	0.953	-0.291
HPLido30	0.956	-0.283	HPPara30	0.890	-0.352
ZeinLido10	0.798	0.569	ZeinPara10	0.806	0.568
ZeinLido30	0.875	0.482	ZeinPara30	0.875	0.482
PEOLido10	0.955	-0.248	PEOPara10	0.955	-0.248
PEOLido30	0.966	0.004	PEOPara30	0.961	0.088
HPIbu10	0.974	-0.168			
HPIbu30	0.988	0.044			
ZeinIbu10	0.955	0.263			
ZeinIbu30	0.969	0.205			
PEOIbu10	0.940	-0.304			
PEOIbu30	0.912	-0.303			

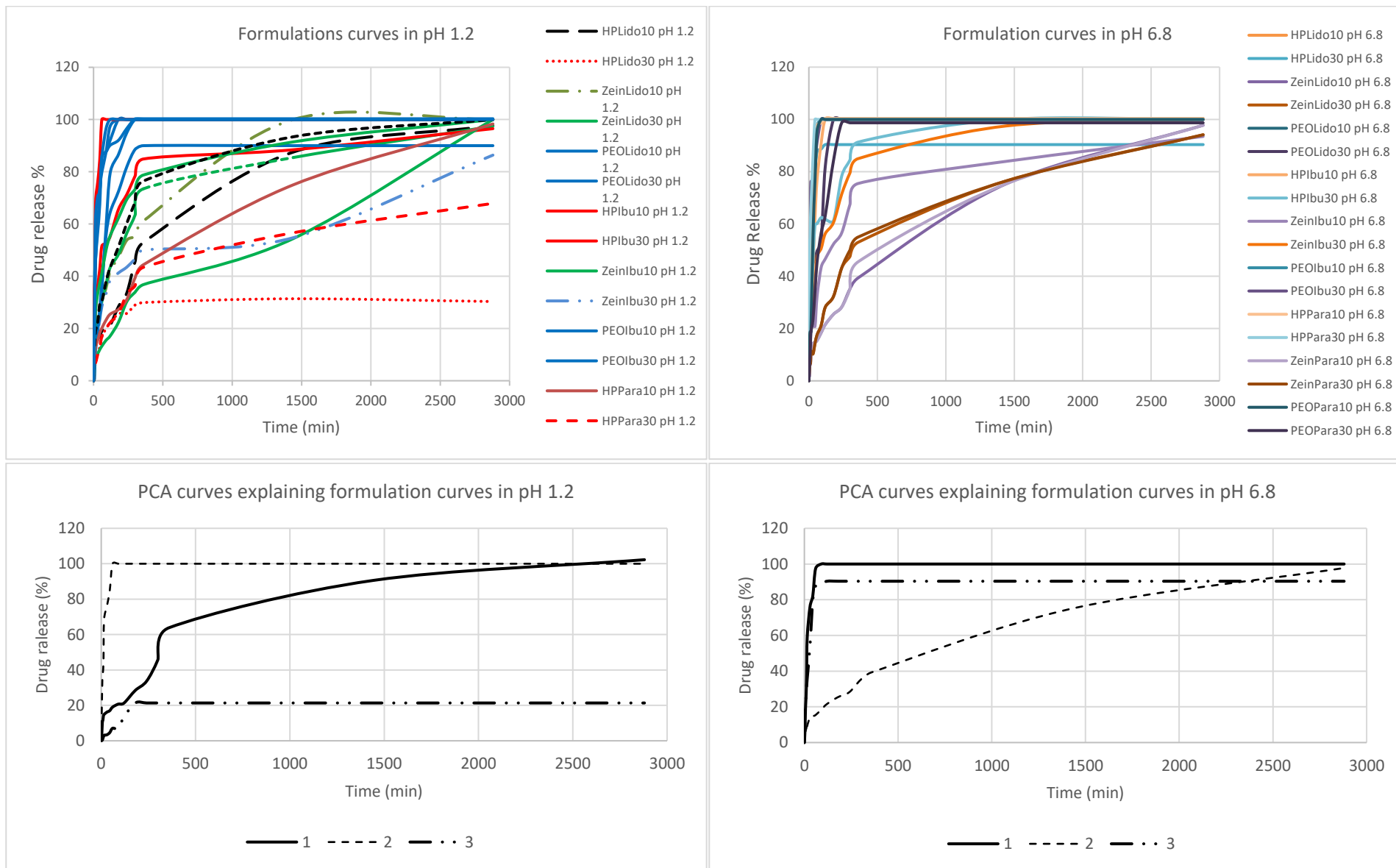


Figure 6-2: Top left) Formulation curves in pH 1.2. Top right) Formulation curves in pH 6.8. Bottom left) PCA performed curve in pH 1.2. Bottom right) PCA performed curve in pH 6.8

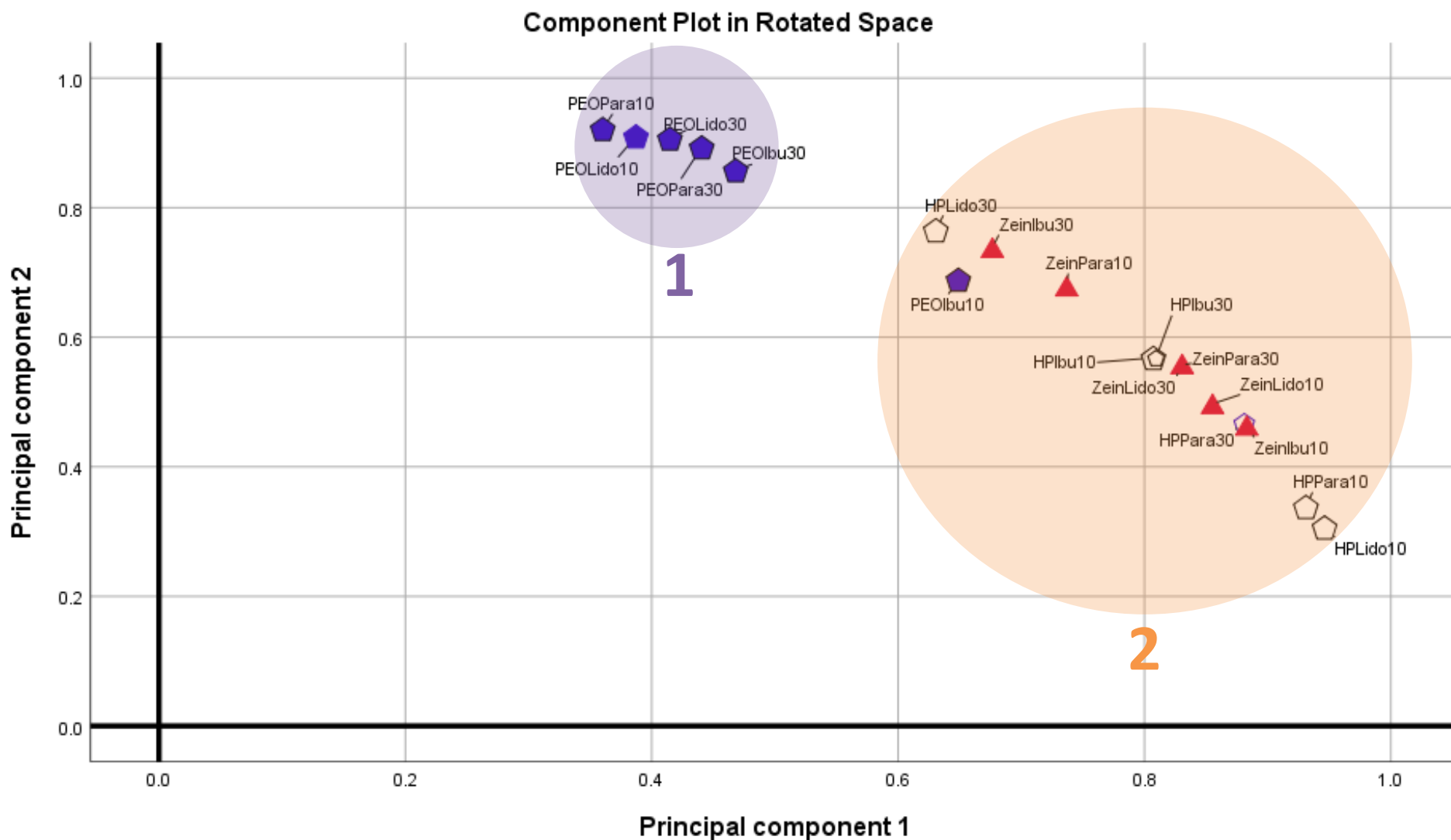


Figure 6-3: PCA rotated loading plot of formulations in pH 1.2. Greater values of PC 1 possibly represent longer release times of formulations and greater PC 2 values possibly represent higher amounts of drug released of the formulations. The rotation method chosen was Varimax rotation. K-means Clustering was done on the points. Clusters numbers are labelled below the cluster.

It can be observed that all the data in Figure 6-3 lie within the first quadrant of the graph where both x and y are positive. Neither release time nor release amount can be negative excluding the possibility of any data in any other quadrants. It can be observed that PEO based formulations have shorter drug release times and achieve a higher drug release in that time frame relative to other formulations. Therefore, PEO polymer can be clustered in terms of drug release in that region of the plot. HPMCAS and zein form the other cluster as zein is very slow in drug release times and release less amount in that time relative to PEO formulations. HPMCAS is insoluble and for all practical purposes, attain the same effect as zein for drug release. Two clusters represent were formed based on the distance to the nearest neighbour. Cluster #1 seem to contain PEO while cluster #2 contains zein and HPMCAS. 10% ibuprofen loaded with PEO seems to be an outlier and is within the region bounded by cluster #2, which in this case is miscategorized.

In pH 6.8, a clear distinct clustering is harder for the polymers. One polymer to note is HPMCAS which is erodible in pH 6.8 has shifted towards PEO in the loading plot of pH 6.8, shown in Figure 6-4. Moreover, three clusters formed can be seen. HPMCAS can be grouped with PEO mostly. Cluster #2 contains both zein, HPMCAS, and PEO. Therefore, a general categorization of polymers may not be possible based on clusters directly. However, one modification that could be done is to calculate the number of polymer formulations that fall within each cluster. If the majority of polymer lies in a cluster, cluster #2 data can be attributed to that cluster. So, for zein formulations, four samples fall in cluster #1 and two samples fall in cluster #2. Based on this, cluster #1 contains 66% (4/6) of the zein samples. Therefore, the two zein formulations from cluster #2 can be taken to be part of cluster #1. Likewise, calculations for PEO and HPMCAS lead to all formulations of cluster #2 to be allocated to cluster #3. The clustered polymers in terms of PCA component interpretation from Figure 6-3 and Figure 6-4 is sorted in Table 6-8.

Table 6-8: Polymer categorization from PCA components for drug release

	Drug Release times		Drug Release amount	
	Short	Long	Low	High
pH 1.2	PEO	Zein, HPMCAS	Zein, HPMCAS	PEO
pH 6.8	PEO, HPMCAS	Zein	Zein	HPMCAS

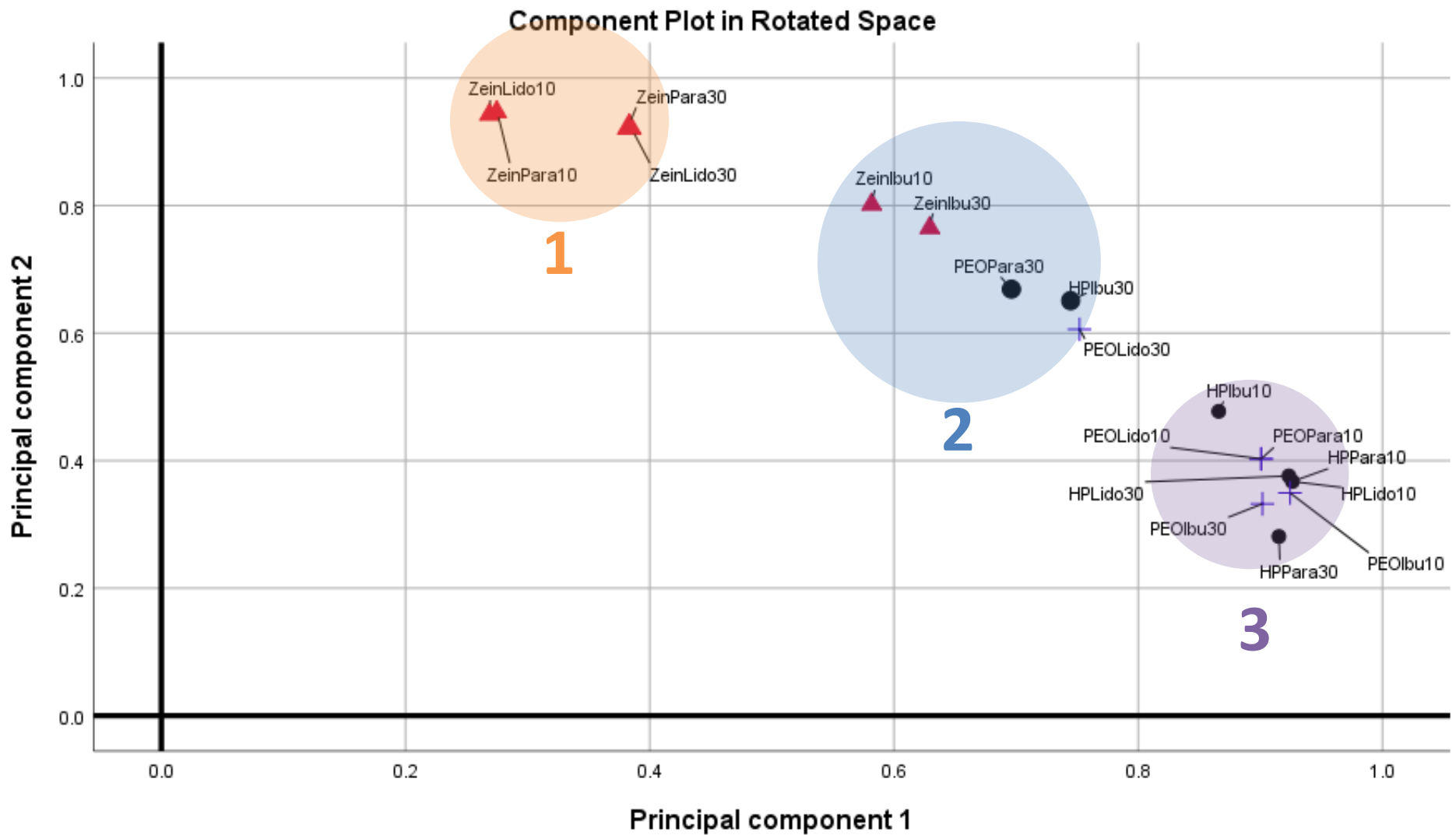


Figure 6-4: PCA rotated loading plot of formulations in pH 6.8. Greater values of PC 1 possibly represent higher amounts of drug released of the formulations and greater PC 2 values possibly represent longer release times of formulations. The rotation method chosen was Varimax rotation. K-means Clustering was done on the points. Clusters numbers are labelled below the cluster.

6.3.3 Relating polymer behaviour clusters to drug release clusters

In sections 6.3.1, the classification of polymer behaviour kinetics which was based on hydration, swelling, and erosion was performed. These classification schemes have not been related to drug release. This is crucial as the aim is to be able to extrapolate a drug release profile based on the polymer behaviour kinetics. The pathway to relating is shown in Figure 6-5.

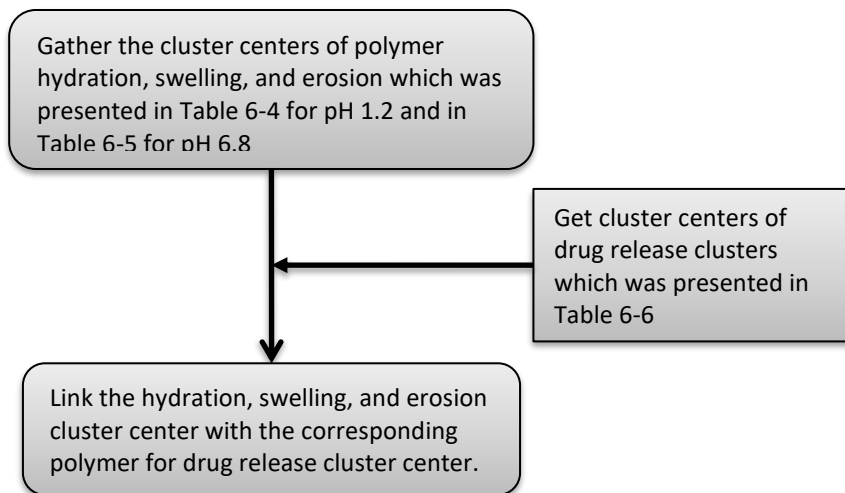


Figure 6-5: Concept of associating polymer behaviour with drug release

So far, the cluster centre information for hydration, swelling, and erosion was omitted but is now enlisted in Table 6-9 for this part of the analysis, which was obtained from *K*-mean clustering. These cluster centres give a single quantified value of the appropriate constants being measured (hydration, swelling, and erosion), which is an approximated value and a common characteristic of all the polymers in that cluster. The cluster centre of the drug release is based on the drug release time and drug release amount.

Table 6-9: *K*-means cluster centres for factors from *K*-means clustering in pH 1.2 and pH 6.8.

	Cluster #1	Cluster #2	Cluster #3	Cluster #4
	No effect	Low t_{50}	Intermediate t_{50}	High t_{50}
pH 1.2				
(Low \longrightarrow High) in minutes				
Hydration	0	24	210	728
Swelling	0	17	25	728
Erosion	0	30	45	86
pH 6.8				
(Low \longrightarrow High) in minutes				
Hydration	0	20	190	728
Swelling	0	26	38	728
Erosion	0	40	52	80

Cross relating Table 6-8 and Table 6-9 in terms of cluster centre yields the main dataset library, shown in Table 6-10, which links the cluster centre of drug release and polymer behaviour.

Table 6-10: Clusters relating polymer behaviour and drug release summarized. The basis of effect interpretation (low, high, etc.) is based on the cluster distinction as noted in Table 6-4 and Table 6-5. The effect interpretation of release time and amount from the clustering of the loading plot is introduced here.

pH 1.2					
	Hydration t₅₀	Swelling t₅₀	Erosion t₅₀	Release time (min)	Release amount (%)
Zein	728	728	0	2304	40
<i>Effect</i>	<i>High</i>	<i>High</i>	<i>None</i>	<i>Slow</i>	<i>Low</i>
HPMCAS	0	0	0	2304	40
<i>Effect</i>	<i>None</i>	<i>None</i>	<i>None</i>	<i>Slow</i>	<i>Low</i>
PEO	24	25	50	146	96
<i>Effect</i>	<i>Low</i>	<i>Intermediate</i>	<i>Intermediate</i>	<i>Fast</i>	<i>High</i>
pH 6.8					
Zein	728	728	0	2649	39
<i>Effect</i>	<i>High</i>	<i>High</i>	<i>None</i>	<i>Slow</i>	<i>Low</i>
HPMCAS	0	0	160	72	95
<i>Effect</i>	<i>None</i>	<i>None</i>	<i>Intermediate</i>	<i>Fast</i>	<i>High</i>
PEO	20	38	52	72	95
<i>Effect</i>	<i>Low</i>	<i>Intermediate</i>	<i>Intermediate</i>	<i>Fast</i>	<i>High</i>

With Table 6-10, it is possible to proceed to the different scenarios of achieving a desired drug release profile. Three possible scenarios can arise. In all the scenarios, it is first important to be able to find the closest resembling ‘reduced curve’ which is similar in the time scale and quantity. The ‘reduced curves’ are found in the bottom of Figure 6-2 for the two pH. Scenarios I is where the drug and the desired drug release profile (which is dictated by the polymer) exists in the library. Scenarios II is where the given drug does not exist but a drug from a similar class exist in the library the desired drug release profile does exist in the library. Scenarios III is where neither the drug nor desired drug release profile exists in the library.

6.3.4 Scenario I

In this scenario, the drug, and the drug release profile both exists in the library. As an example, the choice of drug is lidocaine and the chosen pH is pH 1.2. The chosen drug release profile is a fast drug release profile similar to the reduced curve by component #2 in the bottom left of Figure 6-2. The polymer this ‘reduced curve’ has is PEO. Therefore, the choice of polymer, in this case, would likely be PEO. Moreover, additional reconfirmation is obtained from Table 6-10, where the fast drug release is associated with PEO polymer for

pH 1.2. It could have been any other polymer that shares the commonality of fast release (if the data library of Table 6-10 had more polymers). Thus, for comparison, the experimental lidocaine loaded PEO formulation drug release profiles in pH 1.2 are given along with the predictor curve, which are shown in Figure 6-6. The predictor curve is a 'reduced curve' but the naming switches as it is used for prediction here.

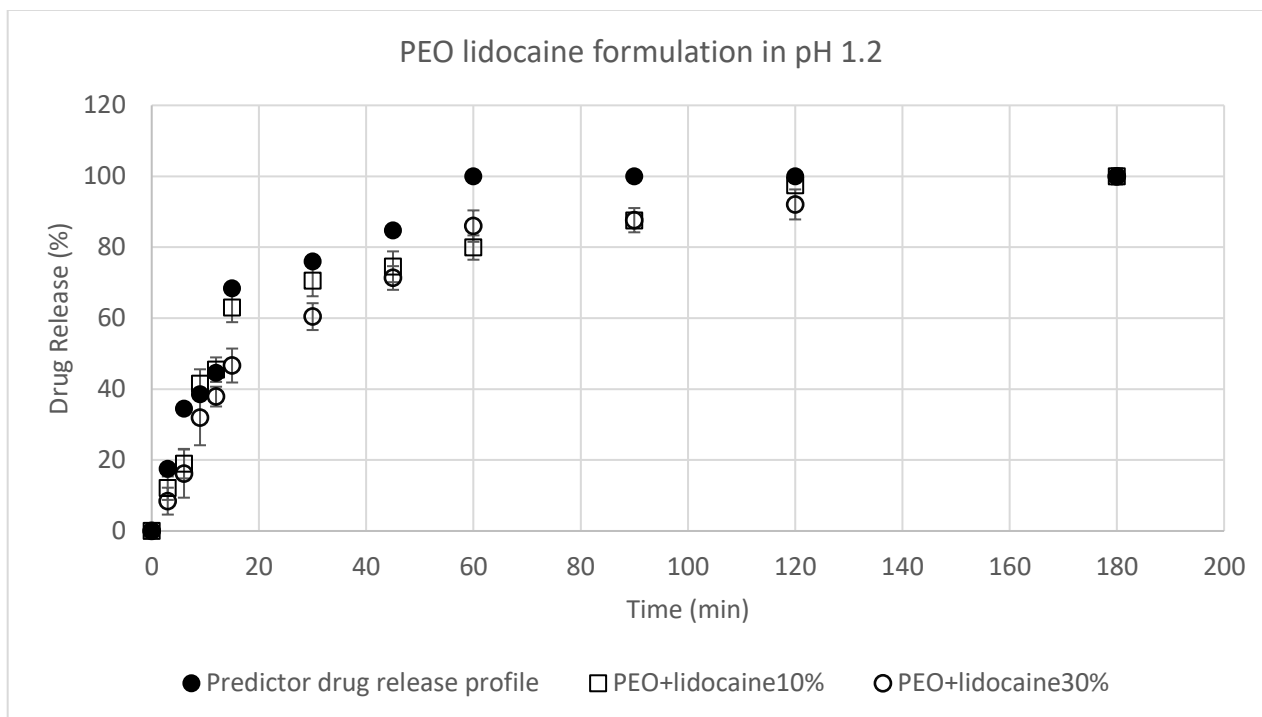


Figure 6-6: PEO-lidocaine experimental and predictor curve compared in pH 1.2

6.3.5 Scenario II

Scenario II is where the drug does not exist in the library but the desired drug release profile does exist in the library. In this scenario, logic would be to predict with another drug release profile which would achieve the identical desired release profile. For this, the first step would be to locate if a substitute drug exists in the library. A well established classification system for drugs is the Biopharmaceutics Classification System (BCS) which consists of four classifications based on solubility and permeability (443, 444). In BCS, the drugs are grouped in four classes with class I being drugs possessing high solubility and high permeability, class II consisting of drugs possessing low solubility and high permeability, while class III consisting of drugs possessing high solubility and low permeability, and class IV consisting of drugs possessing low solubility and low permeability (445). The solubility and permeability in BCS refer to aqueous solubility and intestinal membrane permeability, respectively. Placement of the three drugs (paracetamol (446, 447), ibuprofen

(448, 449), and lidocaine(450)) and other drugs gathered from secondary sources (445) in the BCS are shown in Figure 6-7.

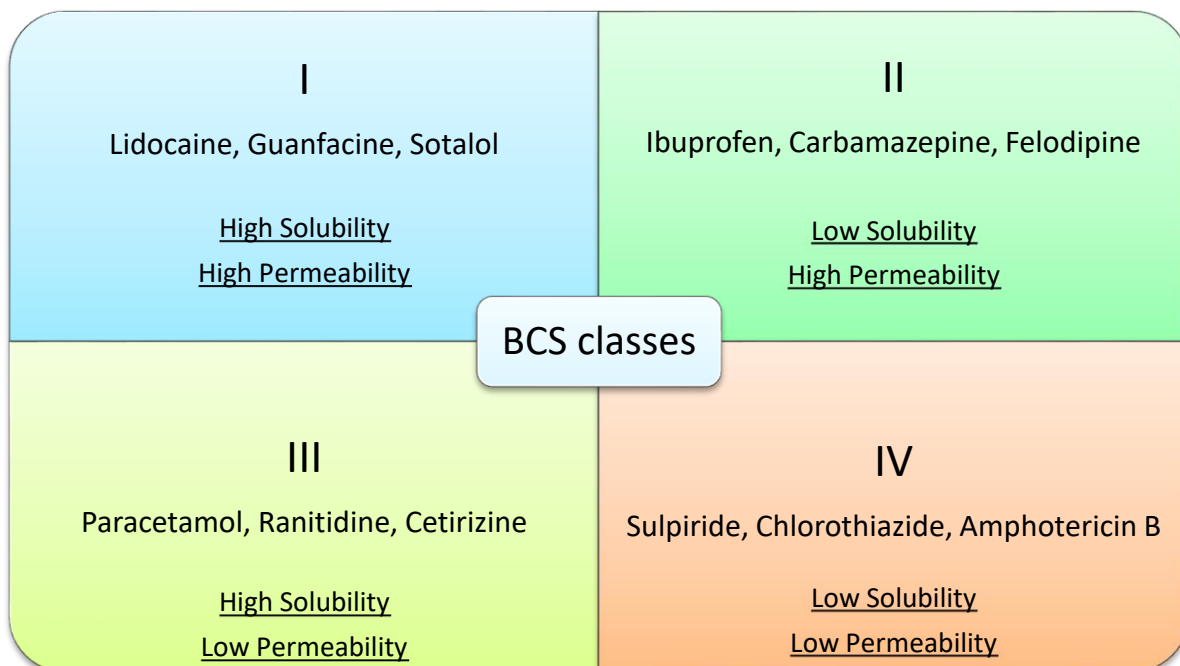


Figure 6-7: Some drugs in the BCS system

An example of scenario II, the chosen drug will be ranitidine, which does not exist in the dataset library in Table 6-10. However, a similar BCS class III drug, paracetamol, does exist in the dataset. The chosen duration of drug release is chosen to be a long duration and the chosen pH is pH 6.8. From Figure 6-2, the only 'reduced curve' which resembles the desired characteristics is that of component #2. That particular curve most resembles is that of zein loaded with 10% lidocaine with a resemblance is 95.2%. Even though from this, it can be deduced that the most likely polymer which should be used is zein, confirmation from Table 6-10 is desired. This indeed is zein from Table 6-10. Therefore, zein formulations with paracetamol can be used to predict the drug release of zein with ranitidine in pH 6.8. Bouman et al investigated zein loaded with 22.2% ranitidine in pH 6.8 (14). The drug release profile obtained from that work will be used for comparing the 'reduced curve', which is used as the predictor curve (term changed based on the perspective of usage criteria), for this work. This is shown in Figure 6-8. Interestingly, zein with 22.2% paracetamol loading in pH 6.8 was also obtained by Bouman et al (14). This is added for comparison of the two paracetamol formulation but not the main focus of Figure 6-8. Scenario III arises when the drug or drug

release profile does not exist in the dataset. In this case, the drug with a polymer that would exhibit similar drug release duration would need to be experimentally performed and added to the dataset.

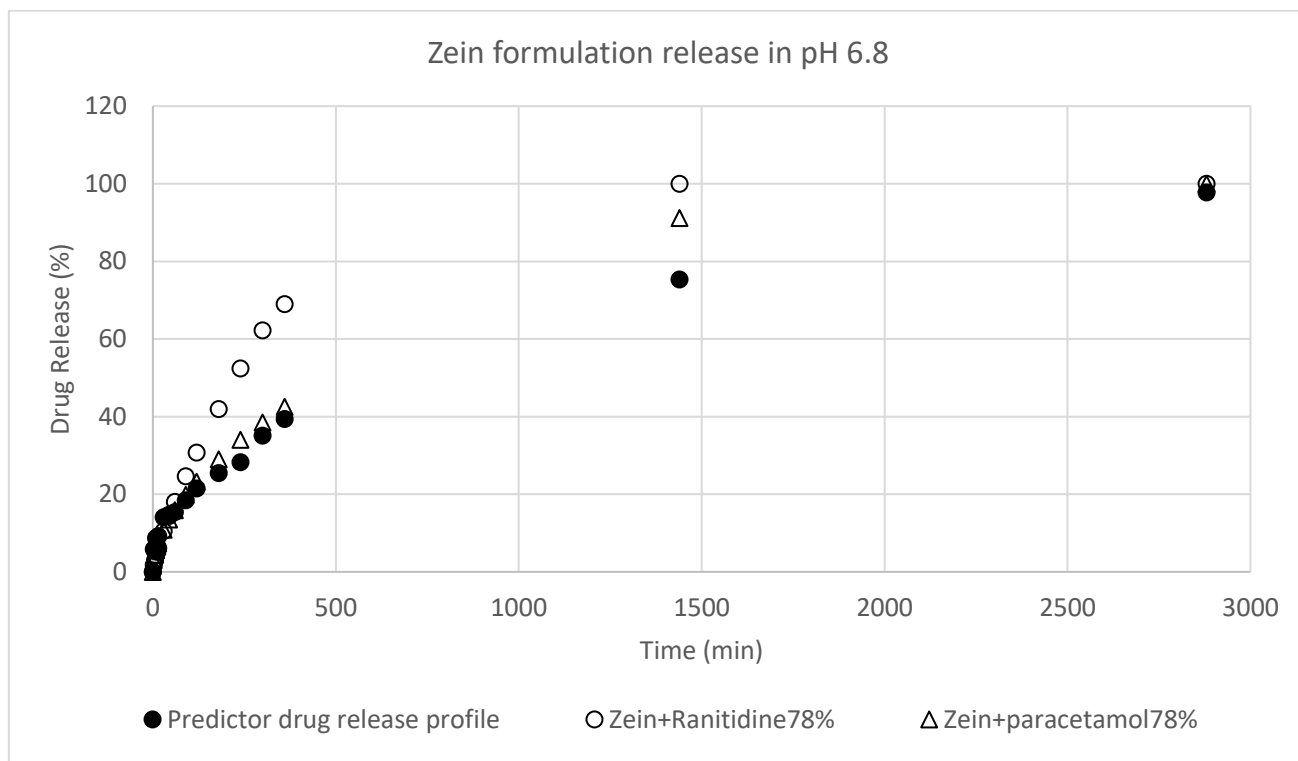


Figure 6-8: Paracetamol loaded zein formulation and predictor curve compared in pH 1.2

6.3.6 ANN as a predictor refinement technique

ANN can be used to rank order the importance of all the inputs in relation to the output. The ranking of the inputs will aid in understanding which factor(s) can be altered to achieve the most variation of this outcome, and thus achieving a refined more accurate desired outcome. ANN was used with the outcome being 'drug release time', shown in Figure 6-9. In this case, there was one hidden layer for performing internal neural network process but however cases of two or three hidden layers have also been performed (451). The outcome, in this case, is also a single factor but cases of two or more factors have been performed (452). Four inputs were provided but the ANN process always automatically adds a bias input. The variable ranking of this particular ANN process is shown in Figure 6-10. However, due to the number of data points, an issue of reproducible consistent results exist. It can be seen that as the ANN process is run, the ranking of the variables differs. Therefore, deducing which variable has the highest effect based on these few runs would be a false deduction. Nevertheless, this approach will produce accurate consistent ranking if the number of observations (data points) for each variable is sufficiently large.

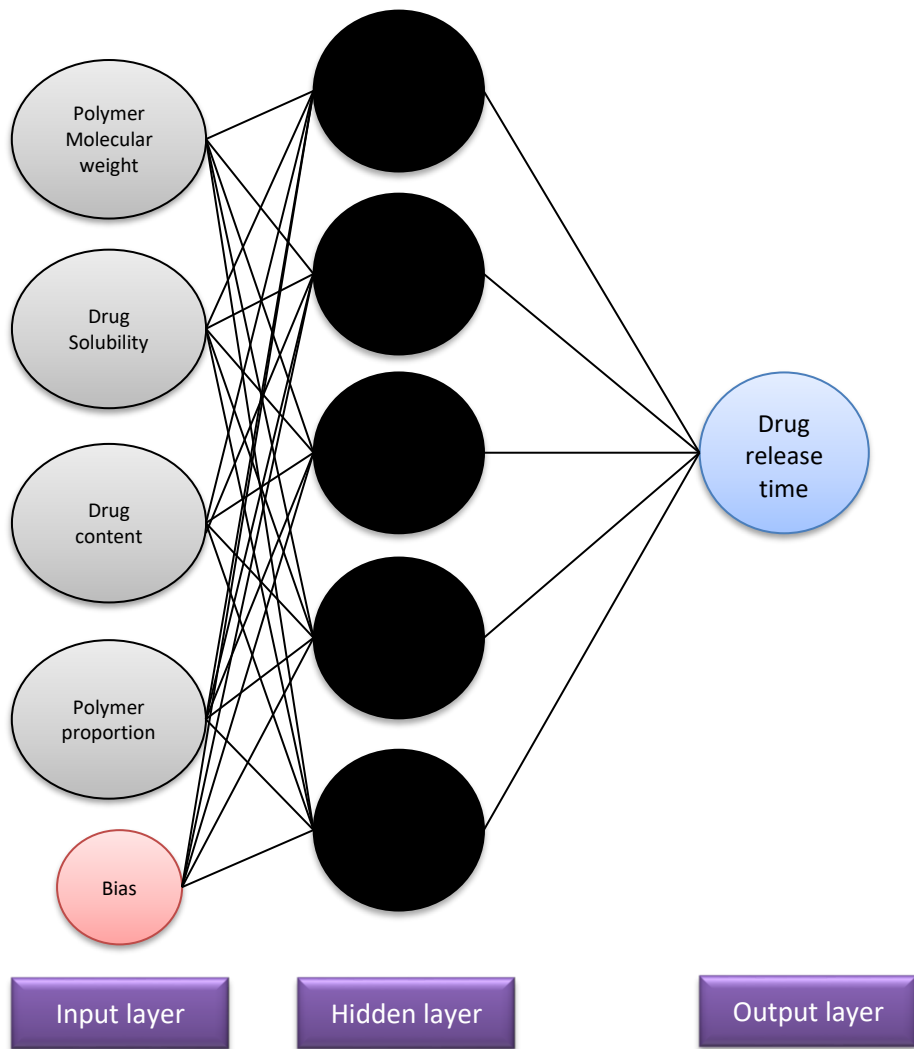


Figure 6-9: ANN performed for the output of drug release time in pH 1.2 with four inputs. The bias is automatically added by ANN.

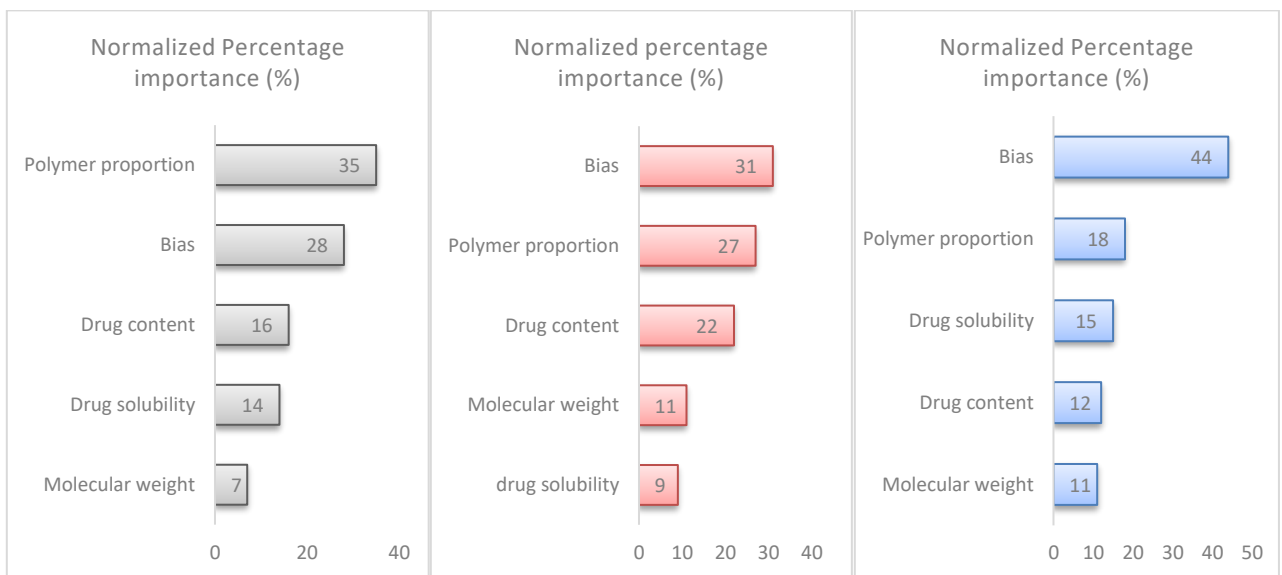


Figure 6-10: Normalized ranking of input factors from ANN

6.4 Limitations

Several limitations exist in the approach used. First, as mentioned, the usage of clustering causes loss of individual attributes and only a cluster-wide common property exists for the cluster such as cluster common hydration constant, or cluster common drug release amount, etc. However, the hope of using clusters is that on large scale varying datasets, common properties can be found to categorize subsets of data. There were cases where cluster miscategorized dataset from PCA component reduction. Numerous classification techniques are being developed to improve categorization (453). Using clusters was the dominant technique in this chapter. This caused the introduction of errors in the form of miscategorization. The proposed method of reducing miscategorization is adding more dataset of with varying nature. This causes more clusters to be created, which can not only reduce errors but give emergence to explain the data more refined. Another limitation was the correlating polymer hydration, erosion, and swelling to the drug release based on clusters. It was not possible to directly relate these factors to drug release constant or drug release index as was shown in chapter 5. A sense of how the drug ionization affects polymer hydration, swelling, or erosion kinetics was summarized in comparison to the pure polymer kinetics. The degree of correlating aspects is less objective to deducing an analytical equation, which has a high degree of objectivity and strict restrictive underlying postulations. The limitation observed with the use of ANN is with the number of data points available and usually preferred by ANN. ANN is capable of learning and predicting indicators to a specific outcome but with a sufficiently large number of data points.

6.5 Conclusion

In this chapter, the method of *K*-mean clustering was used to classify the polymers in terms of polymer behaviour, which included hydration, swelling, and erosion. The interpretation of the classification arose from the data extremes, with one extreme being labelled high and other no observed effect.

Functional PCA was applied to create a reduced model of the full model consisting of all the drug release profiles. This resulted in three curves that explained about 98% of the variances in both pH. Additionally, simplified PCA was performed on all drug release profiles to deduce any distinguishing characteristics of the

polymers and the drugs. Two principal components were chosen based on eigenvalues that had values higher than one, from which loading plots were created. The interpretation of the two principal components was taken to be drug release time and drug release amount. Further *K*-means clustering on the loading plots deduced clusters and their centres which yielded quantitative information about the polymer behaviour, such as common hydration or common swelling ratio, and drug release parameters, such as drug release times and drug release amount, in that cluster, which was correlated. Thereafter, the drug release profile was generated using the PCA 'reduced curve' acting as 'predictor curve'. Several limitations were discussed which affect the possibility of error in the created drug release profile. In the next chapter, further improvements, and areas of investigation to the scope of work in this thesis will be discussed.

Chapter 7: Conclusion remarks and future outlook

Controlled drug release systems (CDRS) deliver the drug locally or systemically at a predetermined rate for a specified duration (454, 455). 3D printing has shown promising potentials of being used to manufacture CDRS. Drug release from CDRS is often dependent on polymer properties. Therefore, a thorough understanding of the drug and polymer's properties and their interactions will facilitate the production of highly reproducible CDRS with the desirable drug release kinetics (456). This indicates two areas of research for improvement: reproducibility and predictability. This was the overarching theme of this work. The issue of reproducibility is related to the minimization of errors that arise during the manufacture and the measurement of the performance CDRS. The issue of predictability is related to polymer, drug and the formed solid dispersion properties and any pharmacokinetic models used to attain the drug release. The reproducibility of CDRS was investigated in chapter 3, and the predictability was investigated in chapters 4 through to chapter 6.

7.1 Reproducibility

Error in the measurement of the drug release profile is unavoidable. In some publications, the error is reported to be as large as $\pm 30\%$ (31). Commercial software such as GastroPlus reports errors based on user's chosen confidence intervals (CI) (200, 202). In this case, a range is defined such that the measurement is within the range (interval) with the specified probability (confidence). For example, a 95% CI indicates that 95% of the measurement from the true mean of the samples exist within that interval.

The sources of error in the drug release profile of 3D printed solid dosage forms was investigated in chapter 3. The sources of error arose from each of the manufacturing steps and the measurement of the drug release at termination. The manufacturing steps included using hot melt extrusion (HME) coupled with 3DP. The drug release profile was measured by using a dissolution machine and subsequently a UV spectrometer and parametrised by the Peppas equation. Since the Peppas equation relates to the initial drug mass and sampled time drug, estimation of errors in drug mass or inferred drug mass from the equipment were substituted in the Peppas equation. The source of error in initial drug mass came from HME and 3DP and

the source of error in sampled drug mass at a sampling timepoint came from the entire process of dissolution and sampling using the UV spectrometer. Two cases arose for the initial drug mass: one was the direct error estimation from weighted 3DP samples and the other was the estimation of error in drug mass from the volume of the 3DP sample in the absence of direct weighing. In the latter case, the drug mass was inferred using the drug mass uniformity from HME technique while verifying that the 3DP process step did not significantly alter the drug mass.

While identifying the sources of error, it was also possible to identify the types of errors in each step. The types of error were systematic and random error. The systematic error indicates the accuracy of the equipment while random error reflects the precision of the equipment. Modifications to the procedure can help minimize the systematic error. Some of the modifications were discussed in the chapter such as optimizing the residence time of HME or optimum temperature to achieve the optimum melt flowability of the filament for 3DP. Further suggestion can include making the HME-FDM a continuous one step process. This can help reduce systematic error observed for die shrinkage from two dies (HME and 3DP stage) to one die (3DP stage). A schematic of this is presented in Figure 7-1.

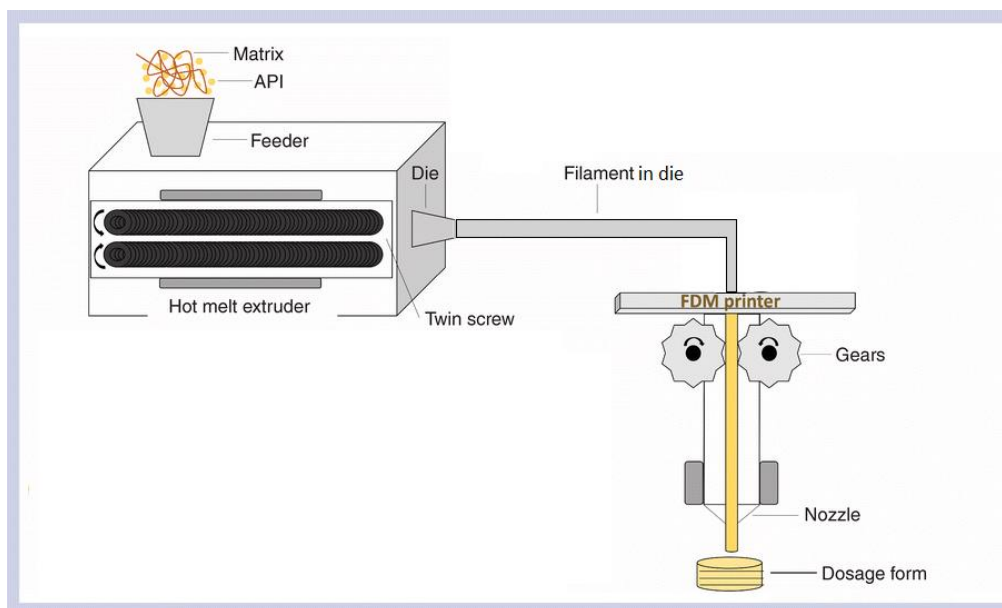


Figure 7-1: HME-3DP as a continuous process. The die through which filament exits the HME is also the beginning of the 3D printing process. Adapted from reference (457).

Systematic errors for dissolution machine that are process related can include sample introduction and multiple point sampling. Samples introduction in the dissolution vessel can be tricky and may not be able to

be performed reproducibly. Samples can have a dissolution rate that is position dependant. For example, if the sample is off-centre, the dissolution rate is high due to shear forces. Alternative, if it is in the centre, coning may occur and the dissolution rate will be lower (458). Such behaviour can be observed in the tori that were used for triplicate studies, which is shown in Figure 7-2. Multiple sampling time points are also an issue. A study conducted by Zhang et al of BCS Class II drug formulations determined that multiple sample pulls from the dissolution vessel when compared to a single-pull resulted in different dissolution rates (459). This could be caused by the additional insertions and residence of the sampling probe in the vessel during multi-point sampling which subsequently causes disturbance of fluid hydrodynamics in the dissolution vessel (458). Hydrodynamic conditions are crucial to the drug release rate (460, 461).

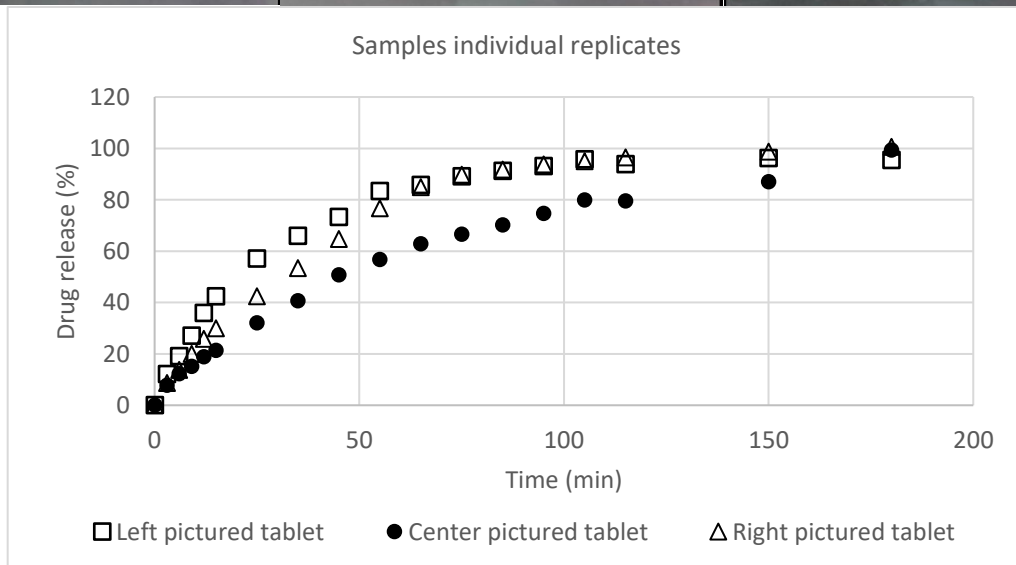
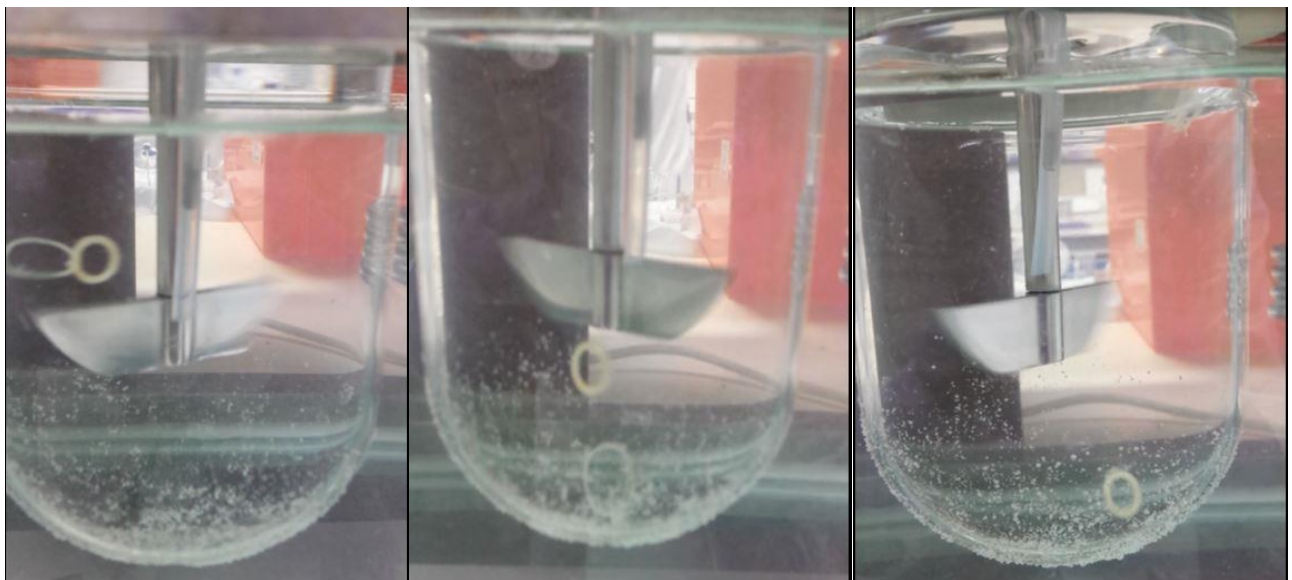


Figure 7-2: The individual sample in different positions during the dissolution after the sample was introduced. The individual drug release profile is shown before the mean is calculated.

Random errors that arise can be minimized with the technological advancement of equipment. More sophisticated HME, 3DP, UV that improve precision will reduce the random variation. Using the cumulative drug release equation, in terms of process error, obtained in chapter 3, the reduced error will lead to a more accurate and precise drug release error estimate which would be valid for any generic sample prepared using the HME-3DP coupled method. Table 7-1 summarises the two types of irreproducible behaviour, which are either manufacture or measurement related, observed in this thesis.

Table 7-1: Summary of the types of irreproducibility and the proposed solution in each case.

Irreproducibility	Solutions
<u>Measurement</u>	
• Calibration curves	• Using multiple calibration curves (minimum three)
• Number of samples	• More than three samples if intra-sample variation is high
• Sample position	• More samples if inter-sample variation is high
• Number of sampling pulls	• Less multiple pulls recommended
• 3D object drug content estimation	• Estimate drug content from weighing samples compared to estimating from volume
<u>Machine</u>	
• Sampling method	• Automated sampling better than manual sampling
• Manufacture process type	• Continuous coupled process (HME+3DP) or (<i>In Vitro</i> +UV) reduces the irreproducibility
• General improvement of machine	• Better precision of all readings across all machines

Some areas can be further investigated for reproducibility of 3D printed samples. Currently, there is no data on an optimum temperature difference between the printing temperature and platform temperature. Further investigation of this which will cause an improvement of systematic error observed for the volume of 3DP sample fluctuating from the design specification.

7.2 Predictability

Predictability was the other key area of this work. Predictability can be divided into three parts. The first is being able to predict the behaviour of the carriers of the formulation, which are the polymers. Chapter 4 investigated the hydration, swelling, and erosion of some common polymers used in 3D printing. The focus was to be able to predict the behaviour, using an ideal polymer mixture model, for a 50/50% w/w miscible and semi-miscible blend that was prepared from two of the individual polymers studied. It was found that ideal polymer mixture laws would only be able to predict a specific behaviour if the constituting polymers

exhibited the same characteristic behaviour in the solvent. For example, the erosion could be predicted for HPMCAS/PEO and HPMCAS/Soluplus blends since HPMCAS, Soluplus, and PEO erodes. Since PEO swells but HPMCAS does not swell, the swelling for HPMCAS/PEO blend could not be predicted.

This approach highlighted the benefits and limitations. The benefit would be that if the ideal mixture laws are valid, then it would be valid for any proportion of the blend. The limitation was due to the parametrisation approach used wherein even if the blend behaviour could be predicted by the semi-empirical model, the model does not yield any insights about the mechanisms of blend behaviour. Also, blend behaviour can only be predicted if the individual polymer behaviour is known. In cases where the approach of ideal polymer mixture laws is invalid, a different approach is required. An alternative approach such as using the solubility parameter could be used. However, an issue exists that there is no good theory that predicts the behaviour of polymer blends generally in the same way that there is no general theory of liquid mixtures so the hope of a unifying theory is unpropitious.

The second part of attempting prediction is being able to predict polymer behaviour in the presence of drugs. Chapter 5 investigated polymer behaviours in the presence of selected drugs. The hypothesis was that ionisable drugs affected the polymer behaviour compared to non-ionised drugs. The effect of ionisation was summarized and, in some cases, significant differences were observed while in other cases, no significant differences were observed. Several limitations existed. It was assumed that drugs do not interact with a polymer to form any drug-polymer complex. Classification and clustering were used to deduce any trend that may exist between the drug release, types of drug, and polymer behaviour. The third part of predictability is to be able to use a mathematical equation that reliably parametrises the drug release. Based on the parametrisation, a model can be used to predict unexperimented drug release profile. Deducing better equations can better predict the drug release with more accuracy and precision but this was not the focus of this work. The Peppas-Korsmeyer equation was used in this work which explains the drug release reasonably well. All data gathered in chapters 4 and 5 were used to create a dataset.

Chapter 6 investigated any trend in drug release profiles and polymer behaviour based on the dataset created. This was achieved by using a classification based on clustering, and principal component analysis (PCA). The first step was the classification of polymer behaviour. PCA performed on the drug release profiles yielded the most distinct reduced curves amongst all formulation curves. This yielded a trend in the drug release profiles based on the quantity released in a given time. Once again, it was observed that drug release is dominated by polymers rather than drug types or drug ionisation. However, pH-sensitive HPMCAS did not follow a clear trend. *K*-mean clustering was further performed on the PCA drug release curves which deduced that HPMCAS formulations are loosely clustered to zein formulation in pH 1.2 but form a different cluster in pH 6.8. The reason for this is, in pH 1.2, HPMCAS is insoluble and shares drug release profile that resembles zein formulation, which is very slow to achieve half release or complete release of the drugs. In 6.8, the HPMCAS formulation resemblance is less like zein and more to PEO formulation but still not close enough to be clustered together with PEO formulation. Although this was successful for the dataset used, a logical extension to this approach would be to be able to predict the desired release profile for any given drug. The bottleneck limitation of the approach occurred at this stage. To be able to predict drug release for any drug, the scale of the dataset has to be sufficiently large and contain a diversity of the drug types and the different polymers candidates, which is discussed next.

7.3 Future works

This section discusses some of the future research areas that can help build on the concepts. These include scaling, simulation, and their potential applications in the design of personalization.

7.3.1 Scaling

A problem that arises with a dataset that is less than optimum is that higher sensitivity to outliers or erroneous data points exists which lead to overfitting, poor generalization, large bias, and variance (462, 463). Figure 7-3 attempts to summarize some issues associated with small datasets.

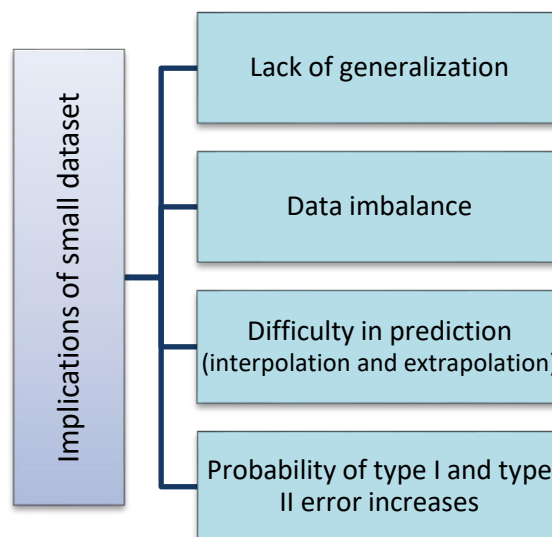


Figure 7-3: Problems encountered with small datasets for analysis. **Type I error** is the rejection of a true null hypothesis while a **type II error** is the acceptance of a false null hypothesis, which occurs in statistical hypothetical testing.

Several methods exist to handle small datasets such as data augmentation, regularization, using confidence intervals, using simpler fitting models to the data, using ensemble approach among others (464). Yet, it has been suggested that the most efficient method is to increase the dataset size (463). With a large, general diverse dataset, additional refinement for the drug release prediction can become possible through deep machine learning (335, 462, 465). An example of deep learning is the artificial neural network (ANN), which has already been applied in chapter 6 and other works predicting drug release profiles (336). Furthermore, ANN is more efficient in learning and predicting any given outcome with scaling up the dataset. ANN is designed to be trained with existing data and predict for new additional untested data. This type of growth of data over time across sectors is known as consortium approach (464).

7.3.2 Simulation

Finally, the simulation will put the prediction into a meaningful application and speed up the process of dosage form development. A possible pipeline is shown in Figure 7-4.

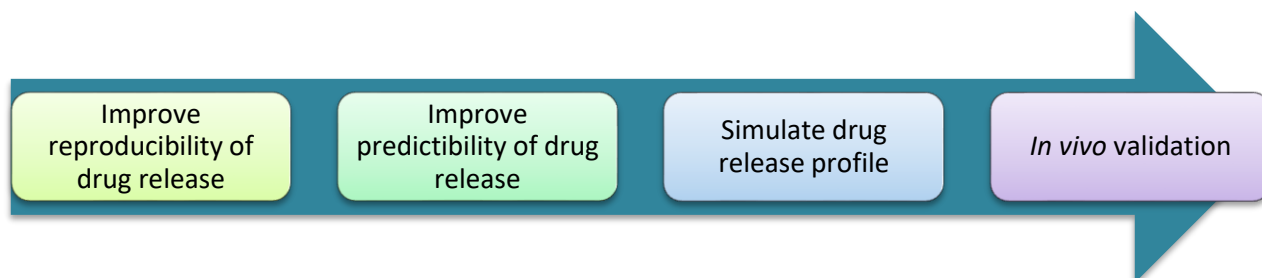


Figure 7-4: Possible milestones to achieving a personalised drug release profile

There are many levels of simulation with the smallest range dealing with angstrom (\AA) to a larger range of meters. Angstrom level simulations are quantum level models (QM) and meter level simulations are multiscale models (MM). In principle, all systems can be simulated by QM but this is extremely time consuming and computationally complex, and thus is impractical. Therefore, depending on particle size, an appropriate level of simulation is chosen. Particles in matrices can be simulated using finite element method (FEM) (466). Such FEM simulation could have a visual animation of drug released from the matrix as well as the predicted drug release profile. Figure 7-5 illustrates a concept of this FEM for a torus geometry that was simulated as time progresses using Blender which is a simulation rendering software.

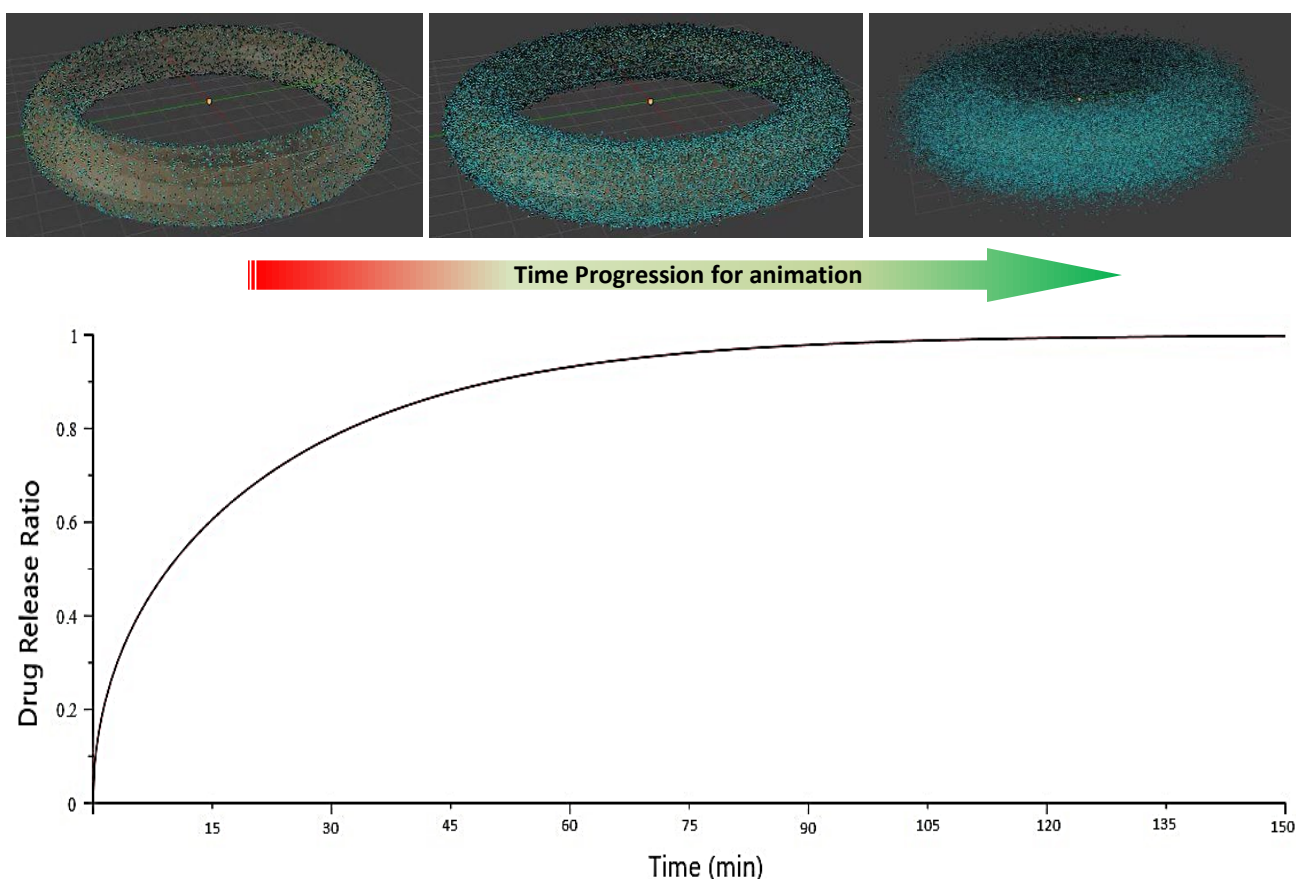


Figure 7-5: Top) Animation of drug particle releasing from a torus using blender software. Three snapshots of the torus are shown at different times. The arrow shows the progression of time for the snapshots. Bottom) The accompanying generated drug release profile.

7.3.3 Personalization

A milestone of achieving desired release profile would be to achieve personalization of multiple drugs. Polypill was mentioned in chapter 1. In this work, the predictability of solid dispersions containing a single drug and a single polymer were investigated. Predictability of multiple drugs with one or more polymers

(polypill) is an area of future investigations with the wider application in personalised polypill development. Such a polypill can also be expected to achieve a more complex profile such as a periodic drug release profile (467). A periodic pulsive drug release profile is where there is a drug release for a certain duration followed by no drug release for a duration and followed by drug release for a duration again. This would require using different layers of polymers or compartmentalizing to control the drug release from the matrix at different times. Such a layered tablet has already been 3D printed (49). A polypill containing up to five compartments has also been printed (468). A concept of layered torus polypill containing two drugs to achieve a periodic drug release profile is shown in Figure 7-6. Simulation of polypills will present a different set of challenges such as highly accurate prediction of drug dissolution profile at a molecular level especially in the case where the drugs can have a drug-drug interaction. As more drugs are added in the polypill, it is expected that the controlled release duration will be longer, and therefore, more sophisticated computer power will be required which can run the simulations at a molecular level for a longer duration.

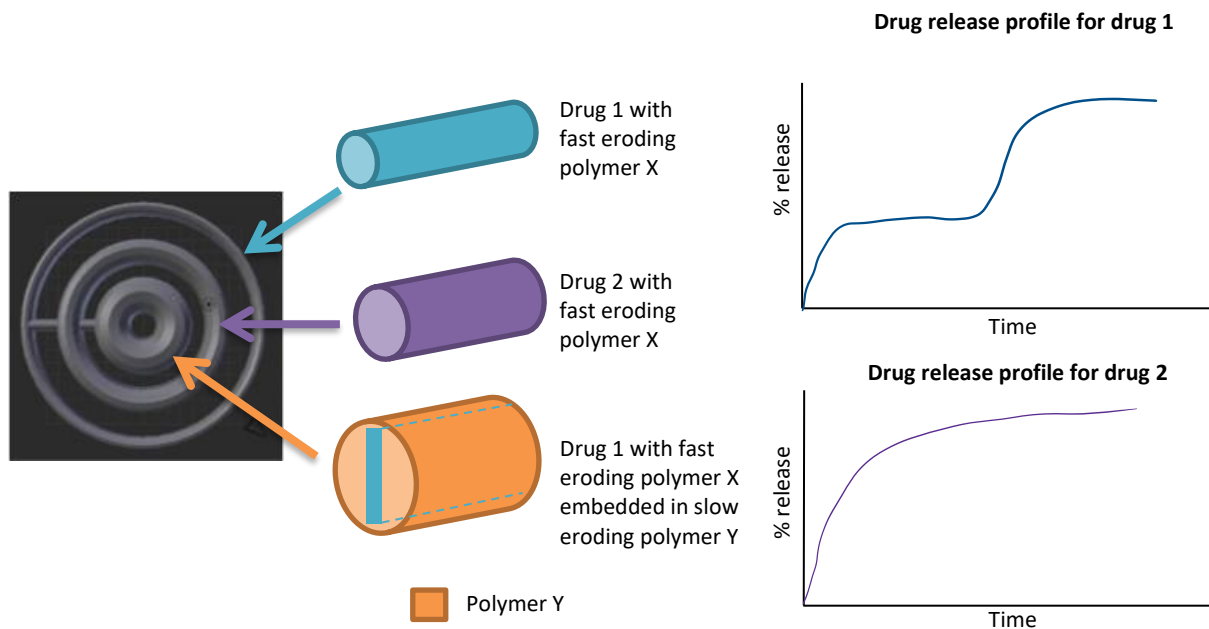


Figure 7-6: Concept of a torus polypill designed to have different release profiles. The drug release profile for drug 1 is an example of a periodic drug release profile. The dashed line indicates the continuation of the formulation not visible on the diagram plane.

Reference

1. Vogenberg FR, Isaacson Barash C, Pursel M. Personalized medicine: part 1: evolution and development into theranostics. *P T*. 2010;35(10):560-76.
2. Garassino DM. Personalized Medicine is not yet here: *BioMed e-Series*; 2015 [cited 2019 15-12]. Available from: <https://pharmaceuticalintelligence.com/tag/personalized-medicine/page/4/>.
3. Curti C, Kirby DJ, Russell CA. Current formulation approaches in design and development of solid oral dosage forms through three-dimensional printing. *Progress in Additive Manufacturing*. 2020;5(2):111-23.
4. Echte A. *Handbuch der technischen Polymerchemie*: VCH-Verlag-Ges.; 1993.
5. Kleinebudde P, Lindner H. Experiments with an instrumented twin-screw extruder using a single-step granulation/extrusion process. *International journal of pharmaceutics*. 1993;94(1-3):49-58.
6. Patil H, Tiwari RV, Repka MA. Hot-Melt Extrusion: from Theory to Application in Pharmaceutical Formulation. *AAPS PharmSciTech*. 2016;17(1):20-42.
7. Stevens M, Covas J. *Extruder principles and operation*: Springer Science & Business Media; 2012.
8. Luker K. *Hot-melt Extrusion: Pharmaceutical Applications*. por Dennis Douroumis 1th Edition A John Wiley. 2012.
9. Thiele W, Ghebre-Selassie I. *Pharmaceutical extrusion technology*. Informa Health Care, New York. 2003.
10. Crowley MM, Zhang F, Repka MA, Thumma S, Upadhye SB, Kumar Battu S, et al. *Pharmaceutical Applications of Hot-Melt Extrusion: Part I. Drug development and industrial pharmacy*. 2007;33(9):909-26.
11. Breitenbach J. Melt extrusion: from process to drug delivery technology. *European Journal of Pharmaceutics and Biopharmaceutics*. 2002;54(2):107-17.
12. Chokshi R, Zia H. Hot-melt extrusion technique: a review. 2004.
13. Swarbrick J, Boylan J. Hot-melt extrusion technology. *Encyclopedia of Pharmaceutical Technology*.19:203-25.
14. Bouman J, Belton P, Venema P, van der Linden E, de Vries R, Qi S. Controlled Release from Zein Matrices: Interplay of Drug Hydrophobicity and pH. *Pharmaceutical research*. 2016;33(3):673-85.
15. Feng X, Vo A, Patil H, Tiwari RV, Alshetai AS, Pimparade MB, et al. The effects of polymer carrier, hot melt extrusion process and downstream processing parameters on the moisture sorption properties of amorphous solid dispersions. *Journal of Pharmacy and Pharmacology*. 2016;68(5):692-704.
16. Ahmed HA, Alfredson TV, Birudaraj K, Brandl MT, Phuapradit W, Shah NH, et al. *Pharmaceutical composition and process*. Google Patents; 2010.
17. Zhang F, McGinity JW. Properties of sustained-release tablets prepared by hot-melt extrusion. *Pharmaceutical development and technology*. 1999;4(2):241-50.
18. Aharoni SM. Increased glass transition temperature in motionally constrained semicrystalline polymers. *Polymers for Advanced Technologies*. 1998;9(3):169-201.
19. Strobl GR, Strobl GR. *The physics of polymers*: Springer; 1997.
20. Statista. Most used 3D printing technologies in 2017 and 2018 *Sculpteo: Sculpteo*; 2018 [cited 2020 30-1]. Available from: <https://www.statista.com/statistics/560304/worldwide-survey-3d-printing-top-technologies/>.
21. Ngo TD, Kashani A, Imbalzano G, Nguyen KTQ, Hui D. Additive manufacturing (3D printing): A review of materials, methods, applications and challenges. *Composites Part B: Engineering*. 2018;143:172-96.
22. Vithani K, Goyanes A, Jannin V, Basit AW, Gaisford S, Boyd BJ. An Overview of 3D Printing Technologies for Soft Materials and Potential Opportunities for Lipid-based Drug Delivery Systems. 2018;36(1):4-54.
23. Jonathan G, Karim A. 3D printing in pharmaceuticals: A new tool for designing customized drug delivery systems. *International journal of pharmaceutics*. 2016;499(1-2):376-94.
24. Andrew K, Yu H. Application of Micro-Scale 3D Printing in Pharmaceuticals. *Pharmaceutics*. 2019;11(8):390-413.
25. Prasad LK, Smyth H. 3D Printing technologies for drug delivery: a review. *Drug development and industrial pharmacy*. 2016;42(7):1019-31.
26. Chia HN, Wu BM. Recent advances in 3D printing of biomaterials. *Journal of Biological Engineering*. 2015;9(1):1-14.
27. Korpela J, Kokkari A, Korhonen H, Malin M, Närhi T, Seppälä J. Biodegradable and bioactive porous scaffold structures prepared using fused deposition modeling. *Journal of Biomedical Materials Research Part B: Applied Biomaterials*. 2013;101(4):610-9.
28. el moumen A, Tarfaoui M, Lafdi K. Modelling of the temperature and residual stress fields during 3D printing of polymer composites. *International Journal of Advanced Manufacturing Technology*. 2019;104:1-16.
29. Alhnan MA, Okwuosa TC, Sadia M, Wan K-W, Ahmed W, Arafat B. Emergence of 3D printed dosage forms: opportunities and challenges. *Pharmaceutical research*. 2016;33(8):1817-32.
30. Nasereddin JM, Wellner N, Alhijaj M, Belton P, Qi S. Development of a Simple Mechanical Screening Method for Predicting the Feedability of a Pharmaceutical FDM 3D Printing Filament. *Pharm Res*. 2018;35(8):151.

31. Goyanes A, Buanz ABM, Hatton GB, Gaisford S, Basit AW. 3D printing of modified-release aminosaliclylate (4-ASA and 5-ASA) tablets. *European Journal of Pharmaceutics and Biopharmaceutics*. 2015;89:157-62.
32. Seyfoddin A, Dezfooli SM, Greene CA. *Engineering Drug Delivery Systems*: Elsevier Science; 2019.
33. Melocchi A, Parietti F, Maroni A, Foppoli A, Gazzaniga A, Zema L. Hot-melt extruded filaments based on pharmaceutical grade polymers for 3D printing by fused deposition modeling. *International journal of pharmaceutics*. 2016;509(1):255-63.
34. Agrawal AM, Dudhedia MS, Zimny E. Hot Melt Extrusion: Development of an Amorphous Solid Dispersion for an Insoluble Drug from Mini-scale to Clinical Scale. *AAPS PharmSciTech*. 2016;17(1):133-47.
35. Foustieris E, Tarantili PA, Karavas E, Bikiaris D. Poly (vinyl pyrrolidone)–poloxamer-188 solid dispersions prepared by hot melt extrusion. *Journal of thermal analysis and calorimetry*. 2013;113(3):1037-47.
36. Major I, McConville C. Hot Melt Extruded and Injection Moulded Dosage Forms: Recent Research and Patents. *Recent patents on drug delivery & formulation*. 2015;9(3):194-200.
37. Tan DK, Maniruzzaman M, Nokhodchi A. *Advanced Pharmaceutical Applications of Hot-Melt Extrusion Coupled with Fused Deposition Modelling (FDM) 3D Printing for Personalised Drug Delivery*. 2018.
38. Tiwari RV, Patil H, Repka MA. Contribution of hot-melt extrusion technology to advance drug delivery in the 21st century. *Expert opinion on drug delivery*. 2016;13(3):451-64.
39. Smith DM, Kapoor Y, Klinzing GR, Procopio AT. Pharmaceutical 3D printing: Design and qualification of a single step print and fill capsule. *International journal of pharmaceutics*. 2018;544(1):21-30.
40. Dizon JRC, Espera Jr AH, Chen Q, Advincula RC. Mechanical characterization of 3D-printed polymers. *Additive Manufacturing*. 2018;20:44-67.
41. Comb J, Priedeman W, Turley PW, editors. *FDM® Technology process improvements*. 1994 International Solid Freeform Fabrication Symposium; 1994.
42. Fuster V, Gambús F, Patriciello A, Hamrin M, Grobbee DE. The polypill approach - An innovative strategy to improve cardiovascular health in Europe. *BMC Pharmacol Toxicol*. 2017;18(1):10-.
43. Selak V, Elley CR, Bullen C, Crengle S, Wadham A, Rafter N, et al. Effect of fixed dose combination treatment on adherence and risk factor control among patients at high risk of cardiovascular disease: randomised controlled trial in primary care. *BMJ*. 2014;348:g3318.
44. Perrie Y, Rades T. *FASTtrack Pharmaceutics: Drug Delivery and Targeting*: Pharmaceutical Press; 2012.
45. Fuenmayor E, Forde M, Healy AV, Devine DM, Lyons JG, McConville C, et al. Comparison of fused-filament fabrication to direct compression and injection molding in the manufacture of oral tablets. *International journal of pharmaceutics*. 2019;558:328-40.
46. Goyanes A, Kobayashi M, Martínez-Pacheco R, Gaisford S, Basit AW. Fused-filament 3D printing of drug products: Microstructure analysis and drug release characteristics of PVA-based caplets. *International journal of pharmaceutics*. 2016;514(1):290-5.
47. Isreb A, Baj K, Wojsz M, Isreb M, Peak M, Alhnan MA. 3D printed oral theophylline doses with innovative 'radiator-like' design: Impact of polyethylene oxide (PEO) molecular weight. *International journal of pharmaceutics*. 2019;564:98-105.
48. Alhijaj M, Nasereddin J, Belton P, Qi S. Impact of Processing Parameters on the Quality of Pharmaceutical Solid Dosage Forms Produced by Fused Deposition Modeling (FDM). *Pharmaceutics*. 2019;11(12):633.
49. Goyanes A, Wang J, Buanz A, Martínez-Pacheco R, Telford R, Gaisford S, et al. 3D Printing of Medicines: Engineering Novel Oral Devices with Unique Design and Drug Release Characteristics. *Molecular Pharmaceutics*. 2015;12(11):4077-84.
50. Weeren RV, Agarwala M, Jamalabad V, Bandyopadhyay A, Vaidyanathan R, Langrana N, et al., editors. *Quality of parts processed by fused deposition*. 1995 International Solid Freeform Fabrication Symposium; 1995.
51. Hwang HH, Zhu W, Victorine G, Lawrence N, Chen S. 3D-Printing of Functional Biomedical Microdevices via Light- and Extrusion-Based Approaches. *Small Methods*. 2018;2(2):1700277.
52. Alhijaj M, Belton P, Qi S. An investigation into the use of polymer blends to improve the printability of and regulate drug release from pharmaceutical solid dispersions prepared via fused deposition modeling (FDM) 3D printing. *European Journal of Pharmaceutics and Biopharmaceutics*. 2016;108:111-25.
53. Okwuosa TC, Stefaniak D, Arafat B, Isreb A, Wan K-W, Alhnan MA. A Lower Temperature FDM 3D Printing for the Manufacture of Patient-Specific Immediate Release Tablets. *Pharmaceutical Research*. 2016;33(11):2704-12.
54. Awad A, Fina F, Trenfield SJ, Patel P, Gaisford S, Basit AW, et al. 3D printed pellets (Miniprintlets): A novel, multi-drug, controlled release platform technology. *Pharmaceutics*. 2019;11(4).
55. Araújo MR, Sa-Barreto LL, Gratieri T, Gelfuso GM, Cunha-Filho M. The digital pharmacies era: How 3D printing technology using fused deposition modeling can become a reality. *Pharmaceutics*. 2019;11(3):128.
56. Mazzanti V, Malagutti L, Mollica F. *FDM 3D Printing of Polymers Containing Natural Fillers: A Review of their Mechanical Properties*. 2019.

57. Singh S, Baghel RS, Yadav L. A review on solid dispersion. *International journal of pharmacy & life sciences*. 2011;2(9).
58. Sekiguchi K, Obi N. Studies on Absorption of Eutectic Mixture. I. A Comparison of the Behavior of Eutectic Mixture of Sulfathiazole and that of Ordinary Sulfathiazole in Man. *Chemical and Pharmaceutical Bulletin*. 1961;9(11):866-72.
59. Goldberg AH, Gibaldi M, Kanig JL. Increasing dissolution rates and gastrointestinal absorption of drugs via solid solutions and eutectic mixtures II: Experimental evaluation of a eutectic mixture: Urea-acetaminophen system. *Journal of pharmaceutical sciences*. 1966;55(5):482-7.
60. Chiou WL, Riegelman S. Pharmaceutical applications of solid dispersion systems. *Journal of pharmaceutical sciences*. 1971;60(9):1281-302.
61. Huang Y, Dai W-G. Fundamental aspects of solid dispersion technology for poorly soluble drugs. *Acta Pharmaceutica Sinica B*. 2014;4(1):18-25.
62. Vasconcelos T, Sarmiento B, Costa P. Solid dispersions as strategy to improve oral bioavailability of poor water soluble drugs. *Drug discovery today*. 2007;12(23-24):1068-75.
63. Vo CL-N, Park C, Lee B-J. Current trends and future perspectives of solid dispersions containing poorly water-soluble drugs. *European journal of pharmaceuticals and biopharmaceutics*. 2013;85(3):799-813.
64. Meng F, Gala U, Chauhan H. Classification of solid dispersions: correlation to (i) stability and solubility (ii) preparation and characterization techniques. *Drug development and industrial pharmacy*. 2015;41(9):1401-15.
65. De Mohac LM, Caruana R, Pavia FC, Cavallaro G, Giammona G, Licciardi M. Multicomponent solid dispersion as a formulation strategy to improve drug permeation: A case study on the anti-colorectal cancer irinotecan. *Journal of Drug Delivery Science and Technology*. 2019;52:346-54.
66. Punčochová K, Ewing AV, Gajdošová M, Pekárek T, Beránek J, Kazarian SG, et al. The combined use of imaging approaches to assess drug release from multicomponent solid dispersions. *Pharmaceutical research*. 2017;34(5):990-1001.
67. Van Duong T, Van den Mooter G. The role of the carrier in the formulation of pharmaceutical solid dispersions. Part I: crystalline and semi-crystalline carriers. *Expert opinion on drug delivery*. 2016;13(11):1583-94.
68. Findlay A. *The phase rule and its applications*: Longmans, Green and Company; 1923.
69. Atkins PW, De Paula J, Keeler J. *Atkins' physical chemistry*: Oxford university press; 2018.
70. Levy G. Effect of particle size on dissolution and gastrointestinal absorption rates of pharmaceuticals. *American journal of pharmacy and the sciences supporting public health*. 1963;135:78-92.
71. Prakash S, Yeom J. Chapter 4 - Advanced Fabrication Methods and Techniques. In: Prakash S, Yeom J, editors. *Nanofluidics and Microfluidics*: William Andrew Publishing; 2014. p. 87-170.
72. Law D, Wang W, Schmitt EA, Qiu Y, Krill SL, Fort JJ. Properties of rapidly dissolving eutectic mixtures of poly (ethylene glycol) and fenofibrate: the eutectic microstructure. *Journal of pharmaceutical sciences*. 2003;92(3):505-15.
73. Figueirêdo CBM, Nadvorny D, de Medeiros Vieira ACQ, Soares Sobrinho JL, Rolim Neto PJ, Lee PI, et al. Enhancement of dissolution rate through eutectic mixture and solid solution of posaconazole and benzimidazole. *International journal of pharmaceutics*. 2017;525(1):32-42.
74. Mullins JD, Macek TJ. Some pharmaceutical properties of novobiocin. *Journal of the American Pharmaceutical Association*. 1960;49(4):245-8.
75. Ford JL. The current status of solid dispersions. *Pharmaceutica Acta Helvetiae*. 1986;61(3):69.
76. Chiou WL, Niazi S. Phase diagram and dissolution-rate studies on sulfathiazole-urea solid dispersions. *Journal of pharmaceutical sciences*. 1971;60(9):1333-8.
77. Chiou WL, Niazi S. Pharmaceutical applications of solid dispersion systems: Dissolution of griseofulvin–succinic acid eutectic mixture. *Journal of pharmaceutical sciences*. 1976;65(8):1212-4.
78. Zajc N, Obreza A, Bele M, Srčič S. Physical properties and dissolution behaviour of nifedipine/mannitol solid dispersions prepared by hot melt method. *International journal of pharmaceutics*. 2005;291(1-2):51-8.
79. Findlay A. *The Phase Rule*, revised by AN Campbell and NO Smith. New York: Dower. 1951:54.
80. Goldberg AH, Gibaldi M, Kanig JL, Shanker J. Method for determining dissolution rates of multiparticulate systems. *Journal of pharmaceutical sciences*. 1965;54(12):1722-5.
81. Moore WJ. *Physical Chemistry (5th Edition)*: Prentice-Hall; 1998.
82. Abbaschian R, Reed-Hill RE. *Physical Metallurgy Principles*: Cengage Learning; 2008.
83. Noh H-J, Myung S-T, Jung H-G, Yashiro H, Amine K, Sun Y-K. Formation of a Continuous Solid-Solution Particle and its Application to Rechargeable Lithium Batteries. *Advanced Functional Materials*. 2013;23(8):1028-36.
84. al kurashy I, Mahdi Z. An Overview on the Recent Technologies and Advances in Drug Delivery of Poorly Water-Soluble Drugs — — — — —. *Al Mustansiriyah Journal of Pharmaceutical Sciences*. 2019;19:180-95.
85. Evans RC. *An Introduction to Crystal Chemistry*: Cambridge University Press; 1966.

86. Kim JY, Kim S, Papp M, Park K, Pinal R. Hydrotropic solubilization of poorly water-soluble drugs. *Journal of pharmaceutical sciences*. 2010;99(9):3953-65.
87. Tran P, Pyo Y-C, Kim D-H, Lee S-E, Kim J-K, Park J-S. Overview of the manufacturing methods of solid dispersion technology for improving the solubility of poorly water-soluble drugs and application to anticancer drugs. *Pharmaceutics*. 2019;11(3):132.
88. Simonelli A, Mehta S, Higuchi W. Dissolution rates of high energy polyvinylpyrrolidone (PVP)-sulfathiazole coprecipitates. *Journal of pharmaceutical sciences*. 1969;58(5):538-49.
89. Sekiguchi K, Obi N, Ueda Y. Studies on Absorption of Eutectic Mixture. II. Absorption of fused Conglomerates of Chloramphenicol and Urea in Rabbits. *CHEMICAL & PHARMACEUTICAL BULLETIN*. 1964;12(2):134-44.
90. Guillory JK, Hwang SC, Lach JL. Interactions between pharmaceutical compounds by thermal methods. *Journal of pharmaceutical sciences*. 1969;58(3):301-8.
91. Benet LZ, Bhatia V, Singh P, Guillory JK, Sokoloski TD. Effect of inert tablet ingredients on drug absorption I. Effect of polyethylene glycol 4000 on the intestinal absorption of four barbiturates. *Journal of pharmaceutical sciences*. 1966;55(1):63-8.
92. Chau V, Park C, Lee B-J. Current trends and future perspectives of solid dispersions containing poorly water-soluble drugs. *European journal of pharmaceutics and biopharmaceutics : official journal of Arbeitsgemeinschaft fur Pharmazeutische Verfahrenstechnik eV*. 2013;85.
93. Chauhan B, Shimpi S, Paradkar A. Preparation and evaluation of glibenclamide-polyglycolized glycerides solid dispersions with silicon dioxide by spray drying technique. *European Journal of Pharmaceutical Sciences*. 2005;26(2):219-30.
94. Van den Mooter G, Weuts I, De Ridder T, Blaton N. Evaluation of Inutec SP1 as a new carrier in the formulation of solid dispersions for poorly soluble drugs. *International journal of pharmaceutics*. 2006;316(1):1-6.
95. Lipatov YS. Phase Separation in Filled Polymer Blends. *Journal of Macromolecular Science, Part B*. 2006;45(5):871-88.
96. Cheremisinoff NP, Cheremisinoff PN. *Handbook of Applied Polymer Processing Technology*: Taylor & Francis; 1996.
97. Sperling LH. *Introduction to Physical Polymer Science*: Wiley; 2015.
98. Eyring H. Viscosity, plasticity, and diffusion as examples of absolute reaction rates. *The Journal of chemical physics*. 1936;4(4):283-91.
99. Vol'kenshtein M, Ptitsyn O, editors. *The relaxation theory of glass transition*. Dokl Akad Nauk SSSR; 1955.
100. Narayanaswamy O. A model of structural relaxation in glass. *Journal of the American Ceramic Society*. 1971;54(10):491-8.
101. Kovacs AJ, Aklonis JJ, Hutchinson JM, Ramos AR. Isobaric volume and enthalpy recovery of glasses. II. A transparent multiparameter theory. *Journal of Polymer Science: Polymer Physics Edition*. 1979;17(7):1097-162.
102. Adam G, Gibbs JH. On the temperature dependence of cooperative relaxation properties in glass-forming liquids. *The journal of chemical physics*. 1965;43(1):139-46.
103. Tropin TV, Schmelzer JW, Aksenov VL. Modern aspects of the kinetic theory of glass transition. *Physics-Usppekhi*. 2016;59(1):42-66.
104. Gibbs JH, DiMarzio EA. Nature of the glass transition and the glassy state. *The Journal of Chemical Physics*. 1958;28(3):373-83.
105. Liu J, Deng Q, Jean YC. Free-volume distributions of polystyrene probed by positron annihilation: comparison with free-volume theories. *Macromolecules*. 1993;26(26):7149-55.
106. Williams ML, Landel RF, Ferry JD. The Temperature Dependence of Relaxation Mechanisms in Amorphous Polymers and Other Glass-forming Liquids. *Journal of the American Chemical Society*. 1955;77(14):3701-7.
107. Hirai N, Eyring H. Bulk viscosity of polymeric systems. *Journal of Polymer Science*. 1959;37(131):51-70.
108. Miller A. Polymer-Melt Viscosity and the Glass Transition: An Evaluation of the Adam-Gibbs and the Free-Volume Models. *The Journal of Chemical Physics*. 1968;49(3):1393-7.
109. Simha R, Boyer R. On a general relation involving the glass temperature and coefficients of expansion of polymers. *The Journal of Chemical Physics*. 1962;37(5):1003-7.
110. Hunter GL, Weeks ER. The physics of the colloidal glass transition. *Reports on progress in physics*. 2012;75(6):066501.
111. Roudaut G, Simatos D, Champion D, Contreras-Lopez E, Le Meste M. Molecular mobility around the glass transition temperature: a mini review. *Innovative Food Science & Emerging Technologies*. 2004;5(2):127-34.
112. Baird JA, Taylor LS. Evaluation of amorphous solid dispersion properties using thermal analysis techniques. *Advanced drug delivery reviews*. 2012;64(5):396-421.
113. Gaikwad AN, Wood ER, Ngai T, Lodge TP. Two calorimetric glass transitions in miscible blends containing poly(ethylene oxide). *Macromolecules*. 2008;41(7):2502-8.

114. Zhang X, Cresswell M. Chapter 2 - Materials Fundamentals of Drug Controlled Release. In: Zhang X, Cresswell M, editors. *Inorganic Controlled Release Technology*. Boston: Butterworth-Heinemann; 2016. p. 17-55.
115. Ghosh Dastidar D, Chakrabarti G. Chapter 6 - Thermoresponsive Drug Delivery Systems, Characterization and Application. In: Mohapatra SS, Ranjan S, Dasgupta N, Mishra RK, Thomas S, editors. *Applications of Targeted Nano Drugs and Delivery Systems*: Elsevier; 2019. p. 133-55.
116. Berthier L, Biroli G. Theoretical perspective on the glass transition and amorphous materials. *Reviews of Modern Physics*. 2011;83(2):587.
117. Fulchiron R, Belyamani I, Otaigbe JU, Bounor-Legaré V. A simple method for tuning the glass transition process in inorganic phosphate glasses. *Scientific Reports*. 2015;5(1):8369.
118. Roos YH, Drusch S. *Phase transitions in foods*: Academic Press; 2015.
119. Williams RJ. Methods for determination of glass transitions in seeds. *Annals of Botany*. 1994;74(5):525-30.
120. Carter B, Schmidt S. Developments in glass transition determination in foods using moisture sorption isotherms. *Food Chemistry - FOOD CHEM*. 2012;132.
121. Amador C, Martín de Juan L. Chapter 19 - Strategies for Structured Particulate Systems Design. In: Martín M, Eden MR, Chemmangattuvalappil NG, editors. *Computer Aided Chemical Engineering*. 39: Elsevier; 2016. p. 509-79.
122. Olabis O. *Polymer-Polymer Miscibility*: Elsevier Science; 2012.
123. Kalogeris IM. *Glass-Transition Phenomena in Polymer Blends*. 2016. p. 1-134.
124. Sperling LH. *Polymeric multicomponent materials: an introduction*: Wiley-Interscience; 1997.
125. Fox T. *Bull. Am. Phys. Soc*. 1956.
126. Miller-Chou BA, Koenig JL. A review of polymer dissolution. *Progress in Polymer Science*. 2003;28(8):1223-70.
127. Ueberreiter K. *The solution process*. Academic Press: New York; 1968. p. 219-57.
128. Manjkow J, Papanu J, Hess D, Soane D, Bell A. Influence of processing and molecular parameters on the dissolution rate of poly-(methyl methacrylate) thin films. *Journal of The Electrochemical Society*. 1987;134(8):2003-7.
129. Ouano A, Carothers J. Dissolution dynamics of some polymers: solvent-polymer boundaries. *Polymer Engineering & Science*. 1980;20(2):160-6.
130. Groele RJ, Rodriguez F. *Dissolution Rates of Polymers and Copolymers Based on Methyl, Ethyl, and Butyl Methacrylate*. CORNELL UNIV ITHACA SCHOOL OF CHEMICAL ENGINEERING, 1988.
131. Gipstein E, Ouano AC, Johnson DE, Need III OU. Parameters, affecting the sensitivity of poly (methyl methacrylate) as a positive lithographic resist. *Polymer Engineering & Science*. 1977;17(6):396-401.
132. Ouano A. Dissolution kinetics of polymers: effect of residual solvent content. *Macromolecular Solutions*: Elsevier; 1982. p. 208-17.
133. Pekcan Ö, Canpolat M, Kaya D. In situ fluorescence experiments for real-time monitoring of annealed high-T latex film dissolution. *Journal of applied polymer science*. 1996;60(12):2105-12.
134. Drummond RK, Boydston GL, Peppas NA. Properties of positive resists. III. The dissolution behavior of poly (methyl methacrylate-co-maleic anhydride). *Journal of applied polymer science*. 1990;39(11-12):2267-77.
135. Parsonage EE, Peppas NA, Lee PI. Properties of positive resists. II. Dissolution characteristics of irradiated poly (methyl methacrylate) and poly (methyl methacrylate-co-maleic anhydride). *Journal of Vacuum Science & Technology B: Microelectronics Processing and Phenomena*. 1987;5(2):538-45.
136. Szymkiewicz A. *Modelling water flow in unsaturated porous media: accounting for nonlinear permeability and material heterogeneity*: Springer Science & Business Media; 2012.
137. Moy P, Karasz F. *The interactions of water with epoxy resins*. ACS Publications; 1980.
138. McBrierty V, Keely C, Coyle F, Xu H, Vij J. Hydration and plasticization effects in cellulose acetate: molecular motion and relaxation. *Faraday Discussions*. 1996;103:255-68.
139. Ellis T, Kahasz F. Enthalpy recovery and physical aging of polymer-diluent binary systems: A network epoxy and water. *Polymer Engineering & Science*. 1986;26(4):290-6.
140. McBrierty V, Martin S, Karasz F. Understanding hydrated polymers: the perspective of NMR. *Journal of molecular liquids*. 1999;80(2-3):179-205.
141. Coyle FM, Martin SJ, McBrierty VJ. Dynamics of water molecules in polymers. *Journal of molecular liquids*. 1996;69:95-116.
142. Rowland SP. *Water in polymers*: ACS Publications; 1980.
143. Ganji F, Vasheghani-Farahani S, Vasheghani-Farahani E. Theoretical description of hydrogel swelling: a review. *Iran Polym J*. 2010;19(5):375-98.
144. Taylor DG, Bushell MC. The spatial mapping of translational diffusion coefficients by the NMR imaging technique. *Physics in Medicine & Biology*. 1985;30(4):345.
145. Eccles CD, Callaghan PT, Jenner CF. Measurement of the Self-Diffusion Coefficient of Water as a Function of Position in Wheat Grain Using Nuclear Magnetic Resonance Imaging. *Biophysical Journal*. 1988;53(1):77-81.

146. Nott KP. Magnetic resonance imaging of tablet dissolution. *European Journal of Pharmaceutics and Biopharmaceutics*. 2010;74(1):78-83.
147. Fu Y, Kao WJ. Drug release kinetics and transport mechanisms of non-degradable and degradable polymeric delivery systems. *Expert opinion on drug delivery*. 2010;7(4):429-44.
148. Bajpai AK, Shukla SK, Bhanu S, Kankane S. Responsive polymers in controlled drug delivery. *Progress in Polymer Science*. 2008;33(11):1088-118.
149. Li H, Ng TY, Yew YK, Lam KY. Modeling and simulation of the swelling behavior of pH-stimulus-responsive hydrogels. *Biomacromolecules*. 2005;6(1):109-20.
150. Tamanna Begam AKN, Reena Singhal. A Comparative Study of Swelling Properties of Hydrogels Based on Poly(acrylamide-co-methyl methacrylate) Containing Physical and Chemical Crosslinks. 2002.
151. Rabin C, Siegel S. Delivery Systems and Dosing for Antipsychotics. *Handbook of experimental pharmacology*. 2012;212:267-98.
152. Edlund U, Albertsson A-C. Polyesters based on diacid monomers. *Advanced drug delivery reviews*. 2003;55(4):585-609.
153. Sackett CK, Narasimhan B. Mathematical modeling of polymer erosion: Consequences for drug delivery. *International journal of pharmaceutics*. 2011;418(1):104-14.
154. Göpferich A. Polymer Bulk Erosion. *Macromolecules*. 1997;30(9):2598-604.
155. Göpferich A. Mechanisms of polymer degradation and erosion. *Biomaterials*. 1996;17(2):103-14.
156. Davison NL, Barrère-de Groot F, Grijpma DW. Chapter 6 - Degradation of Biomaterials. In: Blitterswijk CAV, De Boer J, editors. *Tissue Engineering (Second Edition)*. Oxford: Academic Press; 2014. p. 177-215.
157. Langer R. New methods of drug delivery. *Science*. 1990;249(4976):1527-33.
158. Göpferich A, Langer R. Modeling of polymer erosion in three dimensions: rotationally symmetric devices. *AIChE Journal*. 1995;41(10):2292-9.
159. Abu-Thabit NY, Makhlof ASH. 1 - Historical development of drug delivery systems: From conventional macroscale to controlled, targeted, and responsive nanoscale systems. In: Makhlof ASH, Abu-Thabit NY, editors. *Stimuli Responsive Polymeric Nanocarriers for Drug Delivery Applications, Volume 1: Woodhead Publishing; 2018. p. 3-41.*
160. Berardi A, Bisharat L, Cespi M, Basheti IA, Bonacucina G, Pavoni L, et al. Controlled release properties of zein powder filled into hard gelatin capsules. *Powder Technology*. 2017;320:703-13.
161. Burkersroda Fv, Schedl L, Göpferich A. Why degradable polymers undergo surface erosion or bulk erosion. *Biomaterials*. 2002;23(21):4221-31.
162. Han X, Pan J. A model for simultaneous crystallisation and biodegradation of biodegradable polymers. *Biomaterials*. 2009;30(3):423-30.
163. Sriamornsak P, Thirawong N, Weerapol Y, Nunthanid J, Sungthongjeen S. Swelling and erosion of pectin matrix tablets and their impact on drug release behavior. *European Journal of Pharmaceutics and Biopharmaceutics*. 2007;67(1):211-9.
164. van Bochove B, Grijpma D. Photo-Crosslinked Synthetic Biodegradable Polymer Networks for Biomedical Applications. *Journal of Biomaterials Science Polymer Edition*. 2019.
165. Siepmann J, Siepmann F. Mathematical modeling of drug dissolution. *International journal of pharmaceutics*. 2013;453(1):12-24.
166. Cruz AP, Bertol CD, Stulzer HK, Murakami FS, Costella FT, Rocha HVA, et al. Swelling, Erosion, and Release Behavior of PEO/Primaquine Matrix Tablets. *Pharmaceutical Chemistry Journal*. 2008;42(7):413.
167. Huang X, Brazel CS. On the importance and mechanisms of burst release in matrix-controlled drug delivery systems. *Journal of controlled release*. 2001;73(2-3):121-36.
168. Modesti G, Zimmermann B, Börsch M, Herrmann A, Saalwächter K. Diffusion in model networks as studied by NMR and fluorescence correlation spectroscopy. *Macromolecules*. 2009;42(13):4681-9.
169. Mircioiu C, Voicu V, Anuta V, Tudose A, Celia C, Paolino D, et al. Mathematical Modeling of Release Kinetics from Supramolecular Drug Delivery Systems. *Pharmaceutics*. 2019;11(3):140.
170. Arifin DY, Lee LY, Wang CH. Mathematical modeling and simulation of drug release from microspheres: Implications to drug delivery systems. *Advanced drug delivery reviews*. 2006;58(12-13):1274-325.
171. Varma MVS, Kaushal AM, Garg A, Garg S. Factors Affecting Mechanism and Kinetics of Drug Release from Matrix-Based Oral Controlled Drug Delivery Systems. *American Journal of Drug Delivery*. 2004;2(1):43-57.
172. Narasimhan B, Peppas NA. Molecular analysis of drug delivery systems controlled by dissolution of the polymer carrier. *Journal of pharmaceutical sciences*. 1997;86(3):297-304.
173. Dash S, Murthy PN, Nath L, Chowdhury P. Kinetic modeling on drug release from controlled drug delivery systems. *Acta Pol Pharm*. 2010;67(3):217-23.

174. Siepmann J, Faisant N, Benoit J-P. A new mathematical model quantifying drug release from bioerodible microparticles using Monte Carlo simulations. *Pharmaceutical research*. 2002;19(12):1885-93.
175. Larobina D, Mensitieri G, Kipper MJ, Narasimhan B. Mechanistic understanding of degradation in bioerodible polymers for drug delivery. *AIChE journal*. 2002;48(12):2960-70.
176. Hixson A, Crowell J. Dependence of reaction velocity upon surface and agitation. *Industrial & Engineering Chemistry*. 1931;23(8):923-31.
177. Siepmann J, Göpferich A. Mathematical modeling of bioerodible, polymeric drug delivery systems. *Advanced drug delivery reviews*. 2001;48(2-3):229-47.
178. Ferrero C, Massuelle D, Doelker E. Towards elucidation of the drug release mechanism from compressed hydrophilic matrices made of cellulose ethers. II. Evaluation of a possible swelling-controlled drug release mechanism using dimensionless analysis. *Journal of controlled release : official journal of the Controlled Release Society*. 2010;141(2):223-33.
179. Colombo P, Bettini R, Massimo G, Catellani PL, Santi P, Peppas NA. Drug diffusion front movement is important in drug release control from swellable matrix tablets. *Journal of pharmaceutical sciences*. 1995;84(8):991-7.
180. Brannon-Peppas L, Peppas NA. Solute and penetrant diffusion in swellable polymers. IX. The mechanisms of drug release from pH-sensitive swelling-controlled systems. *Journal of Controlled Release*. 1989;8(3):267-74.
181. Lustig SR, Peppas NA. Solute and penetrant diffusion in swellable polymers. VII. A free volume-based model with mechanical relaxation. *Journal of Applied Polymer Science*. 1987;33(2):533-49.
182. Irimia T, Ghica MV, Popa L, Anuța V, Arsene A-L, Dinu-Pîrvu C-E. Strategies for Improving Ocular Drug Bioavailability and Corneal Wound Healing with Chitosan-Based Delivery Systems. *Polymers*. 2018;10(11):1221.
183. Riley RG, Smart JD, Tsibouklis J, Young SA, Hampson F, Davis A, et al. An in vitro model for investigating the gastric mucosal retention of ¹⁴C-labelled poly(acrylic acid) dispersions. *International journal of pharmaceutics*. 2002;236(1):87-96.
184. Siepmann J, Siepmann F. Modeling of diffusion controlled drug delivery. *Journal of controlled release : official journal of the Controlled Release Society*. 2012;161(2):351-62.
185. Chen C, Yu Y, Wang X, Shi P, Wang Y, Wang P. Manipulation of pH-Sensitive interactions between podophyllotoxin-chitosan for enhanced controlled drug release. *International Journal of Biological Macromolecules*. 2017;95:451-61.
186. Wang G-H, Zhang L-M. Manipulating formation and drug-release behavior of new sol-gel silica matrix by hydroxypropyl guar gum. 2007. p. 10665-70.
187. Bajo J, Hernández JZ, Mathieu P, Campbell A, Fernández-Caballero A, Moreno MN, et al. *Trends in Practical Applications of Agents, Multi-Agent Systems and Sustainability: The PAAMS Collection*: Springer International Publishing; 2015.
188. Haraguchi K, Takehisa T. Nanocomposite hydrogels: a unique organic-inorganic network structure with extraordinary mechanical, optical, and swelling/de-swelling properties. *Advanced Materials*. 2002;14(16):1120.
189. Juárez H, Rico G, Villafuerte L. Influence of admixed carboxymethylcellulose on release of 4-aminopyridine from hydroxypropyl methylcellulose matrix tablets. *International journal of pharmaceutics*. 2001;216(1):115-25.
190. Maggi L, Segale L, Torre ML, Ochoa ME, Conte U. Dissolution behaviour of hydrophilic matrix tablets containing two different polyethylene oxides (PEOs) for the controlled release of a water-soluble drug. Dimensionality study. *Biomaterials*. 2002;23(4):1113-9.
191. Wilson A, Blenner M, Guiseppi-Elie A. Polyplex Formation Influences Release Mechanism of Mono-& Di-Valent Ions from Phosphorylcholine Group Bearing Hydrogels. *Polymers*. 2014;6(9):2451-72.
192. Rask MB, Knopp MM, Olesen NE, Holm R, Rades T. Influence of PVP/VA copolymer composition on drug-polymer solubility. *European Journal of Pharmaceutical Sciences*. 2016;85:10-7.
193. Anurova M, Bakhrushina E, Demina N. Review of Contemporary Gel-Forming Agents in the Technology of Dosage Forms. *Pharmaceutical Chemistry Journal*. 2015;49(9):627-34.
194. Kim S, Ishiyama K. Magnetic Robot and Manipulation for Active-Locomotion With Targeted Drug Release. *Mechatronics, IEEE/ASME Transactions on*. 2014;19:1651-9.
195. Choi M, Choi D, Hong J. Multilayered Controlled Drug Release Silk Fibroin Nanofilm by Manipulating Secondary Structure. *Biomacromolecules*. 2018;19(7):3096-103.
196. Zhao X, Liu Y, Yu Y, Huang Q, Ji W, Li J, et al. Hierarchically porous composite microparticles from microfluidics for controllable drug delivery. 2018. p. 12595-604.
197. Ghasemi-Mobarakeh L, Werzer O, Keimel R, Kolahreze D, Hadley P, Coclite AM. Manipulating drug release from tridimensional porous substrates coated by initiated chemical vapor deposition. *Journal of Applied Polymer Science*. 2019;136(33):N.PAG.
198. Costa P, Sousa Lobo JM. Modeling and comparison of dissolution profiles. *European Journal of Pharmaceutical Sciences*. 2001;13(2):123-33.

199. Dey R, Mulekar MS. A Primer of Statistical Methods for Classification. Modern Statistical Methods for Spatial and Multivariate Data: Springer; 2019. p. 107-29.
200. SimulationPlus. DDDPLUS simulation model description 2016 [cited 2017 06]. Available from: <https://www.simulations-plus.com/resource/dddplus-5-0-product-brochure/>.
201. Duque MD, Issa MG, Silva DA, Barbosa EJ, Lobenberg R, Ferraz HG. In silico simulation of dissolution profiles for development of extended-release doxazosin tablets. Dissolution Technol. 2018;25:14-21.
202. Honório TdS, Pinto EC, Rocha HVA, Esteves VSAD, dos Santos TC, Castro HCR, et al. In Vitro–In Vivo Correlation of Efavirenz Tablets Using GastroPlus®. AAPS PharmSciTech. 2013;14(3):1244-54.
203. National Center for Biotechnology Information. PubChem Database. Acetaminophen C. Acetaminophen 2016 [cited 2019 04 Sept]. Available from: <https://pubchem.ncbi.nlm.nih.gov/compound/Acetaminophen>
204. Sigma-Aldrich. Paracetamol: Specifications 2020 [cited 2020 1-1]. Available from: <https://www.sigmaaldrich.com/catalog/product/sial/bp371?lang=en®ion=GB>.
205. Weinberg L, Peake B, Tan C, Nikfarjam. Pharmacokinetics and pharmacodynamics of lignocaine: A review. M World J Anesthesiol. 2015;4(2):17-29.
206. Souza MFD, Kraychete DC. A ação analgésica da lidocaína intravenosa no tratamento da dor crônica: uma revisão de literatura. Revista Brasileira de Reumatologia. 2014;54:386-92.
207. National Center for Biotechnology Information. PubChem Database. Lidocaine C. Lidocaine 2018 [cited 2019 03 Sept]. Available from: <https://pubchem.ncbi.nlm.nih.gov/compound/Lidocaine>
208. Sigma-Aldrich. Lidocaine: Specifications 2020 [cited 2020 1-1]. Available from: https://www.sigmaaldrich.com/catalog/product/sigma/l7757?lang=en®ion=GB&gclid=CjwKCAiAjMHwBRAVEiwAzdLWGDuZoQ2rMBQFxpIzEFVqHcP_D5abOVNDCjHyAemjHrM_id6lykYGDxoC5B0QAvd_BwE.
209. Irvine J, Afrose A, Islam N. Formulation and delivery strategies of ibuprofen: challenges and opportunities. Drug development and industrial pharmacy. 2018;44(2):173-83.
210. National Center for Biotechnology Information. PubChem Database. Ibuprofen C. Ibuprofen 2012 [cited 2019 4 Sept]. Available from: <https://pubchem.ncbi.nlm.nih.gov/compound/Ibuprofen>.
211. Boggara MB, Krishnamoorti R. Partitioning of nonsteroidal antiinflammatory drugs in lipid membranes: a molecular dynamics simulation study. Biophysical journal. 2010;98(4):586-95.
212. Zayed MA, Hawash M, Fahmey M, El-Gizouli AM. Investigation of ibuprofen drug using mass spectrometry, thermal analyses, and semi-empirical molecular orbital calculation. Journal of thermal analysis and calorimetry. 2012;108(1):315-22.
213. Sigma-Aldrich. Ibuprofen: Specifications 2020 [cited 2020 1-1]. Available from: https://www.sigmaaldrich.com/catalog/product/sigma/i110?lang=en®ion=GB&cm_sp=Inside--prodRecCold_xviews--prodRecCold10-5.
214. INCHEM. Paracetamol 2008 [cited 2020 9-3]. Available from: <http://www.inchem.org/documents/icsc/icsc/eics1330.htm>.
215. Granberg RA, Rasmuson ÅC. Solubility of Paracetamol in Pure Solvents. Journal of Chemical & Engineering Data. 1999;44(6):1391-5.
216. Zhou G, Dong J, Wang Z, Li Z, Li Q, Wang B. Determination and correlation of solubility with thermodynamic analysis of lidocaine hydrochloride in pure and binary solvents. Journal of Molecular Liquids. 2018;265:442-9.
217. Chemspider. Lignocaine 2020 [cited 2020 1-1]. Available from: <http://www.chemspider.com/Chemical-Structure.3548.html>.
218. Nokhodchi A, Amire O, Jelvehgari M. Physico-mechanical and dissolution behaviours of ibuprofen crystals crystallized in the presence of various additives. Daru. 2010;18(2):74-83.
219. Martínez LM, Videá M, López-Silva GA, de los Reyes CA, Cruz-Angeles J, González N. Stabilization of amorphous paracetamol based systems using traditional and novel strategies. International journal of pharmaceuticals. 2014;477(1):294-305.
220. Liu X, Ma X, Kun E, Guo X, Yu Z, Zhang F. Influence of lidocaine forms (salt vs. freebase) on properties of drug–Eudragit® L100-55 extrudates prepared by reactive melt extrusion. International journal of pharmaceuticals. 2018;547.
221. Kim T, Ko J-H, Takayama H, Shibata T, Kojima S. Glass Transition Dynamics of Enantiomer (+)-Ibuprofen. AIP Conference Proceedings. 2013;1518:316-9.
222. Alhalaweh A, Alzghoul A, Mahlin D, Bergström CAS. Physical stability of drugs after storage above and below the glass transition temperature: Relationship to glass-forming ability. International journal of pharmaceuticals. 2015;495(1):312-7.
223. Nagai T, Obara S, Kokubo H, Hoshi N. Application of HPMC and HPMCAS to aqueous film coating of pharmaceutical dosage forms. In: McGinity JW, Ed., editor. Aqueous Polymeric Coatings for Pharmaceutical Dosage Forms 2nd Ed. New York: Marcel Dekker, Inc.; 1997.

224. Chavan RB, Rathi S, Jyothi VGSS, Shastri NR. Cellulose based polymers in development of amorphous solid dispersions. *Asian Journal of Pharmaceutical Sciences*. 2019;14(3):248-64.
225. Friesen DT, Shanker R, Crew M, Smithey DT, Curatolo WJ, Nightingale JAS. Hydroxypropyl Methylcellulose Acetate Succinate-Based Spray-Dried Dispersions: An Overview. *Molecular Pharmaceutics*. 2008;5(6):1003-19.
226. Riedel A, Leopold CS. Degradation of omeprazole induced by enteric polymer solutions and aqueous dispersions: HPLC investigations. *Drug development and industrial pharmacy*. 2005;31(2):151-60.
227. Qiu Y, Chen Y, Zhang GGZ, Yu L, Mantri RV. *Developing Solid Oral Dosage Forms: Pharmaceutical Theory and Practice*: Elsevier Science; 2016.
228. Tipduangta P. Crystallisation of amorphous fenofibrate and potential of the polymer blend electrospun matrices to stabilise in its amorphous form: University of East Anglia; 2016.
229. Shin-etsu. Application Studies of L-HPC and HPMCAS for Pharmaceutical Dosage Forms - Update -. In: Center SCR, editor. Shin-Etsu Chemical Co, Ltd. San Juan: ExcipientFest Americas; 2012.
230. Lawton JW. Zein: A History of Processing and Use. *Cereal Chemistry*. 2002;79(1):1-18.
231. Paulis JW. Comparison of the protein compositions of selected corns and their wild relatives, teosinte and *Tripsacum*. *Journal of agricultural and food chemistry*. 1977;v. 25(no. 2):pp. 265-70-1977 v.25 no.2.
232. Shukla R, Cheryan M. Zein: the industrial protein from corn. *Industrial crops and products*. 2001;13(3):171-92.
233. Esen A. Separation of alcohol-soluble proteins (zeins) from maize into three fractions by differential solubility. *Plant Physiol*. 1986;80(3):623-7.
234. Hagen G, Rubenstein I. Complex organization of zein genes in maize. *Gene*. 1981;13(3):239-49.
235. Gianazza E, Viglienghi V, Righetti PG, Salamini F, Soave C. Amino acid composition of zein molecular components. *Phytochemistry*. 1977;16(3):315-7.
236. Cabra V, Arreguin R, Vazquez-Duhalt R, Farres A. Effect of temperature and pH on the secondary structure and processes of oligomerization of 19 kDa alpha-zein. *Biochimica et Biophysica Acta (BBA)-Proteins and Proteomics*. 2006;1764(6):1110-8.
237. Wilson CM. Multiple zeins from maize endosperms characterized by reversed-phase high performance liquid chromatography. *Plant Physiol*. 1991;95(3):777-86.
238. Berardi A, Bisharat L, Bonacucina G, Casettari L, Logrippo S, Cespi M, et al. Formulation, swelling and dissolution kinetics study of zein based matrix tablets. *Powder Technology*. 2017;310:241-9.
239. Efentakis M, Vlachou M, Choulis NH. Effects of Excipients on Swelling and Drug Release from Compressed Matrices. *Drug development and industrial pharmacy*. 1997;23(1):107-12.
240. Acros. Certificate of Analysis. Acros; 2014.
241. Almeida CBd, Corradini E, Forato LA, Fujihara R, Lopes Filho JF. Microstructure and thermal and functional properties of biodegradable films produced using zein. *Polímeros*. 2018;28:30-7.
242. Shah AP, Bhandary SR. POLYOX (polyethylene oxide) - applications in pharma industry. *Pharmaceutical Reviews*. 2010;8.
243. Ma L, Deng L, Chen J. Applications of poly(ethylene oxide) in controlled release tablet systems: a review. *Drug Development & Industrial Pharmacy*. 2014;40(7):845-51.
244. Vaghani SS, Patel SG, Jivani RR, Jivani NP, Patel MM, Borda R. Design and optimization of a stomach-specific drug delivery system of repaglinide: application of simplex lattice design. *Pharmaceutical development and technology*. 2012;17(1):55-65.
245. Cha KH, Park J, Cho W, Gu DG, Jeong K, Hwang SJ. Design of pH-independent extended release matrix tablets of minocycline hydrochloride for the treatment of dementia. *Archives of pharmaceutical research*. 2009;32(11):1593-8.
246. Liu L, Khang G, Rhee JM, Lee HB. Monolithic osmotic tablet system for nifedipine delivery. *Journal of controlled release : official journal of the Controlled Release Society*. 2000;67(2-3):309-22.
247. Turner S, Federici C, Hite M, Fassihi R. Formulation development and human in vitro-in vivo correlation for a novel, monolithic controlled-release matrix system of high load and highly water-soluble drug niacin. *Drug development and industrial pharmacy*. 2004;30(8):797-807.
248. Peppas NA, Sahlin JJ. Hydrogels as mucoadhesive and bioadhesive materials: a review. *Biomaterials*. 1996;17(16):1553-61.
249. Liu L, Ku J, Khang G, Lee B, Rhee JM, Lee HB. Nifedipine controlled delivery by sandwiched osmotic tablet system. *Journal of controlled release : official journal of the Controlled Release Society*. 2000;68(2):145-56.
250. Rane M, Parmar J, Tiwari S, Rajabi-Siahboomi A. Application of Polyethylene OXide in Hydrophilic Matrix Tablets. *Pharma Times*. 2013;45:41-8.
251. POLYOX. Physico-mechanical Characterization of POLYOX™ for Tablet Manufacture. 2018.
252. Abdullah ZW, Dong Y, Davies IJ, Barbhuiya S. PVA, PVA blends, and their nanocomposites for biodegradable packaging application. *Polymer-Plastics Technology and Engineering*. 2017;56(12):1307-44.

253. Saini I, Sharma A, Dhiman R, Aggarwal S, Ram S, Sharma PK. Grafted SiC nanocrystals: For enhanced optical, electrical and mechanical properties of polyvinyl alcohol. *Journal of Alloys and Compounds*. 2017;714:172-80.
254. Tubbs RK. Sequence distribution of partially hydrolyzed poly (vinyl acetate). *Journal of Polymer Science Part A-1: Polymer Chemistry*. 1966;4(3):623-9.
255. DeMerlis CC, Schoneker DR. Review of the oral toxicity of polyvinyl alcohol (PVA). *Food and chemical toxicology : an international journal published for the British Industrial Biological Research Association*. 2003;41(3):319-26.
256. Halima NB. Poly (vinyl alcohol): review of its promising applications and insights into biodegradation. *Rsc Advances*. 2016;6(46):39823-32.
257. Xu X, Zhao J, Wang M, Wang L, Yang J. 3D Printed Polyvinyl Alcohol Tablets with Multiple Release Profiles. *Scientific Reports*. 2019;9(1):12487.
258. Tagami T, Fukushige K, Ogawa E, Hayashi N, Ozeki T. 3D Printing Factors Important for the Fabrication of Polyvinylalcohol Filament-Based Tablets. *Biological & pharmaceutical bulletin*. 2017;40(3):357-64.
259. Tagami T, Nagata N, Hayashi N, Ogawa E, Fukushige K, Sakai N, et al. Defined drug release from 3D-printed composite tablets consisting of drug-loaded polyvinylalcohol and a water-soluble or water-insoluble polymer filler. *International journal of pharmaceutics*. 2018;543(1-2):361-7.
260. Goodship V, Jacobs D. *Polyvinyl Alcohol: Materials, Processing and Applications: Smithers Rapra Technology*; 2009.
261. Kuraray. Mowiflex C17. https://www.kuraray.eu/fileadmin/Downloads/Mowiflex/technical_data_sheets/TDS_C_17.pdf; Kuraray; 2018.
262. Woodruff MA, Hutmacher DW. The return of a forgotten polymer—Polycaprolactone in the 21st century. *Progress in polymer science*. 2010;35(10):1217-56.
263. Motiwalla MJ, Punyarthi PP, Mehta MK, D'Souza JS, Kelkar-Mane V. Studies on degradation efficiency of polycaprolactone by a naturally-occurring bacterium. *J Environ Biol*. 2013;34(1):43-9.
264. Guarino V, Gentile G, Sorrentino L, Ambrosio L. Polycaprolactone: Synthesis, Properties, and Applications. *Encyclopedia of Polymer Science and Technology* 2017. p. 1-36.
265. Temtem M, Casimiro T, Mano JF, Aguiar-Ricardo A. Preparation of membranes with polysulfone/polycaprolactone blends using a high pressure cell specially designed for a CO₂-assisted phase inversion. *The Journal of Supercritical Fluids*. 2008;43(3):542-8.
266. Raizada A, Bandari A, Kumar B. Polymers in drug delivery: a review. *International Journal of Pharmaceutical Research and Development*. 2010;2:9-20.
267. Sinha VR, Bansal K, Kaushik R, Kumria R, Trehan A. Poly-epsilon-caprolactone microspheres and nanospheres: an overview. *International journal of pharmaceutics*. 2004;278(1):1-23.
268. Arakawa CK, DeForest CA. Chapter 19 - Polymer Design and Development. In: Vishwakarma A, Karp JM, editors. *Biology and Engineering of Stem Cell Niches*. Boston: Academic Press; 2017. p. 295-314.
269. Perstorp. Capa™ 6800: Product data sheet. PERSTORP; 2016.
270. Mondal D, Griffith M, Venkatraman SS. Polycaprolactone-based biomaterials for tissue engineering and drug delivery: Current scenario and challenges. *International Journal of Polymeric Materials and Polymeric Biomaterials*. 2016;65(5):255-65.
271. Pina M, Zhao M, Pinto j, Sousa J, Craig D. The Influence of Drug Physical State on the Dissolution Enhancement of Solid Dispersions Prepared Via Hot-Melt Extrusion: A Case Study Using Olanzapine. *Journal of pharmaceutical sciences*. 2014;103:1214-23.
272. Giri TK, Kumar K, Alexander A, Ajazuddin, Badwaik H, Tripathi DK. A novel and alternative approach to controlled release drug delivery system based on solid dispersion technique. *Bulletin of Faculty of Pharmacy, Cairo University*. 2012;50(2):147-59.
273. Bühler V. *Polyvinylpyrrolidone Excipients for Pharmaceuticals: Povidone, Crospovidone and Copovidone*: Springer Berlin Heidelberg; 2005.
274. Forster A, Hemenstall J, Rades T. Characterization of glass solutions of poorly water-soluble drugs produced by melt extrusion with hydrophilic amorphous polymers. *The Journal of pharmacy and pharmacology*. 2001;53(3):303-15.
275. Lehmkemper K, Kyeremateng SO, Heinzerling O, Degenhardt M, Sadowski G. Long-Term Physical Stability of PVP- and PVPVA-Amorphous Solid Dispersions. *Molecular Pharmaceutics*. 2017;14(1):157-71.
276. Prudic A, Kleetz T, Korf M, Ji Y, Sadowski G. Influence of Copolymer Composition on the Phase Behavior of Solid Dispersions. *Molecular Pharmaceutics*. 2014;11(11):4189-98.
277. Patra CN, Priya R, Swain S, Kumar Jena G, Panigrahi KC, Ghose D. Pharmaceutical significance of Eudragit: A review. *Future Journal of Pharmaceutical Sciences*. 2017;3(1):33-45.
278. Evonik. EUDRAGIT. www.evonik.com/eudragit2017.

279. Parikh T, Gupta SS, Meena A, Serajuddin A. Investigation of thermal and viscoelastic properties of polymers relevant to hot melt extrusion - III: Polymethacrylates and polymethacrylic acid based polymers. *Journal of Excipients and Food Chemicals*. 2014;5:56-64.
280. Basf. Soluplus® Technical Information. 2010.
281. Paaver U, Tamm I, Laidmäe I, Lust A, Kirsimäe K, Veski P, et al. Soluplus graft copolymer: potential novel carrier polymer in electrospinning of nanofibrous drug delivery systems for wound therapy. *Biomed Research International*. 2014;2014:789765-.
282. Basf. Soluplus® Technical Information. Basf; 2019.
283. Butler M. Xanthan Gum : Applications and Research Studies. Hauppauge, New York: Nova Science Publishers, Inc; 2016.
284. Sharma B, Dhuldhoya N, Merchant S, Merchant U. Xanthan Gum-A Boon to Food Industry. *Food Promotion Chronicle*. 2006;1:27-30.
285. Mohammed Z, Haque A, Richardson R, Morris E. Promotion and inhibition of xanthan 'weak-gel' rheology by calcium ions. *Carbohydrate polymers*. 2007;70(1):38-45.
286. Ross-Murphy SB, Morris VJ, Morris ER. Molecular viscoelasticity of xanthan polysaccharide. *Faraday Symposia of the Chemical Society*. 1983;18(0):115-29.
287. Kadajji V, Betageri G. Water Soluble Polymers for Pharmaceutical Applications. *Polymers*. 2011;3.
288. Lee BH. *Fundamentals of food biotechnology*: John Wiley & Sons; 2014.
289. CPKelco. Xantural 180 product data sheet. CPKelco; 2012.
290. Basu S, Shivhare US, Mujumdar AS. Moisture Adsorption Isotherms and Glass Transition Temperature of Xanthan Gum. *Drying Technology*. 2007;25(9):1581-6.
291. Sairam M, Babu VR, Naidu BVK, Aminabhavi TM. Encapsulation efficiency and controlled release characteristics of crosslinked polyacrylamide particles. *International journal of pharmaceutics*. 2006;320(1-2):131-6.
292. McKeen LW. 4 - Styrenic Plastics. In: McKeen LW, editor. *The Effect of Long Term Thermal Exposure on Plastics and Elastomers*. Oxford: William Andrew Publishing; 2014. p. 73-84.
293. Makerbot. ABS Safety Data Sheet 2015 [cited 2020 21-5]. Available from: file:///C:/Users/Salman/Downloads/TDJ5_3D_Printer_Appendix_B_ABS_MSDS.pdf.
294. Abbott AC, Tandon GP, Bradford RL, Koerner H, Baur JW. Process-structure-property effects on ABS bond strength in fused filament fabrication. *Additive Manufacturing*. 2018;19:29-38.
295. Thermo, Scientific. Thermo Scientific HAAKE MiniLab II product specifications 2008. Available from: <http://webcache.googleusercontent.com/search?q=cache:RalxdIS0IRcl:tools.thermofisher.com/content/sfs/brochures/D10557~.pdf+&cd=1&hl=en&ct=clnk&gl=uk>.
296. Makerbot. MAKERBOT PRINT 2018 [cited 2020 22-1]. Available from: <https://pages.makerbot.com/ap-software-and-apps.html>.
297. Chiu MH, Prenner EJ. Differential scanning calorimetry: An invaluable tool for a detailed thermodynamic characterization of macromolecules and their interactions. *J Pharm Bioallied Sci*. 2011;3(1):39-59.
298. Pagel M, Abd-Elghany M, Klapötke T. A review on differential scanning calorimetry technique and its importance in the field of energetic materials. *Physical Sciences Reviews*. 2018;3.
299. Bauer J, Spanton S, Henry R, Quick J, Dziki W, Porter W, et al. Ritonavir: An Extraordinary Example of Conformational Polymorphism. *Pharmaceutical Research*. 2001;18(6):859-66.
300. Patil DG, Brill TB. Thermal decomposition of energetic materials 53. Kinetics and mechanism of thermolysis of hexanitrohexazaisowurtzitane. *Combustion and Flame*. 1991;87(2):145-51.
301. Kissinger HE. Reaction Kinetics in Differential Thermal Analysis. *Analytical Chemistry*. 1957;29(11):1702-6.
302. Coats AW, Redfern JP. Thermogravimetric analysis. A review. *Analyst*. 1963;88(1053):906-24.
303. Ng HM, mohamad saidi N, Omar F, Kasi R, T subramaniam R, Baig S. Thermogravimetric Analysis of Polymers. 2018:1-29.
304. Haladjian J, Carpeni G. *Bull Society; France: Chim*; 1960.
305. Berthomieu C, Hienerwadel R. Fourier transform infrared (FTIR) spectroscopy. *Photosynthesis research*. 2009;101(2-3):157-70.
306. Bunaciu AA, Aboul-Enein HY, Fleschin S. Application of Fourier Transform Infrared Spectrophotometry in Pharmaceutical Drugs Analysis. *Applied Spectroscopy Reviews*. 2010;45(3):206-19.
307. Griffiths PR, De Haseth JA. *Fourier transform infrared spectrometry*: John Wiley & Sons; 2007.
308. Chan KLA, Kazarian SG, Vassou D, Gionis V, Chryssikos GD. In situ high-throughput study of drug polymorphism under controlled temperature and humidity using FT-IR spectroscopic imaging. *Vibrational Spectroscopy*. 2007;43(1):221-6.
309. Krafft C, Shapoval L, Sobottka SB, Geiger KD, Schackert G, Salzer R. Identification of primary tumors of brain metastases by SIMCA classification of IR spectroscopic images. *Biochimica et biophysica acta*. 2006;1758(7):883-91.

310. Chen Y, Zou C, Mastalerz M, Hu S, Gasaway C, Tao X. Applications of Micro-Fourier Transform Infrared Spectroscopy (FTIR) in the Geological Sciences--A Review. *Int J Mol Sci.* 2015;16(12):30223-50.
311. Sharma YR. *Elementary Organic Spectroscopy*: S. Chand Limited; 2007.
312. University n. *Basic UV/Visible Spectrophotometry*nd.
313. GE. *GE Healthcare Life Sciences: Spectrophotometry Handbook*. 2013.
314. PerkinElmer. *UV/Vis Spectrophotometers*. 2011.
315. Kadam SS, Kramer HJM, ter Horst JH. Combination of a Single Primary Nucleation Event and Secondary Nucleation in Crystallization Processes. *Crystal Growth & Design.* 2011;11(4):1271-7.
316. Lakhani P, Bahl R, Bafna P. TRANSDERMAL PATCHES: PHYSIOCHEMICAL AND IN-VITRO EVALUATION METHODS. *International Journal of Pharmaceutical Sciences and Research.* 2015;0:1826-36.
317. USP. *United States Pharmacopeia 34/National Formulary*. 2011.
318. Liu Q, editor *Hydrodynamic effects of a cannula in a USP dissolution testing apparatus 22013*.
319. Pérez-Ortega J, Almanza-Ortega NN, Vega-Villalobos A, Pazos-Rangel R, Zavala-Díaz C, Martínez-Rebollar A. *The K-Means Algorithm Evolution. Clustering: IntechOpen; 2019.*
320. Pearson K. LIII. On lines and planes of closest fit to systems of points in space. *The London, Edinburgh, and Dublin Philosophical Magazine and Journal of Science.* 1901;2(11):559-72.
321. Stein SAM, Loccisano AE, Firestone SM, Evanseck JD. Chapter 13 Principal Components Analysis: A Review of its Application on Molecular Dynamics Data. In: Spellmeyer DC, editor. *Annual Reports in Computational Chemistry. 2: Elsevier; 2006. p. 233-61.*
322. Powell V. Principal Component Analysis: Setosa.io; nd [cited 2020 25-1]. Available from: <http://setosa.io/ev/principal-component-analysis/>.
323. Cattell RB. The meaning and strategic use of factor analysis. *Handbook of multivariate experimental psychology*: Springer; 1988. p. 131-203.
324. Cattell RB. The scree test for the number of factors. *Multivariate behavioral research.* 1966;1(2):245-76.
325. Peres-Neto PR, Jackson DA, Somers KM. How many principal components? stopping rules for determining the number of non-trivial axes revisited. *Computational Statistics & Data Analysis.* 2005;49(4):974-97.
326. Adya M, Collopy F. How effective are neural networks at forecasting and prediction? A review and evaluation. *Journal of forecasting.* 1998;17(5-6):481-95.
327. Jiang Y, Yang C, Na J, Li G, Li Y, Zhong J. A Brief Review of Neural Networks Based Learning and Control and Their Applications for Robots. *Complexity.* 2017;2017:1-14.
328. Gruau F, Whitley D, Pyeatt L, editors. *A comparison between cellular encoding and direct encoding for genetic neural networks. Proceedings of the 1st annual conference on genetic programming; 1996.*
329. de Garis H. An artificial brain ATR's CAM-Brain Project aims to build/evolve an artificial brain with a million neural net modules inside a trillion cell Cellular Automata Machine. *New Generation Computing.* 1994;12(2):215-21.
330. Neocleous C, Schizas C, editors. *Artificial Neural Network Learning: A Comparative Review2002*; Berlin, Heidelberg: Springer Berlin Heidelberg.
331. Gardner MW, Dorling S. Artificial neural networks (the multilayer perceptron)—a review of applications in the atmospheric sciences. *Atmospheric environment.* 1998;32(14-15):2627-36.
332. Zhang G, Patuwo BE, Hu MY. Forecasting with artificial neural networks:: The state of the art. *International journal of forecasting.* 1998;14(1):35-62.
333. Murat YS, Ceylan H. Use of artificial neural networks for transport energy demand modeling. *Energy policy.* 2006;34(17):3165-72.
334. Negnevitsky M. *Artificial intelligence: a guide to intelligent systems*: Pearson education; 2005.
335. Das MK, Chakraborty T. Chapter 14 - ANN in Pharmaceutical Product and Process Development. In: Puri M, Pathak Y, Sutariya VK, Tipparaju S, Moreno W, editors. *Artificial Neural Network for Drug Design, Delivery and Disposition*. Boston: Academic Press; 2016. p. 277-93.
336. Manda A, Walker RB, Khamanga SM. An Artificial Neural Network Approach to Predict the Effects of Formulation and Process Variables on Prednisone Release from a Multipartite System. *Pharmaceutics.* 2019;11(3):109.
337. Goh WY, Lim CP, Peh KK, Subari K. Application of a Recurrent Neural Network to Prediction of Drug Dissolution Profiles. *Neural Computing & Applications.* 2002;10(4):311-7.
338. Paixao P, Gouveia LF, Morais JA. Prediction of the in vitro permeability determined in Caco-2 cells by using artificial neural networks. *European journal of pharmaceutical sciences : official journal of the European Federation for Pharmaceutical Sciences.* 2010;41(1):107-17.
339. Kumar KJ, Panpalia GM, Priyadarshini S. Application of artificial neural networks in optimizing the fatty alcohol concentration in the formulation of an O/W emulsion. *Acta pharmaceutica (Zagreb, Croatia).* 2011;61(2):249-56.

340. Asadi H, Rostamizadeh K, Salari D, Hamidi M. Preparation of biodegradable nanoparticles of tri-block PLA-PEG-PLA copolymer and determination of factors controlling the particle size using artificial neural network. *Journal of microencapsulation*. 2011;28(5):406-16.
341. Patel AD, Agrawal A, Dave RH. Investigation of the effects of process variables on derived properties of spray dried solid-dispersions using polymer based response surface model and ensemble artificial neural network models. *European journal of pharmaceuticals and biopharmaceutics : official journal of Arbeitsgemeinschaft fur Pharmazeutische Verfahrenstechnik eV*. 2014;86(3):404-17.
342. Behzadi SS, Prakasvudhisarn C, Klocker J, Wolschann P, Viernstein H. Comparison between two types of Artificial Neural Networks used for validation of pharmaceutical processes. *Powder Technology*. 2009;195(2):150-7.
343. Ye X, Xiao X, Shi J, Ling M. The new concepts of measurement error theory. *Measurement*. 2016;83:96-105.
344. Menditto A, Patriarca M, Magnusson B. Understanding the meaning of accuracy, trueness and precision. *Accreditation and Quality Assurance*. 2007;12(1):45-7.
345. Taylor J. *Introduction to error analysis, the study of uncertainties in physical measurements* 1997.
346. Bland JM, Altman DG. *Statistics notes: measurement error*. *BMJ*. 1996;312(7047):1654.
347. Rabinovich SG. *Measurement Errors and Uncertainties: Theory and Practice*: Springer New York; 2006.
348. 3D-printer-filaments. *Filament Specs 2020* [cited 2020 3-3]. Available from: <https://3d-printer-filaments.com/filament-specs/>.
349. Makerbot. *MakerBot Replicator 2 Brochure 2019* [cited 2019 21-6]. Available from: http://downloads.makerbot.com/replicator2/MakerBot_Replicator2_brochure.pdf.
350. Goyanes A, Robles Martinez P, Buanz A, Basit AW, Gaisford S. Effect of geometry on drug release from 3D printed tablets. *International journal of pharmaceutics*. 2015;494(2):657-63.
351. Martinez PR, Goyanes A, Basit AW, Gaisford S. Influence of Geometry on the Drug Release Profiles of Stereolithographic (SLA) 3D-Printed Tablets. *AAPS PharmSciTech*. 2018;19(8):3355-61.
352. Stewart J, Clegg DK, Watson S. *Calculus: Early Transcendentals*: Cengage Learning; 2020.
353. University L. *Errors and Percentage Change 2008* [cited 2020 16-3]. Available from: https://learn.lboro.ac.uk/archive/olmp/olmp_resources/pages/workbooks_1_50_jan2008/Workbook18/18_4_errors_n_percntge_chnge.pdf.
354. Mortimer RG. Chapter 16 - Data Reduction and the Propagation of Errors. In: Mortimer RG, editor. *Mathematics for Physical Chemistry (Fourth Edition)*. Boston: Elsevier; 2013. p. 207-22.
355. Liengme BV, Ellert DJ. Chapter 16 - Statistics for Experimenters. In: Liengme BV, Ellert DJ, editors. *A Guide to Microsoft Excel 2007 for Scientists and Engineers*. Boston: Academic Press; 2009. p. 275-97.
356. Dux J. *Handbook of quality assurance for the analytical chemistry laboratory*: Springer Science & Business Media; 2013.
357. Bujang MA, Baharum N. Sample Size Guideline for Correlation Analysis. *World Journal of Social Science Research*. 2016;3:37.
358. Harding B, Tremblay C, Cousineau D. Standard errors: A review and evaluation of standard error estimators using Monte Carlo simulations. *The Quantitative Methods for Psychology*. 2014;10(2):107-23.
359. Explorable.com. *Sampling Error 2009* [cited 2020 6-Jun]. Available from: <https://explorable.com/sampling-error>.
360. Anderson JC, Gerbing DW. The effect of sampling error on convergence, improper solutions, and goodness-of-fit indices for maximum likelihood confirmatory factor analysis. *Psychometrika*. 1984;49(2):155-73.
361. Brooks D. *The Sampling Distribution and Central Limit Theorem*: CreateSpace Independent Publishing Platform; 2012.
362. Repka MA, Bandari S, Kallakunta VR, Vo AQ, McFall H, Pimparade MB, et al. Melt extrusion with poorly soluble drugs – An integrated review. *International journal of pharmaceutics*. 2018;535(1):68-85.
363. Li M, Gogos CG, Ioannidis N. Improving the API dissolution rate during pharmaceutical hot-melt extrusion I: Effect of the API particle size, and the co-rotating, twin-screw extruder screw configuration on the API dissolution rate. *International journal of pharmaceutics*. 2015;478(1):103-12.
364. Gao Y, Muzzio FJ, Ierapetritou MG. A review of the Residence Time Distribution (RTD) applications in solid unit operations. *Powder Technology*. 2012;228:416-23.
365. Censi R, Gigliobianco MR, Casadidio C, Di Martino P. Hot melt extrusion: Highlighting physicochemical factors to be investigated while designing and optimizing a hot melt extrusion process. *Pharmaceutics*. 2018;10(3):89.
366. Tiffour I, Bassaid S, Dehbi A, Abdelkader B, Mourad A-H, Zeinert A. Realization and characterization of a new organic thin film semiconductor. *Surface Review and Letters*. 2017.
367. Mackay ME, Swain ZR, Banbury CR, Phan DD, Edwards DA. The performance of the hot end in a plasticating 3D printer. *Journal of Rheology*. 2017;61(2):229-36.

368. Aho J, Bøtker JP, Genina N, Edinger M, Arnfast L, Rantanen J. Roadmap to 3D-Printed Oral Pharmaceutical Dosage Forms: Feedstock Filament Properties and Characterization for Fused Deposition Modeling. *Journal of pharmaceutical sciences*. 2019;108(1):26-35.
369. ERDOĞDU F, Uyar R, PALAZOĞLU TK. Experimental comparison of natural convection and conduction heat transfer. *Journal of Food Process Engineering*. 2010;33:85-100.
370. Wang S, Capoen L, D'hooge D, Cardon L. Can the melt flow index be used to predict the success of fused deposition modelling of commercial poly(lactic acid) filaments into 3D printed materials? *Plastics, Rubber and Composites*. 2017;47:1-8.
371. Matbase. ABS 2014 [cited 2020 3-3]. Available from: <https://web.archive.org/web/20140617115106/http://www.matbase.com/material-categories/natural-and-synthetic-polymers/commodity-polymers/material-properties-of-acrylonitrile-butadiene-styrene-general-purpose-gp-abs.html#properties>.
372. Cramer D, Howitt DL. *The Sage dictionary of statistics: a practical resource for students in the social sciences*: Sage; 2004.
373. Kim TK. T test as a parametric statistic. *Korean J Anesthesiol*. 2015;68(6):540-6.
374. Schultze AE, Irizarry AR. Recognizing and Reducing Analytical Errors and Sources of Variation in Clinical Pathology Data in Safety Assessment Studies. *Toxicologic pathology*. 2017;45(2):281-7.
375. Ilyés K, Kovács NK, Balogh A, Borbás E, Farkas B, Casian T, et al. The applicability of pharmaceutical polymeric blends for the fused deposition modelling (FDM) 3D technique: Material considerations–printability–process modulation, with consecutive effects on in vitro release, stability and degradation. *European Journal of Pharmaceutical Sciences*. 2019;129:110-23.
376. Pereira BC, Isreb A, Forbes RT, Dores F, Habashy R, Petit J-B, et al. 'Temporary Plasticiser': A novel solution to fabricate 3D printed patient-centred cardiovascular 'Polypill' architectures. *European Journal of Pharmaceutics and Biopharmaceutics*. 2019;135:94-103.
377. Chai X, Chai H, Wang X, Yang J, Li J, Zhao Y, et al. Fused Deposition Modeling (FDM) 3D Printed Tablets for Intra-gastric Floating Delivery of Domperidone. *Scientific Reports*. 2017;7(1):2829-.
378. Arafat B, Qinna N, Cieszynska M, Forbes RT, Alhnan MA. Tailored on demand anti-coagulant dosing: An in vitro and in vivo evaluation of 3D printed purpose-designed oral dosage forms. *European Journal of Pharmaceutics and Biopharmaceutics*. 2018;128:282-9.
379. Gioumouxouzis CI, Katsamenis OL, Bouropoulos N, Fatouros DG. 3D printed oral solid dosage forms containing hydrochlorothiazide for controlled drug delivery. *Journal of Drug Delivery Science and Technology*. 2017;40:164-71.
380. Goyanes A, Det-Amornrat U, Wang J, Basit AW, Gaisford S. 3D scanning and 3D printing as innovative technologies for fabricating personalized topical drug delivery systems. *Journal of controlled release : official journal of the Controlled Release Society*. 2016;234:41-8.
381. Holländer J, Genina N, Jukarainen H, Khajeheian M, Rosling A, Mäkilä E, et al. Three-Dimensional Printed PCL-Based Implantable Prototypes of Medical Devices for Controlled Drug Delivery. *Journal of pharmaceutical sciences*. 2016;105(9):2665-76.
382. Ma H, Hsiao BS, Chu B. Ethyl Cellulose (EC) Membrane. In: Drioli E, Giorno L, editors. *Encyclopedia of Membranes*. Berlin, Heidelberg: Springer Berlin Heidelberg; 2015. p. 1-2.
383. Ashok Kumar P. and Damodar Kumar S. Effect of hydrophilic and hydrophobic polymers and fillers on controlled release matrix tablets of acyclovir. *Der Pharmacia Sinica*. 2013;4(3):143-50.
384. Qi Y, Ma H-L, Du Z-H, Yang B, Wu J, Wang R, et al. Hydrophilic and Antibacterial Modification of Poly(lactic acid) Films by γ -ray Irradiation. *ACS Omega*. 2019;4(25):21439-45.
385. Israelachvili J. The different faces of poly(ethylene glycol). *Proc Natl Acad Sci U S A*. 1997;94(16):8378-9.
386. Bose A, Wong TW. 18 - Oral colon cancer targeting by chitosan nanocomposites. In: Inamuddin, Asiri AM, Mohammad A, editors. *Applications of Nanocomposite Materials in Drug Delivery*: Woodhead Publishing; 2018. p. 409-29.
387. Williams JK, Yoo JJ, Atala A. Chapter 59 - Regenerative Medicine Approaches for Tissue Engineered Heart Valves. In: Atala A, Lanza R, Mikos AG, Nerem R, editors. *Principles of Regenerative Medicine (Third Edition)*. Boston: Academic Press; 2019. p. 1041-58.
388. Glass JE. *Polymers in aqueous media: performance through association*: ACS Publications; 1989.
389. Glass JE. *Associative polymers in aqueous media*: American Chemical Society; 2000.
390. Chaibva FA, Khamanga SMM, Walker RB. Swelling, erosion and drug release characteristics of salbutamol sulfate from hydroxypropyl methylcellulose-based matrix tablets. *Drug development and industrial pharmacy*. 2010;36(12):1497-510.
391. Karadağ E, Saraydın D. Swelling studies of super water retainer acrylamide/crotonic acid hydrogels crosslinked by trimethylolpropane triacrylate and 1,4-butanediol dimethacrylate. *Polymer Bulletin*. 2002;48(3):299-307.

392. McConville JT, Ross AC, Florence AJ, Stevens HNE. Erosion Characteristics of an Erodible Tablet Incorporated in a Time-Delayed Capsule Device. *Drug development and industrial pharmacy*. 2005;31(1):79-89.
393. Göpferich A. Erosion of composite polymer matrices. *Biomaterials*. 1997;18(5):397-403.
394. Gaillard T, George M, Gastaldi E, Nallet F, Fabre P. An experimental and theoretical study of the erosion of semi-crystalline polymers and the subsequent generation of microparticles. *Soft Matter*. 2019;15(41):8302-12.
395. Sánchez-González S, Diban N, Urriaga A. Hydrolytic degradation and mechanical stability of poly (ϵ -Caprolactone)/reduced graphene oxide membranes as scaffolds for in vitro neural tissue regeneration. *Membranes*. 2018;8(1):12.
396. Masuda Y (2003) Superabsorbency. In: Osada Y KKeGh, 1st edn., NTS T.
397. Born KL, V. & Boulenger, P, Weley-VCH, . Xanthan", in: *Biopolymers*. Steinbüchel AV, E. J. & De Baets, S, editor. Weley-VCH: Weinheim; 2002.
398. Telis VRN. *Biopolymer Engineering in Food Processing*: CRC Press; 2012.
399. Chana J, Forbes B, Jones SA. The synthesis of high molecular weight partially hydrolysed poly(vinyl alcohol) grades suitable for nanoparticle fabrication. *Journal of nanoscience and nanotechnology*. 2008;8(11):5739-47.
400. Attwood D, Florence AT. *Physical pharmacy*. 2nd ed. ed: Pharmaceutical Press; 2012.
401. Singh J. *Swelling of Polymer Gels*: McGill University Libraries; 1993.
402. Wu C. Simulated glass transition of poly(ethylene oxide) bulk and film: a comparative study. *The journal of physical chemistry B*. 2011;115(38):11044-52.
403. Lyons JG, Blackie P, Higginbotham CL. The significance of variation in extrusion speeds and temperatures on a PEO/PCL blend based matrix for oral drug delivery. *International journal of pharmaceutics*. 2008;351(1):201-8.
404. Stolwijk NA, Heddier C, Reschke M, Wiencierz M, Bokeloh J, Wilde G. Salt-Concentration Dependence of the Glass Transition Temperature in PEO–NaI and PEO–LiTFSI Polymer Electrolytes. *Macromolecules*. 2013;46(21):8580-8.
405. Wypych G. PEO poly(ethylene oxide). In: Wypych G, editor. *Handbook of Polymers (Second Edition)*: ChemTec Publishing; 2016. p. 390-3.
406. Mudassir J, Ranjha NM. Dynamic and equilibrium swelling studies: crosslinked pH sensitive methyl methacrylate-co-itaconic acid (MMA-co-IA) hydrogels. *Journal of Polymer Research*. 2007;15(3):195-203.
407. Trask C, Roland C. A nearly ideal mixture of high polymers. *Macromolecules*. 1989;22(1):256-61.
408. Xiang TX, Anderson BD. Molecular dynamics simulation of amorphous hydroxypropyl-methylcellulose acetate succinate (HPMCAS): polymer model development, water distribution, and plasticization. *Mol Pharm*. 2014;11(7):2400-11.
409. Altamimi MA, Neau SH. Investigation of the in vitro performance difference of drug-Soluplus® and drug-PEG 6000 dispersions when prepared using spray drying or lyophilization. *Saudi Pharmaceutical Journal*. 2017;25(3):419-39.
410. Rudin A, Choi P. Chapter 5 - Polymer Mixtures. In: Rudin A, Choi P, editors. *The Elements of Polymer Science & Engineering (Third Edition)*. Boston: Academic Press; 2013. p. 231-74.
411. Shibayama M, Jinnai H, Hashimoto T. Chapter 2 - Neutron Scattering. In: Tanaka T, editor. *Experimental Methods in Polymer Science*. Boston: Academic Press; 2000. p. 57-154.
412. Tadros T. Interaction Parameter. In: Tadros T, editor. *Encyclopedia of Colloid and Interface Science*. Berlin, Heidelberg: Springer Berlin Heidelberg; 2013. p. 634.
413. Mark JE. *Physical properties of polymers handbook*: Springer; 2007.
414. Pillai O, Panchagnula R. Polymers in drug delivery. *Current Opinion in Chemical Biology*. 2001;5(4):447-51.
415. Vibhooti P, Rajan G, Seema B. Eudragit and chitosan-the two most promising polymers for colon drug delivery. 2010.
416. Li P, Zhang S, Sun W, Cui M, Wen H, Li Q, et al. Flexibility of 3D Extruded Printing for a Novel Controlled-Release Puerarin Gastric Floating Tablet: Design of Internal Structure. *AAPS PharmSciTech*. 2019;20(6):236.
417. Solanki NG, Tahsin M, Shah AV, Serajuddin ATM. Formulation of 3D Printed Tablet for Rapid Drug Release by Fused Deposition Modeling: Screening Polymers for Drug Release, Drug-Polymer Miscibility and Printability. *Journal of pharmaceutical sciences*. 2018;107(1):390-401.
418. Saviano M, Aquino RP, Del Gaudio P, Sansone F, Russo P. Poly(vinyl alcohol) 3D printed tablets: The effect of polymer particle size on drug loading and process efficiency. *International journal of pharmaceutics*. 2019;561:1-8.
419. Skowrya J, Pietrzak K, Alhnan MA. Fabrication of extended-release patient-tailored prednisolone tablets via fused deposition modelling (FDM) 3D printing. *European Journal of Pharmaceutical Sciences*. 2015;68:11-7.
420. Ishizuka Y, Ueda K, Okada H, Takeda J, Karashima M, Yazawa K, et al. Effect of Drug–Polymer Interactions through Hypromellose Acetate Succinate Substituents on the Physical Stability on Solid Dispersions Studied by Fourier-Transform Infrared and Solid-State Nuclear Magnetic Resonance. *Molecular pharmaceutics*. 2019;16(6):2785-94.
421. Meruva S, Donovan MD. Effects of drug-polymer interactions on tablet properties during the development of abuse-deterrent dosage forms. *AAPS PharmSciTech*. 2019;20(3):93.

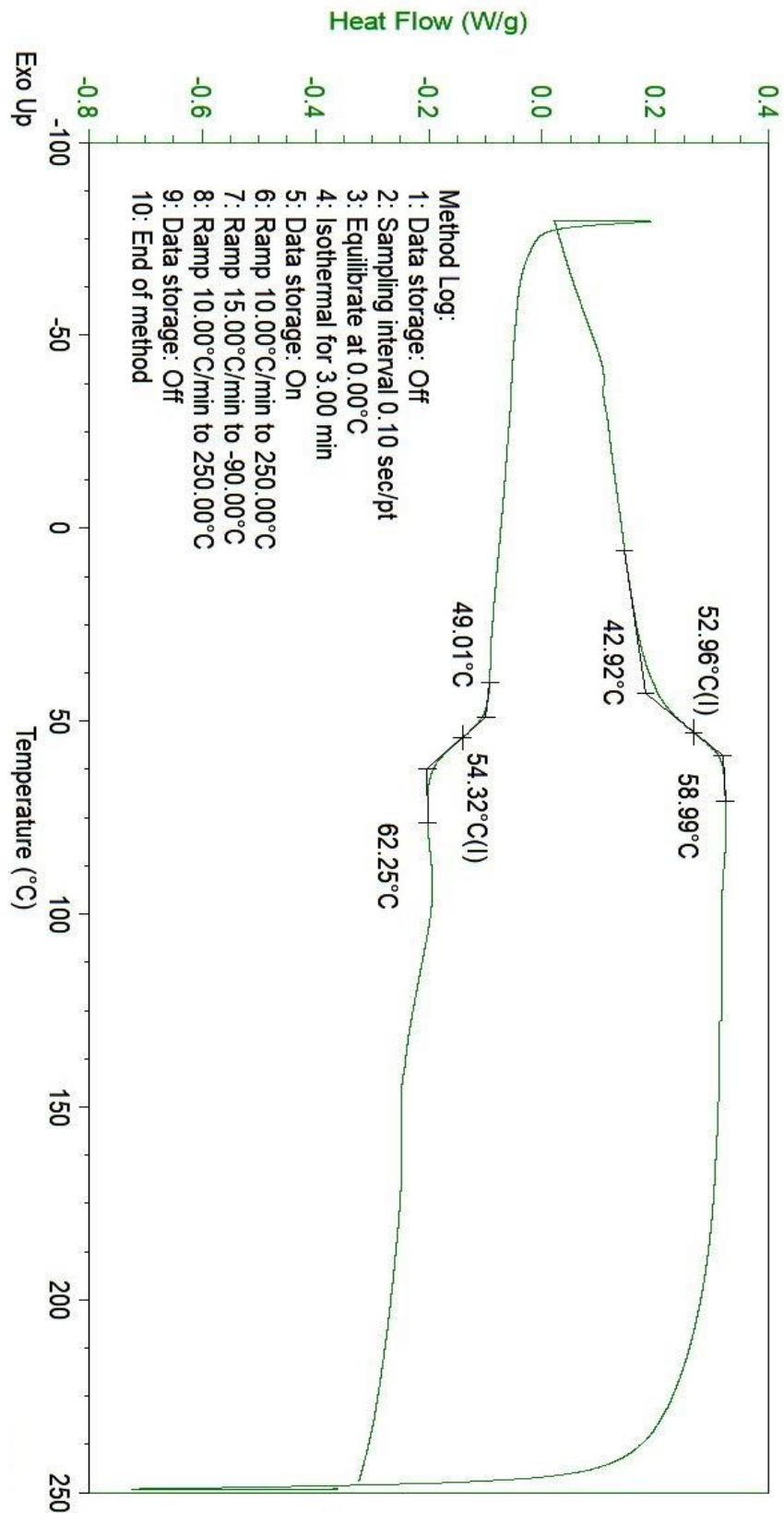
422. Srivastava P, Singh B, Angove M. Competitive Adsorption of Cadmium(II) onto Kaolinite as Affected by pH. 2004.
423. Balogh GT, Tarcsey Á, Keserú GM. Comparative evaluation of pKa prediction tools on a drug discovery dataset. *Journal of Pharmaceutical and Biomedical Analysis*. 2012;67-68:63-70.
424. Prescott L. Kinetics and metabolism of paracetamol and phenacetin. *British journal of clinical pharmacology*. 1980;10(S2):291S-8S.
425. A Bisharat L. An investigation into the use of zein proteins as pharmaceutical excipients for modified drug release applications. 2012.
426. Banik BL, Brown JL. 8 - Interaction of responsive/switchable surfaces with cells. In: Zhang Z, editor. *Switchable and Responsive Surfaces and Materials for Biomedical Applications*. Oxford: Woodhead Publishing; 2015. p. 189-201.
427. Shaw LR, Irwin WJ, Grattan TJ, Conway BR. The Effect of Selected Water-Soluble Excipients on the Dissolution of Paracetamol and Ibuprofen. *Drug development and industrial pharmacy*. 2005;31(6):515-25.
428. Augsburg LL, Brzezczko AW, Shah U, Jung HA. Superdisintegrants: Characterization and function. *Encyclopedia of Pharmaceutical Science and Technology, Six Volume Set (Print)*: CRC Press; 2013. p. 3440-63.
429. Rowell RM, WB B. Water repellency and dimensional stability of wood. Madison, WI: 1985.
430. Ogston Alexander George PBN, Wells J. D. and Snowden J. Mck. On the transport of compact particles through solutions of chain-polymers333*Proc. R. Soc. Lond. A*.
431. Johansson L, Löfroth JE. Diffusion and interaction in gels and solutions. 4. Hard sphere Brownian dynamics simulations. *The Journal of Chemical Physics*. 1993;98(9):7471-9.
432. Amsden B. Solute diffusion in hydrogels.: An examination of the retardation effect. *Polymer Gels and Networks*. 1998;6(1):13-43.
433. Rowe RC, Sheskey PJ, Quinn ME, Association AP. *Handbook of Pharmaceutical Excipients: Pharmaceutical Press*; 2009.
434. Eyjolfsson R. *Design and Manufacture of Pharmaceutical Tablets*: Elsevier Science; 2014.
435. Herzberger J, Niederer K, Pohlit H, Seiwert J, Worm M, Wurm FR, et al. Polymerization of Ethylene Oxide, Propylene Oxide, and Other Alkylene Oxides: Synthesis, Novel Polymer Architectures, and Bioconjugation. *Chemical Reviews*. 2016;116(4):2170-243.
436. Tyrer D. The Theory of Solubility. *The Journal of Physical Chemistry*. 1912;16(1):69-85.
437. Matubayasi N, Nakahara M. Association and Dissociation of Nonpolar Solutes in Super- and Subcritical Water. *The Journal of Physical Chemistry B*. 2000;104(44):10352-8.
438. Kavanagh N, Corrigan OI. Swelling and erosion properties of hydroxypropylmethylcellulose (Hypromellose) matrices—influence of agitation rate and dissolution medium composition. *International journal of pharmaceutics*. 2004;279(1):141-52.
439. Asare-Addo K, Conway BR, Larhrib H, Levina M, Rajabi-Siahboomi AR, Tetteh J, et al. The effect of pH and ionic strength of dissolution media on in-vitro release of two model drugs of different solubilities from HPMC matrices. *Colloids and Surfaces B: Biointerfaces*. 2013;111:384-91.
440. Hamed R, Awadallah A, Sunoqrot S, Tarawneh O, Nazzal S, AlBaraghtli T, et al. pH-Dependent Solubility and Dissolution Behavior of Carvedilol—Case Example of a Weakly Basic BCS Class II Drug. *AAPS PharmSciTech*. 2016;17(2):418-26.
441. Kaushik S. An Introduction to Clustering and different methods of clustering: Analytics Vidhya; 2016 [cited 2019 27-Nov]. Available from: <https://www.analyticsvidhya.com/blog/2016/11/an-introduction-to-clustering-and-different-methods-of-clustering/>.
442. Jolliffe IT, Cadima J. Principal component analysis: a review and recent developments. *Philosophical Transactions of the Royal Society A: Mathematical, Physical and Engineering Sciences*. 2016;374(2065):20150202.
443. Cardot JM, Garcia Arieta A, Paixao P, Tasevska I, Davit B. Implementing the Biopharmaceutics Classification System in Drug Development: Reconciling Similarities, Differences, and Shared Challenges in the EMA and US-FDA-Recommended Approaches. *The AAPS journal*. 2016;18(4):1039-46.
444. Mehta M. *Biopharmaceutics Classification System (BCS): Development, Implementation, and Growth*: Wiley; 2017.
445. Chatzizacharia K, Hatzivramidis D. New frames of reference for mapping drugs in the four classes of the BCS and BDDCS into regions with clear boundaries. *AIChE Journal*. 2015;61(11):3570-9.
446. Kalantzi L, Reppas C, Dressman JB, Amidon GL, Junginger HE, Midha KK, et al. Biowaiver monographs for immediate release solid oral dosage forms: Acetaminophen (paracetamol). *Journal of pharmaceutical sciences*. 2006;95(1):4-14.
447. Lindenberg M, Kopp S, Dressman JB. Classification of orally administered drugs on the World Health Organization Model list of Essential Medicines according to the biopharmaceutics classification system. *European Journal of Pharmaceutics and Biopharmaceutics*. 2004;58(2):265-78.

448. Bolten D, Lietzow R, Türk M. Solubility of Ibuprofen, Phytosterol, Salicylic Acid, and Naproxen in Aqueous Solutions. *Chemical Engineering & Technology*. 2013;36(3):426-34.
449. Rashid A, White ET, Howes T, Litster JD, Marziano I. Effect of Solvent Composition and Temperature on the Solubility of Ibuprofen in Aqueous Ethanol. *Journal of Chemical & Engineering Data*. 2014;59(9):2699-703.
450. Wu C-Y, Benet LZ. Predicting Drug Disposition via Application of BCS: Transport/Absorption/Elimination Interplay and Development of a Biopharmaceutics DrugDisposition Classification System. *Pharmaceutical Research*. 2005;22(1):11-23.
451. Yiping D, Takahiro W, editors. Network on chips structure for mapping two hidden layers bp-anns. ITC-CSCC: International Technical Conference on Circuits Systems, Computers and Communications; 2008.
452. Wray B, Palmer A, Bejou D. Using neural network analysis to evaluate buyer-seller relationships. *European journal of Marketing*. 1994.
453. Aggarwal CC, Reddy CK. *Data Clustering: Algorithms and Applications*: CRC Press; 2018.
454. Nokhodchi A, Raja S, Patel P, Asare-Addo K. The role of oral controlled release matrix tablets in drug delivery systems. *BioImpacts : BI*. 2012;2(4):175-87.
455. Bhowmik D, Gopinath H, Kumar BP, Duraivel S, Kumar KS. Controlled release drug delivery systems. *The Pharma Innovation*. 2012;1(10, Part A):24.
456. Levina M, Rajabi-Siahboomi AR. The influence of excipients on drug release from hydroxypropyl methylcellulose matrices. *Journal of pharmaceutical sciences*. 2004;93(11):2746-54.
457. Cunha-Filho M, Araújo MR, Gelfuso GM, Gratieri T. FDM 3D printing of modified drug-delivery systems using hot melt extrusion: a new approach for individualized therapy. *Therapeutic Delivery*. 2017;8(11):957-66.
458. Dhingra G, Rakha P, Rajera R, Nagpal M. Raising The Issues of Error in Dissolution Testing 123 4. 2010.
459. Zhang L, Ha K, Kleintop B, Phillips S, Scheer B. Differences in in vitro dissolution rates using single-point and multi-point sampling. *Dissolution Technologies*. 2007;14(4):27-31.
460. Shah VP, Gurbarg M, Noory A, Dighe S, Skelly JP. Influence of higher rates of agitation on release patterns of immediate-release drug products. *Journal of pharmaceutical sciences*. 1992;81(6):500-3.
461. Savage TS, Wells CE. Automated sampling of in vitro dissolution medium: effect of sampling probes on dissolution rate of prednisone tablets. *Journal of pharmaceutical sciences*. 1982;71(6):670-3.
462. Yang Y, Ye Z, Su Y, Zhao Q, Li X, Ouyang D. Deep learning for in vitro prediction of pharmaceutical formulations. *Acta Pharmaceutica Sinica B*. 2019;9(1):177-85.
463. Lusci A, Pollastri G, Baldi P. Deep Architectures and Deep Learning in Chemoinformatics: The Prediction of Aqueous Solubility for Drug-Like Molecules. *Journal of Chemical Information and Modeling*. 2013;53(7):1563-75.
464. Eudpristine. Problems of Small Data and How to Handle Them 2016 [cited 2020 3-6]. Available from: <https://www.edupristine.com/blog/managing-small-data#:~:text=Limited%20number%20of%20observations%20means,not%20sampled%20randomly%20from%20population.>
465. Leane MM, Cumming I, Corrigan OI. The use of artificial neural networks for the selection of the most appropriate formulation and processing variables in order to predict the in vitro dissolution of sustained release minitables. *AAPS PharmSciTech*. 2003;4(2):E26.
466. Ouyang D, Smith SC. *Computational pharmaceutics : application of molecular modeling in drug delivery*: John Wiley & Sons, Ltd.; 2015.
467. Youan BBC. *Chronopharmaceutics: Science and Technology for Biological Rhythm Guided Therapy and Prevention of Diseases*: Wiley; 2009.
468. Khaled SA, Burley JC, Alexander MR, Yang J, Roberts CJ. 3D printing of five-in-one dose combination polypill with defined immediate and sustained release profiles. *Journal of Controlled Release*. 2015;217:308-14.

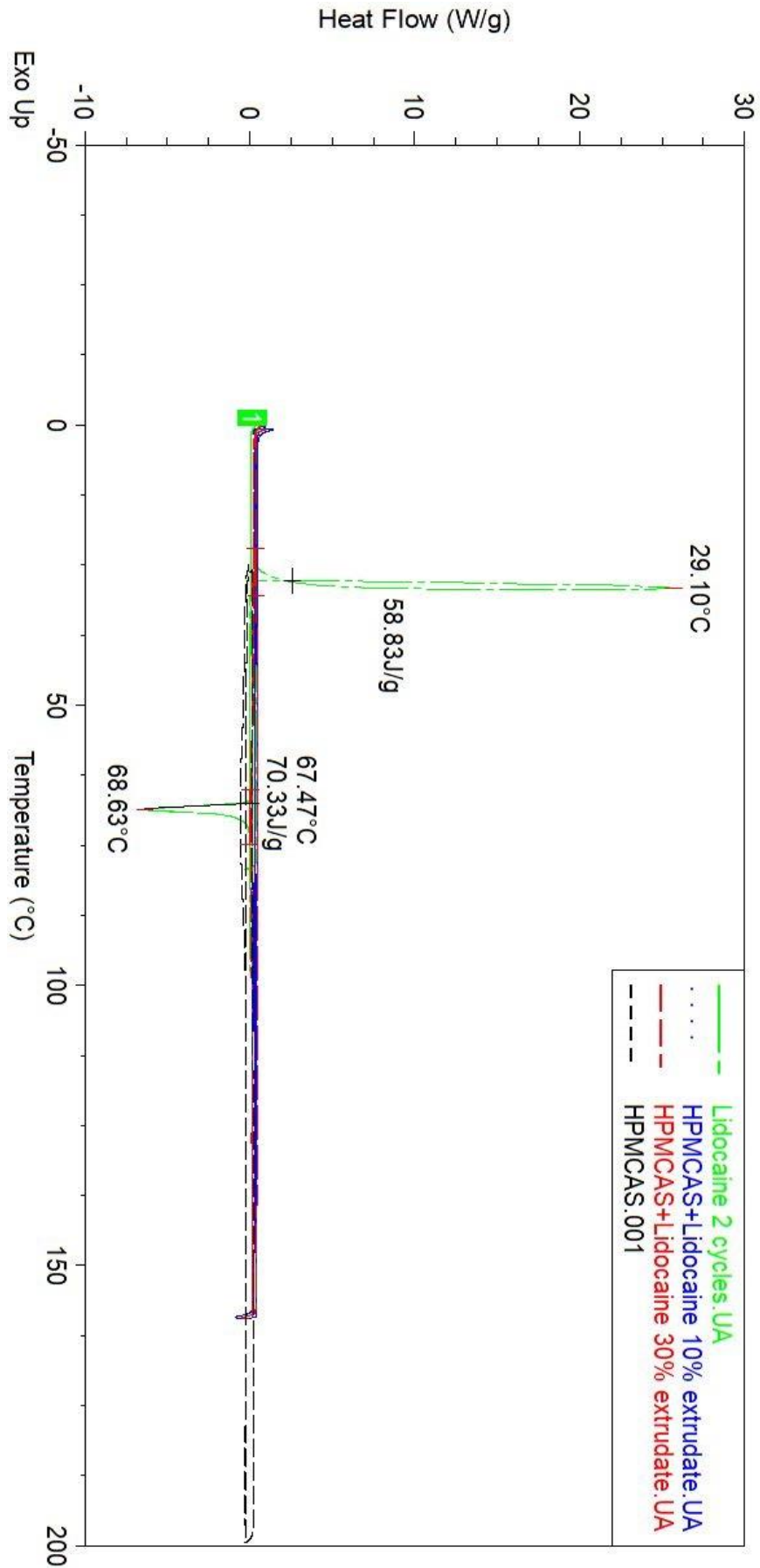
Appendix

DSC thermograms

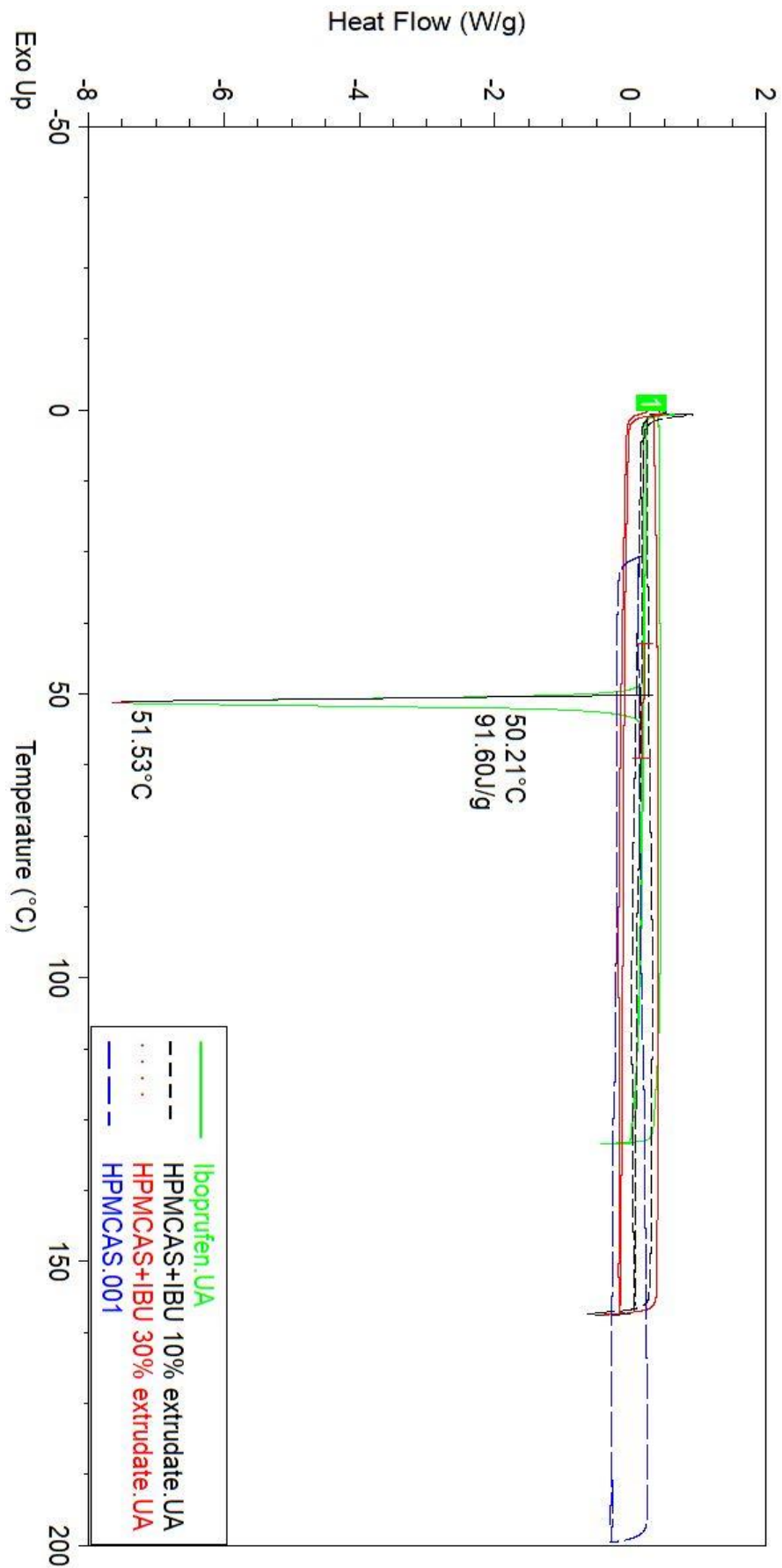
Paracetamol loaded PVA extrudates



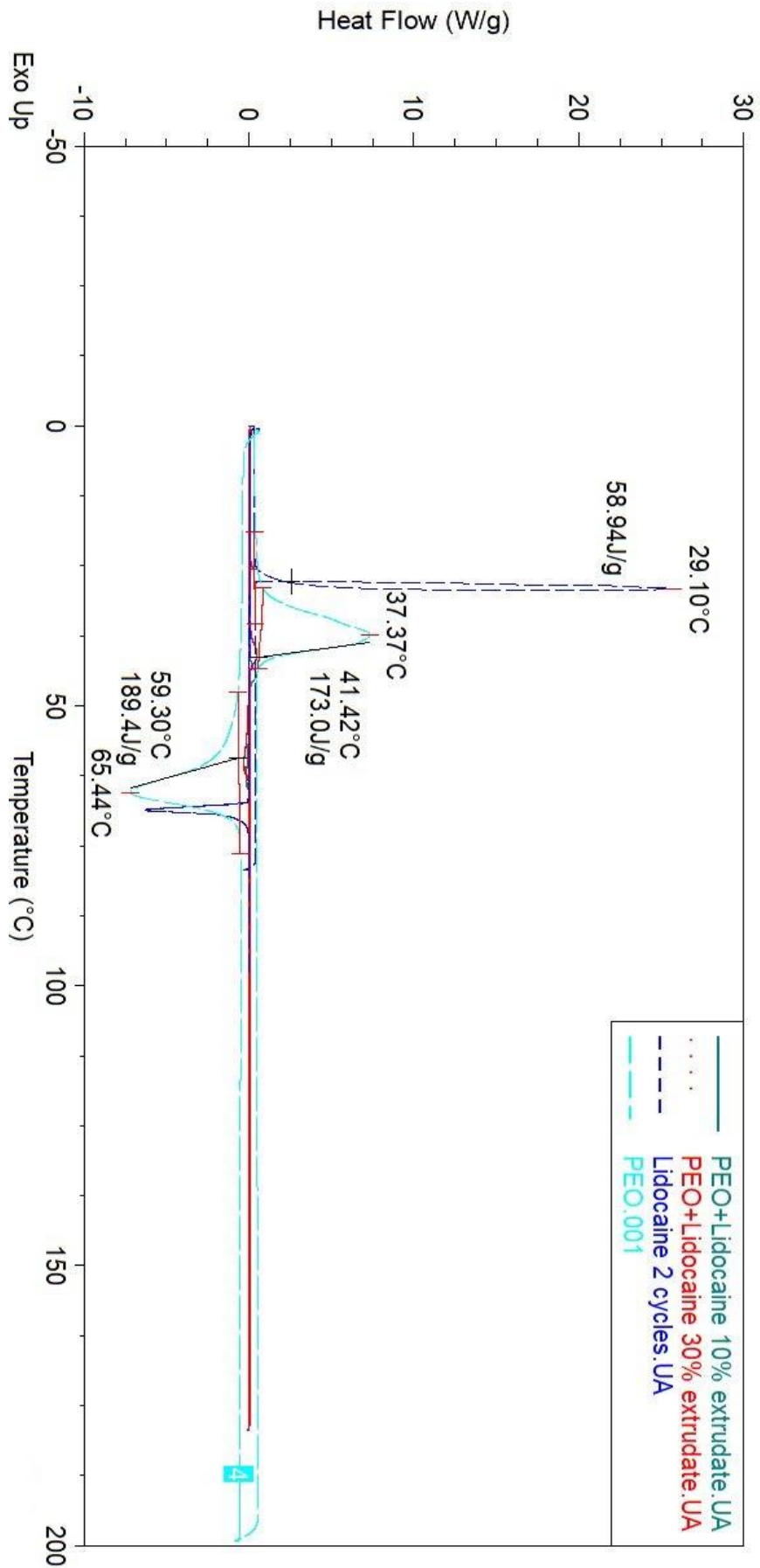
Appendix Figure 1: DSC thermogram of 10% PCM loaded PVA extrudate. The Tg of the mixture is 53.64 °C.



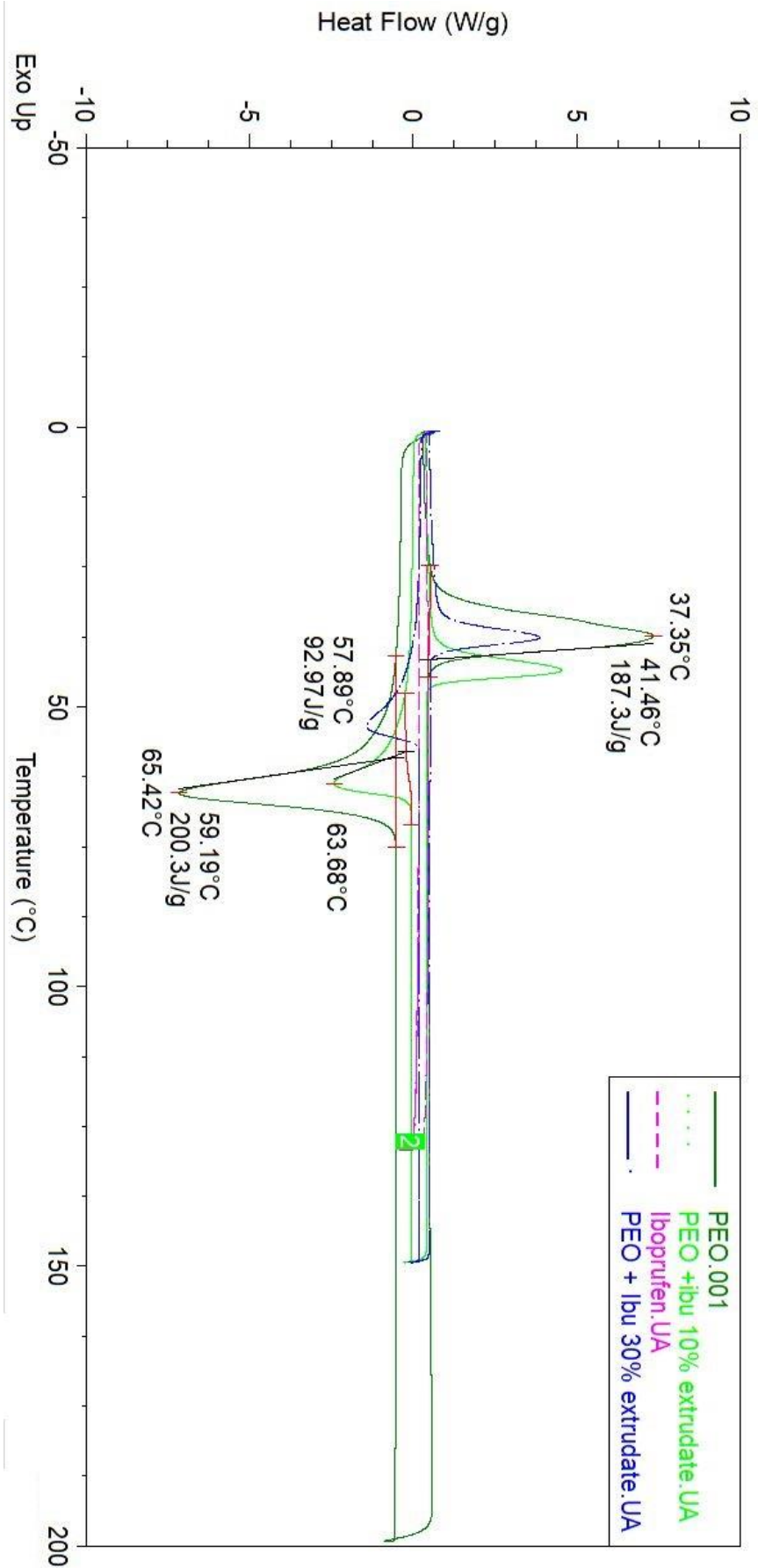
Appendix Figure 2: Lidocaine loaded HPMCAS formulations showing enthalpy of kinetic events



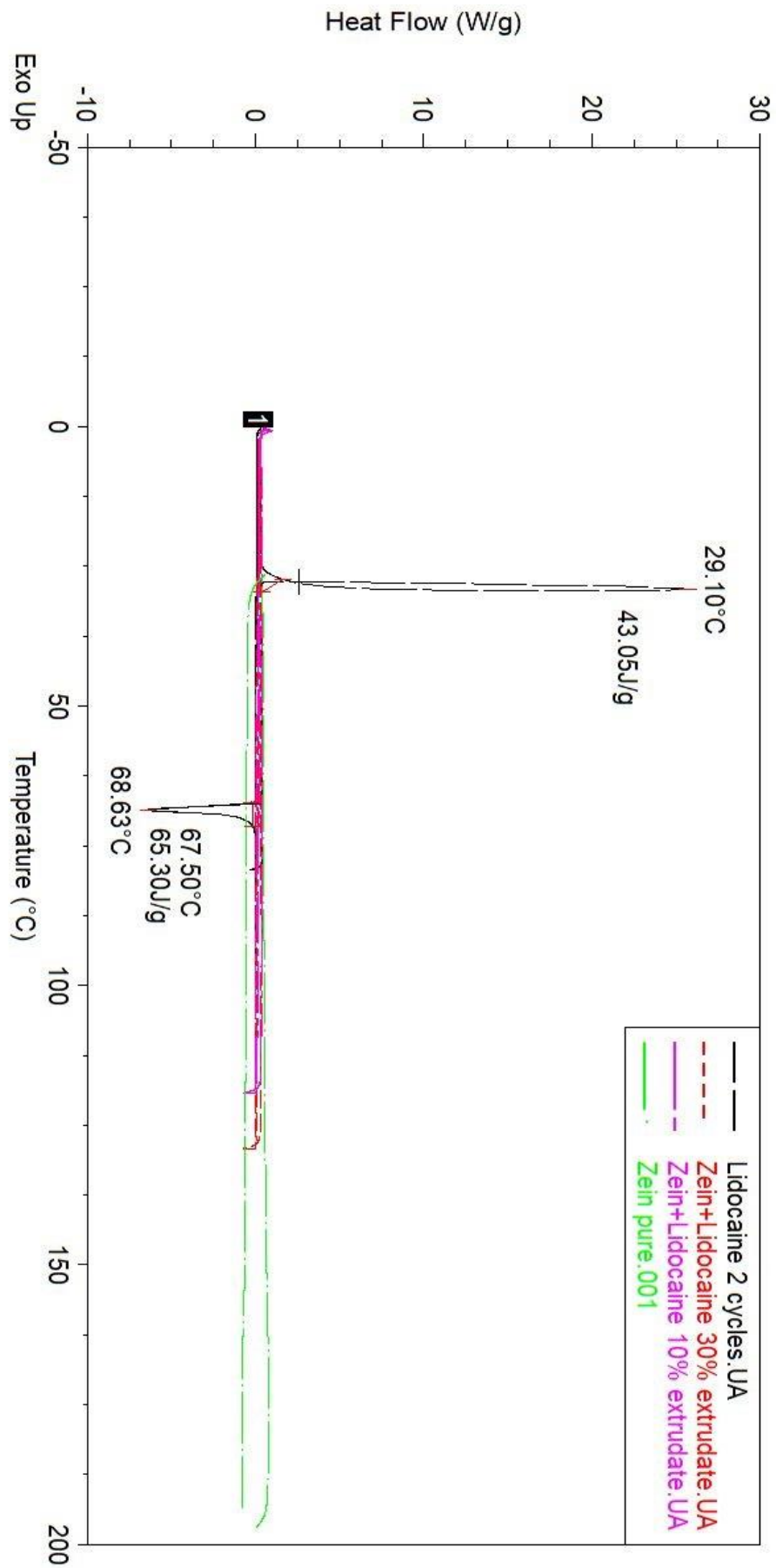
Appendix Figure 3: Lidocaine loaded HPMCAS formulations showing enthalpy of kinetic events



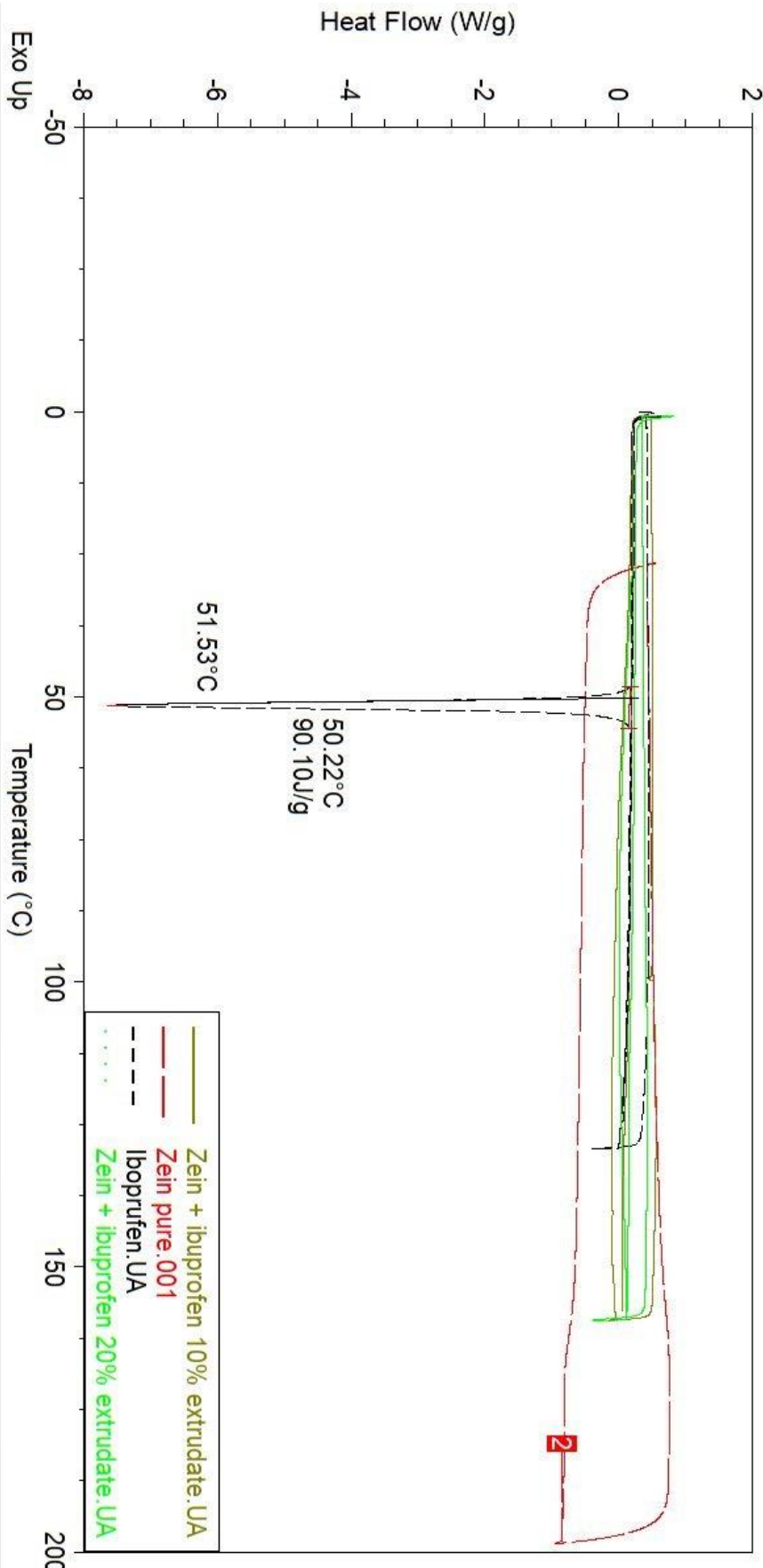
Appendix Figure 4: Lidocaine loaded PEO formulations showing enthalpy of kinetic events



Appendix Figure 5: Ibuprofen loaded PEO formulations showing enthalpy of kinetic events

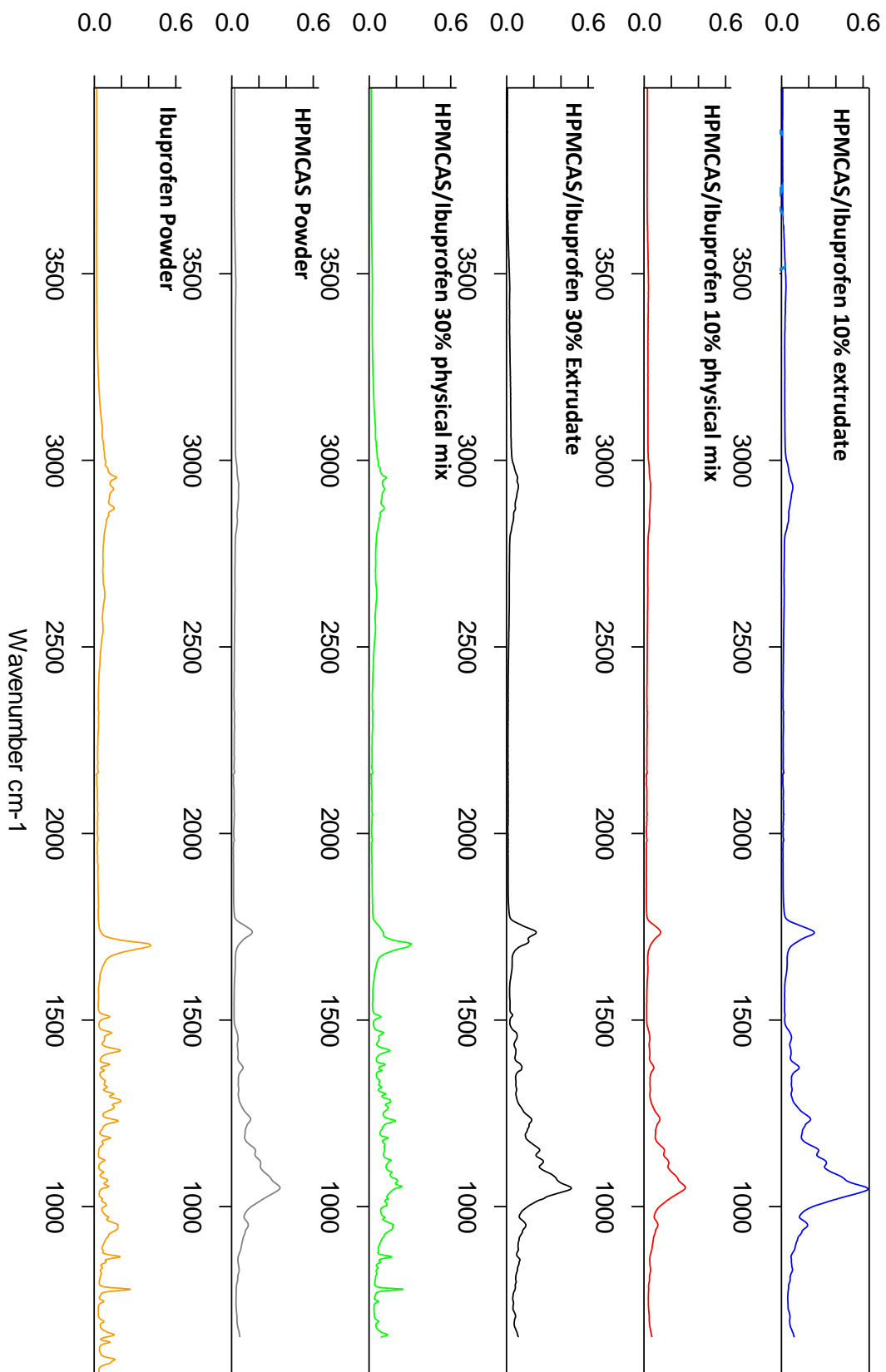


Appendix Figure 6: Lidocaine loaded Zein formulations showing enthalpy of kinetic events

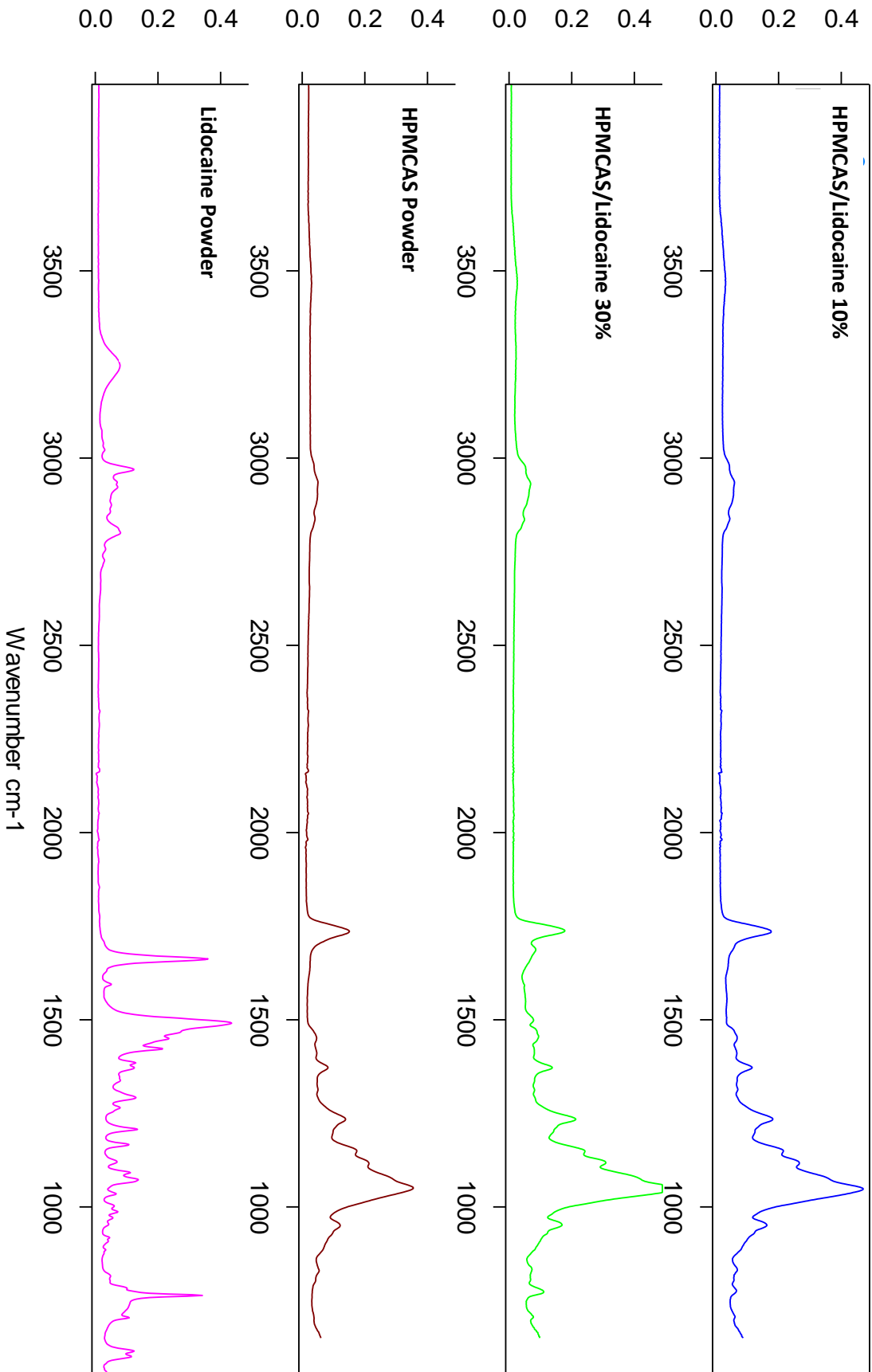


Appendix Figure 7: Ibuprofen loaded Zein formulations showing enthalpy of kinetic events

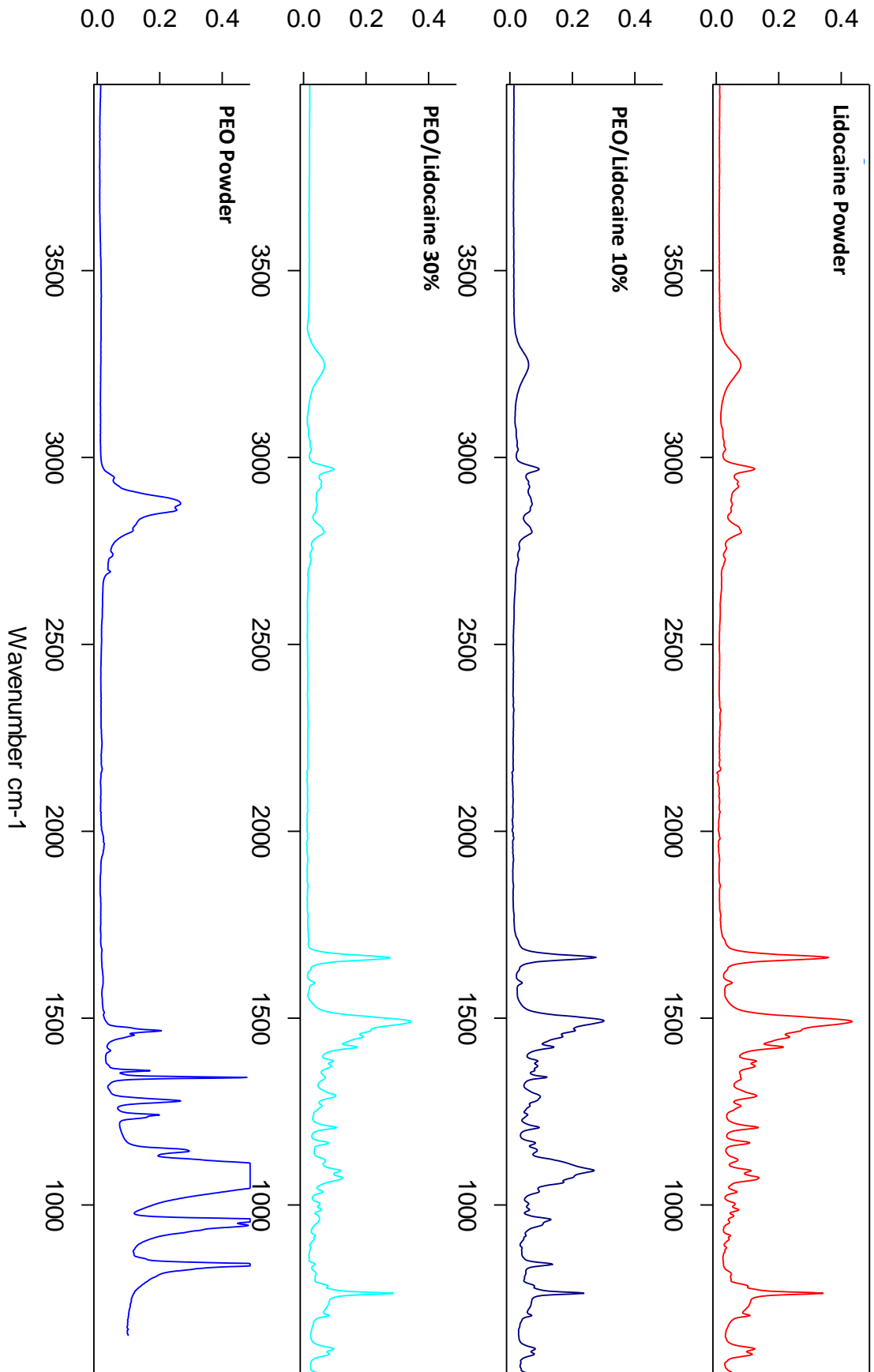
FTIR spectra



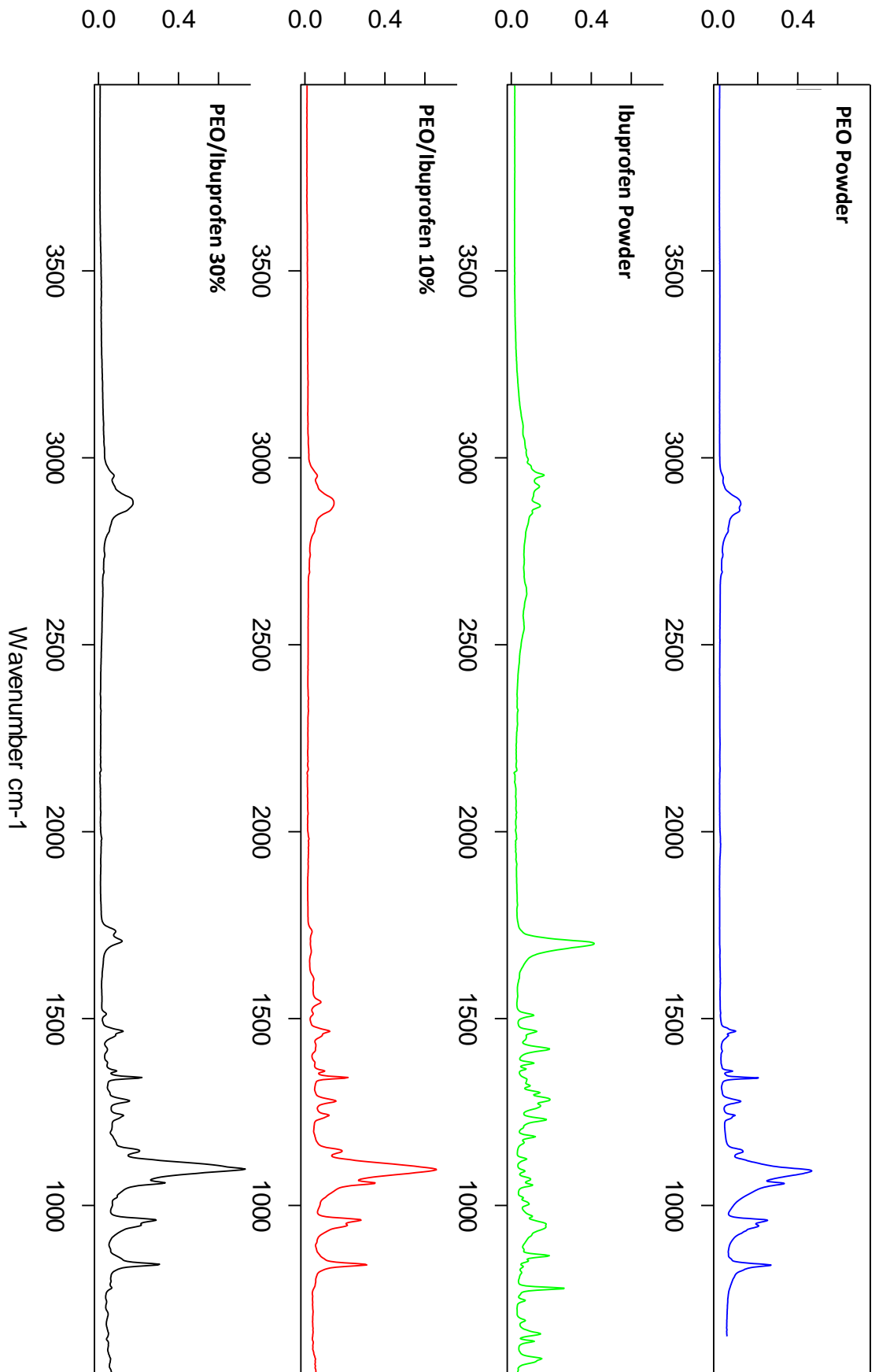
Appendix Figure 8: Ibuprofen loaded HPMCAS formulation



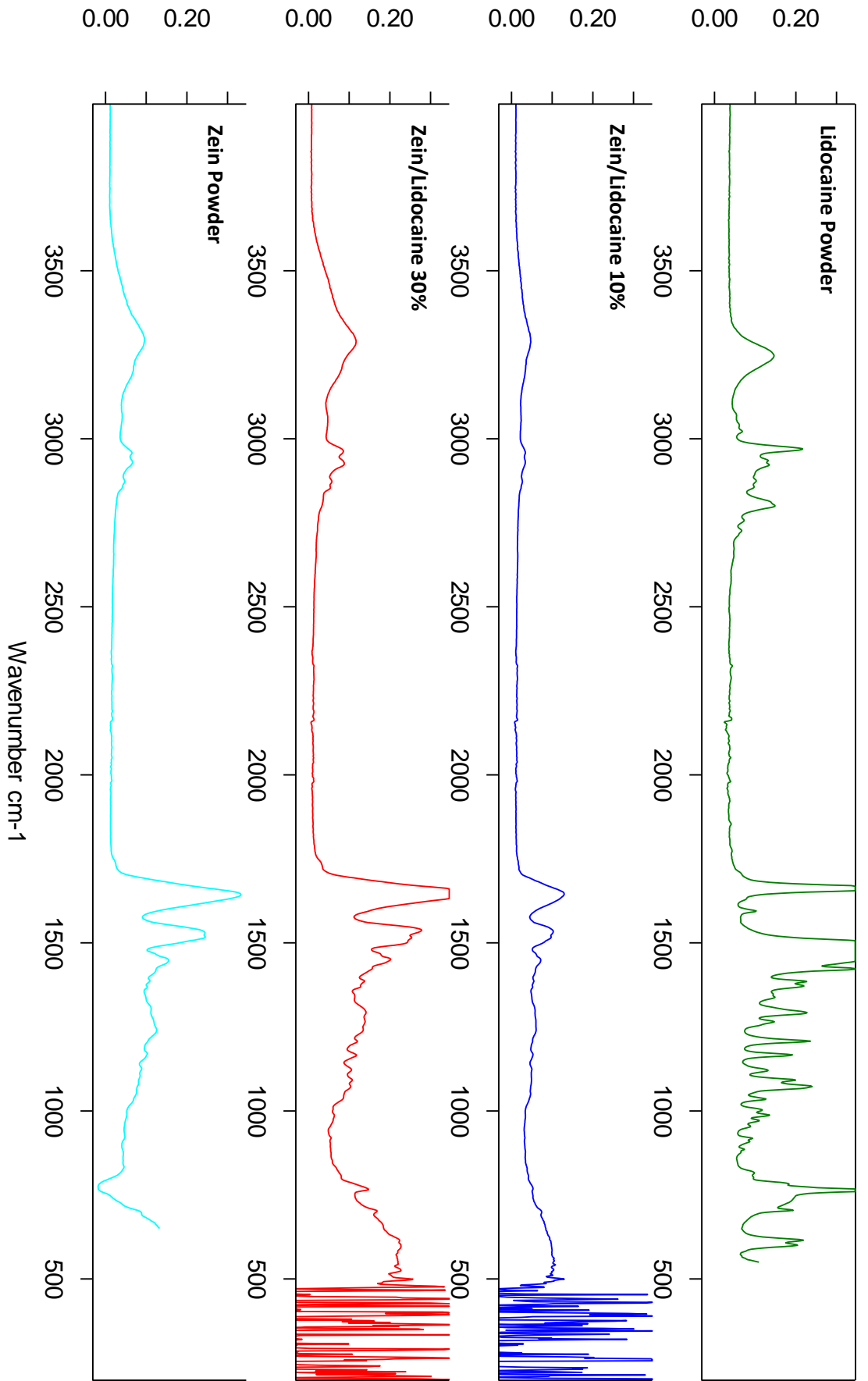
Appendix Figure 9: Lidocaine loaded HPMCAS formulation



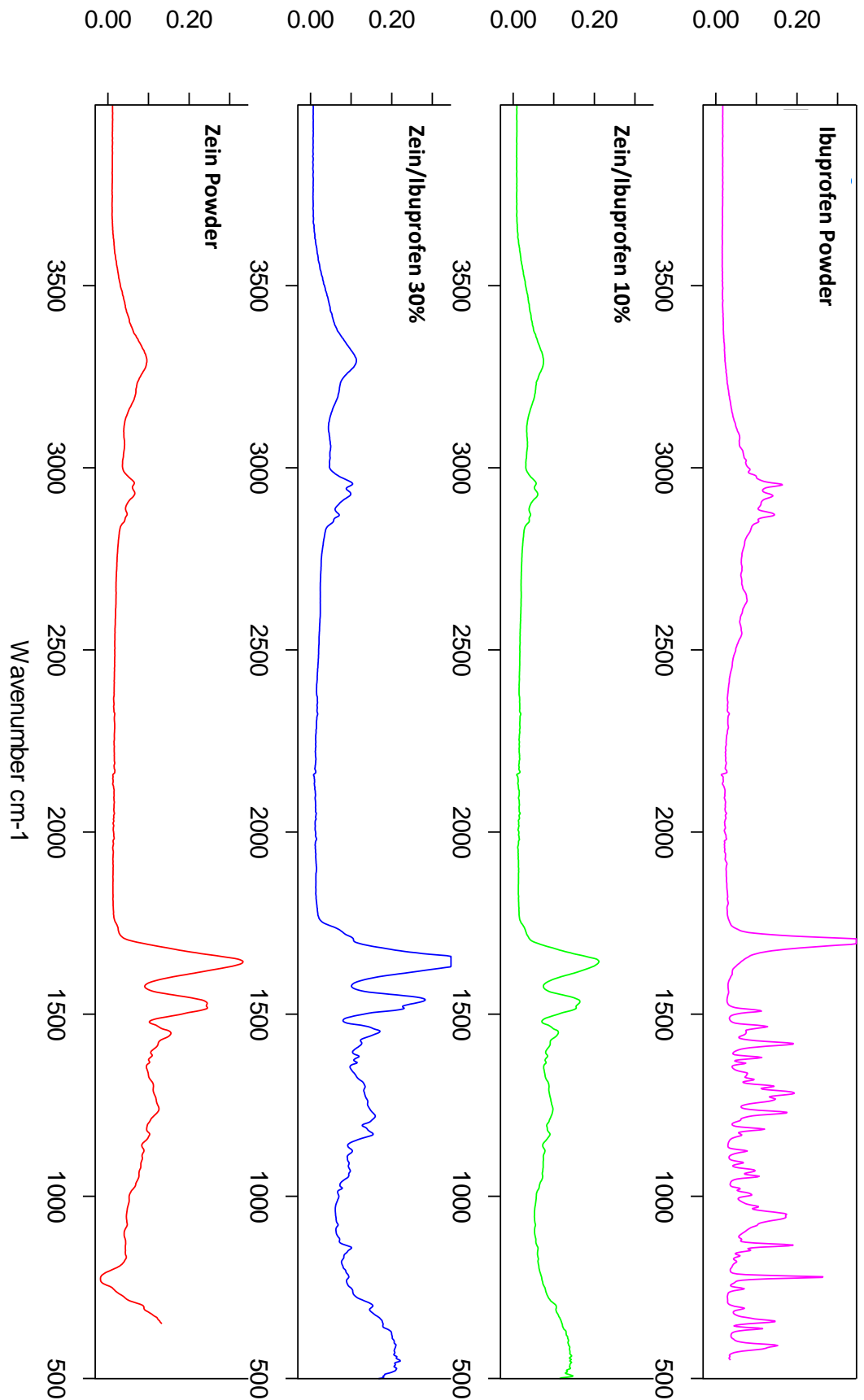
Appendix Figure 10: Lidocaine loaded PEO formulation



Appendix Figure 11: Ibuprofen loaded PEO formulation



Appendix Figure 12: Lidocaine loaded Zein formulation



Appendix Figure 13: Ibuprofen loaded Zein formulation